Numerical Simulation of Unsteady Three-Dimensional Sheet Cavitation

A.H. Koop

Numerical Simulation of Unsteady Three-Dimensional Sheet Cavitation
A.H. Koop

Thesis University of Twente, Enschede - With ref. - With summary in Dutch.
ISBN 978-90-365-2701-9

Copyright © 2008 by A.H. Koop, Enschede, the Netherlands

NUMERICAL SIMULATION OF UNSTEADY THREE-DIMENSIONAL SHEET CAVITATION

PROEFSCHRIFT

ter verkrijging van
de graad van doctor aan de Universiteit Twente,
op gezag van de rector magnificus,
prof. dr. W.H.M. Zijm,
volgens besluit van het College voor Promoties
in het openbaar te verdedigen
op vrijdag 12 september 2008 om 13.15 uur

door

Arjen Hemmy Koop

geboren op 1 juni 1979
te Willemstad, Curaçao, Nederlandse Antillen

Dit proefschrift is goedgekeurd door de promotoren:

prof. dr. ir. H.W.M. Hoeijmakers
prof. dr. -ing. habil. G.H. Schnerr

SUMMARY

This thesis describes the development of a computational method based on the Euler equations to predict the structure and dynamics of 3D unsteady sheet cavitation as it occurs on stationary hydrofoils, placed in a steady uniform inflow.

Since the 1990s numerical methods based on the Euler or Navier-Stokes equations have been developed to predict cavitating flows. Many existing cavitation models depend on empirical parameters for the production and destruction of vapor. In this thesis the equilibrium cavitation model is employed, which assumes local thermodynamic and mechanical equilibrium in the two-phase flow region. This model does not depend on empirical constants for the modeling of cavitation.

From the experimental investigation of Foeth* it has become clear that the shedding of a sheet cavity is governed by the direction and momentum of the re-entrant and side-entrant jets and their impingement on the free surface of the cavity. Therefore, the accurate prediction of the re-entrant and side-entrant jets is paramount for an accurate prediction of the shedding of the sheet cavity. It appears that these effects are inertia driven and it is expected that a numerical method based on the Euler equations is able to capture the phenomena associated with unsteady sheet cavitation.

Due to the dynamics of sheet cavitation strong pressure pulses are often generated, originating from the collapse of shed vapor structures. To be able to predict the dynamics of the pressure waves, in this thesis the fluid is considered as a compressible medium by adopting appropriate equations of state for the liquid phase, the two-phase mixture and the vapor phase of the fluid.

Sheet cavitation occurs on hydrofoils, on impellers of pumps and on ship propellers. To allow for the treatment of geometrically complex configurations and to have the

** The work of Foeth, "The Structure of Three-Dimensional Sheet Cavitation", thesis TU Delft (2008), has been carried out within STW Project TSF.6170. The research presented in the present thesis is part of the same project.*

flexibility to efficiently refine grids locally in regions with cavitation, the numerical method developed is an edge-based, finite-volume method. The present numerical method can handle unstructured grids consisting of any type of elements, i.e. quadrilaterals and/or triangles in 2D and hexahedrons, prisms, tetrahedrons and/or pyramids in 3D.

This research has been conducted in close collaboration with the Department of Maritime Technology at Delft University of Technology (DUT), where experiments have been carried out for flows with cavitation. Within this collaboration a number of hydrofoil configurations have been designed employing the present numerical method. These configurations have been tested in the cavitation tunnel at DUT. In the present thesis the main aspects of the dynamics of the vapor sheet as observed on one of the three-dimensional configurations, i.e. the 3D Twist11 hydrofoil, are summarized and utilized to validate the present numerical method.

The main interest in the formulation of the numerical method is to address the critical aspects of the numerical simulation of the flow of a compressible fluid over a wide range of Mach numbers employing an arbitrary equation of state. Emphasis is on the numerical solution of the low-Mach number flow and the formulation of the boundary conditions for the finite-volume method implemented for an edge-based unstructured mesh.

Schmidt, in the group of Prof. Schnerr at TU Munich, has developed a Riemann-based flux scheme implemented for a structured mesh. This scheme performs excellently for low-Mach number flows without the necessity to use preconditioning. In collaboration with Schmidt and Prof. Schnerr, this flux scheme has been implemented in the present edge-based numerical method for unstructured grids. Second-order accuracy is obtained by employing the limiter of Venkatakrishnan.

In the present research the formulation for the non-reflective in- and outflow boundary conditions for the Euler equations, as proposed by Thompson for the ideal gas equation of state, have been generalized for an arbitrary equation of state. Furthermore, the solid wall boundary conditions at the surface of the hydrofoil are treated by the specially designed Curvature Corrected Symmetry Technique.

Several test cases for single-phase water flow have been carried out to assess the performance of the numerical method. The one-dimensional “Water Hammer” problem and a “Riemann problem for liquid flow” have been considered in order to demonstrate the wave-capturing ability of the numerical method. The low-Mach number flow over a two-dimensional cylinder is calculated to illustrate the capabil-

ity of the present method to accurately calculate steady-state results for these flows without the use of preconditioning methods. The numerical results for the flow about two-dimensional NACA sections illustrate the second-order accuracy of the present method. Furthermore, it is demonstrated that hybrid meshes consisting of multiple element types can be used allowing efficient grid refinement close to the surface of the hydrofoil. The single-phase water flow over the three-dimensional Twist11 hydrofoil is presented to validate the numerical method with experimental results. It is found that the pressure distribution on the foil is accurately predicted. The lift coefficient is predicted to within 2% of the experimentally obtained value.

For cavitating flow, the one-dimensional "Closing Valve" test case and the "Two-Rarefaction waves" test case are considered, which demonstrate the convergence and stability of the developed numerical method. Subsequently, results for cavitating flow about two-dimensional hydrofoils are presented. It is shown that the re-entrant jet, the shedding of the sheet cavity, the collapse of the shed vapor cloud and the periodic nature of the shedding are captured by the present numerical method.

The three-dimensional unsteady cavitating flow about the 3D Twist11 hydrofoil is calculated. It is shown that the formation of the re-entrant flow and of a cavitating horse-shoe vortex are captured by the present numerical method. The calculated results are quite similar to the experimental observations. However, at present the computational time is too long to numerically investigate the unsteady periodic shedding of the sheet cavity on three-dimensional configurations for long enough times.

In addition, the steady cavitating flow about the geometrically more complex 3D Elliptic 11 Rake finite-span hydrofoil is simulated to show the capability of the numerical method to predict sheet cavitation on a complex three-dimensional geometry. It is found that the predicted shape of the sheet cavity corresponds well with the experimental results. However, the cavitation in the generated tip vortex observed in the experiment is not captured in much detail, primarily due to numerical dissipation in the highly rotational flow in the vortex core.

Finally, within the scope of the present research non-equilibrium models for cavitation have been investigated as well. For this the conventional approach is adopted in which it is assumed that the liquid and vapor phase have a constant density. To solve the governing equations for this model, we have applied the JST flux scheme combined with the pre-conditioning method of Weiss & Smith. Some difficulties were encountered with the JST scheme as well as drawbacks of the conventional cavitation models. It is recommended to carry out more research into the non-equilibrium models aimed at obtaining satisfactory results.

SAMENVATTING

Dit proefschrift beschrijft de ontwikkeling van een rekenmethode gebaseerd op de Euler vergelijkingen voor het voorspellen van de structuur en dynamica van 3D, instationaire vliescavitatie zoals voorkomt op een stationaire hydrofoil geplaatst in een stationaire, uniforme aanstroming.

Om het gedrag van caviterende stromingen te voorspellen zijn sinds de jaren 90 numerieke methoden ontwikkeld gebaseerd op de Euler en Navier-Stokes vergelijkingen. Veel bestaande modellen voor caviterende stromingen zijn afhankelijk van empirische parameters voor de produktie en destructie van waterdamp. In dit proefschrift wordt het equilibrium cavitatie model beschouwd, waarin lokaal thermisch en mechanisch evenwicht wordt verondersteld. Dit model is niet afhankelijk van empirische constanten voor het modelleren van cavitatie.

Zoals gevonden in het experimentele onderzoek van Foeth[†] wordt het afschudden van een vliescaviteit bepaald door de richting en momentum van de *re-entrant* en *side-entrant jets* en hun botsing met het vrije oppervlak van het vlies. Om deze reden is de nauwkeurige voorspelling van de *re-entrant* en *side-entrant jets* een kritische factor in een nauwkeurige voorspelling van het afschud-gedrag van de vliescaviteit. Omdat deze effekten gedreven worden door inertia, is aangenomen dat een numerieke methode gebaseerd op de Euler vergelijkingen de fenomenen die optreden bij vliescavitatie kan voorspellen.

De dynamica van vliescavitatie gaat vaak gepaard met sterke druk pulsen, die ontstaan door het ineen klappen van afgeschudde damp strukturen. Om de golf-dynamica van deze druk pulsen te kunnen voorspellen, wordt in dit proefschrift de vloeistof beschouwd als een samendrukbaar medium. Hiertoe zijn geschikte toestandsvergelijkingen voor de water fase, het twee-fase mengsel en de damp fase gekozen.

[†]*Het werk van Foeth, "The Structure of Three-Dimensional Sheet Cavitation", proefschrift TUD (2008), is verricht binnen het STW Project TSF.6170. Het onderzoek gepresenteerd in het huidige proefschrift maakt deel uit van hetzelfde projekt.*

Vliescavitatie komt voor op hydrofoils, op impellers van pompen en op scheepsschroeven. Om geometrisch complexe configuraties te kunnen doorrekenen en om de flexibiliteit te behouden om efficient het rekenrooster lokaal te verfijnen in gebieden met cavitatie, is een *edge-based*, eindige-volume methode ontwikkeld. De huidige rekenmethode kan de caviterende stroming berekenen op ongestruktureerde roosters die bestaan uit verschillende typen elementen, namelijk vierhoeken en/of driehoeken in 2D en kubussen, prisma's, tetraeders en/of pyramiden in 3D.

Dit onderzoek is uitgevoerd in nauwe samenwerking met de afdeling Maritieme Techniek van de Technische Universiteit Delft (TUD), waar experimenten zijn uitgevoerd aan caviterende stromingen. Binnen deze samenwerking zijn een aantal hydrofoil-configuraties ontworpen met de huidige numerieke methode. Deze configuraties zijn getest in de cavitatie tunnel van TUD. De belangrijke aspecten van de dynamica van de vliescaviteit, zoals waargenomen op een van de drie-dimensionale configuraties, namelijk de 3D Twist hydrofoil, zijn in dit proefschrift samengevat en gebruikt om de ontwikkelde numerieke methode te valideren.

Het belangrijkste aspect in de formulering van de numerieke methode is het numerieke schema voor de stroming van een samendrukbare vloeistof, over een groot bereik van het Mach getal, beschreven door een willekeurige toestandsvergelijking. De nadruk ligt op de nauwkeurigheid van het numerieke schema bij lage Mach getallen en op de formulering van de randvoorwaarden voor de eindige-volume methode geïmplementeerd voor een *edge-based* ongestruktureerd rekenrooster.

Schmidt, in de afdeling van Prof. Schnerr aan de TU Munchen, heeft een flux schema ontwikkeld voor laag-Mach getal stroming. Dit flux schema is gebaseerd op de oplossing van het Riemann probleem en maakt geen gebruik van preconditioneringsmethoden. Schmidt heeft zijn flux schema geïmplementeerd in een numerieke methode voor gestruktureerde rekenroosters. Dit *Riemann-based* flux schema is in samenwerking met Schmidt en Prof. Schnerr geïmplementeerd in de huidige *edge-based* numerieke methode voor ongestruktureerde rekenroosters.

In het huidige onderzoek zijn de niet-reflecterende in- en uitstroom randvoorwaarden voor de Euler vergelijkingen, zoals geformuleerd door Thompson voor de toestandsvergelijking voor een ideaal gas, gegeneralizeerd voor een willekeurige toestandsvergelijking. Verder zijn de vaste wand randvoorwaarden op het oppervlak van de hydrofoil opgelegd met de speciaal ontworpen *Curvature Corrected Symmetry* techniek.

Om de prestatie van de numerieke methode te bepalen zijn verschillende test gevallen voor de één-fase stroming van water uitgevoerd. Aan de hand van het één-dimensionale "Water hamer" probleem en een "Riemann probleem voor vloeistof-stroming" is gedemonstreerd dat de ontwikkelde numerieke methode het golf karakter van de oplossing nauwkeurig representeert. De twee-dimensionale stroming rondom een cirkel-cylinder bij een laag Mach getal is berekend om te illustreren dat de huidige numerieke methode zo'n stroming nauwkeurig kan berekenen zonder preconditionerings methoden te gebruiken. De numerieke resultaten voor de twee-dimensionale stroming rond NACA secties illustreren de tweede-orde nauwkeurigheid van de huidige methode. Verder is gedemonstreerd dat hybride rekenroosters bestaande uit meerdere element typen gebruikt kunnen worden, waardoor het rekenrooster vlakbij het oppervlak van de hydrofoil efficient verfijnd kan worden. De één-fase stroming van water over de drie-dimensionale Twist11 hydrofoil is berekend om de numerieke methode te valideren met experimentele resultaten. De druk verdeling op de vleugel wordt nauwkeurig voorspeld. De voorspelde lift coefficient ligt binnen 2% van de experimenteel gevonden waarde.

Voor stromingen met cavitatie zijn het één-dimensionale "*Closing Valve*" test geval en het "twee expansie golven" test probleem beschouwd. De resultaten laten de convergentie en stabiliteit van de ontwikkelde numerieke methode zien. Vervolgens worden de resultaten voor de caviterende stroming rond twee-dimensionale hydrofoil-secties gepresenteerd. De resultaten laten zien dat de huidige numerieke methode de *re-entrant jet*, het afschudden van de vliescaviteit, het ineen klappen van de afgeschudde bellen-wolk en het periodieke gedrag, voorspelt.

De instationaire caviterende stroming rond de 3D Twist11 hydrofoil is berekend. De resultaten van de numerieke methode laten zien dat de ontwikkeling van de *re-entrant flow* en de vorming van een caviterende *horse-shoe* wervel voorspeld kunnen worden. De berekende resultaten komen overeen met de experimentele observaties. Echter, op dit moment is de benodigde rekentijd te lang om de instationaire periodieke afschudding van de vliescaviteit op drie-dimensionale configuraties lang genoeg numeriek te onderzoeken.

Vervolgens is de stationaire caviterende stroming rond de geometrisch complexe 3D Elliptic 11 Rake vleugel met eindige spanwijdte berekend om te demonstreren dat de huidige methode de vliescaviteit kan voorspellen op een complexe drie-dimensionale configuratie. De voorspelde vorm van de vliescaviteit komt goed overeen met die gevonden in de experimenten. Echter, de resolutie van de tip wervel is ontoereikend om tip-wervel cavitatie te voorspellen. Dit is hoofdzakelijk vanwege numerieke dissipatie in de grote gradienten van de oplossing in de kern van de wervel.

Binnen het trajekt van het huidige onderzoek zijn ook niet-evenwichts modellen voor cavitatie onderzocht. Hierbij is de gebruikelijke aanpak gevolgd door aan te nemen dat de dichtheid van zowel de vloeistof- als de dampfase constant zijn. Om de vergelijkingen voor dit model op te lossen, is het JST flux schema toegepast in combinatie met de preconditionings-methode van Weiss & Smith. Tekortkomingen van het JST schema in combinatie met cavitatie zijn gevonden alsmede enkele tekortkomingen van de conventionele modellen voor cavitatie. Meer onderzoek naar niet-evenwichts modellen is noodzakelijk om tot bevredigende resultaten te komen.

TABLE OF CONTENTS

INTRODUCTION

CHAPTER 1

1.1 Introduction to numerical simulation of sheet cavitation

Cavitation is the evaporation of a liquid in a flow when the pressure drops below the saturation pressure of that liquid. The importance of understanding cavitating flows is related to their occurrence in various technical applications, such as pumps, turbines, ship propellers and fuel injection systems, as well as in medical sciences such as lithotripsy treatment and the flow through artificial heart valves. Cavitation does not occur in water only, but in any kind of liquid such as liquid hydrogen and oxygen in rocket pumps or the lubricant in a bearing. The appearance and disappearance of regions with vapor is a major cause of noise, vibration, erosion and efficacy loss in hydraulic machinery. In many technical applications cavitation is hardly avoidable at all operating conditions. When it occurs it needs to be controlled. Therefore, one needs detailed insight in the mechanisms that govern the cavitation phenomena.

There are several types of cavitation. Distinct appearances of cavitation are: sheet cavitation, bubble cavitation and vortex cavitation. The present thesis concerns the dynamics and structure of sheet cavitation. Sheet cavitation occurs on hydrofoils, on blades of pumps and propellers, specifically when the loading is high. This type of cavitation can usually not be avoided, because of high efficiency requirements. The dynamics of sheet cavitation often generates strong pressure fluctuations due to the collapse of shed vapor structures, which might lead to erosion of surface material.

Sheet cavitation is often called “fully-developed”, “attached” or “blade” cavitation. They are all terms for the same large-scale cavitation structure. There are a number of closely related important aspects to sheet cavitation:

- Shape and volume of the cavity. The topology of a sheet cavity is strongly related to the load distribution of the lifting object and thus to the pressure distribution on the object in the flow. Variations in volume cause pressure fluctuations in the liquid that might lead to strong vibrations of nearby structures.

FIGURE 1.1: *Sheet cavitation on 2D hydrofoil. Photo taken by Foeth.*

- Re-entrant flow at the closure region of sheet cavity. The re-entrant and side-entrant flow dictate the behavior of the shedding of the cavity sheet. The shape of the closure region of the cavity sheet dictates the direction of the re-entrant and side-entrant jets.

- Shedding and collapse of vapor structures. The break-up of a sheet cavity causes a vortical flow of bubbly vapor clouds to be convected to regions with higher pressure. Here, these clouds collapse resulting in strong pressure pulses leading to unsteady loads of nearby objects as well as noise production and possible erosion of surface material.

Since the 1990s numerical methods using the Euler or Navier-Stokes equations have been developed to simulate cavitating flows. The development of these methods has been advancing quickly in recent years, but they are still considered to be in a developing stage. The main problem in the numerical simulation of multi-dimensional unsteady cavitating flow is the simultaneous treatment of two very different flow regions: (nearly) incompressible flow of pure liquid in most of the flow domain and low-velocity highly compressible flow of (pure) vapor in relatively small parts of the flow domain. In addition, the two flow regimes can often not be distinguished that clearly, for example in the transition region between vapor and liquid, i.e. the mixture region of liquid and vapor.

Furthermore, unsteady three-dimensional cavitating flow calculations require substantial computer resources both in terms of memory and speed. Also, meshes with appropriate high-resolution mesh density in the cavitating flow region are necessary.

In the present research a numerical method for solving the Euler equations for 3D unsteady cavitating flow is developed. The accurate prediction of the direction and

momentum of the re-entrant and side-entrant jets and their impingement on the cavity surface form the indispensable basis of an accurate prediction of the shedding of the cavity sheet. The direction and momentum of the re-entrant jets are all thought to be inertia driven, so it is expected that a mathematical model based on the Euler equations is able to capture the major structure of sheet cavitation.

1.2 Brief history on cavitation research

Research on cavitation dates back to the days of Euler (1754) who observed the occurrence of cavitation in high speed water flow during his studies on rotating flow machinery. The word cavitation has been introduced by Froude who described the voids filled with vapor as cavities [191]. In 1895 Parsson was amongst the first to observe the negative effects of cavitation on the performance of a ship propeller [112, 196]. He was the first to build a cavitation tunnel to investigate the problems due to cavitation experienced on the propeller on the ship *Turbinia*. The cavitation number $\sigma \equiv \frac{p_\infty - p_v}{\frac{1}{2}\rho_\infty U_\infty^2}$ was introduced by Thoma in 1923 [74, 112] in the context of the experimental investigation on water turbines and pumps.

In order to study the physical aspects of cavitation many experiments have been carried out throughout the years. Theoretical and numerical approaches followed soon with two main areas of research [74]: bubble dynamics and developed- or supercavities.

A large body of work has been published on bubble dynamics. We mention, amongst many others, Rayleigh (1917) [134] and Plesset (1949) [147], after whom the Rayleigh-Plesset equation is named which describes the temporal evolution of the radius of a vapor bubble in an incompressible, viscous liquid. The evolution is driven by effects of pressure variations and surface tension.

The field of developed cavities started more than a century ago, e.g. Helmholz (1868) [89, 112] and Kirchhoff (1869) [24, 111], with the work on free-streamline theory or wake theory by using conformal mapping techniques or the non-linear hodograph technique. Birkhoff & Zarantello [24] described the hodograph technique in detail, see also Wu [222]. Wu points out that this theory can only be used for cavitating flow around simple geometries like bluff bodies and flat plates, but can not be used for cavitating flow around arbitrary bodies like hydrofoils or propeller blades. In 1953 Tulin [29, 197] applied linearization procedures to the problem of the flow about a supercavitating symmetric profile at zero angle of attack and zero cavitation number. Since then many researchers have extended the linear theory to flows around arbitrary bodies at any cavitation number.

The introduction of computers in the 1970s brought about a large number of numerical methods based on linear theory, which has been extended to three-dimensional flow problems by the use of lifting surface theory. Most lifting surface theory methods deal with sheet cavitation by imposing a transpiration type of (linearized) boundary condition on the solid surface below the sheet cavity. The advantages of lifting surface methods are their short computation times, enabling fast assessment and improvement of designs. The drawback of linear theory is that for partial cavity flows around hydrofoils it predicts that the length and volume of a cavity will increase when the thickness of the hydrofoil is increased, which contradicts experimental observations. Also for unsteady sheet cavitation the dynamic motion of a sheet cavity is not predicted [50] and linearized theory has a limited ability to describe complex flows with enough accuracy [3].

Boundary element methods (also referred to as boundary integral methods or panel methods) provided the possibility to consider the flow about geometrically complex bodies and to treat the full non-linear boundary conditions on the sheet cavity interface. These methods are based on the potential flow hypothesis, in which the cavity interface is represented by a streamline of constant pressure. The cavity surface is iterated until both the kinematic and the dynamic boundary condition are satisfied at the cavity surface [50, 206]. However, this model for cavitating flow requires an artificial closure model for the cavity detachment point near the leading edge and one at the end of the cavity sheet. Uhlman [203] (1987) was amongst the first to solve a partial cavity flow on two-dimensional hydrofoils. De Lange [55] introduced a method for the unsteady two-dimensional flow coupled to a re-entrant jet cavity closure model. Dang & Kuiper [51] and Dang [50] extended this method to steady cavitating flow about three dimensional hydrofoils. Nowadays, these methods have become well established due to their matured stage and their ability to predict fully three-dimensional unsteady cavitating flows, e.g. Kinnas [110] and Vaz [206]. However, it remains difficult to predict the detachment and closure of the sheet cavity, which have a strong influence on the topology and dynamics of the sheet cavity. Furthermore, these methods are difficult to extend to more complex physical phenomena such as the shedding of the sheet cavity and vorticity-dominated flow such as the tip vortex cavitation. The tracking of the liquid-vapor interface becomes a challenging task, because of splitting and merging of the main vapor structures and very fast vaporization and condensation phenomena.

A different approach to simulate cavitating flows emerged in the 1990s. Methods using the Euler or Navier-Stokes equations were developed together with a transport equation for the void fraction, with two-phase flow equations or with other cavitation

closure model equations. As classified by the 22nd ITTC special committee in 1999 [3] these approaches can be grouped into a number of categories. 1) Interface tracking methods 2) Volume of Fluid methods 3) Discrete bubble methods and 4) Two-phase flow methods. These methods are discussed in chapter 3. It must be noted that the distinction between some of these groups is not always completely clear and that combinations of the categories are used by different authors. Furthermore, numerical methods exist which use a combination of the lifting surface or boundary element method together with a method based on the Euler or Navier-Stokes equations.

1.3 Objective of present research

The overall objective of the project is to determine a model for the description of the dynamics of three-dimensional sheet cavitation as it occurs on hydrofoils. The aim of this thesis is to develop a numerical method employing the Euler equations for 3D unsteady flow for simulating cavitating flows. The numerical method features the following aspects:

- Three-dimensionality. The configurations with cavitating flow to be considered are three-dimensional or display a three-dimensional flow. Future applications may include flows in pumps and the flow about ship propellers.

- Compressibility. In unsteady cavitating flows strong pressure waves are generated. These waves have a strong impact on the cavitation intensity, i.e. on erosion damage. Therefore, it is necessary to treat the wave dynamics quantitatively correct, especially in the liquid phase.

- Unsteady flow conditions. Cavitating flows feature highly unsteady flow behavior, even under uniform inflow conditions.

- Low-Mach number flows. Numerical methods for density-based flow models are known to experience difficulties for low-Mach number flow conditions. In industrial applications the flow speeds of water are low with respect to the speed of sound in water. Therefore, a proper treatment of the numerical flux schemes is essential to simulate these low-Mach number flows.

- Unsteady in- and outflow boundary conditions. Constant pressure boundary conditions have a strong impact on cavitation dynamics, but they are very rare in experimental and industrial applications. Together with the self-excited periodic oscillations in the unsteady cavitating flow regime, the accurate treatment of non-reflective unsteady in- and outflow boundary conditions is essential.

- Edge-based finite volume method. Unstructured grids allow the treatment of geometrically complex configurations and the flexibility to efficiently refine grids locally.

In this thesis the equilibrium cavitation model for cavitating flows is implemented into an edge-based finite-volume method for three-dimensional, unsteady, compressible flow. The main questions to be addressed are:

- Can the dynamics and structure of three-dimensional sheet cavitation be predicted?
- Can the re-entrant jet be predicted?
- Is the shedding of the cavity sheet captured correctly?
- Can the collapse of the shed vapor structures be predicted?
- Can the unsteady loads on objects in the flow and the unsteady pressure wave dynamics be calculated?

The present research has been conducted in the framework of a STW project in close cooperation with the Department of Maritime Technology at Delft University of Technology. Foeth [67] has carried out experiments for steady and unsteady inflow conditions in the Delft cavitation tunnel for three-dimensional sheet cavities. His main objectives were:

- to provide a better insight in the physical mechanisms of the dynamics of sheet cavitation.
- to provide a detailed and accurate database of benchmark tests for the validation of computational methods.

Within the collaborative research project various hydrofoil geometries have been designed and tested in the cavitation tunnel. These configurations include the 3D Twist11 hydrofoil and the Twisted Eppler hydrofoil, see Koop *et al*. [113], Foeth *et al*. [67, 69] and appendix D.

1.4 Outline of thesis

Chapter 2 provides an overview on the physical aspects of sheet cavitation as it occurs on a hydrofoil. In some detail we discuss the dynamics of the sheet cavity on the 3D Twist11 hydrofoil as found by Foeth [67] in his experiments. The importance of the three-dimensionality of the shape of the cavity and the direction of the re-entrant jet is explained followed by the description of the physical aspects of phase change

of water.

Chapter 3 provides an overview on the mathematical models for cavitation. An inventory of existing models is given followed by the description of the equilibrium cavitation model chosen for the implementation in the numerical method. Furthermore, the homogeneous mixture equations are derived and appropriate equations of state for compressible liquid flows are discussed.

Chapter 4 presents an overview of numerical methods based on the Euler equations for compressible flows. The focus is to address the critical aspects of simulating the flow of a compressible fluid within a wide range of Mach numbers for fluids with an arbitrary equation of state employing an unstructured edge-based finite-volume computational mesh. The treatment of the boundary conditions is considered in detail. In the present work the treatment of Thompson [190] using the ideal gas law as the equation of state, is generalized for an arbitrary equation of state.

In chapter 5 numerical solutions for compressible single-phase water flow are considered. The one-dimensional "Water Hammer" and "Riemann problem for liquid" are test cases considered to demonstrate the wave-capturing ability of the numerical method. The low-Mach number flow over a two-dimensional cylinder is calculated to illustrate the capability to calculate steady-state low-Mach number flows. To assess the performance and the order of convergence of the numerical method the water flow about two-dimensional NACA sections is considered. The single-phase water flow over the three-dimensional Twist11 hydrofoil is presented to validate the numerical method using the experimental results of Foeth [67].

In chapter 6 results of numerical simulations for cavitating flows are presented. First, one-dimensional test cases are considered to assess the convergence and stability of the numerical method for cavitating flows. Then, the results of the two-dimensional test case of Sauer [162] about a 2D NACA 0015 at 6° angle of attack are presented to verify the results of the numerical method. The cavitating flow about the 3D Twist11 hydrofoil is calculated to compare the results with the experiments of Foeth [67]. The formation of the re-entrant flow and the formation of a cavitating horse-shoe vortex are discussed. Lastly, the steady-state cavitating flow about the 3D Elliptic 11 Rake hydrofoil is simulated to illustrate the capability of the present edge-based numerical method to predict the cavitation pattern occurring in the flow about a complex geometry in comparison to the experimental results of Van der Hout [204].

The conclusions and discussion of the present thesis are formulated in chapter 7 and recommendations for future research are given.

PHYSICAL ASPECTS OF SHEET CAVITATION

CHAPTER 2

In this chapter the physical aspects of sheet cavitation are discussed. First, an introduction to the types of cavitation is presented and relevant dimensionless numbers are introduced. Then, the physical aspects of sheet cavitation on the 3D Twist11 hydrofoil are described. In the discussion emphasis is given to the three-dimensionality and the dynamics of the sheet cavity. Finally, the phase change of water is discussed.

2.1 Types of cavitation

When the phase change occurs in flowing liquids, e.g. a decrease of the pressure below the saturation pressure due to an expansion of the fluid, we speak of hydrodynamic cavitation. On the other hand, acoustic cavitation may occur in a quiescent or nearly quiescent liquid. When an oscillating pressure field is enforced on a liquid medium, cavitation bubbles may appear within the liquid when the oscillation amplitude is large enough. Naturally, hydrodynamic cavitation and acoustic cavitation may occur at the same time.

Cavitation can take different forms as it develops from its inception. In case the pressure is mostly above the saturation pressure, cavitation is strongly dependent on the basic non-cavitating or fully-wetted flow. As cavitation develops, the vapor structures disturb and modify the flow and a new often unsteady flow pattern evolves. Cavitation patterns can be divided into different groups [74]:

- Bubble or “traveling” cavitation. Bubbles may appear in regions of low pressure and low pressure gradients as a result of the rapid growth of small air nuclei present in the liquid. The bubbles are carried along by the flow and disappear when they enter a region with higher pressure.

- Attached or sheet cavitation. When a low pressure region is formed near the leading edge of a streamlined object in the flow, the liquid flow separates from the surface and a pocket of vapor is formed.

- Cloud cavitation. When a vapor sheet detaches from the surface and is advected with the flow, a region with a large number of vapor structures is formed. This region is usually called cloud cavitation, although it consists of a vortical flow region with many vapor bubbles. This type is usually erosive when collapsing near a surface.

- Vortex cavitation. In the low-pressure core of vortices the pressure may be low enough for cavitation to occur. This type of cavitation is often found at the tip of lifting surfaces and is therefore also denoted by tip vortex cavitation.

- Shear cavitation. In regions with high shear vorticity is produced. As a result coherent rotational structures are formed and the pressure level drops in the core of the vortices, which become potential sites for cavitation. Flow situations with shear cavitation can be found in wakes, submerged jets at high Reynolds number and separated flow regions which develop on foils at large angles of attack.

For an overview of bubble cavitation see Brennen [29], for vortical cavitation see Arndt [15] and for sheet cavitation see Franc [70, 74].

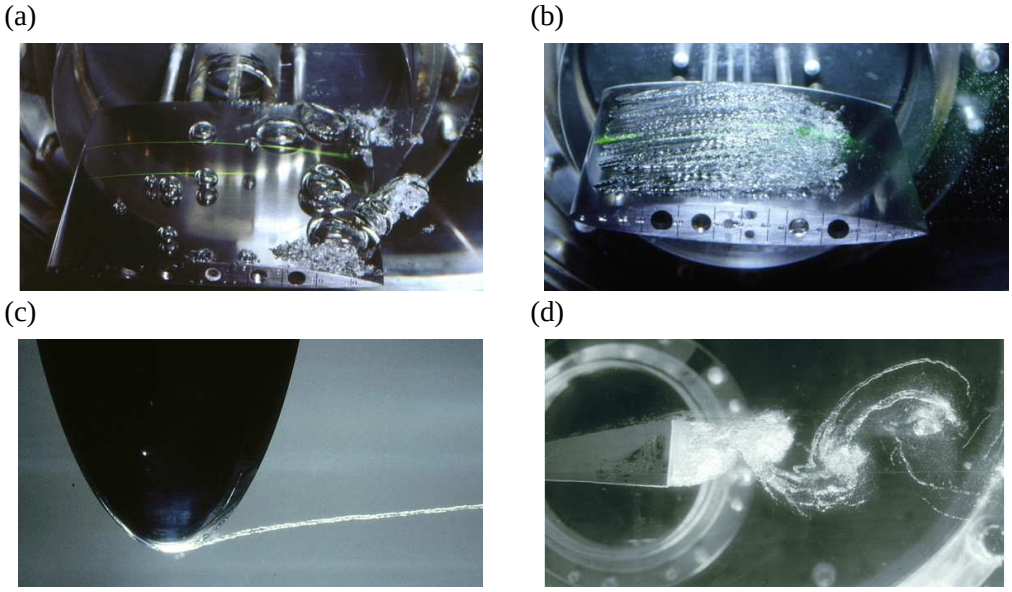

FIGURE 2.1: *Cavitation patterns (a) Traveling bubble cavitation (b) Attached or sheet cavitation (c) Tip vortex cavitation (d) Shear cavitation. Taken from Franc [71].*

2.2 Dimensionless numbers

To facilitate the discussion in this chapter and further on in the thesis, relevant dimensionless numbers are introduced.

2.2.1 Cavitation number σ

The dimensionless cavitation number σ was introduced by Thoma, see Knapp [112]. The number is a measure for the sensitivity of the flow for cavitation to occur and is useful to facilitate the comparison of results of experiments and numerical simulations. The cavitation number σ is defined as:

$$\sigma \equiv \frac{p_\infty - p_{sat}(T)}{\frac{1}{2}\rho_\infty U_\infty^2}, \tag{2.1}$$

where p_∞ [Pa], ρ_∞ [$\mathrm{kg\,m^{-3}}$] and U_∞ [$\mathrm{m\,s^{-1}}$] are the free-stream pressure, free-stream density and free-stream velocity, respectively, and where $p_{sat}(T)$ is the saturation pressure of water at temperature T [K]. Note that a higher cavitation number indicates that the pressure in the flow must decrease more before cavitation occurs. A smaller cavitation number indicates that a smaller decrease in pressure causes cavitation. Thus, a low cavitation number corresponds to a high susceptibility for cavitation.

2.2.2 Void fraction α

The void fraction α within a volume V [$\mathrm{m^3}$] of a fluid follows from the fluid density $\rho = \alpha\rho_{v,sat}(T) + (1-\alpha)\,\rho_{l,sat}(T)$ as

$$\alpha \equiv \frac{V_v}{V} = \frac{\rho - \rho_{l,sat}(T)}{\rho_{v,sat}(T) - \rho_{l,sat}(T)}, \tag{2.2}$$

where V_v [$\mathrm{m^3}$] is the volume of vapor within the volume V of the fluid and where $\rho_{v,sat}(T)$ [$\mathrm{kg\,m^{-3}}$] and $\rho_{l,sat}(T)$ [$\mathrm{kg\,m^{-3}}$] are the saturated vapor and liquid density at temperature T, respectively.

Experimentally, it is very difficult to determine the void fraction at any location in the flow. Numerically, the void fraction is used for visualization and analysis purposes. Employing the equilibrium cavitation model the determination of the void fraction is just a post-processing step evaluating equation (2.2).

2.2.3 Reynolds number Re

The Reynolds number is the ratio of inertial forces to viscous forces and thus it quantifies the relative importance of these two type of forces given the flow conditions.

The Reynolds number Re is defined as:

$$Re \equiv \frac{\rho_\infty U_\infty L}{\mu_\infty} = \frac{U_\infty L}{\nu_\infty}, \tag{2.3}$$

where ρ_∞ is the density of the fluid, U_∞ a characteristic velocity of the flow, L a characteristic length scale $[\mathrm{m}]$, μ_∞ the dynamic fluid viscosity $[\mathrm{Pas}]$, and $\nu_\infty = \mu_\infty/\rho_\infty$ is the kinematic fluid viscosity $[\mathrm{m^2 s^{-1}}]$. The flow about a hydrofoil of chord length $c = 0.15\mathrm{m}$ of pure water* at saturation pressure and at a velocity of $U_\infty = 10$–$50\ \mathrm{ms^{-1}}$ has a Reynolds number within the range of $Re = 1.5$–7.5×10^6. The thicknesses δ and $\bar{\delta}$ of a fully developed laminar and turbulent boundary layer above a flat plate of length x can be estimated to be equal to [176]

$$\frac{\delta}{x} = \frac{5}{\sqrt{Re_x}}, \quad \text{or} \quad \frac{\bar{\delta}}{x} = \frac{0.370}{\sqrt[5]{Re_x}}, \tag{2.4}$$

respectively, with $Re_x = \rho U x/\mu$. Consider a hydrofoil of chord length $0.15\mathrm{m}$, for water the laminar and turbulent boundary layer thickness can be found equal to $\delta = 6.1\times10^{-4}\ \mathrm{m}$ and $\bar{\delta} = 3.2\times10^{-3}\ \mathrm{m}$, respectively, illustrating the thin boundary layers in a water flow. Furthermore, Franc & Michel mention that the influence of the Reynolds number on cavitation is not significant, see also Knapp [112]. In section 2.3.4 the role of viscosity is explained in more detail.

2.2.4 Strouhal number St

The Strouhal number St is employed to quantify the oscillating frequency in unsteady flows. For cavitating flows the Strouhal number St is defined by:

$$St \equiv \frac{f\ell}{U_\infty}, \tag{2.5}$$

where f $[\mathrm{Hz}]$ is the cavity shedding frequency, ℓ is the mean cavity length $[\mathrm{m}]$ and U_∞ is the free stream velocity. Often, it is difficult to accurately obtain a mean cavity length for unsteady cavitation. So, for convenience we define a different Strouhal number St_c based on the chord length c of the foil instead of on the mean cavity length:

$$St_c \equiv \frac{fc}{U_\infty}. \tag{2.6}$$

**The dynamic viscosities of vapor and water at $T = 293\ \mathrm{K}$ and saturation pressure $p = p_{sat}(T) = 2.3\times10^3\,\mathrm{Pa}$, are equal to $\mu_v = 9.72\times10^{-6}\ \mathrm{Pas}$ and $\mu_l = 1.0053\times10^{-3}\ \mathrm{Pas}$, respectively [1]. The corresponding kinematic viscosities $\nu = \mu/\rho$ of vapor and water are equal to $\nu_v = 5.67\times10^{-4}\ \mathrm{m^2 s^{-1}}$ and $\nu_l = 1.01\times10^{-6}\ \mathrm{m^2 s^{-1}}$. Note that at $T = 293\ \mathrm{K}$ and $p = 2.3\times10^3\,\mathrm{Pa}$ the vapor and liquid density are equal to $\rho_v = 0.017\ \mathrm{kgm^{-3}}$ and $\rho_l = 998.19\ \mathrm{kgm^{-3}}$ [1], respectively. The dynamic viscosity μ_l of water at $T = 293\mathrm{K}$ and $p = 10^5\ \mathrm{Pa}$ is equal to $\mu_l = 1.0053\times10^{-3}\ \mathrm{Pas}$.*

2.2.5 Pressure coefficient C_p, lift and drag coefficients

The dimensionless pressure coefficient C_p is defined as

$$C_p \equiv \frac{p - p_\infty}{\frac{1}{2}\rho_\infty U_\infty^2}, \tag{2.7}$$

with p the local pressure in the flow field, and where p_∞, ρ_∞ and U_∞ are the free-stream pressure, the free-stream density and the free-stream velocity, respectively. In the following we usually employ the $-C_p$ coefficient.

Neglecting skin friction, the drag and lift forces can be obtained from

$$\vec{\mathbf{F}} = \int_S p\vec{\mathbf{n}} dS, \tag{2.8}$$

with S surface of the object, p the pressure on the surface of the object and $\vec{\mathbf{n}}$ the unit normal pointing into the object, i.e. out of the computational domain. In 2D we will use lower-case symbols, i.e.

$$\vec{\mathbf{f}} = \int_C p\vec{\mathbf{n}} dC, \tag{2.9}$$

with C the closed curve of the object. For two-dimensional flow about a 2D geometry the lift force ℓ per unit length in span-wise direction is equal to the component of $\vec{\mathbf{f}}$ in the direction normal to the free-stream, which in our case is f_y. For three-dimensional flow the lift force L is equal to F_z. The drag force d per unit length in span-wise direction and the drag force D are equal to f_x and F_x for two-dimensional or three-dimensional flow, respectively. The dimensionless lift C_L, c_l and drag C_D, c_d coefficients are defined as

$$C_L \equiv \frac{L}{\frac{1}{2}\rho_\infty U_\infty^2 S}, \qquad c_l \equiv \frac{\ell}{\frac{1}{2}\rho_\infty U_\infty^2 c}, \tag{2.10}$$

$$C_D \equiv \frac{D}{\frac{1}{2}\rho_\infty U_\infty^2 S}, \qquad c_d \equiv \frac{d}{\frac{1}{2}\rho_\infty U_\infty^2 c}, \tag{2.11}$$

where S is the projected surface area of the object and c the chord length of the body.

2.2.6 Mach number

The Mach number M is defined as the ratio between the magnitude of the fluid velocity $|\vec{\mathbf{u}}|$ and the speed of sound in the fluid:

$$M \equiv \frac{|\vec{\mathbf{u}}|}{c}, \tag{2.12}$$

where $\vec{\mathbf{u}}$ is the velocity and c is the speed of sound $[\mathrm{ms}^{-1}]$.

2.3 Sheet cavitation on a hydrofoil

The main focus of the present research is the cavitating flow around a stationary hydrofoil, placed in a steady uniform flow. Depending on the operating conditions many types of cavitation can be observed on a cavitating hydrofoil: bubble-, sheet-, cloud- and vortex cavitation.

A vapor sheet is attached to the leading edge of a body on the low-pressure side, termed "suction side". Near the leading edge a vapor cavity or sheet is formed and the liquid flow is detached. Franc & Michel [72, 73] and Le *et al.* [123] investigated the dependence of the behavior, the length and the thickness of the vapor sheet as a function of the cavitation number σ and the angle of attack α of a 2D hydrofoil.

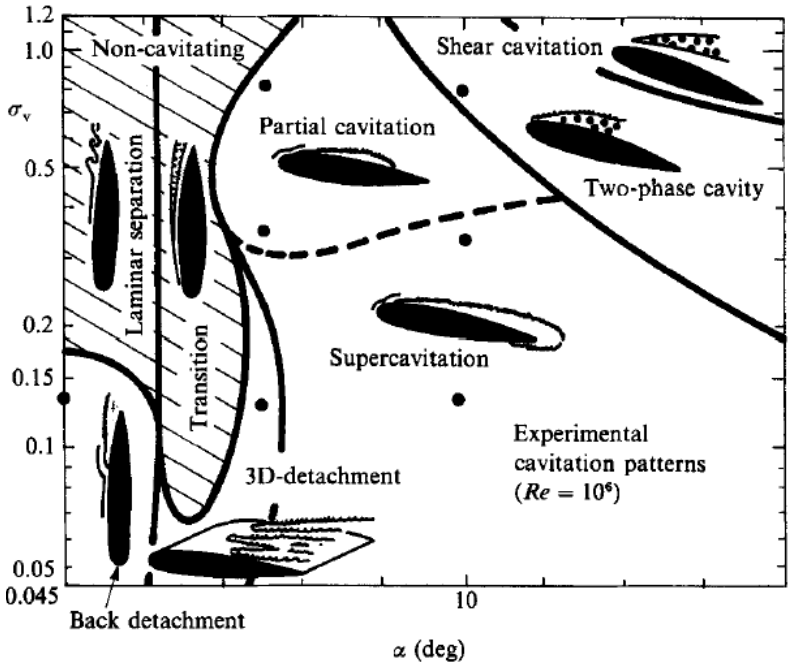

FIGURE 2.2: *Observed cavitation patterns on a 2D NACA 16012 hydrofoil as a function of the angle of attack α and the cavitation number σ. Taken from Franc & Michel [73], note that σ_v is the cavitation number defined as σ in equation (2.1).*

Franc & Michel [72] investigated the cavitation patterns on a 2D NACA 16012 hydrofoil. They mention that for this relatively thin hydrofoil the influence of the Reynolds

number on cavitation is not significant. For cavitating flow they observed different regions in the α–σ plane corresponding to different cavitation patterns, see figure 2.2. At low angle of attack and high values for σ cavitation does not occur. Keeping the cavitation number high, but increasing the angle of attack, results in a partial cavity on the suction side of the hydrofoil. Further increases in the angle of attack result in a two-phase cavity and for very high angle of attack in so-called shear cavitation. For low cavitation numbers and low angle of attack the cavity detachment occurs at the aft part of the foil.† For higher angles of attack the detachment moves upstream and becomes three-dimensional as visible in figure 2.2. For even higher angles of attack, i.e. $\alpha > 6^\circ$ and $\sigma < 0.3$, the sheet cavity extends beyond the trailing edge of the hydrofoil, which is called supercavitation.

Le *et al*. [123] utilized a cavitating foil with a geometry consisting of a flat upper side and circular arc as its lower side. Keeping the length ℓ of the sheet on the upper surface constant and varying both angle of attack α and cavitation number σ, they found a linear dependence of the thickness of the sheet on the cavitation number σ. Furthermore, they found a unique curve, relating the non-dimensional length ℓ/c of the sheet cavity, with c the chord length of the hydrofoil, versus the non-dimensional parameter $\sigma/(\alpha - \alpha_i(\sigma))$ where $\alpha_i(\sigma)$ corresponds with the angle of attack without cavitation at that cavitation number. They also found that for their foil the Strouhal number $S = f\ell/U$ at which the sheet cavity was shed, was nearly constant, i.e. $S \approx 0.28$, where f is the shedding frequency of the sheet cavity, ℓ is the maximum length of the sheet and U the free-stream velocity.

When a vapor sheet is formed the minimum pressure on the foil equals $p_{sat}(T)$, which occurs inside the cavity itself, so the curvature of the surrounding streamlines tends to be directed towards the cavity see figure 2.3. Downstream of the sheet, the flow re-attaches to the hydrofoil and thus splits the liquid flow into two parts:

- the re-entrant jet, which travels upstream along the foil's surface carrying a small quantity of liquid to the inside of the cavity,
- the outer liquid flow, that reattaches to the wall.

Both parts of the liquid flow are separated by a streamline that, if the flow were steady, would meet the wall perpendicularly at a stagnation point. However, if this flow were steady, the cavity would be filled with liquid rapidly.

†*In this experiment leading edge roughness was not applied. At low Reynolds numbers the sheet develops in laminar separation regions, which may be located near the trailing edge for low angles of attack. This does not occur in situations at higher Reynolds number for which a turbulent boundary layer develops.*

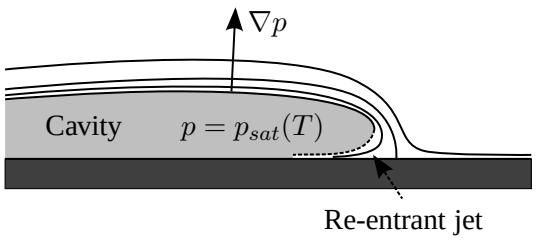

FIGURE 2.3: *Closure region of the cavity sheet. Reconstructed from Franc & Michel [74].*

The re-entrant jet moves upstream towards the leading edge along the surface of the foil underneath the vapor sheet. At some point the re-entrant jet impinges on the liquid-vapor interface, which can be at the leading edge if the re-entrant jet has enough momentum and if the sheet is thick. This leads to separation or shedding of part of the cavity which is then advected by the main flow in downstream direction. The re-entrant jet gives rise to a circulatory flow pattern directed around the sheet cavity. Therefore, at the instant of shedding, circulation exists around this vapor structure, which takes the form of a region with spanwise vorticity above the surface.

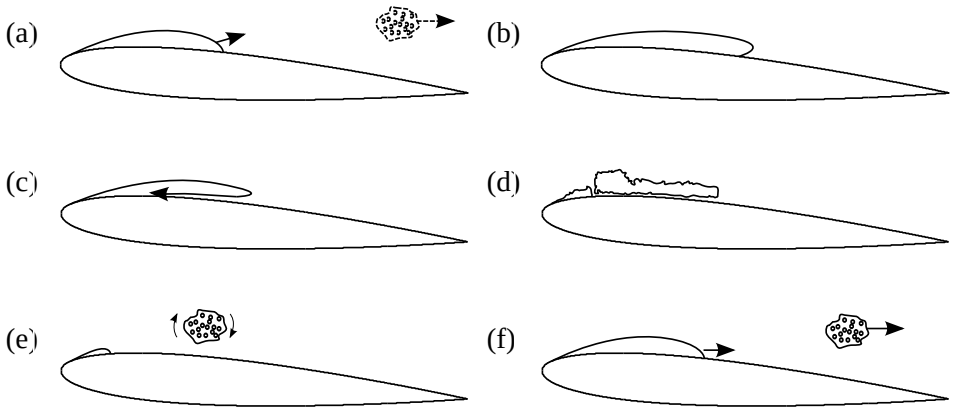

FIGURE 2.4: *The break-off cycle, schematic view. (a) Start of the cycle, vapor sheet is growing, bubble cloud from previous shedding is convected with the flow. (b) Sheet reaches maximum extent, re-entrant jet starts to form. (c) Re-entrant moves upstream. (d) Re-entrant jet impinges on the cavity surface, vapor cloud sheds from main structure. (e) Vapor cloud is convected with the flow, circulation is present around the vapor cloud. (f) Vapor cloud collapses, vapor sheet grows from leading edge. Reconstructed from De Lange & De Bruin [56].*

The shed vapor structure may be broken into smaller vapor structures such as bubbles or cavitating vortices, which may collapse in regions with higher pressure. After the shedding of the vapor cloud, a new cavity develops and a new re-entrant jet is formed. This repeating shedding process, that is mainly controlled by inertia [74], can be either random or periodic depending on the operating conditions. The shedding process is illustrated in figures 2.4(a)–(f) taken from De Lange & De Bruin [56].

2.3.1 Three-dimensionality

In the past cavitation patterns have been observed for two-dimensional geometries such as 2D hydrofoils, see Astolfi *et al*. [17] and a backward facing step, see Callenaere *et al*. [33]. Despite the two-dimensional geometry of the object in the flow, the cavitation sheet was often found to shed vapor clouds irregularly both in time and in space, leading to a three-dimensional flow field. De Lange & de Bruin [122] predicted that the spanwise component of the velocity along the closure line of the sheet cavity should remain constant, see also the thesis of de Lange [55]. Hence, the re-entrant jet should simply be reflected at the closure line and be directed sideways as illustrated in figure 2.5.

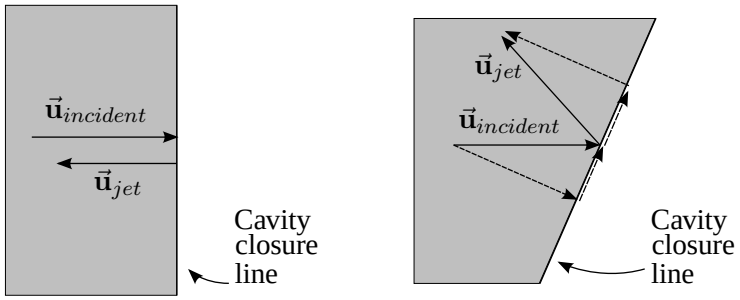

FIGURE 2.5: *Reflection of incident flow by the closure line of the sheet cavity. The flow is from left to right. Reconstructed from De Lange & De Bruin [56].*

Labertaux & Ceccio [121] showed that the leading-edge sweep of the hydrofoil has a significant effect on the topology of the cavity and on the direction of the re-entrant jet. The importance of the re-entrant jet was further demonstrated by Kawanami [108] who blocked the re-entrant jet and showed that the cavitation shedding behavior changed significantly. When two sideways reflected re-entrant jets collide, the fluid is ejected upwards hitting the cavity interface and causing local shedding of the sheet cavity. The closure line of the cavity then becomes even more three-dimensional resulting in highly three-dimensional structures. From these and other experiments it has become clear that the form and the stability of the sheet cavity is very dependent on the three-dimensional geometry of the foil.

Dang & Kuiper [50, 51] designed a twisted foil configuration to localize the three-dimensional effects. The direction of the re-entrant jet was found to be strongly influenced by the cavity topology. In their case the cavity shape was determined by the variation in the spanwise distribution of the loading of the foil and not by sweep angle. The foil spanned the tunnel from wall to wall. The variation in the spanwise loading was accomplished by the distribution of the twist angle of the foil, which was high in the center and zero at the tunnel walls. Based on the geometry of the foil of Dang, a new twisted hydrofoil denoted by 3D Twist11 hydrofoil, see Foeth *et al*. [68], Koop *et al*. [113] and appendix D was designed with a clear and controllable three-dimensional sheet cavity on a relatively simple two-dimensional like configuration.

The 3D Twist11 hydrofoil spans the cavitation tunnel from wall-to-wall and is symmetric with respect to its mid-span plane. The foil has a spanwise varying geometric angle of attack (twist) from 0° at the tunnel wall to 11° at mid-section. This avoids the interaction of the cavitation sheet with the boundary layer along the tunnel wall. In section 5.7.1 a full description of the 3D Twist11 hydrofoil is presented. In the central part of the foil a three-dimensional sheet cavity forms with a planform that is symmetric with respect to the mid-section plane. A top view of the sheet cavity on the twisted foil is presented in figure 2.6 obtained from Foeth [66].

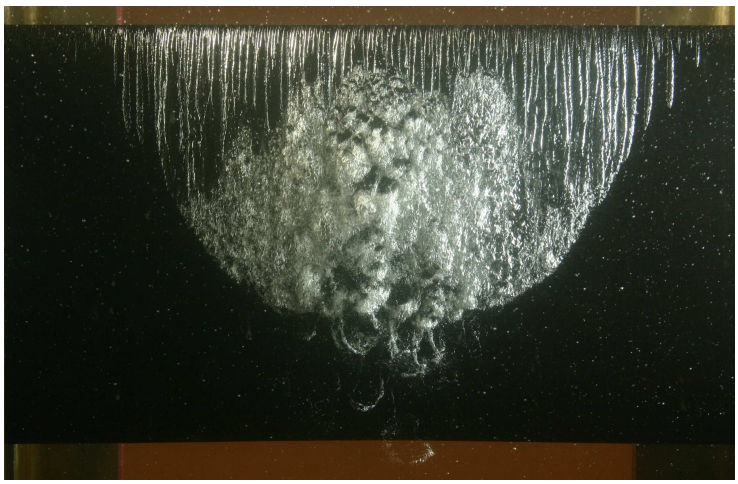

FIGURE 2.6: *Top view of sheet cavitation on 3D Twist11 hydrofoil obtained from Foeth [66]. Flow is from top to bottom, LE is leading edge, TE is trailing edge.*

2.3.2 Dynamics of the vapor sheet on 3D Twist11 hydrofoil

Foeth *et al*. [68] carried out experiments for the 3D Twist11 hydrofoil in steady and unsteady inflow conditions in the cavitation tunnel at Delft University, see also Foeth [67]. Their focus was to generate sheet cavities that are three-dimensional in character similar to ones that occur on ship propellers. In figures 2.7(a)–(t), taken from Foeth *et al*. [69], the process of the vapor shedding is presented. The shedding is periodic, constant in its shedding frequency, and always includes the same macro structural collapse [68]. In figure 2.7(a) the attached cavity has reached its maximum length. Due to the spanwise variation of the twist angle the sheet cavity is three-dimensional and the closure line of the cavity is convex-shaped. The chordwise striations originating close to the leading edge are due to roughness elements positioned at the leading edge. At the closure line of the vapor sheet a re-entrant jet develops which moves in upstream direction along the surface of the foil into the vapor structure. At both sides of the mid-section plane the re-entrant jet is directed towards the plane of symmetry.

In the center plane the re-entrant flow from port side and that from starboard side collide and at this location the cavity quickly changes from a smooth vapor sheet into a cloudy region which detaches from the main structure, see figures 2.7(b)–(h). At the aft end of this structure a vaporous horse-shoe vortex develops. This structure, presumably induced by the colliding side-entrant jets that force the water flow upwards, can be followed to figure 2.7(n). The vapor cloud is advected by the main flow and collapses in the region with higher pressure on the aft part of the foil, see figures 2.7(i)–(t). In the final images of the collapse of the vapor cloud a distinct second, somewhat larger vaporous horse-shoe vortex or ring-vortex like structure is observed, see figures 2.7(q)–(t). This process is repeated on a smaller scale at the two crescent-shaped side-lobes in figures 2.7(i)–(r). In figures 2.7(q) and 2.7(r) a similar, but smaller-scale vortical structure is formed at either side of the center plane due to this secondary shedding process.

Foeth *et al*. [69] showed that the re-entrant jet entering the sheet cavity determines the shedding mechanism of the sheet. To distinguish between various directions of the re-entrant flow, Foeth introduced the term side-entrant jet, which refers to that part of the re-entrant jet originating from the sides of the cavity sheet.[‡] This jet has a strong span-wise velocity component. They reserved the term re-entrant jet for the case this jet originates from that part of the cavity where the closure is more or less perpendicular to the main flow and thus is mainly directed upstream.

In figure 2.8(a) the streamline topology on the cavity surface as given by Foeth *et*

[‡] *For the 3D Twist hydrofoil the side-entrant jets are directed towards the center plane of the foil.*

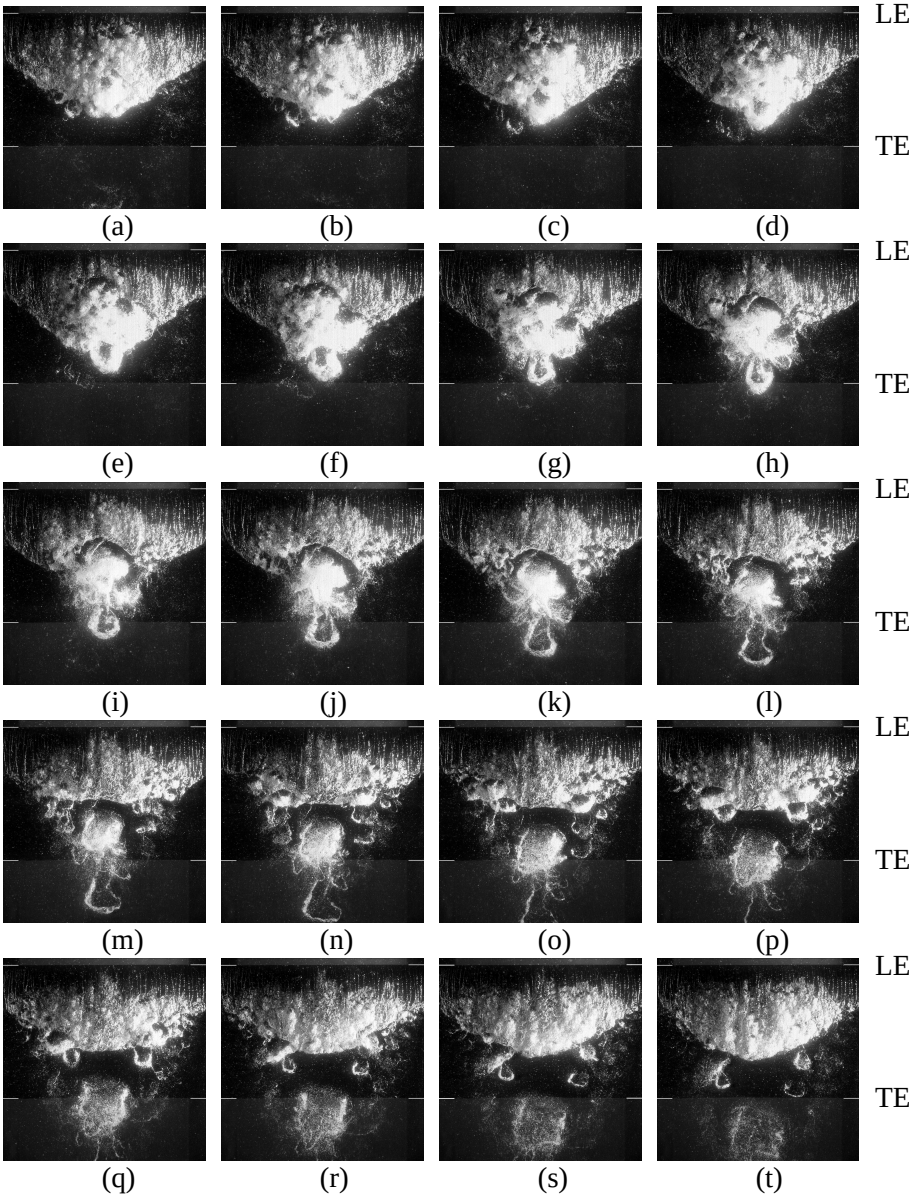

FIGURE 2.7: *Shedding cycle on Twist 11 foil,* $U_\infty = 4.96\mathrm{ms}^{-1} \pm 6.4\%$*,* $\alpha = 1°$*,* $\sigma = 0.66 \pm 7.94\%$*. Shown is every 7th frame of a 2000 Hz recording,i.e. the time between two frames is* $3.5 \times 10^{-3}\,\mathrm{s}$*. Flow is from top to bottom. (a)–(d) Development of re-entrant jet directed towards plane of symmetry. (c)–(f) Shedding starts in center of sheet (e)–(p) Primary shedding, cavity center (p)–(t) Secondary shedding (cavity sides) (q)–(t) Growth of sheet. Taken from Foeth et al. [69], see also the thesis of Foeth [67].*

al. [69] is reproduced. At the closure of the cavity the streamlines are directed into the vapor sheet. Note the difference between the re-entrant jet and the side-entrant jet. When the sheet is growing the side-entrant jets from both sides are directed into the closure region of the sheet. In the center plane of the sheet cavity the two side-entrant jets collide and the fluid is ejected upward through the vapor-liquid interface causing the shedding of part of the vapor sheet and the formation of the horse-shoe vortex, that subsequently is convected by the main flow.

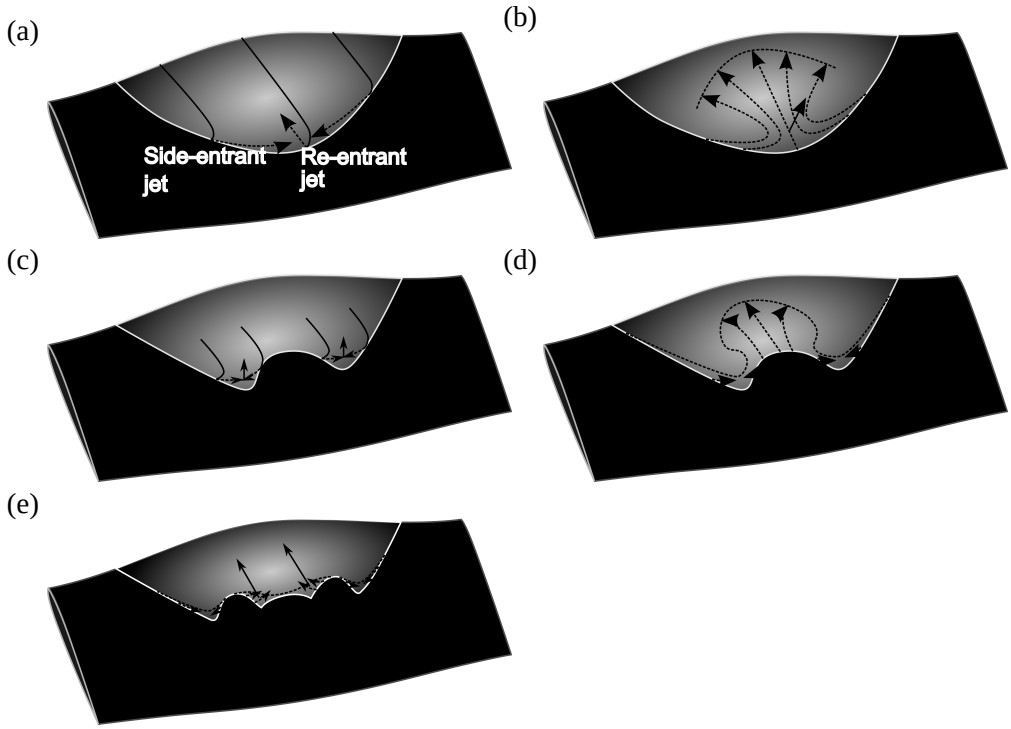

FIGURE 2.8: *Sketches of the re-entrant flow (a) Streamlines over the cavity sheet are directed inward. (b) The side-entrant jets collide in the center plane, part of the re-entrant flow impinges on the interface of the cavity sheet causing the primary shedding, part of the side-entrant flow is reflected towards the center of the side lobes. (c) Process of shedding of (a) and (b) is repeated in side-lobes. (d) Re-entrant flow approaches leading edge. (e) Cavity sheets grows. Reproduced from Foeth et al. [69], see also thesis of Foeth [67].*

In figure 2.8(b) the re-entrant jet is still traveling upstream and the side-entrant jets are reflected away from the center plane. After the shedding of the vapor structure the side-entrant jets in the side-lobes are directed towards each other, as presented in

figure 2.8(c), causing the secondary shedding when these two jets meet, see figures 2.7(i)–(q). Foeth mentions that the mechanism of the secondary shedding does not seem to be different from that of the primary shedding.

As presented in figure 2.8(e), the remaining cavity has a reasonably convex shape of its closure line with two concave regions. Side-entrant flow appears at either side of these latter regions. In the short period of converging side-entrant jets the cavity grows into its convex shape again before the whole cycle is repeated. Foeth mentions that the re-entrant jet directed towards the foil's leading edge in figure 2.8(e) does not always visibly disturb the vapor interface at the leading edge and thus does not seem to cause the detachment of the complete structure.

In summary, Foeth *et al*. [69] conclude that the re-entrant flow from the sides dictate the behavior of the shedding cycle and that the flow from the sides depends on the cavity shape. The re-entrant flow reaching the leading edge appears not to be the only cause for shedding.

2.3.3 Collapse of the vapor cloud

The break-up of a sheet cavity results in bubbly vapor clouds, containing vortical structures, that are convected into regions of higher pressure. Here these clouds collapse leading to strong pressures pulses [172]. During this process, the hydrofoil experiences high-frequency unsteady loads. This may lead to noise production and possibly erosion of the foil's surface. To capture these unsteady wave dynamics in the flow it is essential to consider water as a compressible liquid.

In the literature the collapse mechanism of a single isolated bubble has been studied both theoretically and experimentally. Experimental observations on the collapse of a single bubble as well as a bubble cloud demonstrate that violent radiated pressure waves occur with amplitudes of the order of 100 bar, see for example Fujikawa & Akamatsu [75]. Reismann *et al*. [158] experimentally investigated the break-up and collapse of sheet and vortex cavities and observed strong pressure pulses on the surface. Furthermore, they suggest that shock dynamics is responsible for the damage to surfaces and the generation of noise observed in many cavitating flows. Within the medical application of shock-wave lithotripsy these high pressure pulses are used to destruct kidney stones, see Ikeda *et al*. [103]. Johnson *et al*. [107] investigated this phenomenon numerically.

Schmidt *et al*. [169] developed a numerical method to predict the formation and propagation of shocks and rarefaction waves related to the collapse of vapor regions in cavitating flows. With their compressible flow simulation of the governing equations they indeed reproduced the unsteady loads on hydrofoils. The main focus of

the present research is aimed at predicting the global behavior of the vapor sheet as described in section 2.3.2. However, we will show that with the developed numerical method it is also possible to calculate the high pressure pulses generated by the collapsing vapor clouds and the subsequent unsteady wave dynamics.

2.3.4 Role of viscosity

The accurate prediction of the direction and momentum of the re-entrant and side-entrant jets and their impingement on the cavity surface form the basis of an accurate prediction of the shedding of the sheet cavity. These effects are all expected to be inertia driven [172]. Furthermore, the global pressure dynamics is not controlled by the viscosity of the fluid, so it is expected that numerical simulations based on the Euler equations are able to capture the major (vortical) structures and dynamics of sheet cavitation.

The effect of viscosity is the damping of large gradients and the loss of mechanical energy during the growth and collapse process. The viscosity of water and its vapor is very low and the effects of viscosity on cavitation are assumed to be negligible, see Knapp [112].

Viscous effects are predominant in the detachment of cavitating flow near the leading edge as observed by Arakeri & Acosta [14] and confirmed by Franc & Michel [72] in the case of hydrofoils. They showed that a well-developed cavity always detaches downstream of laminar separation of the boundary layer. Attached cavitating flow can form in a turbulent boundary layer. The natural transition to turbulence on ship propellers occurs near the leading edge resulting in attached leading-edge cavitation. On smooth hydrofoils the natural transition to turbulence will occur at different locations on the hydrofoil. Therefore, to resemble the flow on ship propellers in the experiments of Foeth [67] leading edge roughness is applied to trip the boundary layer into transition. Thus, the leading edge roughness effectively eliminates the laminar flow and causes the cavitation inception to occur at the leading edge. As a consequence the point with minimum surface pressure and the point of cavity detachment are approximately at the same location. Therefore, in the present investigation it is assumed that cavitation occurs when $-C_{p,min} = \sigma$ and consequently, that viscous effects do not play a role in the detachment of cavitation.

For the collapse of vapor bubbles viscosity only plays a role in the final stages of the collapse. The radii of the bubbles are then of the order of $\mathcal{O}(10^{-7}\,\mathrm{m})$ [71]. In combination with the scale of hydrofoils in experiments or propellers it is impossible to capture these small length scales with present-day numerical methods. So the role of viscosity is not considered for the collapse phase of vapor bubbles.

The evolution of the vorticity distribution in shear layers is dominated by viscous flow effects. However, the vorticity production due to density gradients, the so-called baroclinic torque, is only a function of gradients in density perpendicular to gradients in pressure, i.e. $\nabla\rho \times \nabla p$ and does not depend on viscosity.

Flow separation is a viscosity driven phenomenon, so for the validation of a flow model based on the Euler equations it is essential that flow separation does not occur. This is specifically so for the single-phase flow cases used for the validation of the basic numerical method.

The flow in the core of for example a non-cavitating tip vortex is dominated by viscosity, specifically in the viscous subcore. In a cavitating tip vortex viscosity plays a role at the interface between the vaporous core and the vortical liquid flow. An inviscid flow model will capture the flow in the part of the vortical flow region away from the viscous subcore and the liquid-vapor interface.

2.4 Phase change of water

In this thesis we consider the flow of the pure substance water. It may exist in more than one phase, but the chemical composition, denoted by H_2O, is the same for each phase. When two different phases are present simultaneously, the medium is considered as a mixture. In figure 2.9 the phase diagram for water is presented [184]. Note that the specific volume for water increases during freezing. The diagram shows the pressure as function of specific volume and temperature, which is a surface in the (v, T, p)-space.

Each possible equilibrium state is represented by a point on this surface. The regions of the surface that represent a single-phase, i.e. the solid, liquid and vapor phase, are indicated. The triple line is the isotherm line at which all three states may coexist in equilibrium at the same time. In this study we are not interested in the solid state so from now on we only discuss temperatures and pressures higher than the freezing temperature $T_r = 273.15$ K with the corresponding pressure $p_r = 611.7$ Pa and density $\rho_r = 999.79\ \mathrm{kg m^{-3}}$ for water.

The critical point is the temperature above which there is no observable difference between liquid and vapor. The critical temperature T_c, pressure p_c and density ρ_c for water are $T_c = 647.16$ K, $p_c = 221.2{\times}10^5$ Pa and $\rho_c = 322.0\ \mathrm{kg m^{-3}}$, respectively [168]. In this study we do not consider conditions at temperatures higher than the critical temperature, we remain at conditions around room temperature ($T \approx 293$ K).

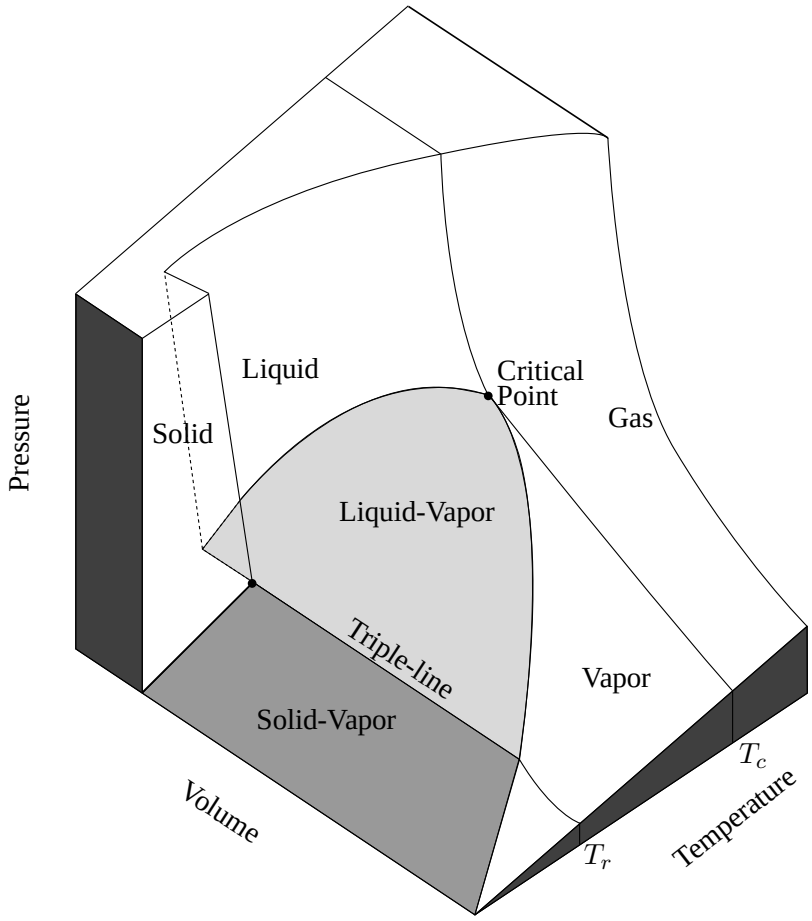

FIGURE 2.9: *Pressure-Volume-Temperature surface for water. T_c is the critical temperature and T_r is the freezing temperature. Figure reconstructed from Sonntag et al. [184].*

Considering temperatures above the triple point, the p-v-T surface presented in figure 2.9 can be projected onto the p-T plane or onto the p-v plane as presented in figures 2.10(a) and 2.10(b), respectively. Note that in the p-T plane the triple line collapses to the triple point T_r.

The term saturation temperature designates the temperature at which phase change takes place at a given pressure. This pressure is called the saturation pressure, which depends on temperature. If a substance exists as liquid at the saturation temperature and pressure, it is called saturated liquid and if a substance exists as vapor at the saturation temperature and pressure, it is called saturated vapor. If for a given pressure

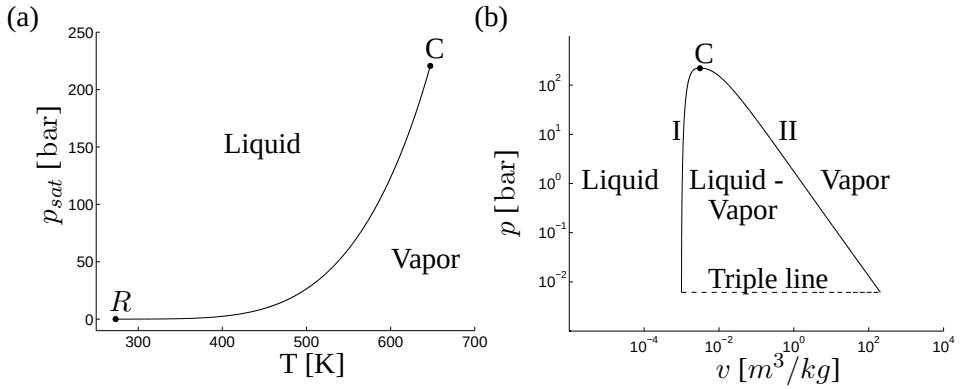

FIGURE 2.10: *Triple point R, $T_r = 273.15$ K, $p_r = 611.7$ Pa, $\rho_r = 999.79$ kgm^{-3}. Critical point C, $T_c = 647.16$ K, $p_c = 221.2\times10^5$ Pa, $\rho_c = 322$ kgm^{-3}. [168] (a) Projection on P-T plane for water, Curve: $p_{sat}(T)$. (b) Projection on p-v plane for water. Curve I: liquid saturation curve $\rho_{l,sat}(T)$, Curve II: vapor saturation curve $\rho_{v,sat}(T)$ with $\rho = 1/v$.*

the temperature of the liquid is lower than the saturation temperature, it is sometimes called either a subcooled or a compressed liquid. When the vapor is at a temperature higher than the saturation temperature for a given pressure, it is sometimes denoted as a superheated vapor. In this thesis we do not use the terms compressed liquid or superheated vapor.

In figure 2.10(a) the saturation pressure curve $p_{sat}(T)$ for water is presented, which is a function of the temperature T given by the expression, see [168]:

$$\ln\left(\frac{p_{sat}(T)}{p_c}\right) = \frac{T_c}{T}\sum_{i=1}^{7} a_i\theta^{\hat{a}_i}, \quad \text{for } T \in [T_r, T_c], \tag{2.13}$$

where $\theta = 1 - T/T_c$ and where the coefficients a_i and $\hat{a}_i$ are presented in table 2.1. This expression fits the known experimental data accurately [168]. The curve from the triple point R at T_r to the critical point C at T_c separates the liquid and vapor domains. This curve is usually denoted as the phase boundary, the saturation curve or the coexistence curve. Crossing that curve represents a reversible transformation at equilibrium conditions, i.e. evaporation or condensation of the water at the saturation pressure $p_{sat}(T)$. Cavitation in a liquid at a given temperature can occur by lowering the pressure below the saturation pressure. Cavitation appears to be a similar process as boiling, except that for boiling the driving mechanism is a temperature change at constant pressure. Actually, in view of figure 2.10(a) both processes can be thought of as the same process, i.e. as a crossing of the saturation pressure curve from the liquid region to the vapor domain.

In figure 2.10(b) the p-v diagram for water is presented. The region of the liquid-vapor equilibrium states is bounded by the triple line and the saturation curves for the saturation densities of the liquid $\rho_{l,sat}(T)$ (Curve I) and vapor $\rho_{v,sat}(T)$ (Curve II), respectively. These saturation densities are given by the approximate expressions [168]

$$\frac{\rho_{l,sat}(T)}{\rho_c} = \sum_{i=1}^{7} b_i \theta^{\hat{b}_i}, \quad \text{for } T \in [T_r, T_c], \tag{2.14}$$

$$\ln\left(\frac{\rho_{v,sat}(T)}{\rho_c}\right) = \sum_{i=1}^{7} c_i \theta^{\hat{c}_i}, \quad \text{for } T \in [T_r, T_c], \tag{2.15}$$

where $\theta = 1 - T/T_c$ and where the coefficients b_i, $\hat{b}_i$, c_i and $\hat{c}_i$ are included in table 2.1.

Index	a_i	$\hat{a}_i$	b_i	$\hat{b}_i$	c_i	$\hat{c}_i$
1	0	0	1	0	0	0
2	-7.85823	1	1.99206	$1/3$	-2.02957	$2/6$
3	1.83991	$3/2$	1.10123	$2/3$	-2.68781	$4/6$
4	-11.7811	3	-0.512506	$5/3$	-5.38107	$8/6$
5	22.6705	$7/2$	-1.75263	$16/3$	-17.3151	$18/6$
6	-15.9393	4	-45.4485	$43/3$	-44.6384	$37/6$
7	1.77516	$15/2$	-6.75615×10^5	$110/3$	-64.3486	$71/6$

TABLE 2.1: *Parameters for the saturation relations [168].* $T_c = 647.16$ K, $p_c = 221.2\times10^5$ Pa, $\rho_c = 322.0$ kgm^{-3}, $T_r = 273.15$ K.

2.4.1 Non-equilibrium states

It must be kept in mind that the saturation curves are not absolute boundaries between the liquid and vapor states. For example in the case of rapid expansion of a liquid, the liquid may cross the saturation curve without phase transition to vapor occurring. Another example is the rapid expansion of vapor in a convergent-divergent nozzle, where the temperature rapidly drops below the saturation temperature without phase transition to liquid. The resulting states are called supersaturated states or metastable states and the medium is considered to be in metastable equilibrium. It must be noted that although the term "equilibrium" is used, a fluid in metastable state is highly sensitive to impurities and disturbances. Transition to another phase may happen very rapidly. The term "equilibrium" suggests stability and this is certainly not the case.

Water in metastable equilibrium can even withstand a negative absolute pressure, i.e. tension, without phase change. For cavitation the tensile strength of the liquid is

the magnitude of the tension $\Delta p = p_{sat}(T) - p$ at which rupture occurs. The forces tending to hold liquid particles together are external pressure and intermolecular cohesive forces, see Knapp [112].

The tensile strength of the liquid is determined by weak spots in the liquid, see Brennen [29]. These weak spots may form the onset, the nuclei, of cavitation. They appear in two forms, i.e. homogeneous and heterogeneous nucleation. Homogeneous nucleation is determined by thermal motions within the liquid that result in microscopic voids that can act as the nuclei necessary for rupture. In a pure liquid surface tension is one of the forces that keep molecules together and prevent the formation of large voids. The term heterogeneous nucleation refers to rupture of the liquid at sites of impurity in the flow. In practical engineering the major weak spots in the liquid occur at the boundary between liquid and solid walls or between the liquid and small solid particles or micron-sized vapor and/or gas bubbles suspended in the liquid.

Experimentally, it would be hard to distinguish between homogeneous nucleation on one side and heterogeneous nucleation on small sub-micron sized contaminant particles in the liquid on the other side. In water, micro-bubbles of undissolved gas and roughness of surfaces of objects in the flow will always be present and thus cavitation is conventionally considered as a heterogeneous nucleation process.

For homogeneous nucleation in pure water the theoretical tensile strength is approximately equal to 1320 bar at $T = 298$ K [65, 141]. However, in experiments, due to the problem of cleaning and degassing of the water and equipment, this value is not found. Briggs [32], employing centrifugal force, was able to reach a pressure of -277 Pa before phase change from liquid water to vapor occurred.

Metastable states are important to consider for cavitation inception as well as for the final collapse phase of vapor bubbles. However, for engineering problems the water must be highly purified for metastable states to occur, whereas ordinary tap water does not show this behavior. The large number of impurities present in tap water immediately results in heterogeneous nucleation and thus, in the formation of vapor bubbles.

Furthermore, the leading edge roughness applied on the hydrofoils provides enough nuclei for cavitation to occur. As the specific volume of water vapor is much larger than the specific volume of liquid water, the phase transition results in fast pressure equalization close to saturation conditions. Therefore, we assume that cavitation occurs when the pressure is equal to the saturation pressure so that metastable states do not occur.

MATHEMATICAL MODELS FOR CAVITATING FLOWS

CHAPTER 3

The present research aims at developing a method for numerically simulating three-dimensional unsteady cavitating flows that incorporates the most important phenomena for sheet cavitation. This chapter first discusses the most recent developments for numerically simulating cavitating flows. Then, in section 3.2 the equations for the flow of a homogeneous mixture are derived. In section 3.3 equations of state for compressible liquids are discussed. In section 3.4 the equilibrium cavitation model employed in the present research is explained. Lastly, the extension to non-equilibrium models for cavitation is discussed in section 3.5.

3.1 Mathematical models for simulating cavitating flows

Computational methods for cavitating flows have evolved in parallel with computational resources. Starting in the 1970s and 80s with lifting surface and boundary element techniques, the level of the physical models underlying the numerical methods has increased substantially. However, it has proven to be a difficult task to predict the very complicated cavitation phenomena, involving phase change, surface tension, turbulence, (non-equilibrium) thermodynamic effects, etc.

The main numerical problem in cavitating flow simulations is the simultaneous treatment of two very different flow regions: (nearly) incompressible flow of pure liquid in most of the domain and low-velocity highly compressible flow of (pure) vapor in a relatively small part of the flow domain. In addition, the two flow regimes can often not be distinguished that clearly, for example in the transition region between vapor and liquid in the closure region of a sheet cavity. Furthermore, unsteady three-dimensional cavitating flow calculations require substantial computer resources both in terms of memory and speed. Also, meshes with appropriate high-resolution mesh densities in the cavitating region are necessary.

In the distant future it might be possible to calculate the full Navier-Stokes equa-

tions for each of the phases present in the flow and to compute every detail including the motion of every interface within a cavitating flow. Unfortunately, the computer power, speed and memory required to capture all the processes occurring over a wide range of time and length scales is far beyond the present capability. Therefore, simplifications are necessary to obtain a realistic model to simulate cavitating flows.

In the 1990s methods using the Euler or Navier-Stokes equations were developed, coupled with a transport equation for the void fraction, or coupled with two-phase flow equations or other cavitation closure model equations. As classified by the 22nd ITTC special committee in 1999 [3] this approach can be grouped into a number of categories.

- Interface-tracking methods
- Volume-of-Fluid methods
- Discrete-bubble methods
- Two-phase flow methods

3.1.1 Interface-tracking methods

Interface-tracking methods such as the level set method, marker particles and surface-fitting methods track the interface between the liquid and vapor based on a pressure streamline criterion. Note that this type of modeling corresponds with a Lagrangian type of approach. The cavitating flow region is assumed to be at a constant pressure equal to the saturation pressure. They require the presence of distinct interfaces to be tracked. For the aft part of the cavity sheet, where the distinction between liquid and vapor is not so clear, some wake model must be introduced. Examples are, amongst others: Furness & Hutton [76], Chen & Heister [37], Deshpande *et al*. [59], Hirschi *et al*. [92], Sussman *et al*. [187], Van der Pijl [205] and Dijkhuizen [61]. These methods do not allow the description of the unsteady behavior of pulsating cavities, including phenomena like the re-entrant jet, cavity breakdown or vapor cloud shedding.

3.1.2 Volume-of-Fluid methods

Volume-of-Fluid (VoF) methods as originally proposed by Hirt & Nichols in 1981 [93] can be classified as interface capturing methods. They include a transport equation for the void fraction α defined as the ratio of vapor volume to the total volume of the computational cell. In order to avoid smearing of the interface, special methods are used to derive the values of the void fraction at the faces of the computational cell. For that reason the Compressive Interface Capturing on Arbitrary Meshes (CICSAM) scheme has been developed by Ubbink [201, 202]. The standard VoF method is used for capturing distinct interfaces without phase transition, e.g. free surface flow or the

motion of single bubbles. To account for cavitation the standard VoF methods are extended to include, in addition to the convective transport, the change of the void fraction due to phase transition, see for example Dieval *et al*. [60], Molin *et al*. [140] and Sauer [162]. Sauer & Schnerr [163] developed a VoF method with bubble dynamics based on the Rayleigh equation, see also Yuan *et al*. [223]. This approach is also followed by Bouziad *et al*. [26, 27].

3.1.3 Discrete bubble methods

Discrete bubble methods consider single or multiple cavity bubbles which grow and collapse as they travel through the pressure field. Plesset & Prosperetti [148] analytically described the growth and collapse of a single vapor bubble, see also Rayleigh [134] and Plesset [147]. Since then many researchers have numerically studied the behavior of single or of multiple bubbles. Examples include the application of a varying pressure field, the flow through a convergent-divergent nozzle, the behavior of a collapsing bubble cloud and also the interaction of bubble clouds with shock waves. See amongst many others Fujikawa & Akamatsu [75], Brennen *et al*. [31], Colonius *et al*. [43], Preston *et al*. [151, 152], Delale *et al*. [57], Johnsen & Colonius [107], Wang & Brennen [215, 216].

3.1.4 Two-phase flow methods

Two-phase flow methods can be subdivided into different types of methods: (a) homogeneous-mixture methods and (b) multiple-species or multi-component flows. Homogenous-mixture methods treat the fluid as a pseudo-fluid with average properties such as density and viscosity. Thus, the fluid is treated in the whole computational domain as a compressible fluid with a greatly varying density. The inside and outside of the cavitating flow region is treated as a single medium or homogeneous mixture of liquid and vapor, who share the same velocity, pressure and temperature. This group of methods can be subdivided further into: transport equation-based methods, barotropic-flow methods and homogeneous-equilibrium methods. In a overview this can be summarized as:

(a) Homogeneous-mixture methods

- Transport Equation-based Methods (TEM)
  - Bubble two-phase Transport models (BFT)
  - mass transfer rate models
- barotropic-flow methods
- homogeneous-equilibrium methods

(b) Multi-component methods

Transport-Equation based Methods (TEM) treat the flow of the vapor or liquid by means of a transport equation for the volume or mass fraction of liquid or vapor (and sometimes even a third fraction, e.g. for an inert gas). The transport equation-based methods assume that the pressure, velocity and temperature of different phases are equal (homogeneous mixture assumption). Transition from one phase to the other is accounted for by physical rate processes that appear as source terms in the transport equation. These methods have the advantage that they can take into account the time dependency of the mass transfer phenomena through empirical laws for the source term. However, the choice of the constants in the empirical relations appears to be somewhat arbitrary. Two different classes can be distinguished: Two-phase Bubble models and mass transfer rate models.

Kubota *et al*. [116] proposed to relate the density of the mixture to the motion of bubbles and their dynamics in the flow. Cavitation is thus modeled as the growth and collapse process of vapor bubbles. The bubbles originate from nuclei, which already exist in the bulk flow and grow or collapse depending on the surrounding conditions, e.g. pressure and temperature. The evolution of the vapor bubbles is governed by the Rayleigh or Rayleigh-Plesset equation, [134, 147]. Many studies have adopted this approach for example: Chen & Heister [38], Sauer [162], Sauer & Schnerr [163], Yuan & *et al*. [224, 223], Bouziad *et al*. [27, 26], Susan-Resiga *et al*. [186]. Furthermore, some authors included empirical parameters for production and destruction of vapor: see e.g. Singhal [182] and Zwart *et al*. [227, 226].

Merkle *et al*. [139] developed a pressure-based method with vaporization/condensation source terms to account for the mass transfer between the two phases. The vapor and liquid components are solved employing mass-conservation equations for the vapor, liquid and/or mixture or by transport equations for the vapor/liquid volume or mass fraction. Their source terms have proven to offer flexibility for cavitation modeling and offer the possibility to include time dependency in the mass transfer phenomena. However, the values for the empirical constants in the source terms chosen by different authors vary significantly. Merkle's approach has been used in different and extended forms in combination with the Euler equations, see Neaves & Edwards [144], Reynolds Averaged Navier-Stokes (RANS) equations, see Kunz *et al*. [117, 118, 119, 120], Venkateswaran *et al*. [209, 210], Ahuja & Hosangadi [9, 8, 96, 97], Medvitz *et al*. [137], Dauby *et al*. [54], Senocak & Shyy [173, 174, 175], Shin *et al*. [177], Saito *et al*. [161], Zhou & Wang [225] and Large Eddy Simulations (LES), see Wikström *et al*. [220] and Persson [146, 99]. Senocak & Shyy [174, 175] evaluated different formulations of this type of models. They concluded that the results of the methods for the pressure distribution generally agree, but that the difference in density distributions is significant, implying that the com-

pressibility characteristics embodied in the cavitation source terms differ. They proposed an empiricism-free model based on interfacial dynamics which needs further research.

The transport equation-based methods can be considered as non-equilibrium methods. Besides being based on bubble dynamics or empirical mass transfer rates, methods are emerging based on thermodynamic considerations for the source terms. See for example Iben *et al*. [100], Berg *et al*. [22] and Barberon & Helluy [19]. In these models the full set of continuity equation, momentum and energy conservation equations for the mixture and the continuity equation for vapor or liquid are solved. To close the system of equations an appropriate equation of state for the pure phases and the mixture phase must be added, which must result in a system of equations accounting for two different pressures and preserving the hyperbolic consistency.

Barotropic flow models: Delannoy & Kueny [58] proposed a formulation that couples the mixture density to the pressure through a barotropic law $\rho(p)$ ranging from the liquid density through a transitional zone to the vapor density. Vorticity production is an important aspect of cavitating flows, especially in the closure region of the sheet cavity, see Gopalan & Katz [80]. Specifically, this vorticity production is a consequence of the baroclinic generation term of the vorticity transport equation, $\nabla\frac{1}{\rho} \times \nabla p$ [174]. However, when a barotropic relation is employed, then the gradients of density and pressure are always parallel, hence the baroclinic torque is zero. Nevertheless, many other researchers have applied this model with different barotropic laws, see Reboud & Delannoy [157], Hoeijmakers *et al*. [95], Arndt *et al*. [16], Coutier-Delgosha *et al.* [44, 47, 45, 46, 48], Reboud *et al*. [156], Qin [154] and Sinibaldi *et al*. [183]. In appendix F a barotropic flow model developed in our group is described, see Veldhuis [207] and Koop *et al*. [113]. This model has been used in the design of the Twist hydrofoils.

Homogeneous equilibrium models: Saurel *et al*. [166], Schmidt *et al*. [169] and Schnerr *et al*. [171] formulated the equilibrium cavitation model employing the full set of continuity, momentum and energy conservation equations for the flow of a homogeneous mixture. The pure water and vapor phase are described by suitable equations of state such that the governing equations are hyperbolic in time and space. The two-phase regime is enforced to be in thermodynamic and mechanical equilibrium at all locations in the flow. In regions where two phases can exist the homogeneous equilibrium model returns a prediction of the bulk density of the two-fluid mixture, from which a volume fraction of vapor is obtained given temperature-dependent saturation-state relations. This method is capable of capturing phase transitions, condensation shocks and other multi-phase flow features, but non-equilibrium effects are

by definition excluded. Furthermore, due to the hyperbolic nature of the equations for all phases, single-phase as well as two-phase wave propagation phenomena can be studied. This model for cavitating flows is independent of empirical parameters, other than in the equation of state for the pure phases.

To close the description for the two-phase mixture and for the compressible water physical mixture properties can be obtained from for example tabulated steam tables for $\rho = 1/v(p,h)$, $e = e(h,p)$, see Ventikos & Tzabiras [211]. Others employed a different equation of state for the description of the liquid. Edwards & Franklin [63] employed the Sanchez-Lacombe equation of state for real-fluid flows accompanied with the equilibrium assumption in the two-phase region to guarantee a real-valued speed of sound.* Iga [102] adopted the Tammann equation of state for the liquid phase. However, he did not take saturation conditions into account. In [101] he extended his model to include a source term in the continuity equation for the vapor phase to drive the two-phase flow towards saturation conditions.

The use of tabulated steam data and the use of equations of state that result in non-hyperbolic systems can be avoided by employing an approximation for the caloric equation of state for water [165] along with appropriate equations of state for the liquid† and vapor phase and temperature-dependent saturation conditions for phase change. This is the cavitation model pursued in this thesis. In section 3.4 the equilibrium cavitation model and the equations of state for compressible pure water and compressible pure vapor are presented.

Multi-component models or multiple-species methods have first been proposed by Baer & Nunziatio [18] for detonation waves in granular explosives and modified by Saurel & Abgrall [164] for the resolution of multi-phase mixtures and interface problems between pure compressible materials. These models describe the cavitating flow by adopting a full set of equations, i.e. continuity, momentum and energy conservation equations, for the vapor phase, the liquid phase and sometimes even an inert gas phase together with their own thermodynamic relations. They allow for both mechanical and thermal non-equilibrium to be taken into account. The coupling between the different phases is accounted for by appropriate transfer relations derived from two-phase flow modeling considerations. Most models lead to non-conservation forms due to the interface interaction terms [34]. These methods are assumed to possess more generality, but they are computationally expensive since a full set of equations

**For densities between the spinodal values, the acoustic eigenvalues for the Sanchez-Lacombe equation of state and also the van der Waals equation of state are complex, implying that the system of Euler equations coupled with these equations of state is not hyperbolic.*

†IAPWS [1] provides experimental data for water. In section 3.4 it is shown that the modified Tait equation of state used in the present study agrees with the IAPWS data.

for each component has to be solved. Various authors have followed this approach[‡], see for example: Saurel *et al*. [164, 167, 125], Abgral [5], Allaire *et al*. [11], Paillére *et al*. [145, 78], Cocchi *et al*. [40, 41], Quirk & Karni [155], Murrone & Guillard [143]. Abgrall & Karni [6], Castro & Toro [34], Johnsen & Colonius [107], Andrianov *et al*. [13], Chang & Liou [35].

3.2 Homogeneous mixture equations

In this section the flow equations for a homogeneous mixture are derived. A good overview and introduction are provided by the review article of Drew [62] and the books of Brennen [30] and Wallis [214]. Homogeneous flow theory provides the simplest description for analyzing multi-phase or multi-component flows. By definition a phase is simply one of the states of matter, which can be either a gas, a liquid or a solid. Multi-phase flow is the simultaneous flow of several phases. The term multi-component flow is sometimes used to describe flows in which the phases present do not consist of the same chemical substance. The equations describing multi-phase or multi-component flows are identical [214]. Therefore, the terms component and phase are used indiscriminately throughout this thesis.

In homogeneous flow theory the relative motion between the phases is neglected. The mixture is treated as a pseudo-fluid whose properties are suitable averages of the properties of the components in the flow. The method of determining the flow equations and the properties of the mixture is to start from separate equations for each phase. The approach is based on the view that it is sufficient to describe each phase as a continuum obtained from a microscopic description by a suitable averaging process.

3.2.1 Conservation of mass

Conservation of mass of a component k of the fluid flow requires that

$$\frac{\partial \rho_k \alpha_k}{\partial t} + \frac{\partial \rho_k \alpha_k u_{k,i}}{\partial x_i} = \mathcal{M}_k, \tag{3.1}$$

where ρ_k denotes the density of component k, $\alpha_k = V_k/V$ the volume fraction of component k with V_k the volume occupied by phase k in a volume V, $\vec{\mathbf{u}}_k$ the velocity of component k and $\mathcal{M}_k$ the rate of mass transfer to phase k from the other phases. The quantities $\mathcal{M}_k$ are denoted as mass interaction terms. For each phase or component in the flow there is a continuity equation like equation (3.1). We assume

[‡]Not all authors take phase-change into account, implying that the source terms are chosen equal to zero.

that the whole domain is occupied by all phases considered, i.e.

$$\sum_k \alpha_k = 1. \tag{3.2}$$

Since the total mass must be conserved it follows that the sum of the mass-interaction terms is equal to zero, i.e.

$$\sum_k \mathcal{M}_k = 0. \tag{3.3}$$

Taking the sum of all continuity equations results in the continuity equation for the mixture:

$$\frac{\partial}{\partial t}\left(\sum_k \rho_k \alpha_k\right) + \frac{\partial}{\partial x_i}\left(\sum_k \rho_k \alpha_k u_{k,i}\right) = 0. \tag{3.4}$$

Defining the mixture density ρ as

$$\rho = \sum_k \rho_k \alpha_k, \tag{3.5}$$

and assuming that relative motion between the phases does not occur and thus that the phases have the same velocity $\vec{\mathbf{u}}_k = \vec{\mathbf{u}}$, equation (3.4) reduces to the continuity equation for the mixture, which is identical to that for a single-phase flow:

$$\frac{\partial \rho}{\partial t} + \frac{\partial (\rho u_i)}{\partial x_i} = 0. \tag{3.6}$$

3.2.2 Conservation of momentum

In the absence of effects of viscosity and of body forces, the conservation of momentum in the j-th direction of phase k can be written as

$$\frac{\partial \rho_k \alpha_k u_{k,j}}{\partial t} + \frac{\partial}{\partial x_i}\left(\rho_k \alpha_k u_{k,j} u_{k,i}\right) = -\frac{\partial \alpha_k p_k}{\partial x_j} + \mathcal{F}_{k,j}, \tag{3.7}$$

where p_k is the pressure within phase k, which can be thought of as the average of the microscopic pressure. $\mathcal{F}_{k,j}$ is the force imposed on phase k by the other phases or components. The source term $\mathcal{F}_{k,j}$ incorporates forces such as surface tension, buoyancy[§], and other forces due to the interface between the phases and mass transfer from one phase to another. As in the case of the mass interaction $\mathcal{M}_k$, it follows that [62]

$$\sum_k \mathcal{F}_{k,j} = 0. \tag{3.8}$$

[§] *which is often written as $p_{k,i}\nabla\alpha_k$ with $p_{k,i}$ the interfacial pressure*

Defining the mixture pressure p as

$$p = \sum_k \alpha_k p_k, \tag{3.9}$$

and assuming that all the phases have the same pressure $p_k = p$ and velocity $\vec{\mathbf{u}}_k = \vec{\mathbf{u}}$ and taking the sum of all momentum equations in direction j results in the mixture momentum equation in direction j:

$$\frac{\partial \rho u_j}{\partial t} + \frac{\partial}{\partial x_i}\left(\rho u_j u_i\right) = -\frac{\partial p}{\partial x_j}. \tag{3.10}$$

3.2.3 Conservation of energy

Neglecting gravity, the total specific energy E_k for phase k is the sum of the internal specific energy e_k and the kinetic energy $\frac{1}{2}\vec{\mathbf{u}}_k \cdot \vec{\mathbf{u}}_k$ of phase k

$$E_k = e_k + \frac{1}{2}\vec{\mathbf{u}}_k \cdot \vec{\mathbf{u}}_k. \tag{3.11}$$

An appropriate statement of the first law of thermodynamics for each phase is as follows [30]:

Rate of increase of total energy of phase k
+ Net flux of total energy of phase k
=
Rate of heat addition to phase k from outside: $\mathcal{Q}_k$
+ Rate of work done to phase k by the exterior surroundings: $\mathcal{W}_k$
− Rate of work done by stresses acting on phase k
+ Rate of heat transfer to phase k from other phases: $\mathcal{QM}_k$
+ Rate of work done to phase k by other phases or components: $\mathcal{WM}_k$

The first two terms can be written as

$$\frac{\partial}{\partial t}\left(\rho_k \alpha_k E_k\right) + \frac{\partial}{\partial x_i}\left(\rho_k \alpha_k E_k u_{k,i}\right). \tag{3.12}$$

The rate of heat addition due to external heating and to conduction of heat $\mathcal{Q}_k$ is neglected as well as the rate of external work $\mathcal{W}_k$. Neglecting effects of viscosity, the work done by stresses only consists of a pressure term. The energy equation for the individual phase may then be written as

$$\frac{\partial \rho_k \alpha_k E_k}{\partial t} + \frac{\partial}{\partial x_i}\left(\rho_k \alpha_k E_k u_{k,i}\right) = \mathcal{QM}_k + \mathcal{WM}_k - \frac{\partial \alpha_k p_k u_{k,i}}{\partial x_i}. \tag{3.13}$$

The two terms involving exchange of energy between the phases can be combined into an energy interaction term $\mathcal{E}_k$ given by

$$\mathcal{E}_k = \mathcal{Q}\mathcal{M}_k + \mathcal{W}\mathcal{M}_k. \tag{3.14}$$

As in the case of mass interaction it follows that

$$\sum_k \mathcal{E}_k = 0. \tag{3.15}$$

All the energy equations for the individual phases can be summed to obtain the energy equation for the mixture:

$$\frac{\partial}{\partial t}\left(\sum_k \rho_k \alpha_k E_k\right) + \frac{\partial}{\partial x_i}\left(\sum_k \rho_k \alpha_k E_k u_{k,i}\right) = -\frac{\partial}{\partial x_i}\left(\sum_k \alpha_k p_k u_{k,i}\right). \tag{3.16}$$

Using the mixture density ρ (3.5), the mixture pressure p (3.9) and the mixture specific internal energy e defined by

$$\rho e = \sum_k \rho_k \alpha_k e_k, \tag{3.17}$$

and assuming that the phases have the same pressures and velocities the mixture energy equation can be written as

$$\frac{\partial \rho E}{\partial t} + \frac{\partial}{\partial x_i}\left(\rho E u_i\right) = -\frac{\partial p u_i}{\partial x_i}, \tag{3.18}$$

where E denotes the total specific energy of the mixture given by

$$E = e + \frac{1}{2}\vec{\mathbf{u}}\cdot\vec{\mathbf{u}}. \tag{3.19}$$

It must be noted that when modeling multi-phase flows by the mixture equations many modeling questions arise, see e.g. Brennen [30]. Most multi-phase flow modeling efforts concentrate on the individual phase equations of motion and therefore they focus on constructing the interaction terms $\mathcal{M}_k$, $\mathcal{F}_k$ and $\mathcal{E}_k$, see also Drew [62]. However, to model these interaction terms there does not exist a general applicable method that is independent of the flow topology. So, they must be constructed empirically given a particular flow pattern. In this thesis we adopt the equilibrium model for cavitating flows assuming that the mixture remains in thermodynamic and mechanical equilibrium as described in the next section. Therefore, the homogeneous mixture equations (3.6), (3.10) and (3.18) describe the flow of the mixture.

The set of mixture equations is not closed, there are 5 equations and 6 unknowns, namely ρ, $\vec{\mathbf{u}}$, p, e. So an additional equation must be provided. In the following section 3.3 equations of state for compressible liquid flows are discussed. In section 3.4 the equilibrium cavitation model is addressed that will close the set of equations for the two-phase mixture.

3.3 Equations of state for compressible liquids

In this section equations of state for compressible liquids are discussed. For reference the Maxwell relations for thermodynamics are presented in appendix E. Considered are the following equations of state:

- **Stiffened gas equation of state** or Tammann equation of state, see Harlow & Amsden [85, 136]:

$$p = (\gamma - 1)\rho e - \gamma p_\infty, \tag{3.20}$$

  with γ and p_∞ liquid-dependent constants. Note that for $1 < \gamma < 2$ and $p_\infty = 0$ the equation of state for a perfect gas is obtained.

- **Tait equation of state**

$$p = K_0 \left(\frac{\rho}{\rho_0} - 1 \right)^N + p_0, \tag{3.21}$$

  with K_0 and N liquid dependent constants and ρ_0 and p_0 constant reference density and reference pressure, respectively. Hayward [88] points out that the equation to which Tait's name has been attached is not proposed by Tait. It appears to have originated through an unfortunate misquotation by Tammann of Tait's original equation. Slightly different forms compared with equation (3.21) are used by various authors. We refer to Tait's equation of state as presented in equation (3.21).

- **Modified Tait equation of state**, see Saurel *et al*. [166]

$$p = K_0 \left(\frac{\rho}{\rho_{sat}(T)} - 1 \right)^N + p_{sat}(T), \tag{3.22}$$

  with K_0 and N liquid dependent constants and $\rho_{sat}(T)$ and $p_{sat}(T)$ temperature dependent saturation density and saturation pressure, respectively. Saurel *et al*. [166] adapted the Tait equation of state by including the temperature dependent saturation pressure $p_{sat}(T)$ and corresponding liquid saturation density $\rho_{sat}(T)$ as reference states, to treat the water as the saturated liquid component of a two-phase mixture.

3.3.1 Speed of sound

The speed of sound c is the velocity at which infinitesimal pressure waves travel through a compressible fluid. The variations in pressure are very small and we assume

that effects of viscosity and heat conduction are negligible. The definition of the speed of sound is

$$c^2 \equiv \left(\frac{\partial p}{\partial \rho}\right)_S = -\frac{1}{v^2}\left(\frac{\partial p}{\partial v}\right)_S. \tag{3.23}$$

Many forms for the speed of sound can be derived, for example

$$c^2 = -\frac{1}{v^2}\frac{c_p(p,T)}{c_v(v,T)}\frac{\left(\frac{\partial S}{\partial v}\right)_T}{\left(\frac{\partial S}{\partial p}\right)_T}, \quad \text{or} \quad c^2 = \left(\frac{\partial p}{\partial \rho}\right)_e + \frac{p}{\rho^2}\left(\frac{\partial p}{\partial e}\right)_\rho. \tag{3.24}$$

From an eigenvalue analysis of the Jacobians of the flux vectors and choosing primitive variables $[p, u, v, w, T]^T$, so that equations of state are required in the form $\rho = \rho(p, T)$ and $h = h(p, T)$, we have derived relation (A.19) for the speed of sound as

$$c^2 = \frac{\rho\left(\frac{\partial h}{\partial T}\right)_p}{\rho\left(\frac{\partial \rho}{\partial p}\right)_T\left(\frac{\partial h}{\partial T}\right)_p + \left(\frac{\partial \rho}{\partial T}\right)_p\left\{1 - \rho\left(\frac{\partial h}{\partial p}\right)_T\right\}}, \tag{3.25}$$

which can be found directly from the equations of state $\rho(p, T)$ and $h(p, T)$.

3.3.2 Stiffened gas equation of state

The so-called stiffened gas equation of state [85] or Tammann equation of state can be used to describe compressible liquids (and even solids [178]) at high pressures [104]. The stiffened gas equation of state reads

$$p = p(\rho, e) = (\gamma - 1)\rho e - \gamma p_\infty, \tag{3.26}$$

where p, ρ and e are the pressure, density and specific internal energy, respectively. The specific internal energy is given by [35, 145]:

$$e = \frac{c_p}{\gamma}T + \frac{p_\infty}{\rho}, \tag{3.27}$$

with c_p the specific heat at constant pressure assumed to be constant. From equation (3.25) we find the speed of sound to be equal to

$$c^2 = \frac{\gamma}{\rho}\left(p + p_\infty\right). \tag{3.28}$$

The value for the pressure constant p_∞ and for the polytropic constant γ are liquid-dependent and can be determined from laboratory experiments [136] via an empirical fit [104, 178]. Cocchi *et al*. [40] presented a derivation of the parameters p_∞ and γ. Le Metayer *et al*. [124] derived values of the parameters γ and p_∞ for water in presence of its vapor. For water, various values for γ and p_∞ are found in the literature,

see table 3.1. Note that Chang & Liou [35] adapted a non-physical value for the specific heat at constant pressure equal to $C_p = 8095.08\,\mathrm{J\,kg^{-1}K^{-1}}$ to match the values of the density and speed of sound at $T = 298\mathrm{K}$.

Reference	γ	p_∞ [10^8 Pa]
Chang & Liou (2007) [35]	1.932	11.645
Paillère *et al*. (2003) [145]	2.8	8.5
Barberon & Helluy (2005) [19]	3.0	8.533
Haller *et al*. (2003) [84]	4.0	6.13
Saurel & Abgrall (1999) [164, 165] Abgrall (2003) [7] Shyue (2006) [180] Cochi (1996, 1997) [40, 41]	4.4	6.0
Shye (1998) [178] Johnsen (2006) [107]	5.5	4.92115
Shyue (1999) [179]	7.0	3.0
Luo *et al*. (2004) [135]	7.0	3.03975
Gallouët (2002) [77]	7.15	3.0

TABLE 3.1: *Stiffened gas equation of state. Values of γ and p_∞ for water as used by various authors.*

To investigate the validity of the stiffened gas equation of state for water at low pressures, the analytical values from equation (3.26) are compared with experimental data [1, 2, 213].

Comparison with experimental data

Using the parameter values of Chang & Liou [35], Paillère *et al*. [145] and Le Mètayer *et al*. [124] the density and the speed of sound are compared with the experimental NIST data [2] in figure 3.1.

For the pressure range from 0 to 10 bar it is shown that the density for water as found from using the stiffened gas equation of state deviates from the NIST data by approximately 6% and 37% for the parameter values of Paillère and Le Mètayer, respectively. The speed of sound found with the parameter values of Paillère correspond very well with the NIST data, whereas the speed of sound found with the parameter values of Le Mètayer deviates by approximately 12%. The values of Chang & Liou for the density and speed of sound correspond excellently with the experimental data. However, to achieve this they have changed the value for the specific heat at constant pressure

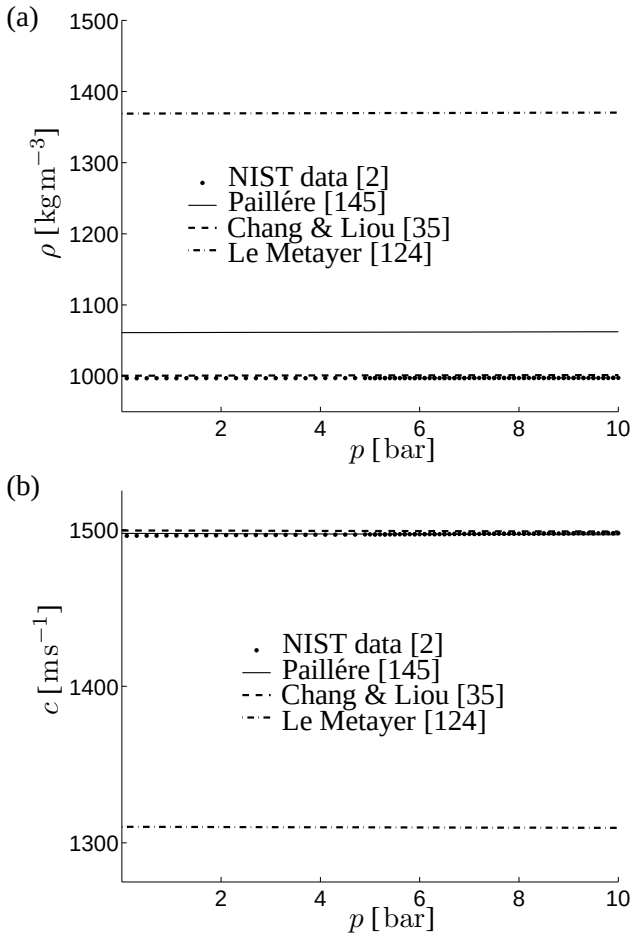

FIGURE 3.1: *Stiffened gas equation of state,* $T = 298$ K. *The values of Chang & Liou [35], Paillère et al. [145] and Le Métayer et al. [124] are compared with NIST data [2] as a function of pressure* $p \in$ *[0,10]* bar. *(a) density* ρ *(b) speed of sound* c*.*

c_p to a non-physical value, i.e. $c_p = 8095.08\,\mathrm{J\,kg^{-1}K^{-1}}$.

From this comparison we conclude that, using the stiffened gas equation of state, a different liquid saturation density at saturation pressure is obtained compared with the physical saturation value. Thus, we state that the stiffened gas equation of state is not suitable to use in combination with cavitation, since the saturation values for the liquid density at low pressures do not match the experimental data. ¶

¶*The author would like to thank S. Schmidt and Prof. Schnerr from the TU Munich for pointing out this conclusion, see also Schmidt et al. [169].*

3.3.3 Modified Tait equation of state

To treat the water as the saturated liquid component of a two-phase mixture Saurel *et al*. [166] adapted the Tait equation to include the temperature dependent saturation pressure $p_{sat}(T)$ and corresponding liquid saturation density $\rho_{sat}(T)$ as reference states. The modified Tait equation of state for liquid then reads:

$$p(\rho,T) = K_0\left[\left(\frac{\rho}{\rho_{sat}(T)}\right)^N - 1\right] + p_{sat}(T). \tag{3.29}$$

From the Maxwell relations and equation (E.1) it is found that

$$\left(\frac{\partial c_v(v,T)}{\partial v}\right)_T = T\frac{NK_0}{v^N\rho_{sat}^{N+2}}\left[(N+1)(\rho'_{sat})^2 - \rho_{sat}(T)\rho''_{sat}\right] + Tp''_{sat}. \tag{3.30}$$

where the prime denotes differentiation with respect to T. Thus c_v is a function of v and T and not just of T. The specific internal energy $e(v,T)$ can be found by using equation (E.4) and the Maxwell relations

$$\left(\frac{\partial e}{\partial T}\right)_v = c_v(v,T), \quad \left(\frac{\partial e}{\partial v}\right)_T = -p + T\left(\frac{\partial p}{\partial T}\right)_v, \tag{3.31}$$

yielding

$$\begin{aligned} e(\rho,T) &= \int_{T_{ref}}^{T} c_v(\rho_{ref},\hat{T})\mathrm{d}\hat{T} + e(\rho_{ref},T_{ref}) + \frac{(Tp'_{sat} - p_{sat} + K_0)}{\rho_{ref}}\underbrace{\left(\frac{\rho_{ref}}{\rho} - 1\right)}_{I} \\ &+ \frac{K_0}{N-1}\left(\rho_{sat}(T) + NT\rho'_{sat}\right)\underbrace{\left((\frac{\rho}{\rho_{sat}(T)})^{N-1} - (\frac{\rho_{ref}}{\rho_{sat}(T)})^{N-1}\right)}_{II}. \end{aligned} \tag{3.32}$$

Instead of using the specific internal energy from equation (3.32) Saurel *et al*. [166] proposed a simplification for water:

$$e(T) = c_v(T - T_{ref}) + e_0, \tag{3.33}$$

where c_v is taken constant. This simplification can be justified by considering terms I and II in equation (3.32). Since the density in water is approximately constant we find that $\rho_{ref} \approx \rho$, $\rho \approx \rho_{sat}(T)$ and $\rho_{ref} \approx \rho_{sat}(T)$ yielding that term I and term II are approximately equal to zero. Furthermore, for water at low temperatures it is valid to assume that $c_v(\rho_{ref},T)$ is constant and thus we find equation (3.33) for the specific internal energy.

Now, the speed of sound is found from equation (3.25) as

$$c^2 = \frac{N(p - p_{sat}(T) + K_0)}{\rho} \tag{3.34}$$

$$+\frac{p}{\rho^2 c_v}\left(p'_{sat}(T) - \frac{N(p - p_{sat}(T) + K_0)}{\rho_{sat}(T)}\rho'_{sat}(T)\right). \tag{3.35}$$

3.4 Equilibrium model for cavitating flows

Following Saurel *et al*. [166] and Schmidt *et al*. [169] the equilibrium cavitation model is described. The physical model is based on the assumption that the two-phase flow regime can be described as a homogeneous mixture that remains in thermodynamic and mechanical equilibrium. This implies an equilibrium of local temperature, local pressure and local velocity between the vapor and liquid components of the two-phase mixture. Under these assumptions, the flow of the mixture can be described by the mixture equations of section 3.2 together with an appropriate equation of state that covers all fluid states possible: the compressible pure liquid state, the compressible two-phase mixture state and the compressible pure vapor state. The equations of state must be such that the hyperbolic nature of the system of governing equations is preserved in order to study finite propagation speed wave motions in the fluid.

Summarizing, the governing equations are the Euler equations in conservation form for the mixture variables written here for Cartesian coordinates as:

$$\frac{\partial \mathbf{U}}{\partial t} + \frac{\partial \mathbf{F}_x(\mathbf{U})}{\partial x} + \frac{\partial \mathbf{F}_y(\mathbf{U})}{\partial y} + \frac{\partial \mathbf{F}_z(\mathbf{U})}{\partial z} = 0, \tag{3.36}$$

where $\mathbf{U} = [\rho, \rho u, \rho v, \rho w, \rho E]^T$ is the vector of conserved variables and $\mathbf{F}_x(\mathbf{U})$, $\mathbf{F}_y(\mathbf{U})$ and $\mathbf{F}_z(\mathbf{U})$ are the three components of the flux vectors given as

$$\mathbf{F} = \left[\begin{array}{ccc} \mathbf{F}_x(\mathbf{U}) & \mathbf{F}_y(\mathbf{U}) & \mathbf{F}_z(\mathbf{U}) \end{array}\right] = \left[\begin{array}{ccc} \rho u & \rho v & \rho w \\ \rho u^2 + p & \rho uv & \rho uw \\ \rho uv & \rho v^2 + p & \rho vw \\ \rho uw & \rho vw & \rho w^2 + p \\ \rho H u & \rho H v & \rho H w \end{array}\right], \tag{3.37}$$

where the total specific enthalpy H is equal to

$$H = E + \frac{p}{\rho} = h + \frac{1}{2}\vec{\mathbf{u}}\cdot\vec{\mathbf{u}}, \tag{3.38}$$

with the total specific energy E defined in equation (3.19). The speed of sound c is defined in equation (3.25). For closure of the system of equations it is necessary

to adopt equations of state $\rho = \rho(p,T)$ and $h = h(p,T)$ that describe each of the three possible states: the liquid state, the vapor state and the mixture state. In the following the liquid phase is denoted by subscript l, the vapor phase by subscript v and saturation conditions by subscript sat.

Before continuing with the equations of state the saturation curves of section 2.4 are repeated here for clarity. The relation between pressure and temperature during phase change is given by the analytical expression [168]:

$$\ln\left(\frac{p_{sat}(T)}{p_c}\right) = \frac{T_c}{T}\sum_{i}^{7} a_i \theta^{\hat{a}_i}, \tag{3.39}$$

where $\theta = 1 - T/T_c$ and where p_c and T_c represent the critical pressure and critical temperature, which for water are equal to $p_c = 22.120\times10^6$ Pa and $T_c = 647.16$ K, respectively. The coefficients a_i and $\hat{a}_i$ are given in table 2.1. In figure 3.2 the values from equation (3.39) for the saturation pressure p_{sat} as a function of the temperature T are compared with the experimental data [2]. It shows that the analytical expression fits the experimental data accurately.

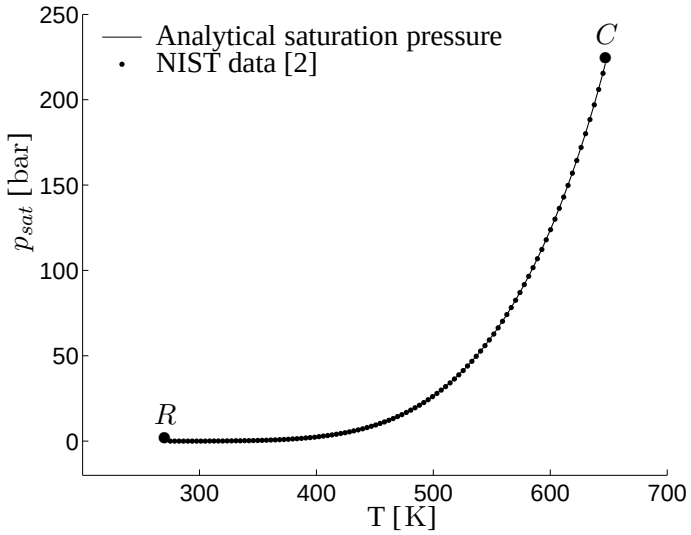

FIGURE 3.2: *Comparison between analytical expression for the saturation pressure* p_{sat} $[\mathrm{bar}]$ *(line) and experimental saturation data [2] (dots) versus temperature* T $[\mathrm{K}]$. R *is the triple point and* C *is the critical point.*

The liquid and vapor saturation densities along the saturation curves are given by, see

[168]

$$\frac{\rho_{l,sat}(T)}{\rho_c} = \sum_{i=1}^{7} b_i \theta^{\hat{b}_i}, \tag{3.40}$$

$$\ln\left(\frac{\rho_{v,sat}(T)}{\rho_c}\right) = \sum_{i=1}^{7} c_i \theta^{\hat{c}_i}, \tag{3.41}$$

where ρ_c is the critical density for water equal to $\rho_c = 322\ \mathrm{kg\,m^{-3}}$. In figure 3.3 the values from equations (3.40) and (3.41) from for the liquid saturation density $\rho_{l,sat}$ and vapor saturation density $\rho_{v,sat}$ are compared with the experimental data [2]. This again shows that the analytical expressions fit the experimental data accurately.

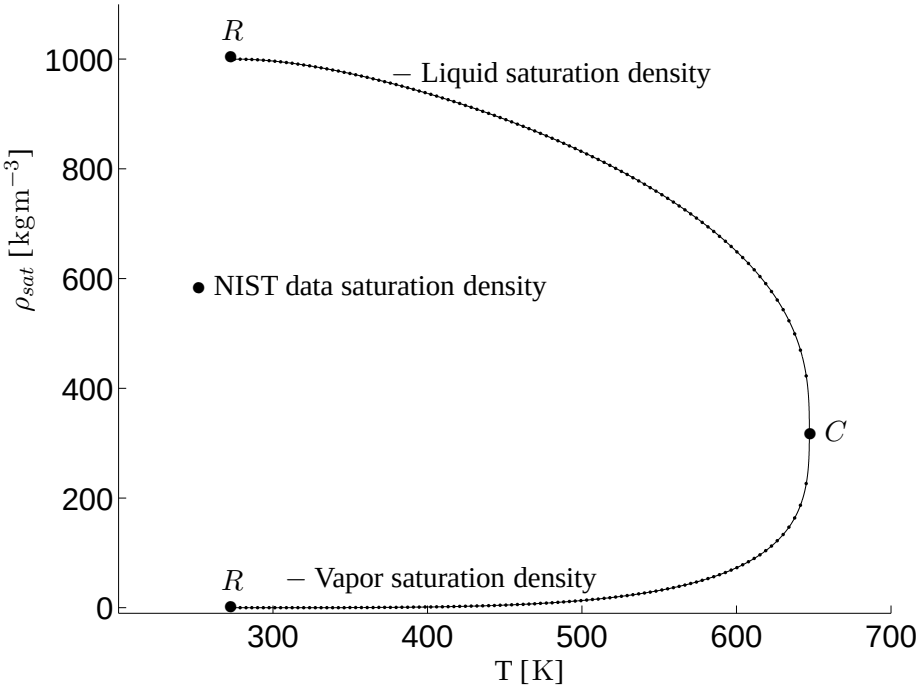

FIGURE 3.3: *Comparison between analytical expression for saturation curves (solid lines) and experimental saturation data [2] (dots) for the vapor saturation density* $\rho_{v,sat}\ [\mathrm{kg\,m^{-3}}]$ *and liquid saturation density* $\rho_{l,sat}\ [\mathrm{kg\,m^{-3}}]$ *versus temperature* $T\ [K]$. R *is the triple point and* C *is the critical point.*

3.4.1 Liquid phase

As presented in section 3.3 we follow Saurel *et al.* [166] by adopting a modification of the Tait equation of state to describe the pressure of the liquid as a function of the

density and temperature:

$$p_l(\rho_l, T_l) = K_0 \left[\left(\frac{\rho_l}{\rho_{l,sat}(T_l)} \right)^N - 1 \right] + p_{sat}(T_l), \tag{3.42}$$

where for water $K_0 = 3.3{\times}10^8$ Pa and $N = 7.15$ are taken to be constant. A caloric equation of state that is a good approximation, see section 3.3, is given by

$$e_l(T_l) = C_{vl}(T_l - T_0) + e_{l0}, \tag{3.43}$$

where C_{vl} is the specific heat at constant volume for liquid, T_0 is a reference temperature and e_{l0} is the internal energy at this reference temperature. For water these constants have the values $C_{vl} = 4180$ $\mathrm{J kg^{-1} K^{-1}}$, $T_0 = 273.15$ K and $e_{l0} = 617.0$ $\mathrm{J kg^{-1}}$, respectively. Applying equation (3.25), the speed of sound c_l in the liquid is given by:

$$c_l^2 = \frac{N\bar{p}(T_l)}{\rho_l} + \frac{p_l}{\rho_l^2 C_{vl}} \left(p'_{sat}(T_l) - \frac{N\bar{p}(T_l)}{\rho_{l,sat}(T_l)} \rho'_{l,sat}(T_l) \right), \tag{3.44}$$

where $\bar{p}(T) = p_l - p_{sat}(T) + K_0$, $p'_{sat}(T) = \frac{\mathrm{d}p_{sat}(T)}{\mathrm{d}T}$ and $\rho'_{l,sat}(T) = \frac{\mathrm{d}\rho_{l,sat}(T)}{\mathrm{d}T}$.

3.4.2 Vapor phase

Saurel *et al*. [166] use the ideal gas equation of state for the vapor phase

$$p_v(\rho_v, e_v) = (\gamma - 1)\rho_v e_v, \quad \text{or} \quad p_v(\rho_v, T_v) = \rho_v R T_v, \tag{3.45}$$

with γ the ratio of specific heats and $R = \hat{R}/\hat{M}$ the specific gas constant for vapor with $\gamma = 1.327$ and $R = 461.6$ $\mathrm{J kg^{-1} K^{-1}}$. The corresponding caloric equation of state is

$$e_v(T_v) = C_{vv}(T_v - T_0) + L_v(T_0) + e_{l0}, \tag{3.46}$$

where L_v represents the latent heat of vaporization and C_{vv} the specific heat at constant volume with values $L_v(T_0) = 2.3753 \times 10^6$ $\mathrm{J kg^{-1} K^{-1}}$, $C_{vv} = 1410.8$ $\mathrm{J kg^{-1} K^{-1}}$, $T_0 = 273.15$ K, respectively. The speed of sound of vapor c_v is given by

$$c_v^2 = \gamma \frac{p_v}{\rho_v} = \gamma R T_v. \tag{3.47}$$

Table 3.2 gives an overview of values of the parameters used in the equations of state for liquid and vapor.

Liquid		Vapor	
parameter	value	parameter	value
N	7.15	γ	1.327
K_0	3.3 $\times 10^8$ Pa	R	461.6 $\mathrm{J kg^{-1} K^{-1}}$
C_{vl}	4180 $\mathrm{J kg^{-1} K^{-1}}$	C_{vv}	1410.8 $\mathrm{J kg^{-1} K^{-1}}$
T_0	273.15 K	T_0	273.15 K
e_{l0}	617.0 $\mathrm{J kg^{-1}}$	$L_v(T_0)$	2.753 $\times 10^6$ $\mathrm{J kg^{-1} K^{-1}}$

TABLE 3.2: *Parameters for liquid and vapor phase of water.*

3.4.3 Mixture phase

The two phases in the mixture are assumed to be in thermal and mechanical equilibrium and the pressure in the mixture phase is taken to be equal to the saturation pressure:

$$p_l = p_v = p, \quad \text{and} \quad T_l = T_v, \tag{3.48}$$

$$p = p_{sat}(T). \tag{3.49}$$

The mixture density ρ and mixture internal energy e are defined by

$$\rho = \alpha\rho_{v,sat}(T) + (1-\alpha)\rho_{l,sat}(T), \tag{3.50}$$

$$\rho e = \alpha\rho_{v,sat}(T)e_v(T) + (1-\alpha)\rho_{l,sat}(T)e_l(T), \tag{3.51}$$

where the void fraction of the vapor $\alpha \equiv V_v/V$ is obtained from equation (3.50) as

$$\alpha = \frac{\rho - \rho_{l,sat}(T)}{\rho_{v,sat}(T) - \rho_{l,sat}(T)}. \tag{3.52}$$

For the two-phasic states, the temperature is determined from definition (3.51) of the internal energy of the mixture by substituting equations (3.43) and (3.46)

$$\rho e = (T - T_0)\left\{\alpha\rho_{v,sat}(T)C_{vv} + (1-\alpha)\rho_{l,sat}(T)C_{vl}\right\} + \alpha\rho_{v,sat}(T)L_v(T_0) + \rho e_{l0}.$$

The model is based on thermodynamic equilibrium and thus the equilibrium speed of sound in a saturated mixture can be calculated by the formula of Wallis [214]

$$\frac{1}{\rho c^2} = \frac{\alpha}{\rho_{v,sat}(T)c_v^2} + \frac{1-\alpha}{\rho_{l,sat}(T)c_l^2}. \tag{3.53}$$

In figure 3.4 the resulting mixture speed of sound is presented. It can be seen that for values of the void fraction between $0.1 \leq \alpha \leq 0.9$ the corresponding speed of sound is lower than 10 $\mathrm{m s^{-1}}$.

Equations (3.50)–(3.53) represent a closed algebraic system that permits the computation of all thermodynamic variables for equilibrium states inside the saturation zones. The equations of state for all three possible phases are represented in the $p-v$ diagram shown in figure 3.5. The liquid density and vapor density are compared with the IAPWS experimental data represented by the black dots in figure 3.5.

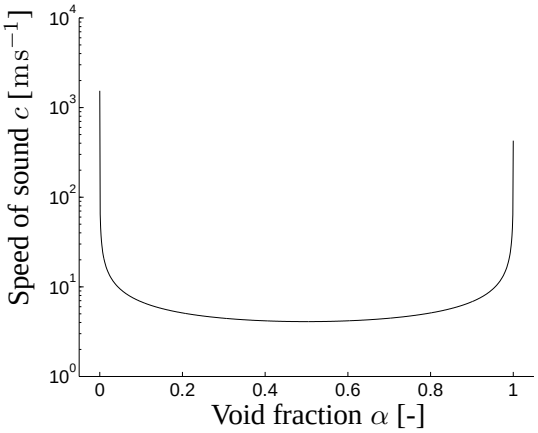

FIGURE 3.4: *The mixture speed of sound* $c\ [\mathrm{ms}^{-1}]$ *at* $T = 298\ \mathrm{K}$ *as a function of the void fraction* α*. Note that, for liquid (*$\alpha = 0$*) the speed of sound is approximately equal to 1540* ms^{-1}*, for vapor (*$\alpha = 1.0$*) the speed of sound is 420* ms^{-1} *and for* $\alpha = 0.5$ *the speed of sound is equal to 4.1* ms^{-1}*.*

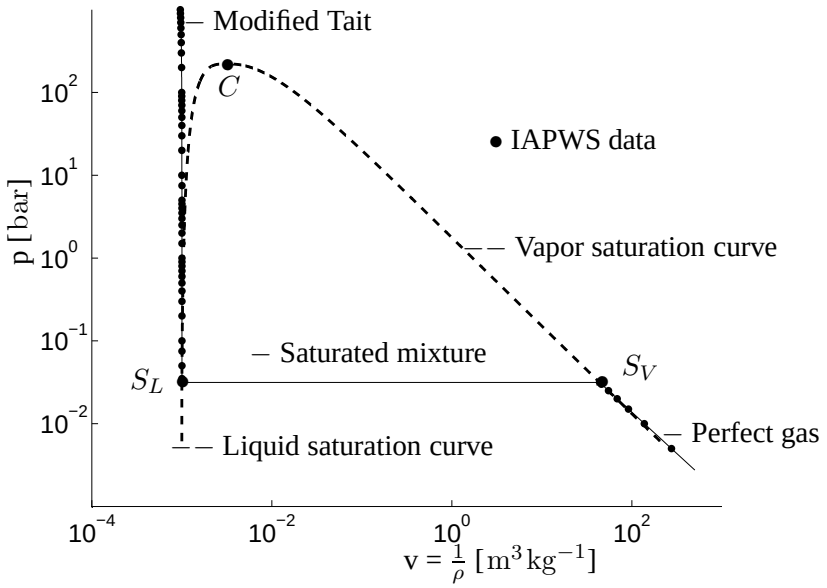

FIGURE 3.5: p-v *diagram for water with isotherm at reference temperature* $T_\infty = 298\ \mathrm{K}$*. Presented are the IAPWS experimental data [2] (black dots), the saturation curves for liquid and vapor (dashed lines), the saturation points* S_L *and* S_V *at* $T = 298\ \mathrm{K}$ *for liquid and vapor, respectively, the modified Tait equation of state for the liquid, mixture state and the perfect gas equation of state (solid lines).* C *is critical point.*

3.5 Remark on extension to non-equilibrium models

The formulation presented in the preceding section does not require the solution of an additional transport equation for the mass fraction or volume fraction of vapor. To incorporate non-equilibrium effects the equilibrium conditions $p_v = p_l = p_{sat}(T)$ and $T_l = T_v$ are relaxed and the following conservation equation for the vapor mass is added:

$$\frac{\partial \alpha \rho_v}{\partial t} + \nabla \cdot (\alpha \rho_v \vec{\mathbf{u}}) = \mathcal{M}_v, \tag{3.54}$$

with $\mathcal{M}_v$ a finite-rate mass transfer source term for vapor. This last equation offers the possibility to include a relaxation term in order to model non-equilibrium processes and thermodynamic effects, which offers more flexibility to describe phase transition in cavitation. However, in the existing (incompressible) flow models this flexibility comes at the prize of user-defined free parameters in particular in the source terms. These empirical parameters must be chosen very carefully. We have investigated non-equilibrium models for incompressible flows as presented in appendix G. More research should be conducted to obtain the adequate values for these parameters in order to enable prediction of cavitation with smaller uncertainty. Source terms without empirical parameters such as proposed by Senocak & Shyy [173] or source terms based on thermodynamic considerations as proposed by Iben *et al*. [100], do not depend on user-defined free parameters and are preferable over the more conventional methods.

Furthermore, we experienced numerical instabilities when the density ratio ρ_l/ρ_v was increased to a value exceeding 100. As discussed in section 4.5 one of the possibilities for these instabilities might be the JST flux scheme, which we have used in combination with the non-equilibrium models. Employing a different flux scheme such as the HLLC flux scheme as described in section 4.5, may remove these instabilities.

When a compressible water-vapor medium is considered an additional and major challenge lies in preserving the hyperbolic consistency of the system of equations. Furthermore, when both water and vapor are present in one computational control volume two different pressures need to be accounted for through appropriate equations of state. The pressure in the liquid phase will become "negative", i.e. a tensile stress. The question is which equation of state can be used for this regime. For densities between the spinodal values the acoustic eigenvalues for the Sanchez-Lacombe equation of state as used by Edwards & Liou [63][‖] or the Van der Waals equation of

[‖] *Edwards & Liou [63] employed the Sanchez-Lacombe equation of state for real-fluid flows accompanied with the equilibrium assumption in the two-phase region to guarantee a real-valued speed of sound.*

state are complex-valued, implying that the system of Euler equations coupled with these equations of state is not hyperbolic in the whole flow field. The equations of state for liquid flow, as discussed in section 3.3, need to be accompanied with an appropriate equation of state for the vapor phase. However, when returning to a positive pressure in the vapor phase from a negative pressure in the liquid phase an inflection point appears in the p-v-diagram resulting in complex-valued eigenvalues.

NUMERICAL METHODS FOR COMPRESSIBLE FLOWS

CHAPTER 4

For the simulation of cavitating flows the fluid is considered as a homogeneous, compressible, inviscid medium as presented in sections 3.2–3.4. The flow of such a medium can be described by the three-dimensional unsteady Euler equations, which are presented in section 4.1.

The literature on the numerical simulation of compressible flows is extensive, see amongst others the books by Toro [194], Blazek [25], Feistauer [64], Laney [122] and Hirsch [90, 91]. In this chapter an overview of the relevant numerical methods is presented. The focus is on addressing the critical aspects of simulating a compressible flow over a wide range of Mach numbers with an arbitrary equation of state employing a numerical method implemented on an unstructured edge-based finite-volume computational mesh.

In the present study the edge-based finite-volume method for unstructured meshes is employed, which offers great flexibility and easy applicability to the solution of flow problems in domains with a complicated geometry. The finite volume mesh is presented in section 4.2 followed by the finite volume formulation in section 4.3.

In section 4.4 the time-integration method is outlined followed in section 4.5 by the description of several different flux schemes. In section 4.6 the MUSCL-type higher order spatial reconstruction for unstructured grids is described, which is necessary to extend the numerical method to second-order spatial accuracy. In section 4.7 the low-Mach number problem is addressed and an adaptation to the flux schemes in order to overcome this problem is presented.

The formulation of the boundary conditions are presented in section 4.8. In the present work the boundary condition treatment of Thompson [190] using the perfect gas law as the equation of state, is generalized to an arbitrary equation of state. Lastly, the solution procedure is presented in section 4.9.

4.1 Three-dimensional unsteady Euler equations

The equations of motion describing an inviscid, non-heat-conducting, compressible flow are the Euler equations. These five equations form a non-linear system, expressing the conservation of mass, momentum and energy. Considering a physical domain Ω at a fixed position with boundary $A = \partial\Omega$, the Euler equations read in integral conservation form

$$\frac{\partial}{\partial t}\iiint_{\Omega} \mathbf{U}\,\mathrm{d}\Omega + \iint_{A} \vec{\mathbf{F}}(\mathbf{U})\cdot\vec{\mathbf{n}}\,\mathrm{d}A = \mathbf{0}, \tag{4.1}$$

where $\mathbf{U} = [\rho, \rho u, \rho v, \rho w, \rho E]^T$ is the vector of conserved variables with ρ the density, $\vec{\mathbf{u}} = [u, v, w]^T$ the velocity vector, $E = e + \frac{1}{2}\vec{\mathbf{u}}\cdot\vec{\mathbf{u}}$ the specific total energy, and e the specific internal energy. The out of the control volume directed unit normal vector $\vec{\mathbf{n}} = [n_x, n_y, n_z]^T$ denotes the orientation of surface A. The tensor of fluxes $\vec{\mathbf{F}}(\mathbf{U})$ written as $[\mathbf{F}_x(\mathbf{U}), \mathbf{F}_y(\mathbf{U}), \mathbf{F}_z(\mathbf{U})]$ is given by

$$\vec{\mathbf{F}}(\mathbf{U}) = \begin{bmatrix} \rho u & \rho v & \rho w \\ \rho u^2 + p & \rho v u & \rho w u \\ \rho u v & \rho v^2 + p & \rho v w \\ \rho u w & \rho v w & \rho w^2 + p \\ \rho u H & \rho v H & \rho w H \end{bmatrix}, \tag{4.2}$$

where p is the pressure and $H = E + p/\rho = h + \frac{1}{2}\vec{\mathbf{u}}\cdot\vec{\mathbf{u}}$ is the specific total enthalpy. The inviscid flux $\vec{\mathbf{F}}(\mathbf{U})\cdot\vec{\mathbf{n}}$ in equation (4.1) can now be found by

$$\vec{\mathbf{F}}(\mathbf{U})\cdot\vec{\mathbf{n}} = \mathbf{F}_x(\mathbf{U})n_x + \mathbf{F}_y(\mathbf{U})n_y + \mathbf{F}_z(\mathbf{U})n_z, \tag{4.3}$$

which yields

$$\vec{\mathbf{F}}(\mathbf{U})\cdot\vec{\mathbf{n}} = \begin{bmatrix} \rho\hat{u} \\ \rho\hat{u}u + pn_x \\ \rho\hat{u}v + pn_y \\ \rho\hat{u}w + pn_z \\ \rho\hat{u}H \end{bmatrix}, \tag{4.4}$$

where $\hat{u}$ is the contravariant velocity component normal to the surface A defined by

$$\hat{u} = \vec{\mathbf{u}}\cdot\vec{\mathbf{n}} = un_x + vn_y + wn_z. \tag{4.5}$$

The system of equations (4.1) is not closed and an appropriate equation of state is required, which preserves the hyperbolic nature of the system of equations as discussed in sections 3.2–3.5. We choose the equations of state $\rho = \rho(p, T)$ and $h = h(p, T)$ of section 3.4.

4.2 Finite-volume mesh

Let $\Omega \subset \mathbb{R}^3$ be the physical domain occupied by the fluid and let Ω_h be a polygonal or polyhedral approximation of Ω. The set of finite volumes or control volumes $V_h = \{V_i\}_{i \in J}$, where $J \subset \mathbb{Z}^+ = \{1, 2, \ldots\}$, is called a finite volume mesh in Ω_h, if all control volumes V_i are closed polygons or polyhedrons with mutually disjoint interiors such that

$$\bar{\Omega}_h = \bigcup_{i \in J} V_i. \tag{4.6}$$

In unstructured meshes the control volumes have no particular ordering, i.e. neighboring control volumes cannot be directly identified by their indices. Employing the numerical program Favomesh* [109], the control volumes are constructed from a finite element mesh by means of a node-centered dual mesh, see the theses of Put [153] and Kelleners [109]. The finite element meshes can consist of only one type, triangles or quadrilaterals in 2D and tetrahedrons or hexahedra in 3D as well as of a mix of different element types, quadrilaterals and triangles in 2D and hexahedra, tetrahedra, prisms and pyramids in 3D, see the MSc-thesis of Hospers [98]. The mixed grids are usually called hybrid grids. In the present numerical method any combination of any type of elements can be employed offering great flexibility in constructing a mesh of good quality around a complex body and fitting this mesh inside a bounding box. As an illustration the reader could think of a hybrid mesh around a ship propeller, which is located inside a cavitation tunnel.

In figure 4.1 a dual finite-volume mesh associated with a triangular grid is illustrated. A control volume (grey polygon) associated with a vertex (●) of the triangular grid is defined as a closed polygon. This polygon is obtained by joining the centers of gravity (◐) of every triangle that contains the vertex with the midpoint (○) of every edge containing the vertex. If the vertex belongs to the boundary of the computational domain, then the control volume is closed by the straight segments joining the vertex with the midpoints of the boundary sides that contain the vertex.

As illustrated in figure 4.1, for 2D the face between two control volumes now consists of two segments, denoted by S_1 and S_2 in figure 4.1 with unit normal vectors $\vec{\mathbf{n}}_1$ and $\vec{\mathbf{n}}_2$. In 3D the number of sub-faces that form the face of the control volume is arbitrary. For the present numerical method these segments are combined into one single face with one single unit normal vector. For more details see the thesis of Kelleners [109]. Note that the total number of control volumes N_{cv} is equal to the total number of vertices of the finite element mesh.

The numerical program Favomesh has been provided by P. Kelleners. For this, the author would like to express his gratitude.

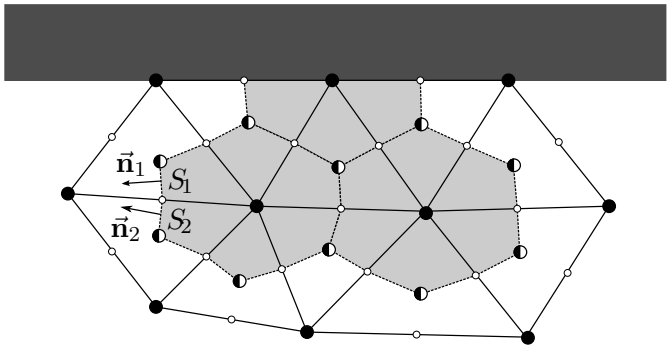

FIGURE 4.1: *Construction of the node-centered finite volume mesh in 2D from the triangular elements. The two segments S_1 and S_2 separating the two control volumes, with their unit normal vectors $\vec{\mathbf{n}}_1$ and $\vec{\mathbf{n}}_2$, are combined into one segment with one unit normal vector, see for more details the thesis of Kelleners [109].*

Denote the set of all interior faces by S_I, the set of all boundary faces by S_B and the set of all faces by $S_{I,B} = S_I \cup S_B$. Two control volumes V_i and V_j are either disjoint or their intersection is formed by a common part of their boundaries ∂V_i and ∂V_j. If $\partial V_i \cap \partial V_j$ contains at least one segment or one manifold then V_i and V_j are called neighbors and their shared segments are denoted by the interior face S_{ij}:

$$S_{ij} = \partial V_i \cap \partial V_j = S_{ji}. \tag{4.7}$$

In the numerical method S_{ij} consists of only one segment or manifold. The following notation is introduced: $|V_i|$ is the area (2D) or volume (3D) of control volume V_i, $|S_{ij}|$ is the length (2D) or area (3D) of face S_{ij}, the vector $\vec{\mathbf{n}}_{ij}$ is the outer normal unit vector to ∂V_i on S_{ij}. Define the set $s(i)$ as the set of indices of all the neighbors of control volume V_i:

$$s(i) = \{j \in J; i \neq j \quad | \quad \partial V_i \cap \partial V_j \neq \emptyset\}. \tag{4.8}$$

The segments or manifolds of the boundary ∂V_i of the control volume that are part of the boundary $\partial\Omega_h$ of the computational domain are denoted by S_{ij}, where $j \in J_B \subset \mathbb{Z}^- = \{-1, -2, \ldots\}$, thus $S_{ij} \subset \partial V_i \cap \partial\Omega_h$. Note that, $J \cap J_B = \emptyset$, meaning that the boundary faces are not part of the interior faces and vice versa. Define the set $s_b(i)$ as the set of the indices of all the faces of control volume V_i which belong to the boundary $\partial\Omega_h$ of the computational domain

$$s_b(i) = \{j \in J_B \quad | \quad S_{ij} \subset \partial V_i \cap \partial\Omega_h\}, \tag{4.9}$$

and thus we have that

$$\partial V_i \cap \partial\Omega_h = \bigcup_{j \in s_b(i)} S_{ij}. \tag{4.10}$$

Now the set $S(i)$ of all the indices of the faces of control volume V_i are formed by putting

$$S(i) = s(i) \bigcup s_b(i), \tag{4.11}$$

resulting in

$$\partial V_i = \bigcup_{j \in S(i)} S_{ij}, \tag{4.12}$$

$$|\partial V_i| = \sum_{j \in S(i)} |S_{ij}|. \tag{4.13}$$

Defining N_{f_i} as the total number of faces S_{ij} of control volume V_i, i.e. $N_{f_i} = |S(i)|$ and defining a one-to-one mapping from $S(i) \rightarrow \hat{S}(i) \subset \mathbb{Z}^+$, we can write equations (4.12) and (4.13) as

$$\partial V_i = \sum_{j=1}^{N_{f_i}} S_{ij}, \tag{4.14}$$

$$|\partial V_i| = \sum_{j=1}^{N_{f_i}} |S_{ij}|. \tag{4.15}$$

4.3 Finite-volume formulation

In order to derive a finite volume scheme equation (4.1) can be considered for each control volume V_i with boundary ∂V_i:

$$\frac{\partial}{\partial t} \iiint_{V_i} \mathbf{U} \, \mathrm{d}V + \iint_{\partial V_i} \vec{\mathbf{F}}(\mathbf{U}) \cdot \vec{\mathbf{n}}_{ij} \, \mathrm{d}\partial V_i = \mathbf{0}. \tag{4.16}$$

Defining the control volume averages $\bar{\mathbf{U}}_i$ as[†]

$$\bar{\mathbf{U}}_i = \frac{1}{|V_i|} \iiint_{V_i} \mathbf{U} \, \mathrm{d}V, \tag{4.17}$$

[†] *It can be shown that the control volume averages $\bar{\mathbf{U}}_i$ are up to second order equal to $\mathbf{U}_{cg}$, the function value at the center of gravity or centroid of the control volume, see thesis of Kelleners [109].*

with $|V_i|$ the volume of control volume V_i and taking into account equation (4.14) yields

$$\frac{\partial \bar{\mathbf{U}}_i}{\partial t} + \frac{1}{|V_i|} \sum_{j=1}^{N_{f_i}} \iint_{S_{ij}} \vec{\mathbf{F}}(\mathbf{U}) \cdot \vec{\mathbf{n}}_{ij} \, \mathrm{d}S_{ij} = \mathbf{0}. \tag{4.18}$$

The flux $\vec{\mathbf{F}}(\mathbf{U}) \cdot \vec{\mathbf{n}}$ can be evaluated by considering equation (4.3), i.e.

$$\vec{\mathbf{F}}(\mathbf{U}) \cdot \vec{\mathbf{n}} = \mathbf{F}_x(\mathbf{U}) n_x + \mathbf{F}_y(\mathbf{U}) n_y + \mathbf{F}_z(\mathbf{U}) n_z. \tag{4.19}$$

However, this would require three different flux evaluations. Instead, the flux can be evaluated by exploiting the rotational invariance property of the Euler equations[‡], which states that

$$\mathbf{F}_x(\mathbf{U}) n_x + \mathbf{F}_y(\mathbf{U}) n_y + \mathbf{F}_z(\mathbf{U}) n_z = \mathbf{T}^{-1} \mathbf{F}_x(\mathbf{T}\mathbf{U}), \tag{4.20}$$

with $\mathbf{T}$ the rotation matrix and $\mathbf{T}^{-1}$ its inverse given in terms of the elements of the unit normal vector $\vec{\mathbf{n}} = [n_x, n_y, n_z]^T$ by

$$\mathbf{T} = \begin{bmatrix} 1 & 0 & 0 & 0 & 0 \\ 0 & n_x & n_y & n_z & 0 \\ 0 & t_{1,x} & t_{1,y} & t_{1,z} & 0 \\ 0 & t_{2,x} & t_{2,y} & t_{2,z} & 0 \\ 0 & 0 & 0 & 0 & 1 \end{bmatrix}, \quad \mathbf{T}^{-1} = \begin{bmatrix} 1 & 0 & 0 & 0 & 0 \\ 0 & n_x & t_{1,x} & t_{2,x} & 0 \\ 0 & n_y & t_{1,y} & t_{2,y} & 0 \\ 0 & n_z & t_{1,z} & t_{2,z} & 0 \\ 0 & 0 & 0 & 0 & 1 \end{bmatrix}, \tag{4.21}$$

where the unit vectors $\vec{\mathbf{n}}$, $\vec{\mathbf{t}}_1$ and $\vec{\mathbf{t}}_2$ form an orthogonal system, i.e $\vec{\mathbf{n}} \cdot \vec{\mathbf{t}}_1 = 0$, $\vec{\mathbf{n}} \cdot \vec{\mathbf{t}}_2 = 0$ and $\vec{\mathbf{t}}_1 \cdot \vec{\mathbf{t}}_2 = 0$. Note that, $\vec{\mathbf{n}} = \vec{\mathbf{t}}_1 \times \vec{\mathbf{t}}_2$.

Thus, the flux $\vec{\mathbf{F}}(\mathbf{U}) \cdot \vec{\mathbf{n}}$ can be evaluated by first applying the rotation matrix $\mathbf{T}$ to the original column vector with the conserved variables $\mathbf{U}$ yielding the rotated conserved variables $\hat{\mathbf{U}} = \mathbf{T}\mathbf{U}$. Note that $\hat{\mathbf{U}}$ is aligned with a new Cartesian frame $(\hat{x}, \hat{y}, \hat{z})$, where the coordinate $\hat{x}$ is in the direction normal to the boundary S_{ij} in the direction of $\vec{\mathbf{n}}$ and $\hat{y}$, $\hat{z}$ are in the directions tangential to the boundary S_{ij}. Then, the inter-cell flux $\mathbf{F}_x(\hat{\mathbf{U}})$ is evaluated and rotated back to the (x, y, z) directions by applying the inverse of the rotation matrix. Equation (4.18) can now be written as:

$$\frac{\partial \bar{\mathbf{U}}_i}{\partial t} + \frac{1}{|V_i|} \sum_{j=1}^{N_{f_i}} \iint_{S_{ij}} \mathbf{T}^{-1} \mathbf{F}_x(\mathbf{T}\mathbf{U}) \, \mathrm{d}S_{ij} = \mathbf{0}. \tag{4.22}$$

[‡]*The proof of the rotational invariance property of the Euler equations is usually presented in two dimensions, see for example Toro [194]. In appendix B the proof is presented for three dimensions with the rotation matrix* $\mathbf{T}$ *of equation (4.21). Note that the proof for the hyperbolicity of the Euler equations can be formulated similarly, see for example Feistauer [64], but is omitted in this thesis.*

The inter-cell flux $\mathbf{F}_x(\mathbf{TU})$ can be approximated by the numerical flux $\mathbf{H}(\mathbf{TU}_L, \mathbf{TU}_R)$:

$$\mathbf{F}_x(\mathbf{TU}) \approx \mathbf{H}(\mathbf{TU}_L, \mathbf{TU}_R), \tag{4.23}$$

where $\mathbf{U}_L$ and $\mathbf{U}_R$ depend on the control volume averages $\bar{\mathbf{U}}_i$ and $\bar{\mathbf{U}}_j$. Before proceeding the following notation is introduced for the numerical flux:

$$\mathbf{T}^{-1}\mathbf{F}_x(\mathbf{TU}) \approx \mathbf{T}^{-1}\mathbf{H}(\mathbf{TU}_L, \mathbf{TU}_R) \equiv \mathbf{H}(\mathbf{U}_L, \mathbf{U}_R, \vec{\mathbf{n}}_{ij}), \tag{4.24}$$

where the unit normal vector $\vec{\mathbf{n}}_{ij}$ defines the rotation matrices $\mathbf{T}$ and $\mathbf{T}^{-1}$. When the face S_{ij} belongs to the boundary Ω_h of the computational domain, then it is necessary to determine $\mathbf{U}_R$ from boundary conditions. Note that, when $\mathbf{U}_L = \bar{\mathbf{U}}_i$ and $\mathbf{U}_R = \bar{\mathbf{U}}_j$ the finite volume scheme is first-order accurate when an approximate Riemann solver is used. The extension to higher order is presented in section 4.6. Also, note that when $\mathbf{U}_L$ and $\mathbf{U}_R$ depend on the control volume averages at the previous time level(s) only, the scheme is explicit. When $\mathbf{U}_L$ and $\mathbf{U}_R$ also depend on the control volume averages at the current time level, the scheme is implicit.

Applying equation (4.24) to (4.22) and assuming that the numerical flux $\mathbf{H}$ is constant over the face S_{ij}, the semi-discretized form of the finite-volume formulation reads:

$$\frac{\partial \bar{\mathbf{U}}_i}{\partial t} + \frac{1}{|V_i|}\sum_{j=1}^{N_{f_i}} \mathbf{H}(\mathbf{U}_L, \mathbf{U}_R, \vec{\mathbf{n}}_{ij})\,|S_{ij}| = 0. \tag{4.25}$$

The finite-volume approximate solution of equation (4.1) at time $t = t^k$ is defined as the piece-wise constant vector-valued functions $\bar{\mathbf{U}}_h^k$, which are obtained from equation (4.25). The vector $\bar{\mathbf{U}}_i^k$, i.e. the control-volume-averaged value of control volume V_i can be considered as the value of the approximate solution at the centroid of the finite volume V_i at time $t = t^k$.

4.3.1 Properties of the numerical flux

The numerical flux $\mathbf{H}$ should have the following properties:

1. $\mathbf{H}(\mathbf{U}, \mathbf{V}, \vec{\mathbf{n}})$ is consistent:

$$\mathbf{H}(\mathbf{U}, \mathbf{U}, \vec{\mathbf{n}}) = \vec{\mathbf{F}}(\mathbf{U})\cdot\vec{\mathbf{n}} \tag{4.26}$$

2. $\mathbf{H}(\mathbf{U}, \mathbf{V}, \vec{\mathbf{n}})$ is conservative:

$$\mathbf{H}(\mathbf{U}, \mathbf{V}, \vec{\mathbf{n}}) = -\mathbf{H}(\mathbf{V}, \mathbf{U}, -\vec{\mathbf{n}}). \tag{4.27}$$

If $\mathbf{H}$ satisfies conditions (4.26) and (4.27) then the method (4.25) is called consistent and conservative, respectively.

4.3.2 Riemann problem

(Approximate) Riemann solvers define the numerical flux $\mathbf{H}$ by adopting a Riemann problem at every cell interface S_{ij} as illustrated in the left picture of figure 4.2. Denote the location of the centroid of the interface by $\vec{\mathbf{x}}_f$. In terms of the rotated coordinates $\hat{x}$, $\hat{y}$ and $\hat{z}$ with $\hat{x}$ in the direction normal to the interface and where $\hat{y}$ and $\hat{z}$ are in the tangential directions, the interface is located at $\hat{x} = 0$. The Riemann problem at time level t^n at the interface S_{ij} is denoted by $RP_{ij}^n\left(\hat{\mathbf{U}}_L^n, \hat{\mathbf{U}}_R^n\right)$ and has initial conditions

$$\hat{\mathbf{U}}\left(\hat{x}, t^n\right) = \begin{cases} \hat{\mathbf{U}}_L^n = \mathbf{T}\mathbf{U}_L^n & \text{if } \hat{x} < 0 \\ \hat{\mathbf{U}}_R^n = \mathbf{T}\mathbf{U}_R^n & \text{if } \hat{x} > 0 \end{cases}, \tag{4.28}$$

as presented in the left picture of figure 4.2.

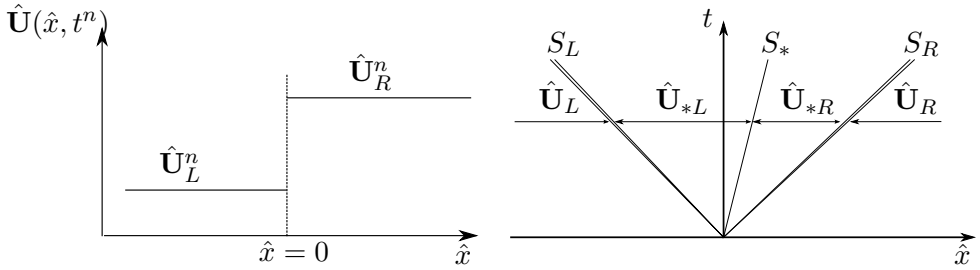

FIGURE 4.2: *Riemann problem (left) at the interface located at $\vec{\mathbf{x}}_f$ corresponding to $\hat{x} = 0$, at time-level $t = t^k$ and Riemann fan (right) with four solution states, i.e. $\hat{\mathbf{U}}_L$, $\hat{\mathbf{U}}_{*L}$, $\hat{\mathbf{U}}_{*R}$, $\hat{\mathbf{U}}_R$, separated by a left wave, a contact wave and a right wave whose speeds are denoted by S_L, S_* and S_R, respectively.*

For t–t^n not too large, the Riemann problem $RP_{ij}^n\left(\hat{\mathbf{U}}_L^n, \hat{\mathbf{U}}_R^n\right)$ has a similarity solution that is constant along plane manifolds $s = \hat{x}/(t - t^n) = const$ in the $(\hat{x}, t)$ plane. A possible configuration of the solution is presented in the right picture of figure 4.2. The waves denoted by S_L and S_R correspond to two nonlinear waves across which all primitive variables change. These waves can be either shocks or rarefactions. The wave S_* in between the left wave S_L and right wave S_R correspond to three linear waves, which always lie between the nonlinear waves. One of these linear waves correspond to a contact wave across which only the density changes. The other two linear waves correspond to shear waves across which only the tangential velocity components $\hat{v}$ and $\hat{w}$ change, respectively. In the solution of the Riemann problem two states $\hat{\mathbf{U}}_{*L}$ and $\hat{\mathbf{U}}_{*R}$ between the nonlinear and linear waves exist. The pressure p^* and the normal velocity $\hat{u}^*$ in the two star-regions are equal to each other, i.e. $p_L^* = p_R^*$, $\hat{u}_L^* = \hat{u}_R^*$. The density changes across the contact wave and thus it is different in the two star-regions.

Now denote this similarity solution by $\mathbf{U}^n_{RP}(s)$. The value along $s = 0$ gives the solution at the interface S_{ij} and thus the numerical flux $\mathbf{H}$ can be defined by

$$\mathbf{H}(\mathbf{U}^n_L, \mathbf{U}^n_R, \vec{\mathbf{n}}_{ij}) = \mathbf{T}^{-1}\mathbf{F}_x(\mathbf{U}^n_{RP}(0)). \tag{4.29}$$

Methods based on the solution of the Riemann problem are called Godunov-type methods after Godunov [79], who presented a first-order upwind scheme which could capture shock waves without introducing spurious oscillations. Godunov‘s method and its various derivatives have become very popular due to their robustness and ability to achieve high resolution of discontinuities. The original Godunov scheme assumed the construction of an exact solution of the Riemann problem, which is in general difficult. This drawback can be avoided by the use of an approximation of the exact solution resulting in a so-called approximate Riemann solver.

4.4 Time-integration

The semi-discretized form of the finite-volume formulation is presented in equation (4.25). Defining the residual $\mathbb{R}^n_i$ at time-level t^n for control volume V_i as:

$$\mathbb{R}^n_i = \frac{1}{|V_i|}\sum_{j=1}^{N_{f_i}} \mathbf{H}(\mathbf{U}^n_L, \mathbf{U}^n_R, \vec{\mathbf{n}}_{ij})\,|S_{ij}|, \tag{4.30}$$

then equation (4.25) can be written as

$$\frac{\partial \bar{\mathbf{U}}_i}{\partial t} + \mathbb{R}^n_i = 0. \tag{4.31}$$

To advance the solution from time-level t^n to time-level t^{n+1} a standard low-storage four-stage Runge-Kutta time-integration method is employed, which is defined as follows:

$$\begin{aligned} \mathbf{U}^{(0)}_i &= \bar{\mathbf{U}}^n_i, \\ \mathbf{U}^{(k)}_i &= \mathbf{U}^{(0)}_i - \alpha_k \Delta t \mathbb{R}^{k-1}_i, \quad \text{for } k = 1, \ldots, 4 \\ \bar{\mathbf{U}}^{n+1}_i &= \mathbf{U}^{(4)}_i, \end{aligned} \tag{4.32}$$

with the coefficients α_k equal to $[0.1084, 0.2602, 0.5052, 1.0]$, resulting in second-order accuracy in time [25]. For unsteady flow calculations the time step Δt is a global time step defined as the minimum of the local time steps of all control volumes

$$\Delta t = \min_i \Delta t_i, \tag{4.33}$$

where the local time step is defined by

$$\Delta t_i = C \frac{\ell_i}{\max\left(|\vec{\mathbf{u}}_i| + c_i, |\vec{\mathbf{u}}_i|\right)}, \tag{4.34}$$

with ℓ_i a characteristic length of control volume V_i defined as the diameter of the smallest inscribed sphere of control volume V_i and where $\vec{\mathbf{u}}_i$ and c_i are the local velocity vector and speed of sound in control volume V_i, respectively. The constant CFL number C is set to 0.8 unless stated otherwise.

For steady-flow calculations local time stepping can be applied to accelerate the solution to steady-state. Then, assigned to each control volume V_i is Δt_i defined in equation (4.34) instead of the global time step Δt from equation (4.33).

4.5 Flux schemes

In the present research a number of classical flux schemes have been investigated. At first, the Jameson-Schmidt-Turkel (JST) scheme with the preconditioning method of Weiss & Smith [218] was employed following the theses of Habing [83] and Verhoeff [212]. However, it was found that for cavitating flows the JST scheme introduced small oscillations at sharp gradients of the density in the flow. These oscillations were disastrous for the stability and accuracy of the numerical method. In the search for a more robust, stable and accurate scheme other flux schemes have been considered. For clarity and completeness in later chapters, these schemes are described in this section.

The stability and accuracy of the scheme is not only influenced by sharp gradients of the density in the flow. The so-called low-Mach number problem is also very important. This problem is addressed in section 4.7.

4.5.1 Jameson-Schmidt-Turkel scheme

One of the most widely known and used flux schemes is the Jameson-Schmidt-Turkel (JST) scheme [106]. The numerical flux at a face S_{ij} is calculated by averaging the conservative variables to the left and to the right of the face:

$$\mathbf{H}_{jst}\left(\mathbf{U}_L, \mathbf{U}_R, \vec{\mathbf{n}}_{ij}\right) = \frac{1}{2}\left(\mathbf{F}(\bar{\mathbf{U}}_i) + \mathbf{F}(\bar{\mathbf{U}}_j)\right) \cdot \vec{\mathbf{n}}_{ij}. \tag{4.35}$$

Note that for the left and right states at the face the control-volume-averages are substituted. The central discretization of equation (4.35) is known to be unstable. To suppress odd-even decoupling and to avoid spurious oscillations near discontinuities

an explicit artificial dissipation[§] term $\mathbf{D}_i$ is added to the right hand side of the finite-volume formulation in equation (4.25). On structured grids it is based on a blend of 2nd- and 4th- differences scaled by the maximum eigenvalue of the convective flux Jacobian. On unstructured grids a combination of an undivided Laplacian and biharmonic operator is employed [105]. Here, the formulation of Verhoeff [212] is followed:

$$\mathbf{D}_i = \frac{1}{|V_i|}\left(\mathbf{D}_i^{(2)} - \mathbf{D}_i^{(4)}\right), \tag{4.36}$$

with $|S_{ij}|$ the surface area of the face and where $\mathbf{D}_i^{(2)}$ is a second-order dissipation term related to the control volume-averaged value of the Laplacian of $\mathbf{U}$, i.e. $\overline{\Delta\mathbf{U}} = \overline{\nabla\cdot\nabla\mathbf{U}}$, which is computed in flux form as:

$$\mathbf{D}_i^{(2)} = \sum_{j=1}^{N_{f_i}} \lambda_{ij}\epsilon_{ij}^{(2)}\left(\bar{\mathbf{U}}_j - \bar{\mathbf{U}}_i\right)|S_{ij}|. \tag{4.37}$$

The fourth-order dissipation term $\mathbf{D}_i^{(4)}$ is related to the control-volume-averaged value of $\overline{\Delta\Delta\mathbf{U}}$. In flux form $\mathbf{D}_i^{(4)}$ is defined by

$$\mathbf{D}_i^{(4)} = \sum_{j=1}^{N_{f_i}} \lambda_{ij}\epsilon_{ij}^{(4)}\left(\sum_{k=1}^{N_{f_j}}\left(\bar{\mathbf{U}}_k - \bar{\mathbf{U}}_j\right) - \sum_{k=1}^{N_{f_i}}\left(\bar{\mathbf{U}}_k - \bar{\mathbf{U}}_i\right)\right)|S_{ij}|. \tag{4.38}$$

The coefficient λ_{ij} is an estimate of the spectral radius of the local flux Jacobian at the face:

$$\lambda_{ij} = \frac{1}{2}\left(|\vec{\mathbf{u}}_i| + c_i + |\vec{\mathbf{u}}_j| + c_j\right), \tag{4.39}$$

with $\vec{\mathbf{u}}$ the local velocity vector and c the local speed of sound, respectively. The dimensionless artificial dissipation coefficients $\epsilon^{(2)}$ and $\epsilon^{(4)}$ are defined as:

$$\epsilon_{ij}^{(2)} = \min\left(\kappa_2\nu_{ij}, \frac{1}{2}\right), \tag{4.40}$$

$$\epsilon_{ij}^{(4)} = \max\left(0, \kappa_4 - \alpha_\kappa\nu_{ij}\right), \tag{4.41}$$

where κ_2, κ_4 and α_κ are user-defined dimensionless constants, typical values are $\kappa_2 \in [1/4, 1/2]$, $\kappa_4 \in [1/64, 1/32]$ and $\alpha_\kappa = 2.0$, depending on the flow problem considered, see Wesseling [219]. The dimensionless parameter ν_{ij} is the so-called "shock sensor" defined as

$$\nu_{ij} = \max\left(\nu_i, \nu_j\right), \tag{4.42}$$

$$\nu_i = \sum_{k=1}^{N_{f_i}} \frac{|p_k - p_i|}{|p_k + p_i|}. \tag{4.43}$$

[§] *so-called because of its resemblance with viscous terms*

For cavitating flows the shock sensor needs to be defined on the density as well in order to detect sharp gradients in density. Near sharp gradients the coefficient ν_i is large and thus the fourth-order dissipation will have the value 0 and only the second-order dissipation is present. In smooth regions of the flow ν_i is small and thus the second-order dissipation will become small while the fourth-order dissipation will remain non-zero.

Failure of the JST scheme for cavitating flows

It was found that the JST scheme fails to calculate solutions for cavitating flows due to under- and overshoots at discontinuities with large density ratios. As an illustration, we select a Riemann problem employing the equation of state for a perfect gas, which resembles a moving contact surface with a large jump in density in a constant pressure field. The Riemann problem is defined in equation (4.28) and figure 4.2. Here, we adopt the values for the left and right state $\mathbf{V}_L = [\rho_L, u_L, p_L]^T = [1.0, 1.0, 1.0]^T$ and $\mathbf{V}_R = [1/10, 1.0, 1.0]^T$, respectively.

Note that in this problem, the density ratio ρ_L/ρ_R is equal to 10. For cavitating flow at a temperature $T = 293$ K with saturation pressure $p_{sat} = 2,318$ Pa, the liquid and vapor density are equal to $\rho_{l,sat} = 998.19\ \mathrm{kg m^{-3}}$ and $\rho_{v,sat} = 0.0172\ \mathrm{kg m^{-3}}$, respectively [2], resulting in a density ratio $\rho_{l,sat}/\rho_{v,sat} \approx 58,000$.

For a quadrilateral grid with 100 points in x-direction the solution for the density at $t = 0.25\mathrm{s}$ is presented in figure 4.3. The solution obtained with the JST scheme with the shock sensor based on the pressure is compared with the exact solution and the numerical solution obtained with the second-order HLLC scheme. The solutions for the pressure and velocity are always found to be constant throughout the domain.

In the solution obtained with the JST scheme distinct under- and overshoots are present around the contact surface. With the shock sensor based on the pressure it is not possible to calculate the solution for higher density ratios, because the undershoot generates negative values for the density resulting in failure of the numerical method. Adopting a shock sensor based on the density improves the solution. The undershoots are reduced significantly, such that problems with density ratios ρ_L/ρ_R up to a value of 100 can be calculated. However, the undershoots in density are not completely removed. Tuning the values for the constants κ_2, κ_4 and α_k improve the results, but even then the over-and undershoots are not completely removed. For cavitating flow problems with allowable density ratios larger than 50,000, it was found that the undershoots result in negative values for the density and thus in failure of the numerical method.

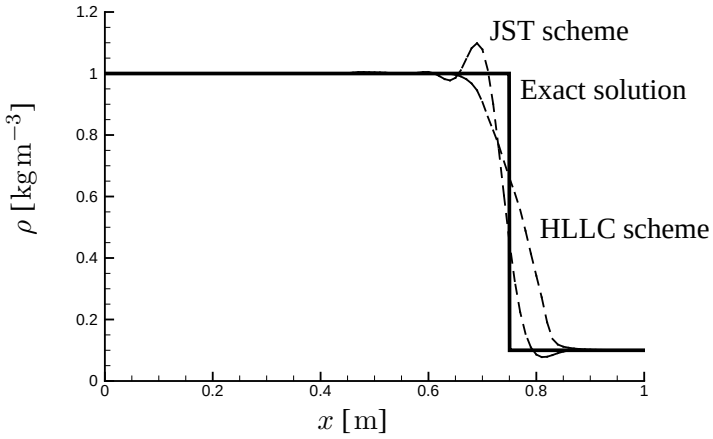

FIGURE 4.3: *Solution of Riemann problem, representing a moving contact surface with a jump* $\rho_L/\rho_R = 10$ *in density. Presented are the exact solution (solid line) and the numerical solutions obtained with the JST scheme for* $\kappa_2 = 0.5$, $\kappa_4 = 0.025$, $\alpha_\kappa = 2.0$ *and second-order HLLC scheme, respectively.* $\Delta x = 0.01$, $CFL = 0.8$.

4.5.2 HLLC flux scheme

Harten, Lax and van Leer [87] presented an approach for solving the Riemann problem approximately. The resulting Riemann solvers have become known as HLL Riemann solvers. In this approach an approximation for the numerical flux at the interfaces of the control volumes is obtained directly. The idea is to assume a wave configuration for the solution that consists of two waves with given speeds separating three constant states. However, the assumption of a two-wave configuration is not correct for the Euler equations. The resolution of contact waves and material interfaces is inaccurate. Toro *et al*. [195] modified the HLL solver to improve the solution around such contacts. This modification has become known as the HLLC Riemann solver. The derivation of the relations can be found in the book of Toro [194]. Batten *et al*. [21] showed that with an appropriate choice for the acoustic and contact wave velocities the HLLC solver yields the exact resolution of isolated shock and contact waves. Furthermore, they demonstrated that this solver is positively conservative, which forces the numerical method to preserve initially positive pressures and densities. Here, the formulation of Batten *et al*. [21] is followed to construct a HLLC solver for an unstructured mesh.

As illustrated in the right picture of figure 4.2 the Riemann problem at the cell interface has a similarity solution with four possible states, separated by three waves. The HLLC scheme considers an approximation of the Riemann solution as a simplified

Riemann fan with four possible constant states, i.e. $\hat{\mathbf{U}}_L$, $\hat{\mathbf{U}}_{*L}$, $\hat{\mathbf{U}}_{*R}$ and $\hat{\mathbf{U}}_R$, separated by a left wave, a contact wave and a right wave with speed S_L, S_* and S_R, respectively. Note that the states $\hat{\mathbf{U}}_K$ are the rotated conserved variables: $\hat{\mathbf{U}}_K = \mathbf{T}\mathbf{U}_K$ with $\mathbf{T}$ the rotation matrix defined in equation (4.21). The wave speeds are defined by

$$S_L = \min(\hat{u}_L - c_L, \hat{u}_R - c_R), \tag{4.44}$$

$$S_R = \max(\hat{u}_L + c_L, \hat{u}_R + c_R), \tag{4.45}$$

$$S_* = \frac{\rho_R \hat{u}_R(S_R - \hat{u}_R) - \rho_L \hat{u}_L(S_L - \hat{u}_L) + p_L - p_R}{\rho_R(S_R - \hat{u}_R) - \rho_L(S_L - \hat{u}_L)}, \tag{4.46}$$

with c the speed of sound and $\hat{u}$ the velocity in normal direction, i.e. $\hat{u} = \vec{\mathbf{u}} \cdot \vec{\mathbf{n}}$. The approximate solution $\hat{\mathbf{U}}_*$ is given by

$$\hat{\mathbf{U}}_* = \begin{cases} \hat{\mathbf{U}}_L & \text{if } S_L \geq 0 \\ \hat{\mathbf{U}}_{*L} & \text{if } S_L < 0 \leq S_* \\ \hat{\mathbf{U}}_{*R} & \text{if } S_* < 0 \leq S_R \\ \hat{\mathbf{U}}_R & \text{if } S_R < 0 \end{cases}. \tag{4.47}$$

To determine the intermediate states $\hat{\mathbf{U}}_{*L}$ and $\hat{\mathbf{U}}_{*R}$ the following conditions are assumed:

$$\hat{u}_{*L} = \hat{u}_{*R} = \hat{u}_* = S_*, \qquad p_{*L} = p_{*R} = p_*, \tag{4.48}$$

where p_* is given by

$$p_* = \rho_L(\hat{u}_L - S_L)(\hat{u}_L - S_*) + p_L = \rho_R(\hat{u}_R - S_R)(\hat{u}_R - S_*) + p_R. \tag{4.49}$$

The intermediate state vectors $\hat{\mathbf{U}}_{*L,R}$ are now given by

$$\hat{\mathbf{U}}_{*K} = \rho_K \left(\frac{S_K - \hat{u}_K}{S_K - S_*}\right) \begin{bmatrix} 1 \\ \hat{u}_k \\ \hat{v}_k \\ \hat{w}_k \\ E_k \end{bmatrix} + \left(\frac{1}{S_K - S_*}\right) \begin{bmatrix} 0 \\ p_* - p_K \\ 0 \\ 0 \\ p_* S_* - p_K \hat{u}_K \end{bmatrix}, \tag{4.50}$$

and the numerical HLLC flux $\mathbf{H}_{hllc}$ can be written as

$$\mathbf{H}_{hllc}(\mathbf{U}_L, \mathbf{U}_R, \vec{\mathbf{n}}_{ij}) = \mathbf{T}^{-1} \begin{cases} \mathbf{F}_x(\hat{\mathbf{U}}_L) & \text{if } S_L \geq 0 \\ \mathbf{F}_x(\hat{\mathbf{U}}_L) + S_L(\hat{\mathbf{U}}_{*L} - \hat{\mathbf{U}}_L) & \text{if } S_L < 0 \leq S_* \\ \mathbf{F}_x(\hat{\mathbf{U}}_R) + S_R(\hat{\mathbf{U}}_{*R} - \hat{\mathbf{U}}_R) & \text{if } S_* < 0 \leq S_R \\ \mathbf{F}_x(\hat{\mathbf{U}}_R) & \text{if } S_R < 0 \end{cases}. \tag{4.51}$$

4.5.3 AUSM family of schemes

Liou & Steffen [133] proposed a simple and accurate flux splitting scheme denoted by Advection Upstream Splitting Method (AUSM). The under-lying idea of the method is the observation that the inviscid flux consists of two physically distinct parts, namely a convective part and a pressure part. So the basis is to determine an appropriately defined cell-face advection Mach number using values from the two neighboring control volumes via associated characteristic speeds. Also, a pressure splitting is applied. For different purposes, a number of extensions and modifications to the scheme have been proposed. Amongst others we recall the AUSM+ scheme [130], which is designed to remove pressure oscillations around slowly moving shocks and contacts for cases in which the flow is aligned with the grid, the AUSM+-up and the AUSM+-up for all speeds schemes [131, 132] which are designed to improve accuracy for the case of low-Mach number flows.

The starting point is to split the inviscid flux $\vec{\mathbf{F}}(\mathbf{U})\cdot\vec{\mathbf{n}}$ into two parts, a convective flux $\mathbf{F}^{(c)}$ and a pressure flux $\mathbf{F}^{(p)}$:

$$\vec{\mathbf{F}}(\mathbf{U})\cdot\vec{\mathbf{n}} = \mathbf{F}^{(c)} + \mathbf{F}^{(p)} = \dot{m}\boldsymbol{\psi} + \mathbf{F}^{(p)}, \tag{4.52}$$

with the mass flux $\dot{m}$ equal to $\dot{m} = \rho(\vec{\mathbf{u}}\cdot\vec{\mathbf{n}})$, the vector $\boldsymbol{\psi}$ defined by $\boldsymbol{\psi} = [1, u, v, w, H]^T$ and with the pressure flux equal to $\mathbf{F}^{(p)} = p\,[0, n_x, n_y, n_z, 0]^T$. The numerical inviscid flux $\mathbf{H}$ is also split in two parts, a numerical convective flux $\mathbf{H}^{(c)}$ and a numerical pressure flux $\mathbf{H}^{(p)}$:

$$\mathbf{H}(\mathbf{U}_L, \mathbf{U}_R, \vec{\mathbf{n}}_{ij}) = \mathbf{H}^{(c)}(\mathbf{U}_L, \mathbf{U}_R, \vec{\mathbf{n}}_{ij}) + \mathbf{H}^{(p)}(\mathbf{U}_L, \mathbf{U}_R, \vec{\mathbf{n}}_{ij}). \tag{4.53}$$

The numerical convective flux $\mathbf{H}^{(c)}$ is defined in the following general upwind form

$$\mathbf{H}^{(c)}(\mathbf{U}_L, \mathbf{U}_R, \vec{\mathbf{n}}_{ij}) = \dot{m}^+\boldsymbol{\psi}_L + \dot{m}^-\boldsymbol{\psi}_R, \tag{4.54}$$

where the contributions $\boldsymbol{\psi}_L$ and $\boldsymbol{\psi}_R$ are weighted by the split mass fluxes $\dot{m}^+$ and $\dot{m}^-$, which follow the consistency requirement

$$\dot{m} = \dot{m}^+ + \dot{m}^-, \tag{4.55}$$

the proper upwinding conditions

$$\dot{m}^+ \geq 0, \quad \dot{m}^- \leq 0, \tag{4.56}$$

and the mutually exclusive requirement

$$(\dot{m}^+)(\dot{m}^-) = 0. \tag{4.57}$$

The split mass fluxes are defined by

$$\dot{m}^+ = \bar{c}\,\rho_L M^+, \quad \dot{m}^- = \bar{c}\,\rho_R M^-, \tag{4.58}$$

with $\bar{c}$ a common speed of sound defined by $\bar{c} = \frac{1}{2}(c_L + c_R)$ and where M^+ and M^- can be combined into the interface Mach number $\bar{M}$ with $\bar{M} = M^+ + M^-$, which is defined later on. Using the properties (4.55)–(4.57) the numerical convective flux can be rewritten as

$$\mathbf{H}^{(c)}(\mathbf{U}_L, \mathbf{U}_R, \vec{\mathbf{n}}_{ij}) = \bar{c}\,\bar{M}\,\rho_{L/R}\,\boldsymbol{\psi}_{L/R}, \tag{4.59}$$

where

$$(\cdot)_{L/R} = \begin{cases} (\cdot)_L & \text{if } \bar{M} \geq 0 \\ (\cdot)_R & \text{if } \bar{M} < 0 \end{cases}. \tag{4.60}$$

The numerical pressure flux $\mathbf{H}^{(p)}$ is defined as

$$\mathbf{H}^{(p)}(\mathbf{U}_L, \mathbf{U}_R, \vec{\mathbf{n}}_{ij}) = \bar{p} \begin{bmatrix} 0 \\ n_x \\ n_y \\ n_z \\ 0 \end{bmatrix}. \tag{4.61}$$

The AUSM, AUSM+ and AUSM+-up schemes differ in their definition of $\bar{M}$ and $\bar{p}$. To facilitate the formulation of the different schemes the following polynomial functions are defined:

$$\mathcal{M}^{\pm}_{(1)}(M) = \frac{1}{2}(M \pm |M|), \tag{4.62}$$

$$\mathcal{M}^{\pm}_{(2)}(M) = \pm\frac{1}{4}(M \pm 1)^2, \tag{4.63}$$

$$\mathcal{M}^{\pm}_{(4)}(M) = \begin{cases} \mathcal{M}^{\pm}_{(1)}(M) & \text{if } |M| \geq 1 \\ \mathcal{M}^{\pm}_{(2)}(M)\left(1 \mp 16\beta\mathcal{M}^{\mp}_{(2)}(M)\right) & \text{if } |M| < 1 \end{cases}, \tag{4.64}$$

$$\mathcal{P}^{\pm}_{(5)}(M) = \begin{cases} \dfrac{1}{M}\mathcal{M}^{\pm}_{(1)}(M) & \text{if } |M| \geq 1 \\ \mathcal{M}^{\pm}_{(2)}(M)\left((\pm 2 - M) \mp 16\alpha M\,\mathcal{M}^{\mp}_{(2)}(M)\right) & \text{if } |M| < 1 \end{cases} \tag{4.65}$$

The left and right Mach numbers M_L and M_R are defined by

$$M_L = \frac{\vec{\mathbf{u}}_L \cdot \vec{\mathbf{n}}}{\bar{c}}, \quad M_R = \frac{\vec{\mathbf{u}}_R \cdot \vec{\mathbf{n}}}{\bar{c}}. \tag{4.66}$$

AUSM scheme

The AUSM scheme [133] is defined by using the numerical convective flux $\mathbf{H}^{(c)}$ in equation (4.59) and the numerical pressure flux $\mathbf{H}^{(p)}$ in equation (4.61) and by setting $\bar{M}$ equal to

$$\bar{M} = \mathcal{M}^{+}_{(4)}(M_L) + \mathcal{M}^{-}_{(4)}(M_R), \tag{4.67}$$

with $\beta = 0$ in equation (4.64) and by setting $\bar{p}$ equal to

$$\bar{p} = p_L \mathcal{P}^{+}_{(5)}(M_L) + p_R \mathcal{P}^{-}_{(5)}(M_R), \tag{4.68}$$

with $\alpha = 0$ in equation (4.65).

AUSM+ scheme

The AUSM+ scheme [130] is defined by using the numerical convective flux $\mathbf{H}^{(c)}$ in equation (4.59) and the numerical pressure flux $\mathbf{H}^{(p)}$ in equation (4.61) and by setting $\bar{M}$ equal to

$$\bar{M} = \mathcal{M}^{+}_{(4)}(M_L) + \mathcal{M}^{-}_{(4)}(M_R), \tag{4.69}$$

with $\beta = \frac{1}{8}$ in equation (4.64) and by setting $\bar{p}$ equal to

$$\bar{p} = p_L \mathcal{P}^{+}_{(5)}(M_L) + p_R \mathcal{P}^{-}_{(5)}(M_R), \tag{4.70}$$

with $\alpha = \frac{3}{16}$ in equation (4.65).

AUSM+-up scheme

The AUSM+-up scheme [131, 132] is defined by using the numerical convective flux $\mathbf{H}^{(c)}$ in equation (4.59) and the numerical pressure flux $\mathbf{H}^{(p)}$ in equation (4.61) and by setting $\bar{M}$ equal to

$$\bar{M} = \mathcal{M}^{+}_{(4)}(M_L) + \mathcal{M}^{-}_{(4)}(M_R) + M_p, \tag{4.71}$$

with M_p defined by

$$M_p = -K_p \max(1 - \sigma \tilde{M}^2, 0) \frac{p_R - p_L}{\bar{\rho}\bar{c}^2}, \tag{4.72}$$

where

$$\bar{\rho} = \frac{1}{2}\left(\rho_L + \rho_R\right), \quad \tilde{M}^2 = \frac{1}{2}\left(M_L^2 + M_R^2\right), \tag{4.73}$$

and with the coefficients equal to $\sigma = 1.0$, $K_p = \frac{1}{4}$ and $\beta = \frac{1}{8}$.

$\hat{p}$ is set equal to

$$\bar{p} = p_L \mathcal{P}^{+}_{(5)}(M_L) + p_R \mathcal{P}^{-}_{(5)}(M_R) + P_u, \tag{4.74}$$

where P_u is equal to

$$P_u = -2K_u\bar{\rho}\bar{c}^2\ \mathcal{P}^+_{(5)}(M_L)\mathcal{P}^-_{(5)}(M_R)\ (M_R - M_L), \tag{4.75}$$

with $K_u = \frac{3}{4}$ and $\alpha = \frac{3}{16}$.

AUSM+-up for all speeds scheme

The AUSM+-up scheme for all speeds [131, 132] is defined by adopting the AUSM+-up scheme by using the numerical convective flux $\mathbf{H}^{(c)}$ in equation (4.59) and the numerical pressure flux $\mathbf{H}^{(p)}$ in equation (4.61) and by setting $\bar{M}$ equal to

$$\bar{M} = \mathcal{M}^+_{(4)}(M_L) + \mathcal{M}^-_{(4)}(M_R) + \bar{M}_p, \tag{4.76}$$

with $\bar{M}_p$ defined by

$$\bar{M}_p = -\frac{K_p}{f_a}\max(1 - \sigma\bar{M}^2, 0)\frac{p_R - p_L}{\bar{\rho}\bar{c}^2}, \tag{4.77}$$

where

$$\bar{\rho} = \frac{1}{2}\left(\rho_L + \rho_R\right), \quad \bar{M}^2 = \frac{1}{2}\left(M_L^2 + M_R^2\right), \tag{4.78}$$

and

$$f_a(M_0) = M_0(2 - M_0), \tag{4.79}$$

with

$$M_0 = \min\left(1, \max(\bar{M}^2, M_{co}^2)\right), \tag{4.80}$$

and with the coefficients equal to $\sigma = 1.0$, $K_p = \frac{1}{4}$, $\beta = \frac{1}{8}$ and $M_0 = 10^{-2}$.

$\bar{p}$ is set equal to

$$\bar{p} = p_L\mathcal{P}^+_{(5)}(M_L) + p_R\mathcal{P}^-_{(5)}(M_R) + \bar{P}_u, \tag{4.81}$$

where $\bar{P}_u$ is equal to

$$\bar{P}_u = -2f_aK_u\bar{\rho}\bar{c}^2\ \mathcal{P}^+_{(5)}(M_L)\mathcal{P}^-_{(5)}\ (M_R)(M_R - M_L), \tag{4.82}$$

with

$$\alpha = \frac{3}{16}(-4 + 5f_a^2), \tag{4.83}$$

and with $K_u = \frac{3}{4}$.

4.6 MUSCL-type higher order spatial reconstruction

To extend the numerical method from first- order to second-order, a MUSCL-type reconstruction method has been implemented. The Monotone Upstream-Centred Scheme for Conservation Laws (MUSCL) is based on the work of van Leer [127]. The MUSCL approach implies higher-order accuracy obtained by employing data reconstructions and the avoidance of spurious oscillations by constraining the reconstruction with the use of a limiter method.

The semi-discretized form of the finite-volume formulation is described in equation (4.25). Taking the control volume average values $\bar{\mathbf{U}}_i$ and $\bar{\mathbf{U}}_j$ for the left and right states $\mathbf{U}_L$ and $\mathbf{U}_R$ for the numerical flux, results in a spatial discretization which is only first-order accurate. To obtain higher-order accuracy, the left and right states $\mathbf{U}_L$ and $\mathbf{U}_R$ can be taken from higher order polynomials $\tilde{\mathbf{U}}_i(\vec{\mathbf{x}})$ representing the solution in control volume V_i. Here, we consider piece-wise linear data reconstructions.

Higher-order methods will produce spurious oscillations in the vicinity of high gradients. The use of monotone schemes would prevent such oscillations. Unfortunately, Godunov stated that monotone linear schemes are at most first-order accurate. Thus to get higher-order accuracy, non-linear versions of these schemes should be constructed by applying limiter functions to the piece-wise linear reconstructions. We are seeking the following desired properties:

1. second-order or higher accuracy when the solution is smooth.
2. the produced solutions do not have spurious oscillations near high gradients.
3. the schemes produce high-resolution of discontinuities.

For structured meshes many techniques and limiter functions have been constructed, see for example the books of Leveque [128] and Toro [194]. Harten [86] introduced the useful concept of Total Variation Diminishing (TVD) or Total Variation Non Increasing schemes based on non-linear stability theory. The TVD schemes are based on a concept aimed at preventing the generation of new extrema in the flow solution. Sweby [188] introduced the TVD region and the second order TVD region giving design rules for limiters. A few of the most popular limiters are the *minmod limiter* [128], the *superbee limiter* [194], the *van Leer limiter* [126] and the *van Albada limiter* [10].

Schemes for multi-dimensional structured meshes can be constructed relatively easy by dimensional splitting. However, Suresh [185] has shown that for multi-dimensional problems most TVD limiters give rise to large spurious oscillations near discontinuities. The cause of these oscillations can be traced back to reconstructions that are not

bounded by neighboring cell averages. Suresh [185] proved that if the reconstruction in each cell is bounded by the cell averages of first-order neighbors then the MUSCL scheme is positivity preserving.

These TVD-schemes can not be extended directly to multi-dimensional unstructured meshes. This is specifically due to the difficulty in implementing and enforcing a monotonicity criterion that relies on next-neighbor information. In structured grids this information is available, but it is missing in unstructured grids. Darwish and Moukalled [53] gave a nice overview on TVD schemes for unstructured grids. Barth & Jespersen [20] introduced a MUSCL-type reconstruction method for unstructured grids, which is bounded over the whole control volume by all its immediate neighbors. Darwish & Moukalled [53] mention that the limiter of Barth & Jespersen and the van Leer limiter were found to be similar. Venkatakrishnan [208] adjusted the method of Barth & Jespersen with a van Albada type limiter. In the present numerical method the limiter method for unstructured grids of Barth & Jespersen [20] and of Venkatakrishnan [208] is implemented.

4.6.1 Piece-wise linear reconstruction

Considering piece-wise linear data reconstructions in each control volume the reconstruction polynomials $\tilde{\mathbf{U}}_i(\vec{\mathbf{x}})$ representing the solution for either the conserved variables ρ, ρu, ρv, ρw and ρE or the primitive variables ρ, u, v, w and e in control volume V_i can be written as:

$$\tilde{\mathbf{U}}_i(\vec{\mathbf{x}}) = \bar{\mathbf{U}}_i + (\nabla \mathbf{U})_{cg,i} \cdot (\vec{\mathbf{x}} - \vec{\mathbf{x}}_{cg,i}), \tag{4.84}$$

where $(\nabla \mathbf{U})_{cg,i}$ is the gradient of the variables $\mathbf{U}$ at the centroid of control volume V_i and $\vec{\mathbf{x}}_{cg,i}$ is the location of the center of gravity of control volume V_i. For linear reconstructions the extrema of $\tilde{\mathbf{U}}_i(\vec{\mathbf{x}})$ occur at the boundaries of the control volume. We are interested in the value at the centroid $\vec{\mathbf{x}}_{ij}$ of an interface S_{ij} between control volumes V_i and its neighbor V_j. For each face S_{ij} of control volume V_i the extrapolated values $\mathbf{U}_{ij}$ are equal to

$$\mathbf{U}_{ij} = \bar{\mathbf{U}}_i + (\nabla \mathbf{U})_{cg,i} \cdot (\vec{\mathbf{x}}_{ij} - \vec{\mathbf{x}}_{cg,i}). \tag{4.85}$$

The gradient $(\nabla \mathbf{U})_{cg,i}$ in control volume V_i is computed using the Green-Gauss linear reconstruction from approximate forms of the exact relation

$$\int_{V_i} \nabla \mathbf{U} dV = \int_{\partial V_i} \mathbf{U} \vec{\mathbf{n}} \, \mathrm{d}S. \tag{4.86}$$

So that

$$(\nabla \mathbf{U})_{cg,i} \equiv \frac{1}{|V_i|} \int_{V_i} \nabla \mathbf{U} dV = \frac{1}{|V_i|} \int_{\partial V_i} \mathbf{U} \vec{\mathbf{n}} \, \mathrm{d}S, \tag{4.87}$$

with $|V_i|$ the volume of control volume V_i. For a node-centered dual mesh the gradient is calculated by taking the sum over all faces of the value $\mathbf{U}_f$ at the face, i.e.

$$(\nabla \mathbf{U})_{cg,i} = \frac{1}{|V_i|} \sum_{j=1}^{N_{f_i}} \mathbf{U}_f \, |S_{ij}| \vec{\mathbf{n}}_{ij}, \tag{4.88}$$

with N_{f_i} the number of faces of control volume V_i, $|S_{ij}|$ the surface area of face S_{ij} and where the value $\mathbf{U}_f$ is taken as the weighted mean of the control-volume-averaged values at both sides of the face:

$$\mathbf{U}_f = \frac{|V_i| \bar{\mathbf{U}}_j + |V_j| \bar{\mathbf{U}}_i}{|V_i| + |V_j|}. \tag{4.89}$$

To avoid spurious oscillations the extrapolated boundary values $\mathbf{U}_{ij}$ obtained from equation (4.85) must be constrained with the application of a limiter function $\mathbf{\Psi}$. The limited extrapolated boundary values are then used for the left and right states $\mathbf{U}_L$ and $\mathbf{U}_R$:

$$\mathbf{U}_L = \bar{\mathbf{U}}_i + \mathbf{\Psi}_i \left[(\nabla \mathbf{U})_{cg,i} \cdot (\vec{\mathbf{x}}_{ij} - \vec{\mathbf{x}}_{cg,i}) \right], \tag{4.90}$$

$$\mathbf{U}_R = \bar{\mathbf{U}}_j + \mathbf{\Psi}_j \left[(\nabla \mathbf{U})_{cg,j} \cdot (\vec{\mathbf{x}}_{ij} - \vec{\mathbf{x}}_{cg,j}) \right], \tag{4.91}$$

where $\mathbf{\Psi} \in [0, 1]$ is the limiter function yet to be defined.

Barth & Jespersen [20] enforced the monotonicity criterion by stating that the values of the reconstructed polynomials within a control volume should not exceed the maximum and minimum control-volume-averaged solutions of the neighbors of the control volume including the one of control volume V_i. Thus Barth & Jespersen required that

$$\mathbf{U}_i^{min} \leq \mathbf{U}_L, \mathbf{U}_R \leq \mathbf{U}_i^{max}, \tag{4.92}$$

where $\mathbf{U}_i^{min} = \min\left(\bar{\mathbf{U}}_i, \bar{\mathbf{U}}_{neighbours}\right)$ and $\mathbf{U}_i^{max} = \max\left(\bar{\mathbf{U}}_i, \bar{\mathbf{U}}_{neighbours}\right)$.

The value for the limiter function $\mathbf{\Psi}_i$, satisfying equation (4.92) is equal to

$$\mathbf{\Psi}_i = \min\left(\mathbf{\Psi}_{ij}\right), \tag{4.93}$$

with $\mathbf{\Psi}_{ij}$ the limiter function at the face S_{ij}.

Limiter function of Barth & Jespersen [20]

Barth & Jespersen defined the limiter function $\mathbf{\Psi}_{ij}$ as

$$\mathbf{\Psi}_{ij} = \begin{cases} \Phi\left(\dfrac{\mathbf{U}_i^{max} - \bar{\mathbf{U}}_i}{\mathbf{U}_{ij} - \bar{\mathbf{U}}_i}\right) & \text{if } \mathbf{U}_{ij} - \bar{\mathbf{U}}_i > 0 \\ \Phi\left(\dfrac{\mathbf{U}_i^{min} - \bar{\mathbf{U}}_i}{\mathbf{U}_{ij} - \bar{\mathbf{U}}_i}\right) & \text{if } \mathbf{U}_{ij} - \bar{\mathbf{U}}_i < 0 \\ 1 & \text{if } \mathbf{U}_{ij} - \bar{\mathbf{U}}_i = 0 \end{cases}, \tag{4.94}$$

which ensures that the argument of Φ is always ≥ 0. The function $\Phi(x)$ is defined by

$$\Phi(x) = \min(1, x), \tag{4.95}$$

which renders $\mathbf{\Psi}_{ij} \in [0, 1]$. Venkatakrishnan [208] proposed a modified version of the limiter of Barth & Jespersen to reduce its problems with convergence to steady-state, which can be related to the use of non-differentiable functions such as the min function.

Limiter function of Venkatakrishnan [208]

Venkatakrishnan [208] proposes a modification of the van Albada limiter in combination with the method of Barth & Jespersen. With the unlimited extrapolated values $\mathbf{U}_{ij}$ defined by equation (4.85), let Δ_- be equal to

$$\Delta_- = \mathbf{U}_{ij} - \bar{\mathbf{U}}_i, \tag{4.96}$$

and let Δ_+ be defined by

$$\Delta_+ = \begin{cases} \mathbf{U}_i^{max} - \bar{\mathbf{U}}_i & \text{if } \Delta_- > 0 \\ \mathbf{U}_i^{min} - \bar{\mathbf{U}}_i & \text{if } \Delta_- < 0 \end{cases}. \tag{4.97}$$

The limiter function $\mathbf{\Psi}_{ij}$ of Barth & Jespersen, equation (4.94), is then defined by

$$\mathbf{\Psi}_{ij} = \Phi\left(\frac{\Delta_+}{\Delta_-}\right) \tag{4.98}$$

$$= \left(\frac{1}{\Delta_-}\right)\left[\Delta_- \Phi\left(\frac{\Delta_+}{\Delta_-}\right)\right]. \tag{4.99}$$

Venkatakrishnan proposed to modify the term $\Delta_- \Phi\left(\frac{\Delta_+}{\Delta_-}\right)$ yielding $\mathbf{\Psi}_{ij}$ as

$$\mathbf{\Psi}_{ij} = \frac{1}{\Delta_-}\left[\frac{(\Delta_+^2 + \epsilon^2)\Delta_- + 2\Delta_-^2\Delta^+}{\Delta_+^2 + 2\Delta_-^2 + \Delta_-\Delta_+ + \epsilon^2}\right], \tag{4.100}$$

where Venkatakrishnan takes ϵ^2 to be equal to $(K\Delta x)^3$ with $K = 0.3$ and Δx a relevant local grid size. Venkatakrishnan mentions that a small value suffices, so taking $\epsilon^2 = 10^{-12}$ to revert to the unlimited scheme for smooth solutions would be a valid option. Taking a value of $K = 0.0$ is known to stall convergence to steady-state, whereas a higher value, such as $K = 5.0$, leads to oscillations near discontinuities, see for more details Blazek [25]. To prevent division by a very small value Δ_- in the term $\frac{1}{\Delta_-}$ should be replaced by $sign(\Delta_-)(|\Delta_-| + \omega)$ with $\omega = 10^{-12}$.

In the present numerical method we adopt a value of $K = 0.3$ for steady flow calculations. For unsteady flow calculations we take $K = 0.0$.

4.7 Low-Mach number flows

From the beginning of CFD in the 1960s two separate classes of numerical methods for numerically simulating flows have been used: density-based and pressure-based methods have been used for compressible and incompressible flow, respectively. However, many flow problems exist in which a part of the flow region is nearly incompressible, whereas significant compressibility effects occur in other regions of the flow. Cavitating flow problems have a large domain filled with almost incompressible liquid flow and much smaller vaporous regions in which the flow is compressibe and even supersonic flow may occur. In recent years, many efforts have been made to develop unified numerical approaches capable of solving a larger range of fluid flow problems, see amongst many others Wesseling [219] and Koren [114, 115]. For this purpose, either typical "incompressible"-flow methods are generalized to high-speed compressible flows, or the "compressible"-flow methods are extended to low-Mach number flows or incompressible flows.

However, two major problems have been found to occur when solving low-Mach number flows with "compressible"-flow methods: (1) extremely slow or stalled convergence (2) globally incorrect flow solutions. To solve these problems a popular technique has been to introduce suitable preconditioners, e.g. Turkel [200] and Weiss & Smith [218]. In more recent years, adaptation of the flux schemes by scaling or modifying the numerical dissipation in regions with low-Mach number flows have been found to be successful, e.g. Guillard & Viozat [82], Liou [132] and Schmidt *et al*. [169].

The difficulty with slow convergence in solving the compressible-flow equations for low-Mach number flows is associated with the large disparity in acoustic wave speeds, $|\vec{\mathbf{u}}| + c$ and $|\vec{\mathbf{u}}| - c$, and the waves convected at fluid speed, $|\vec{\mathbf{u}}|$ [200]. The "stiffness" of the equations is determined by the characteristic condition number C_N

[25] defined as the ratio of the largest eigenvalue to the smallest eigenvalue:

$$C_N = \frac{|\vec{\mathbf{u}}| + c}{|\vec{\mathbf{u}}|} = 1 + \frac{1}{M}, \tag{4.101}$$

with M the local Mach number. The allowable local time step is limited by the fastest wave, i.e. by $|\vec{\mathbf{u}}| + c$, such that in one time step the wave moves over one computational cell at most. During one time step, the slowest waves, however, move only over a fraction of the cell width. Thus a large value of the condition number, $M \to 0$, reduces the efficiency of wave propagation resulting in a slow convergence of the numerical method.

The reason for the globally incorrect solutions in the low-Mach number limit has been identified by Turkel *et al.* [200] and Guillard & Viozat [82] to relate to the amount of artificial dissipation in schemes for compressible flows. The physical pressure fluctuations scale with the square of the Mach number, while the solutions of the discrete system contain pressure fluctuations of the order of the Mach number [81, 82]. Thus, the artificial dissipation in the numerical scheme does not scale correctly for Mach numbers approaching zero and the accuracy and stability of such schemes suffer at low-Mach number. The use of second-order schemes and/or finer grids improves the accuracy, but the additional computational cost is substantial, especially for 2D and 3D calculations. Additionally, Liou [131] and Schmidt *et al.* [169] illustrated that for the classical Riemann solvers the dissipation in the numerical approximation for the pressure for compressible flows is scaled by a term of $\mathcal{O}(\rho c \Delta u)$, whereas the changes in pressure due to smooth changes in the flow scale with $\mathcal{O}(\rho u \Delta u)$. For air at standard conditions ρc is of $\mathcal{O}(10^2)$ and for water ρc is of $\mathcal{O}(10^6)$ from which it can be concluded that for the calculation of a water flow this effect is even stronger. Schmidt *et al.* [169] introduced a modified pressure flux formulation to improve the numerical results, which is outlined in section 4.7.2.

4.7.1 Preconditioning

Preconditioning methods cope with the spreading of the values of the eigenvalues by pre-multiplying the term with the time-derivative in the system of equations by a suitable preconditioning matrix which alters the speed of the acoustic waves. This makes their speed of the same order of magnitude as the local velocity of the flow and thus removes the disparity in wave-speeds. In this manner, a well-conditioned system is recovered, together with good convergence properties. In 1967 Chorin [39] introduced the method of artificial compressibility for incompressible flows by adding an artificial time derivative of the pressure in the continuity equation. Since then many preconditioning methods have been developed, e.g. the family of preconditioners introduced by Turkel [198, 199]. We also mention the preconditioning method of Weiss & Smith [218] which provides a modified expression for the derivatives of density

with respect to pressure for an arbitrary equation of state.

A drawback of preconditioning methods is that due to the adaptation of the speed of the acoustic waves time-accuracy is lost. The preconditioned equations only have steady-state solutions in common with those of the original system. Another drawback is the lack of robustness of the method near stagnation points, which may be due to artificial dissipation, where solution eigenvectors become almost parallel [52], causing small perturbations to be amplified over short time-scales. For time-dependent problems, the "dual-time stepping" technique has been developed [218], in which the derivative with respect to physical time are treated as source terms. During each physical time-step, the system of preconditioned equations is advanced in artificial or "pseudo" time to reach a pseudo-steady-state in pseudo-time.

Unfortunately, the preconditioning method converges slowly when the physical time step Δt is chosen of the same order of magnitude as the pseudo-time step $\Delta\tau$. Furthermore, when highly unsteady flows are considered, such as cavitating flows, or when fast moving shocks and waves need to be captured, such is the case in liquid flows, many small physical time steps need to be taken and the dual-time stepping method becomes inefficient.

4.7.2 Adaptation of flux schemes

Wallis [214] formulated the terms continuity waves (also denoted by kinematic waves or hydrodynamic coupling) and dynamic waves. Continuity waves are a quasi-steady-state phenomenon and occur due to smooth changes in the flow, one steady-state value simply propagates into another. The change in pressure across such waves is related to the change in velocity as $\Delta p \approx \rho u \Delta u$. On the other hand, dynamic waves are usually due to forces or sharp discontinuities in the flow. The change in pressure across such waves is then related to the change in velocity as $\Delta p \approx \rho c \Delta u$.

Classical Riemann solvers assume that the solution consists of dynamic waves. Many authors only consider shock tube problems when studying numerical flux schemes. For these type of problems the solution consists of dynamic waves and thus the classical Riemann solvers work very well. However, for steady-state low-Mach number flows the classical Riemann solvers become too dissipative since the solution then consists of continuity waves.

In the literature on the preconditioning methods it is found, that the numerical methods can be improved by modifying the flux schemes by proper scaling of the numerical dissipation for low-Mach number flows [81, 82]. An example of such a modified scheme is the "AUSM+-up for all speeds" scheme of Liou [131, 132], which is also applied to compressible liquid flows [35].

Schmidt *et al.* [169] proposed a hybrid solution approach to overcome the inaccurate calculations of the pressure field for (low-Mach number) liquid flows. They combined the HLLC flux scheme and the AUSM flux scheme to obtain a flux scheme that is able to handle time-dependent wave phenomena as well as low-Mach number liquid flows. They followed the general philosophy of the family of AUSM schemes, in which the Euler fluxes are split in a convective part and a pressure part. The mass flux is calculated with the HLLC mass flux defined in equation (4.51) and the pressure flux is determined with the AUSM pressure splitting defined in equations (4.68), (4.70), (4.74) and (4.81), respectively. In later chapters we refer to this flux formulation as the hybrid HLLC/AUSM flux scheme.

Schmidt *et al*. [170, 172] formulated the hybrid solution approach in a slightly different flux formulation showing that this newer formulation is uniformly consistent for $M \rightarrow 0$. Following discussions with Schmidt and Schnerr we have implemented their formulation into the present edge-based numerical method.¶

4.8 Boundary conditions

The treatment of the boundary conditions is based on the common ghost-cells approach, which implies that the numerical flux over a boundary interface is determined with the same numerical flux as used for internal cells. When the face S_{ij} considered is located on the boundary Ω_h of the computational domain the right state $\mathbf{U}_R$ for the numerical flux $\mathbf{H}(\mathbf{U}_L, \mathbf{U}_R, \vec{\mathbf{n}}_{ij})$ at the cell-interface can be reconstructed from the state $\mathbf{U}_g$ in a virtual control volume or "ghost" cell. The state $\mathbf{U}_g$ in the ghost cell is specified by applying suitable boundary conditions to obtain the control-volume-averaged values of the ghost cell.

For the in- and outflow boundaries the right state $\mathbf{U}_R$ for the numerical flux is taken equal to the state in the ghost cell $\mathbf{U}_g$. For the solid wall the state in the ghost cell is used to obtain the reconstructed value $\mathbf{U}_L$ at the boundary interface. By applying the non-permeability condition using $\mathbf{U}_L$ the reconstructed right value $\mathbf{U}_R$ at the boundary interface is then obtained.

First, in section 4.8.1 the time-dependent in- and outflow boundary conditions are described. In the present work the method of Thompson for time-dependent non-reflecting boundary conditions is generalized for arbitrary equations of state as pre-

¶*During the development of the present numerical method we profited very much from extensive discussion with S. Schmidt and Prof. Schnerr of the TU Munich. For this the author would like to express his gratitude.*

sented in appendix A. Then, in section 4.8.2 the boundary conditions for solid walls are presented.

4.8.1 Time-dependent in- and outflow boundary conditions

In appendix A, the time-dependent, non-reflecting, in- and outflow boundary conditions for the hyperbolic Euler equations are derived for arbitrary equation of state and for an arbitrary orientation of the boundary. Briefly, the outgoing characteristics are explicitly calculated and allowed to move out of the domain. Incoming characteristics are handled by setting the time-derivative of their amplitude equal to zero, thus ensuring that waves do no enter the domain during simulation giving the boundary conditions a non-reflective character.

Rudy & Strikwerda [160] presented a non-reflecting subsonic outflow boundary condition for the numerical simulation of the time-dependent linearized compressible Navier-Stokes equations, for the case that these equations are used to obtain a steady state solution. Their boundary condition effectively reduces reflections of outgoing waves at the boundary and increases the convergence towards steady-state. Thompson [189, 190] introduced a unified formalism for the time-dependent treatment of boundary conditions for the system of hyperbolic equations formed by the Euler equations using the perfect gas law as the equation of state. A similar approach is followed in the books of Hirsch [91] and Feistauer [64]. Poinsot & Lele [149] extended the formalism of Thompson to the Navier-Stokes equations. All non-physical reflections from the in- and outflow boundaries can be completely removed by the formalism of Thompson. Colonius [42] presented an overview on modeling artificial boundary conditions for compressible flow. In the present work, the method of Thompson is generalized for an arbitrary equation of state and for arbitrary orientation of the boundary.

The central concept is that a hyperbolic system of equations represents the propagation of waves and that at any boundary some of the waves are propagating into the computational domain while others are propagating outwards. The number and type of conditions at a boundary of a multi-dimensional domain are defined by the eigenvalues of the Jacobian of the component of the flux vector in the direction normal to the boundary. Each eigenvalue λ_i represents the characteristic velocity at which a particular wave propagates. The behavior of outgoing waves is completely described by the solution within and at the boundary of the computational domain, while the behavior of the incoming waves is specified by data external to the computational domain.

Thus, because of the wave structure of the hyperbolic equations, the number of boundary conditions that may be imposed depends on the physics of the problem

and may not be specified arbitrarily, i.e.

the number of boundary conditions which must be specified at a point on the boundary is equal to the number of incoming waves at that point.

The number of boundary conditions required at any point on the boundary may change in time. Also, the number of boundary conditions required at any time may vary with position on the boundary. Table 1 presents the number of physical boundary conditions for different types of boundaries.

Boundary type	Number of physical boundary conditions
Supersonic inflow	5
Subsonic inflow	4
Supersonic outflow	0
Subsonic outflow	1

TABLE 4.1: *Number of physical boundary conditions for different types of the boundary of the computational domain.*

The dependance of the characteristics on an arbitrary equation of state turns out to be reduced to the formulation of the two variables c, the speed of sound, and ψ, which are defined by

$$c^2 = \frac{\rho\left(\frac{\partial h}{\partial T}\right)_p}{\rho\left(\frac{\partial \rho}{\partial p}\right)_T\left(\frac{\partial h}{\partial T}\right)_p + \left(\frac{\partial \rho}{\partial T}\right)_p\left\{1-\rho\left(\frac{\partial h}{\partial p}\right)_T\right\}}, \tag{4.102}$$

$$\psi = \frac{1-\rho\left(\frac{\partial h}{\partial p}\right)_T}{\left(\frac{\partial h}{\partial T}\right)_p}. \tag{4.103}$$

The spatial derivatives in normal direction in the definitions of $\mathfrak{L}_i$ in equations (A.28)-(A.32) are calculated by employing a first order forward discretizaton

$$\frac{\partial \phi}{\partial \hat{x}} = \frac{\phi_g - \phi_i}{\Delta \hat{x}}, \tag{4.104}$$

where ϕ_g denotes the value of variable ϕ in the ghost cell at the previous time-level and $\Delta\hat{x}$ is the distance between the ghost cell and the center of gravity of the control volume, which is equal to the characteristic length ℓ of the control volume defined as

the diameter of the smallest inscribed sphere of the control volume. The time derivatives in equations (A.41)–(A.45) are calculated with the time integration method described in section 4.4 to obtain the new rotated primitive variables $\hat{\mathbf{Q}}_g^+$ in the ghost cells yielding:

$$\hat{\mathbf{Q}}_g^+ = \hat{\mathbf{Q}}_g - \Delta t \left(\mathbf{d} + \mathbf{C} \right), \tag{4.105}$$

with $\mathbf{d}$ and $\mathbf{C}$ defined in equations (A.40) and (A.14), respectively. The new rotated primitive variables $\hat{\mathbf{Q}}_g^+$ are then rotated back to (x, y, z) coordinates by multiplying with the inverse $\mathbf{T}^{-1}$ of the rotation matrix defined in equation (4.21). The new conserved variables $\mathbf{U}_g^+$ in the ghost points can then be obtained through the appropriate equations of state $\rho_g^+ = \rho(p_g^+, T_g^+)$ and $h_g^+ = h(p_g^+, T_g^+)$.

Specifying the boundary conditions

Specifying the boundary conditions determines the values of $\mathfrak{L}_i$ in equations (A.41)–(A.45) for incoming waves, while for outgoing waves the values of $\mathfrak{L}_i$ are determined by equations (A.28)–(A.32). Note that $\mathfrak{L}_1$ and $\mathfrak{L}_5$ describe the left and right acoustic waves, $\mathfrak{L}_2$ the wave related to entropy and that $\mathfrak{L}_3$ and $\mathfrak{L}_4$ describe the wave associated with the convection of the shear waves.

Besides the solid wall, four different situations are possible:

- subsonic inflow
- supersonic inflow
- subsonic outflow
- supersonic outflow

In figure 4.4 each of these situations are illustrated for the wave-speeds $\lambda_1 = \hat{u} - c$, $\lambda_2 = \lambda_3 = \lambda_4 = \hat{u}$ and $\lambda_5 = \hat{u} + c$ on the boundary located at $\hat{x} = 0$ with unit normal vector $\vec{\mathbf{n}}$ pointing out of the computational domain and with $\hat{x}$ in the direction of $\vec{\mathbf{n}}$.

Subsonic inflow is characterized by $-c < \hat{u} < 0$, so that $\lambda_{1-4} < 0$ and $\lambda_5 > 0$. Thus $\mathfrak{L}_5$ is computed from its definition in equation (A.32) and the other four $\mathfrak{L}_i$ are specified from boundary conditions. Subsonic outflow is characterized by $0 < \hat{u} < c$, so that $\lambda_1 < 0$ and $\lambda_{2-5} > 0$. Thus $\mathfrak{L}_{2-5}$ are computed from its definition in equations (A.29)–(A.32) and $\mathfrak{L}_1$ is specified from boundary conditions. Supersonic inflow is specified by $\hat{u} < -c$, so that all $\lambda_i < 0$. This means that all values $\mathfrak{L}_i$ must be specified from boundary conditions. Supersonic outflow at the boundary is characterized by $\hat{u} > c$ so that all $\lambda_i > 0$. Consequently, no boundary conditions can be specified at all. In this case all $\mathfrak{L}_i$ are determined from equations (A.28)–(A.32).

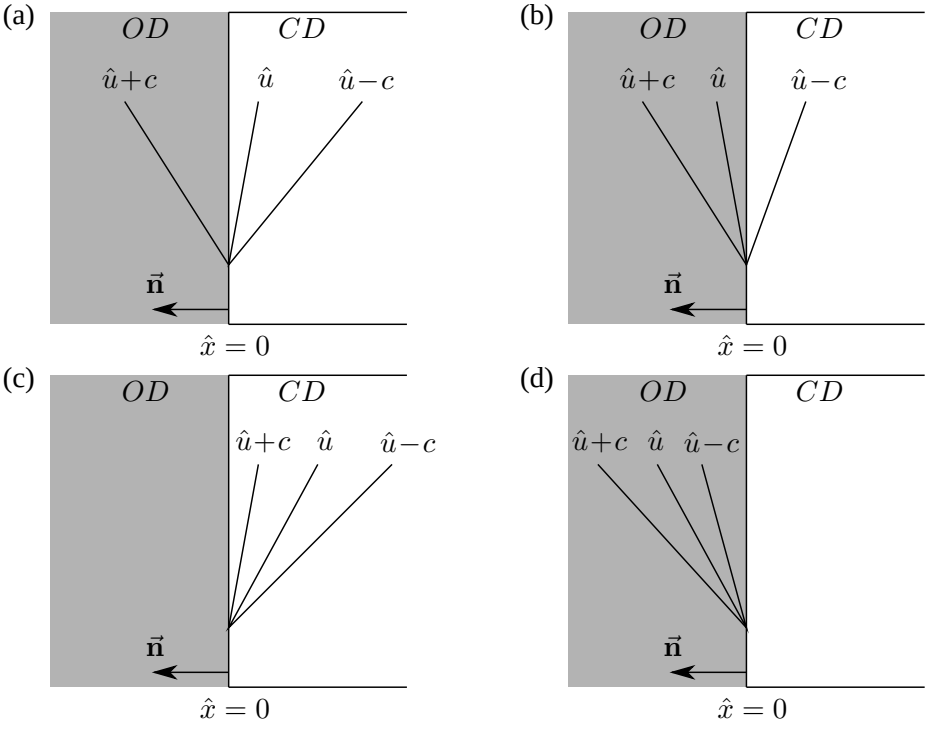

FIGURE 4.4: *Four different situations for in- and outflow boundary conditions. OD denotes the Outer Domain, CD denotes the Computational Domain. $\hat{u}-c$, $\hat{u}$ and $\hat{u}+c$ denote the characteristic wave speeds at the boundary of the computational domain located at $\hat{x}=0$. (a) subsonic inflow (b) subsonic outflow (c) supersonic inflow (d) supersonic outflow.*

In the remainder of this section practical examples for the boundary conditions are presented. First, the fully non-reflective boundary conditions for the four different situations of figure 4.4 are formulated. Then, an asymptotic non-reflective subsonic outflow boundary condition can be prescribed [149, 160] by defining a relaxation condition around a prescribed time-averaged mean pressure p_∞. Lastly, we discuss the classical constant pressure outflow boundary condition, which turns out to be fully reflective at the outflow boundary.

Non-reflecting boundary conditions

The non-reflecting boundary condition demands that the amplitude of an incoming wave is constant in time, which is equivalent to stating that there is no incoming wave. If we now set the corresponding $\mathfrak{L}_i$ equal to zero then that wave amplitude remains constant. Note that $\mathfrak{L}_2$ describes the inflow of entropy, so setting $\mathfrak{L}_2 = 0$

states that the inflow entropy is constant in the normal direction. Setting $\mathfrak{L}_3 = 0$ and $\mathfrak{L}_4 = 0$ will hold the tangential velocities $\hat{v}$ and $\hat{w}$ velocities constant in the absence of tangential effects.

The subsonic and supersonic non-reflecting boundary conditions are now specified in table 4.2. Defining $\nu = \Delta t/\Delta\hat{x}$ the non-reflective boundary conditions in terms of the new rotated primitive variables are presented in table 4.5.

Subsonic inflow: $-c < \hat{u} < 0$	Subsonic outflow: $0 < \hat{u} < c$
$\mathfrak{L}_1 = 0$	$\mathfrak{L}_1 = 0$
$\mathfrak{L}_2 = 0$	$\mathfrak{L}_2 = \lambda_2\left(-\frac{\psi}{\rho}\frac{\partial p}{\partial \hat{x}} + \frac{\partial T}{\partial \hat{x}}\right)$
$\mathfrak{L}_3 = 0$	$\mathfrak{L}_3 = \lambda_3\frac{\partial \hat{v}}{\partial \hat{x}}$
$\mathfrak{L}_4 = 0$	$\mathfrak{L}_4 = \lambda_4\frac{\partial \hat{w}}{\partial \hat{x}}$
$\mathfrak{L}_5 = \lambda_5\left(\frac{\partial p}{\partial \hat{x}} + \rho c\frac{\partial \hat{u}}{\partial \hat{x}}\right)$	$\mathfrak{L}_5 = \lambda_5\left(\frac{\partial p}{\partial \hat{x}} + \rho c\frac{\partial \hat{u}}{\partial \hat{x}}\right)$
Supersonic inflow: $\hat{u} < -c$	**Supersonic outflow: $\hat{u} > c$**
$\mathfrak{L}_1 = 0$	$\mathfrak{L}_1 = \lambda_1\left(\frac{\partial p}{\partial \hat{x}} - \rho c\frac{\partial \hat{u}}{\partial \hat{x}}\right)$
$\mathfrak{L}_2 = 0$	$\mathfrak{L}_2 = \lambda_2\left(-\frac{\psi}{\rho}\frac{\partial p}{\partial \hat{x}} + \frac{\partial T}{\partial \hat{x}}\right)$
$\mathfrak{L}_3 = 0$	$\mathfrak{L}_3 = \lambda_3\frac{\partial \hat{v}}{\partial \hat{x}}$
$\mathfrak{L}_4 = 0$	$\mathfrak{L}_4 = \lambda_4\frac{\partial \hat{w}}{\partial \hat{x}}$
$\mathfrak{L}_5 = 0$	$\mathfrak{L}_5 = \lambda_5\left(\frac{\partial p}{\partial \hat{x}} + \rho c\frac{\partial \hat{u}}{\partial \hat{x}}\right)$

TABLE 4.2: *Sub- and supersonic non-reflective boundary conditions for time-dependent in- and outflow.*

Subsonic inflow: $-c < \hat{u} < 0$

$$
\begin{aligned}
p_g^+ &= p_g - \tfrac{1}{2}\nu(\hat{u}_g + c_g)\left[p_g - p_i + \rho_g c_g(\hat{u}_g - \hat{u}_i)\right] \\
\hat{u}_g^+ &= \hat{u}_g - \tfrac{1}{2}\nu\tfrac{(\hat{u}_g + c_g)}{\rho_g c_g}\left[p_g - p_i + \rho_g c_g(\hat{u}_g - \hat{u}_i)\right] \\
\hat{v}_g^+ &= \hat{v}_g \\
\hat{w}_g^+ &= \hat{w}_g \\
T_g^+ &= T_g - \tfrac{1}{2}\nu\tfrac{\psi(\hat{u}_g + c_g)}{\rho_g}\left[p_g - p_i + \rho_g c_g(\hat{u}_g - \hat{u}_i)\right]
\end{aligned}
$$

Subsonic outflow: $0 < \hat{u} < c$

$$
\begin{aligned}
p_g^+ &= p_g - \tfrac{1}{2}\nu(\hat{u}_g + c_g)\left[p_g - p_i + \rho_g c_g(\hat{u}_g - \hat{u}_i)\right] \\
\hat{u}_g^+ &= \hat{u}_g - \tfrac{1}{2}\nu\tfrac{(\hat{u}_g + c_g)}{\rho_g c_g}\left[p_g - p_i + \rho_g c_g(\hat{u}_g - \hat{u}_i)\right] \\
\hat{v}_g^+ &= \hat{v}_g - \nu\hat{u}_g(\hat{v}_g - \hat{v}_i) \\
\hat{w}_g^+ &= \hat{w}_g - \nu\hat{u}_g(\hat{w}_g - \hat{w}_i) \\
T_g^+ &= T_g - \tfrac{1}{2}\nu\left[\psi\tfrac{(c_g - \hat{u}_g)}{\rho_g}(p_g - p_i) + \psi(\hat{u}_g + c_g)c_g(\hat{u}_g - \hat{u}_i) + 2\hat{u}_g(T_g - T_i)\right]
\end{aligned}
$$

Supersonic inflow: $\hat{u} < -c$

$$
\begin{aligned}
p_g^+ &= p_g \\
\hat{u}_g^+ &= \hat{u}_g \\
\hat{v}_g^+ &= \hat{v}_g \\
\hat{w}_g^+ &= \hat{w}_g \\
T_g^+ &= T_g
\end{aligned}
$$

Supersonic outflow: $\hat{u} > c$

$$
\begin{aligned}
p_g^+ &= p_g - \nu\left[\hat{u}_g(p_g - p_i) + \rho_g c_g^2(\hat{u}_g - \hat{u}_i)\right] \\
\hat{u}_g^+ &= \hat{u}_g - \nu\left[\tfrac{(p_g - p_i)}{\rho_g} + \hat{u}_g(\hat{u}_g - \hat{u}_i)\right] \\
\hat{v}_g^+ &= \hat{v}_g - \nu\hat{u}_g(\hat{v}_g - \hat{v}_i) \\
\hat{w}_g^+ &= \hat{w}_g - \nu\hat{u}_g(\hat{w}_g - \hat{w}_i) \\
T_g^+ &= T_g - \nu\left[\psi c_g(\hat{u}_g - \hat{u}_i) + \hat{u}_g(T_g - T_i)\right]
\end{aligned}
$$

TABLE 4.3: *Rotated primitive variables in ghost cell for sub- and supersonic non-reflective in- and outflow.*

Asymptotic pressure non-reflective outflow boundary condition

Poinsot & Lele [149], see also Rudy & Strickwerda [160], discussed a method to use a non-reflecting boundary condition as presented above and additionally incorporate some physical information on the mean static pressure at infinity p_∞ (for example a free surface in a cavitation tunnel). Imposing the pressure at infinity does not fix any of the dependent variables on the boundary. The constant pressure at infinity is now used to obtain the amplitude variation of the ingoing wave $\mathfrak{L}_1$. If the outlet pressure is not close to p_∞, weak reflected waves will enter the domain through the outlet to bring the pressure at the outlet back to a value close to p_∞. A simple way to do this is to set

$$\mathfrak{L}_1 = K(p - p_\infty), \tag{4.106}$$

where K is equal to $K = \sigma(1 - M^2)c/\Delta\hat{x}$ [149]. For subsonic water flow we apply the value $K = c/\Delta\hat{x}$. The resulting set of boundary conditions are specified in table 4.4. Defining $\nu = \Delta t/\Delta\hat{x}$ the asymptotic non-reflective subsonic outflow boundary conditions in terms of the new rotated primitive variables are presented in table 4.5.

$$\begin{array}{lcl}
\mathfrak{L}_1 & = & K(p - p_\infty) \\
\mathfrak{L}_2 & = & \lambda_2 \left(-\frac{\psi}{\rho}\frac{\partial p}{\partial \hat{x}} + \frac{\partial T}{\partial \hat{x}} \right) \\
\mathfrak{L}_3 & = & \lambda_3 \frac{\partial \hat{v}}{\partial \hat{x}} \\
\mathfrak{L}_4 & = & \lambda_4 \frac{\partial \hat{w}}{\partial \hat{x}} \\
\mathfrak{L}_5 & = & \lambda_5 \left(\frac{\partial p}{\partial \hat{x}} + \rho c \frac{\partial \hat{u}}{\partial \hat{x}} \right)
\end{array}$$

TABLE 4.4: *Asymptotic non-reflecting subsonic boundary conditions*

Subsonic outflow: $0 < \hat{u} < c$

$$\begin{array}{lcl}
p_g^+ & = & p_g - \frac{1}{2}\nu \left[(\hat{u}_g + c_g) \left[p_g - p_i + \rho_g c_g (\hat{u}_g - \hat{u}_i) \right] + c_g (p_g - p_\infty) \right] \\
\hat{u}_g^+ & = & \hat{u}_g - \frac{1}{2}\nu \left[\frac{\hat{u}_g p_g + c_g p_\infty - (\hat{u}_g + c_g) p_i}{\rho_g c_g} + (\hat{u}_g + c_g)(\hat{u}_g - \hat{u}_i) \right] \\
\hat{v}_g^+ & = & \hat{v}_g - \nu \hat{u}_g (\hat{v}_g - \hat{v}_i) \\
\hat{w}_g^+ & = & \hat{w}_g - \nu \hat{u}_g (\hat{w}_g - \hat{w}_i) \\
T_g^+ & = & T_g - \frac{1}{2}\nu \frac{\psi}{\rho_g} \left((2c_g - \hat{u}_g) p_g - c_g p_\infty + (\hat{u}_g - c_g) p_i \right) \\
 & & + \frac{1}{2}\nu \left[\psi (\hat{u}_g + c_g) c_g (\hat{u}_g - \hat{u}_i) + 2\hat{u}_g (T_g - T_i) \right]
\end{array}$$

TABLE 4.5: *Asymptotic subsonic non-reflective boundary conditions for time-dependent in- and outflow.*

Remark on constant pressure outflow boundary condition

Within the scope of the presented formalism the constant pressure subsonic outflow boundary condition can be considered. When the pressure is known to be a constant at the boundary, then $\frac{\partial p}{\partial t} = 0$ in equation (A.41). This is satisfied if $\mathfrak{L}_5 + \mathfrak{L}_1 = 0$, or $\mathfrak{L}_1 = -\mathfrak{L}_5$ giving the boundary conditions specified in table 4.6. It is now clear that,

$\mathfrak{L}_1$	=	$-\mathfrak{L}_5$
$\mathfrak{L}_2$	=	$\lambda_2 \left(-\frac{\psi}{\rho}\frac{\partial p}{\partial \hat{x}} + \frac{\partial T}{\partial \hat{x}} \right)$
$\mathfrak{L}_3$	=	$\lambda_3 \frac{\partial \hat{v}}{\partial \hat{x}}$
$\mathfrak{L}_4$	=	$\lambda_4 \frac{\partial \hat{w}}{\partial \hat{x}}$
$\mathfrak{L}_5$	=	$\lambda_5 \left(\frac{\partial p}{\partial \hat{x}} + \rho c \frac{\partial \hat{u}}{\partial \hat{x}} \right)$

TABLE 4.6: *Constant pressure subsonic outflow boundary conditions*

when specifying a constant pressure at the outflow boundary, the amplitude of the incoming wave $\mathfrak{L}_1$ becomes equal to the negative amplitude of the outgoing wave $\mathfrak{L}_5$. This implies that the outgoing wave $\mathfrak{L}_5$ is completely reflected into the domain. For steady flow calculations these reflected waves deteriorate the convergence to steady-state solution. For unsteady calculations these reflected waves un-physically interfere with the unsteady solution in the computational domain. Furthermore, when cavitating flows are considered, if the amplitude of the outgoing wave is large enough, then through the reflection the pressure drops to saturation pressure, causing cavitation to occur at the outflow boundary. Thus, it becomes clear that the non-reflective treatment of in- and outgoing waves is essential for unsteady cavitating flows.

4.8.2 Solid wall boundary conditions

The formulation in the previous subsection could also be used for a slip solid wall boundary condition [190]. However, we prefer to follow the formulation of Rizzi [159], Dadone [49] and Wang [217]. Applying the non-permeability condition on a solid wall, i.e. $\hat{u} = \vec{\mathbf{u}} \cdot \vec{\mathbf{n}} = 0$, results in that the mass and energy flux vanish as can be seen in equation (4.4). The only nonzero flux term is the pressure contribution in the momentum equations. However, this would result in a different flux formulation for the solid wall faces than for the internal faces.

Instead, the same flux formulation of equation (4.24) is employed. The right extrapolated values $\mathbf{U}_R$ are determined from the left extrapolated variables $\mathbf{U}_L$ by aplying the symmetry technique. The values $\mathbf{U}_g$ in the ghost cells on the solid walls are obtained by applying either the classical Symmetry Technique for tunnel walls or the Curvature Corrected Symmetry Technique for surfaces of the hydrofoil in the flow.

Rizzi [159] derived an auxiliary relation for the pressure at the solid wall incorporating the surface geometry. Dadone *et al.* [49] extended this idea and denoted their method Curvature Corrected Symmetry Technique (CCST). Wang and Sun [217] formulated the CCST method for unstructured grids. Here the formulation of Wang [217] is followed. First, the classical symmetry technique is discussed. Then the CCST for unstructured grids is presented.

A wall boundary as shown in figure 4.5 is considered. The solid wall is denoted by the thick black curved line, the (triangular) grid is represented with the solid lines, the control volumes are illustrated with the grey polygons with their faces denoted by the dashed lines. Ghost cells are employed as mirror images of the interior control volumes and assumed to be located at the grey circles. In the following the flow variables in the interior control volume V_i and in the ghost cells are denoted by subscript i and g, respectively.

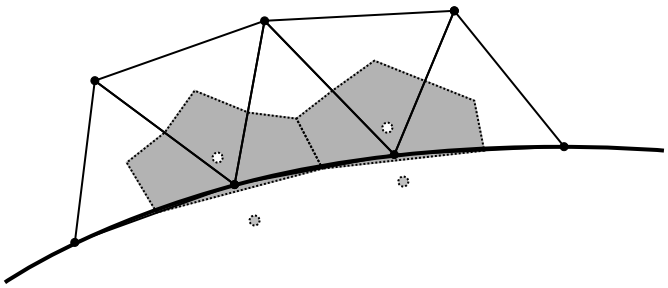

FIGURE 4.5: *Solid wall boundary. Thick black solid line denotes the solid wall. The triangles denote the grid, the control volumes are depicted by the grey polygons with their faces denoted by the dashed lines. The circles are the center of gravities of the control volume and the filled circles are the associated ghost points.*

Classical Symmetry Technique

In the classical Symmetry Technique the non-permeability condition is applied by assigning the values of the velocity vector of the ghost cell as mirror images of those at the interior control volume. Furthermore, the wall is assumed to be adiabatic, i.e. $T_g = T_i$, resulting in:

$$p_g = p_i, \tag{4.107}$$

$$\rho_g = \rho_i, \tag{4.108}$$

$$\vec{\mathbf{u}}_g = \vec{\mathbf{u}}_i - 2(\vec{\mathbf{u}}_i \cdot \vec{\mathbf{n}})\vec{\mathbf{n}}, \tag{4.109}$$

$$h_g = h(p_g, T_i). \tag{4.110}$$

Curvature Corrected Symmetry Technique

The basic idea of CCST is to use the local momentum equation to specify the pressure at the ghost cell. Therefore, the following equation is applied locally, [159]

$$\frac{\partial p}{\partial \hat{x}} = -\rho |\vec{\mathbf{u}}|^2 \kappa, \tag{4.111}$$

where κ is the local curvature of the boundary, which is provided by the mesh program Favomesh, see for details the thesis of Kelleners [109]. Applying equation (4.111) to the ghost cell yields

$$p_g = p_i - \Delta\hat{x}\rho_w |\vec{\mathbf{u}}_w|^2 \kappa, \tag{4.112}$$

where ρ_w and $\vec{\mathbf{u}}_w$ are chosen to be the density and tangential velocity at control volume V_i:

$$\rho_w = \rho_i \tag{4.113}$$

$$\vec{\mathbf{u}}_w = \vec{\mathbf{u}}_i - (\vec{\mathbf{u}}_i \cdot \vec{\mathbf{n}})\vec{\mathbf{n}}. \tag{4.114}$$

The distance $\Delta\hat{x}$ is determined by assuming that the internal control volume V_i is mirrored in the solid wall. Thus, the center of the ghost cell is at distance $\Delta\hat{x} = |\vec{\mathbf{x}}_{cg,i} - \vec{\mathbf{x}}_f|$ from the solid wall, where $\vec{\mathbf{x}}_f$ is the location of the boundary face. The velocity at the ghost cell is again computed according to

$$\vec{\mathbf{u}}_g = \vec{\mathbf{u}}_i - 2(\vec{\mathbf{u}}_i \cdot \vec{\mathbf{n}})\vec{\mathbf{n}}. \tag{4.115}$$

Assuming that the temperature is equal to the temperature in control volume V_i, the density and the specific total enthalpy at the ghost cell are computed from

$$\rho_g = \rho(p_g, T_i), \tag{4.116}$$

$$h_g = h(p_g, T_i). \tag{4.117}$$

4.9 Solution procedure for equilibrium cavitation model

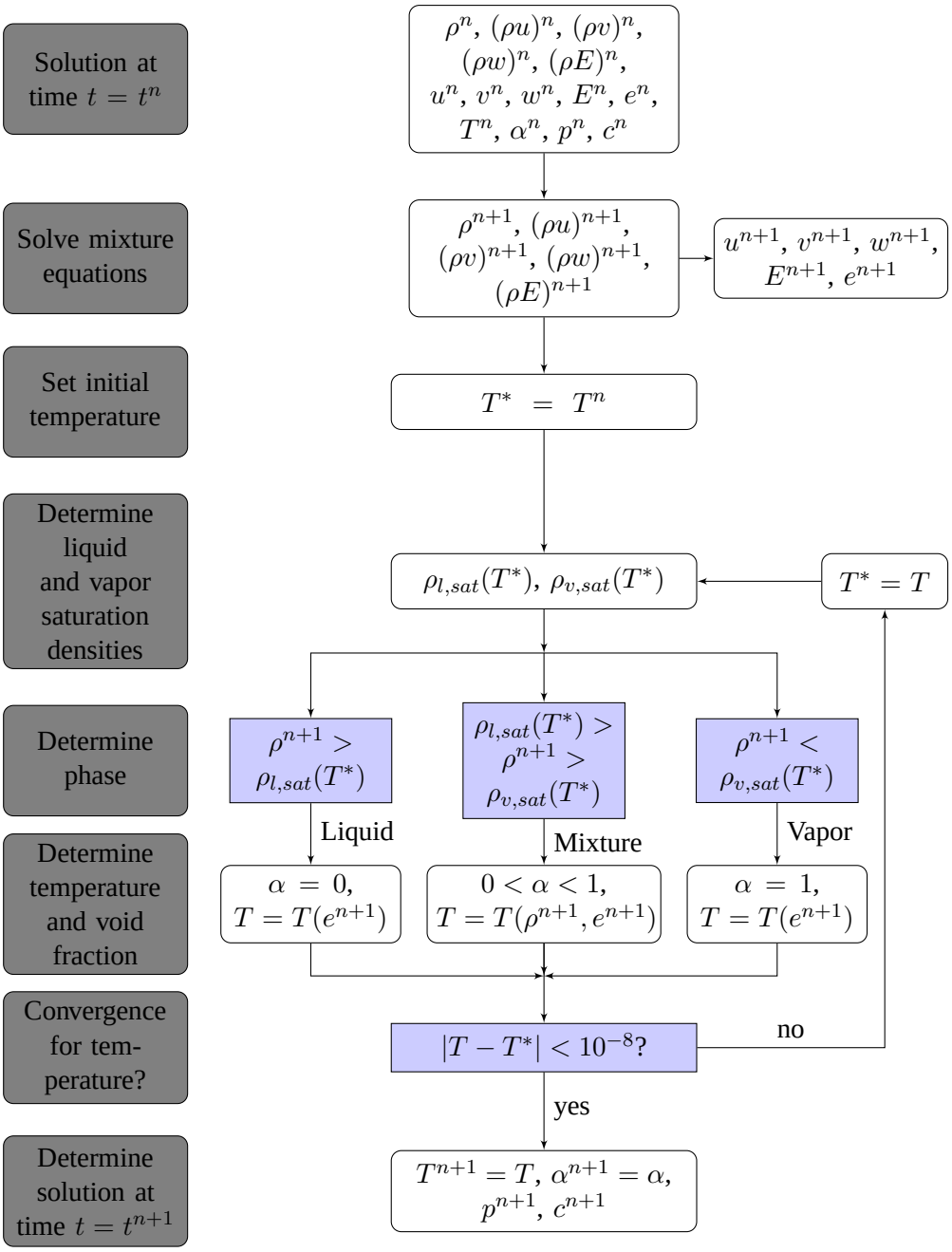

RESULTS SINGLE PHASE WATER FLOW

5 CHAPTER

In this chapter numerical solutions for compressible single-phase water flow are considered. The single-phase pure water flow is calculated by assuming that the water cannot turn into vapor. Thus, the modified Tait equation of state given in equation (3.42) is adopted and the liquid is allowed to follow the pressure-density curve for water below the saturation pressure as presented in figure 3.5.

First in section 5.2, the one-dimensional "Water Hammer" test case is considered to demonstrate the wave-capturing ability of the numerical method followed by a 1D Riemann problem for liquid flow in section 5.3.

Then, in section 5.4 the low-Mach number flow over a two-dimensional cylinder is calculated employing the different flux schemes presented in sections 4.5 and 4.7.2. The solutions are compared with the analytical incompressible potential flow solution. This test case illustrates the improvement of the steady-state flow results for low-Mach number flows achieved by adopting the modified flux formulation of Schmidt *et al*. [169, 170] presented in section 4.7.2. Furthermore, the results for the Curvature-Corrected Symmetry Technique (CCST) and the classical symmetry technique (ST) for the solid wall boundary conditions are compared to illustrate the improvement obtained with the CCST technique presented in section 4.8.2.

In section 5.5 the order of convergence of the numerical method is investigated by calculating the solution for steady-state water flow over a two-dimensional NACA0012 hydrofoil employing hybrid meshes of increasing grid density. In section 5.6 the numerical results for single-phase flow about a two-dimensional NACA0015 at 6° angle of attack are compared with a reference solution of Wrobel [221].

Finally, in section 5.7 the single-phase water flow over a three-dimensional Twist11 hydrofoil is presented to validate the numerical method with the experimental results of Foeth [67], who measured the lift force as well as the pressure on the hydrofoil for flow at high values of the cavitation number σ, i.e. for single-phase water flow.

5.1 Parameters

To facilitate the discussion in this chapter we introduce the L_2 norm for the residual and for the global error. As a measure for the convergence towards the steady-state solution, the L_2-norm $\mathcal{L}_2^n(\mathbb{R})$ of the residual at time level n is defined as

$$\mathcal{L}_2^n(\mathbb{R}) = \sqrt{\frac{1}{N}\sum_{i=1}^{N} \mathbb{R}_i^n}, \tag{5.1}$$

with N the number of points and the residual $\mathbb{R}_i^n$ defined in equation (4.30).

As a measure for the global error in a quantity ϕ, the L_2-norm $\mathcal{L}_2(\phi)$ is defined as:

$$\mathcal{L}_2(\phi) = \sqrt{\frac{1}{N}\sum_{i=1}^{N} (\phi_{i,num} - \phi_{i,ana})^2}, \tag{5.2}$$

with N the number of points, $\phi_{i,num}$ the numerical solution for ϕ in point i and $\phi_{i,ana}$ the analytical or exact solution for ϕ in point i.

5.2 1D time dependent test case: "Water Hammer"

To demonstrate the wave capturing ability of the present numerical method for a compressible liquid, we consider the so-called "Water Hammer" problem, which is sometimes called the "Joukowsky shock" [181].

Consider an initially steady flow of liquid through a pipe with a constant cross-section. The initial velocity of the liquid is denoted by u_0 and the initial pressure and temperature are denoted by p_0 and T_0, respectively. At an arbitrary time, say $t = 0$, the entire outflow boundary is closed instantly. At that instant a pressure rise occurs at the solid wall of the outflow boundary resulting in an upstream traveling shock wave. After passage of the shock wave the fluid will be at rest.

The Joukowsky equation [181] or Joukowsky-Frizell equation* approximates the change in pressure $\Delta p = p - p_0$ to the change in velocity $\Delta u = u - u_0$ accross the shock wave:

$$\Delta p = -\rho_0 c_0 \Delta u, \tag{5.3}$$

**The first explicit statement in the context of water hammer is usually attributed to Joukowsky (1898). Frizell (1898) and Allievi (1902) also found equation (5.3), but they did not provide any experimental validation. Tijsseling [192] points out that Johannes von Kries published the theory of water hammer in 1883 in a study on blood flow in arteries. Therefore, von Kries derived the Joukowsky formula 15 years before Joukowsky and Frizell in 1898.*

where ρ_0 is the density and c_0 the speed of sound of the liquid at temperature T_0 and pressure p_0. The Joukowsky equation is derived from linearized acoustic theory. The verification of the validity of this assumption is presented in Appendix C.

Evaluating equation (5.3) for the pressure p after the passage of the shock wave results in:

$$p = p_0 + \rho_0 c_0 u_0. \tag{5.4}$$

The boundary condition for the outflow is simply set to a reflective solid wall at $t = 0$ and for the inflow boundary the non-reflective boundary conditions are applied. Following Berg *et al*. [22] we choose the initial pressure p_0 and the initial velocity u_0 equal to $p_0 = 10^5$ Pa and $u_0 = 1.0\ \mathrm{ms}^{-1}$, respectively and we consider four different initial temperatures $T_0 = 293$ K, 313 K, 333 K and 353 K, respectively.

Note that, for a flow of liquid the pressure rise Δp_{liq} calculated with equation (5.4) is approximately equal to $\Delta p_{liq} \approx 15$ bar. For a flow of air the pressure rise Δp_{air} is found to be only equal to $\Delta p_{air} \approx 4$ mbar, illustrating the tremendous pressure pulses possible in compressible liquid flows compared with gas flows.

T_0 [K]	ρ_{exp} [$\mathrm{kg\,m^{-3}}$]	ρ_{Tait} [$\mathrm{kg\,m^{-3}}$]	$\frac{\lvert\rho_{exp}-\rho_{Tait}\rvert}{\rho_{exp}}$ [-]	c_{exp} [$\mathrm{ms^{-1}}$]	c_{Tait} [$\mathrm{ms^{-1}}$]	$\frac{\lvert c_{exp}-c_{Tait}\rvert}{c_{exp}}$ [-]
293	998.24	998.23	0.001%	1481.9	1537.66	3.8%
313	992.27	992.26	0.001%	1528.7	1542.26	0.89%
333	983.27	983.26	0.001%	1550.9	1549.27	0.11%
353	971.88	971.88	0.0%	1554.5	1558.26	0.24%

TABLE 5.1: *Comparison of the data from the modified Tait equation of state for the density and speed of sound with the experimental values [1] for* $p_0 = 10^5\,\mathrm{Pa}$ *and four temperatures* T_0.

In table 5.1 the density ρ_{Tait} and speed of sound c_{Tait} obtained with the modified Tait equation of state are compared with the experimental data [1] for the density ρ_{exp} and speed of sound c_{exp}, respectively. We find that the relative errors in density and speed of sound are less than 0.001% and 3.8%, respectively, showing that experimental values for the density of the water can be reproduced accurately by the modified Tait equation of state and that errors up to 4% may exist in the speed of sound.

For the four temperatures the analytical estimate for the pressure $p_{ana} = p_0 + \rho_{Tait} c_{Tait} u_0$ after the passage of the shock wave is compared with the pressure p_{num}

T_0 [K]	p_{ana} [10^6 Pa]	p_{num} [10^6 Pa]	$\frac{p_{ana}-p_{num}}{p_{ana}}$ [-]
293	1.635	1.637	0.12%
313	1.630	1.632	0.12%
333	1.623	1.626	0.18%
353	1.611	1.617	0.37%

TABLE 5.2: *Comparison of the analytical (equation (5.4)) and numerical results for the pressure after the passage of the Joukowsky shock for* $u_0 = 1.0\ \mathrm{ms}^{-1}$ *and* $p_0 = 10^5$ Pa.

obtained with the present numerical method. As presented in table 5.2 the maximum relative difference for the pressure after the shock is equal to 0.37%. These results indicate that we can accurately represent a shock wave in a compressible liquid with the present numerical method.

In figure 5.1 the solution for the pressure and velocity at three different time instances $t_1 = 0.2\mathrm{ms}$, $t_2 = 0.4\mathrm{ms}$ and $t_3 = 0.6\mathrm{ms}$ after the closure of the outflow boundary is presented for $T_0 = 293$ K. We applied the second-order hybrid HLLC/AUSM+up scheme with the limiter of Venkatakrishnan for a 2D quadrilateral and 2D triangular mesh with 100 elements in x-direction and 4 elements in y-direction. The results for both types of grids are identical to plotting accuracy. In figure 5.1 it is shown that the shock, which generates a pressure increase of about 15 bar, is sharply captured without any oscillations in the pressure or velocity distribution in the pipe.

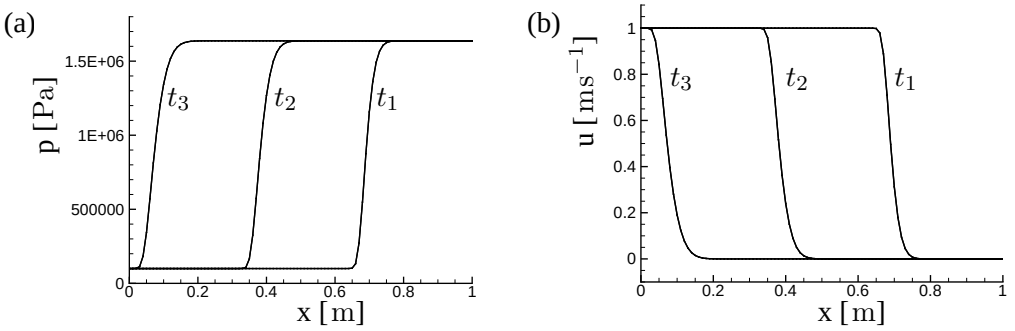

FIGURE 5.1: *Numerical solution for the Joukowsky shock with second-order hybrid HLLC/AUSM+up scheme for (a) pressure (b) velocity at* $t_1 = 0.2$ ms, $t_2 = 0.4$ ms, $t_3 = 0.6$ ms *for* $T_0 = 293$ K. *Flow is from left to right with the right boundary at* $x = 1$ m *closed at* $t = 0$ s. *The shock travels from right to left. Results are for a 2D quadrilateral grid with 100 points in* x*-direction and 4 points in* y*-direction.* CFL=0.8.

5.3 1D Riemann problem for liquid flow

The solution for the Riemann problem for flows with the perfect gas law as equation of state is well known, see Menikoff [138] and Toro [194]. For liquid flow the numerical solution for the Riemann problem is very challenging. Ivings *et al*. [104] presented the exact solution for the stiffened gas equation of state and the Tait equation of state. Note that, it is not possible to construct the exact solution the modified Tait equation of state as discussed in section 5.3.1.

The initial conditions for the left and right state are chosen in analogy with the classical Sod's shock tube test case for the flow of a perfect gas. Similar to the "Water Hammer" problem in section 5.2 the numerical results demonstrate the capability of the method to capture and predict the wave dynamics in compressible liquid flows. Amongst others, Chen & Cooke [36] and Schmidt *et al*. [170] also considered the numerical solution of a Riemann problem for liquid flow.

A tube with a length of 1m is considered filled with water and closed at both ends. In the center of the tube at $x = 0.5\mathrm{m}$ a diaphragm is placed separating two reservoirs of fluid. Both reservoirs have an initial temperature T_0. The left and right reservoir have a chosen initial pressure $p_{0L} = 1.0\times10^8\,\mathrm{Pa}$ and $p_{0R} = 1.0\times10^4\,\mathrm{Pa}$, respectively and a velocity $u_{0L} = 0$ and $u_{0R} = 0$, respectively. At $t = 0$ the membrane separating the two reservoirs is removed. The density in the two reservoirs is obtained using the modified Tait equation given in equation (3.42). The initial conditions are described in table 5.3. The numerical solutions are obtained on a triangular mesh with 100 elements in x-direction and 4 elements in y-direction. We have also considered a quadrilateral mesh of equal mesh density but the results are equivalent to plotting accuracy. The second-order hybrid HLLC/AUSM+up scheme of section 4.7.2 is employed.

p_{0L} [Pa]	u_{0L} [ms^{-1}]	T_{0L} [K]	p_{0R} [Pa]	u_{0R} [ms^{-1}]	T_{0R} [K]
1.0×10^8	0.0	293	1.0×10^4	0.0	293

TABLE 5.3: *Initial data for Riemann problem in tube.*

The solution of this Riemann problem consists of a left running expansion wave, a right running contact wave and a right running shock wave as presented in figure 5.2. The expansion wave hits the solid wall at the left end of the tube and reflects as an expansion wave running towards the center of the domain. The right running shock is reflected at the right solid wall of the tube and reflects to the left as a shock wave.

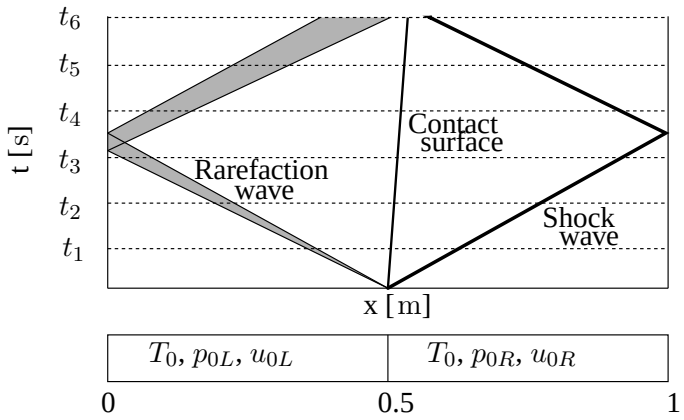

FIGURE 5.2: *Initial conditions and resulting characteristics of the solution of the Riemann problem with closed left and right boundaries.*

To illustrate the wave-dynamic character of the flow the solution is considered at different time-instants t_N, where $t_N = N\Delta t$, with $\Delta t = 0.9{\times}10^{-4}\,\mathrm{s}$ and $N = 1, 2, .., 6$.

In figures 5.3 the time-dependent solutions for the pressure and velocity are presented. In figures 5.3(a) and (b), the left-running expansion wave and the right-running shock wave are about to hit the solid wall at the ends of the tube at $t = t_3$. In figures 5.3(c) and (d) the expansion wave has reflected as a right-running expansion wave and the shock wave has reflected as a left-running shock wave. At $t = t_6$ the reflected waves are about to meet each other. The shock and expansion waves are captured without any oscillations in the pressure and velocity. Note that the width of the expansion wave is much smaller compared to that of an expansion wave in gas flows.

5.3.1 Analytical solution for liquid flow

For the modified Tait equation of state it is not possible to construct the exact solution for the Riemann problem. Ivings *et al.* [104] presented the exact solution for the Tait equation of state. In this section we compare the numerical solution ϕ_{TAIT} for the Tait equation of state with the exact solution ϕ_{ex}. Furthermore, the numerical solution $\phi_{modTAIT}$ for the modified Tait equation of state presented in figure 5.3 can then be compared to the numerical solution ϕ_{TAIT} for the Tait equation of state.

In figure 5.4 the three solutions ϕ_{ex}, ϕ_{TAIT} and $\phi_{modTait}$ are presented at time-instant $t_2 = 1.8 \times 10^{-4}\,\mathrm{s}$ for the pressure, velocity, density and speed of sound, respectively. It is shown that the numerical solution ϕ_{TAIT} (dashed line) predicts the location of the rarefaction and the shock accurately compared to the exact solution ϕ_{ex} (solid line). Furthermore, the numerical solution $\phi_{modTAIT}$ (dotted line) corre-

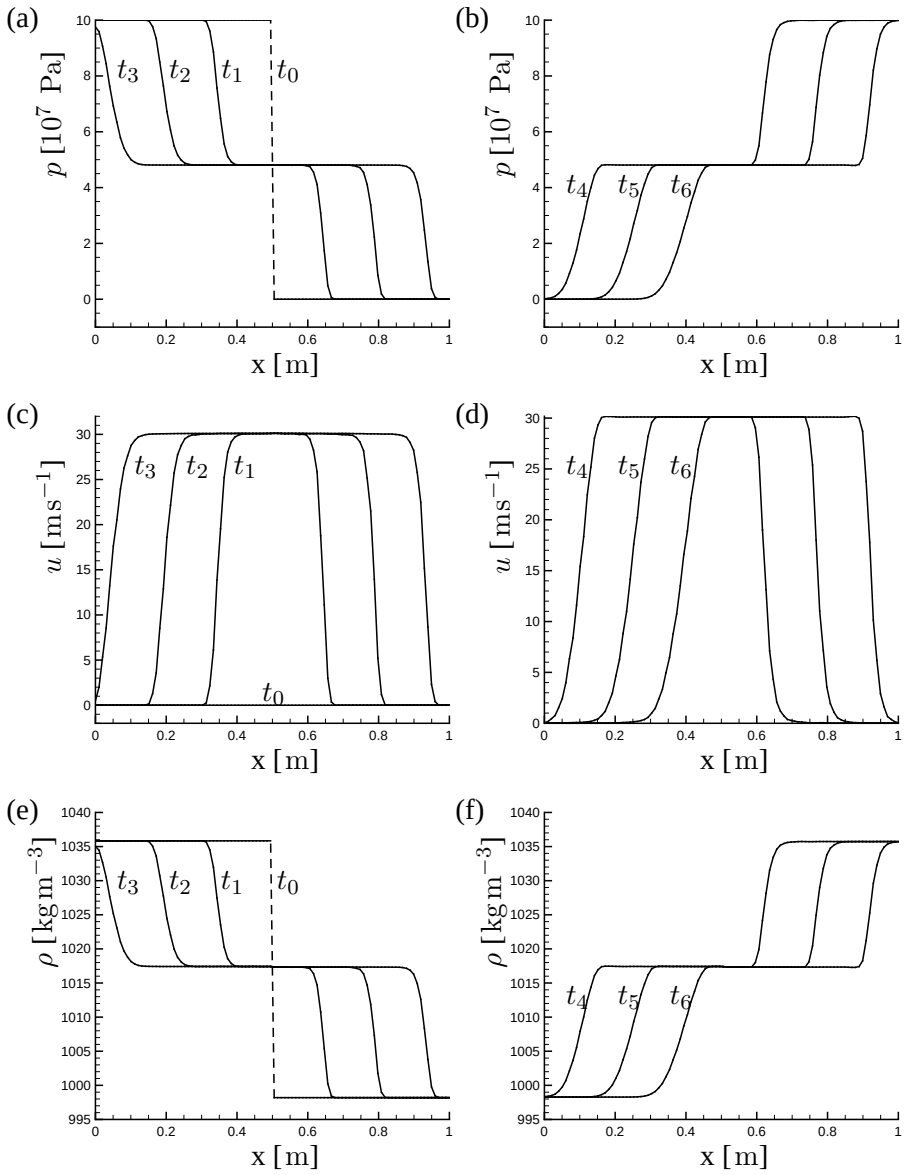

FIGURE 5.3: *Solution Riemann problem for liquid flow. (a)-(b) pressure (c)-(d) velocity (e)-(f) density at time-instants t_0–t_3 (left) and t_4–t_6 (right). $t_N = N\Delta t$, with $\Delta t = 0.9\times10^{-4}$ s. Results are obtained with second-order hybrid HLLC/AUSM+up scheme on a triangular grid with 100 points in x-direction and 4 points in y-direction. $Cfl = 0.8$, $\Delta t_{cfl}\approx 1.17\times10^{-6}$ s. $p_{0L}=10^8$ Pa, $p_{0R}=10^4$ Pa, $u_{0L}=0$, $u_{0R}=0$, $T_{0L}=T_{0R}=293$ K,*

sponds to plotting accuracy with the numerical solution ϕ_{TAIT}. A small deviation in the value for the speed of sound is found due to the temperature related terms in equation (3.44), which are not present in the speed of sound for the Tait equation of state. From figure 5.4 we conclude that the present numerical method accurately predicts the wave dynamics in a compressible water flow compared to the exact solution of the Riemann problem for the Tait equation of state.

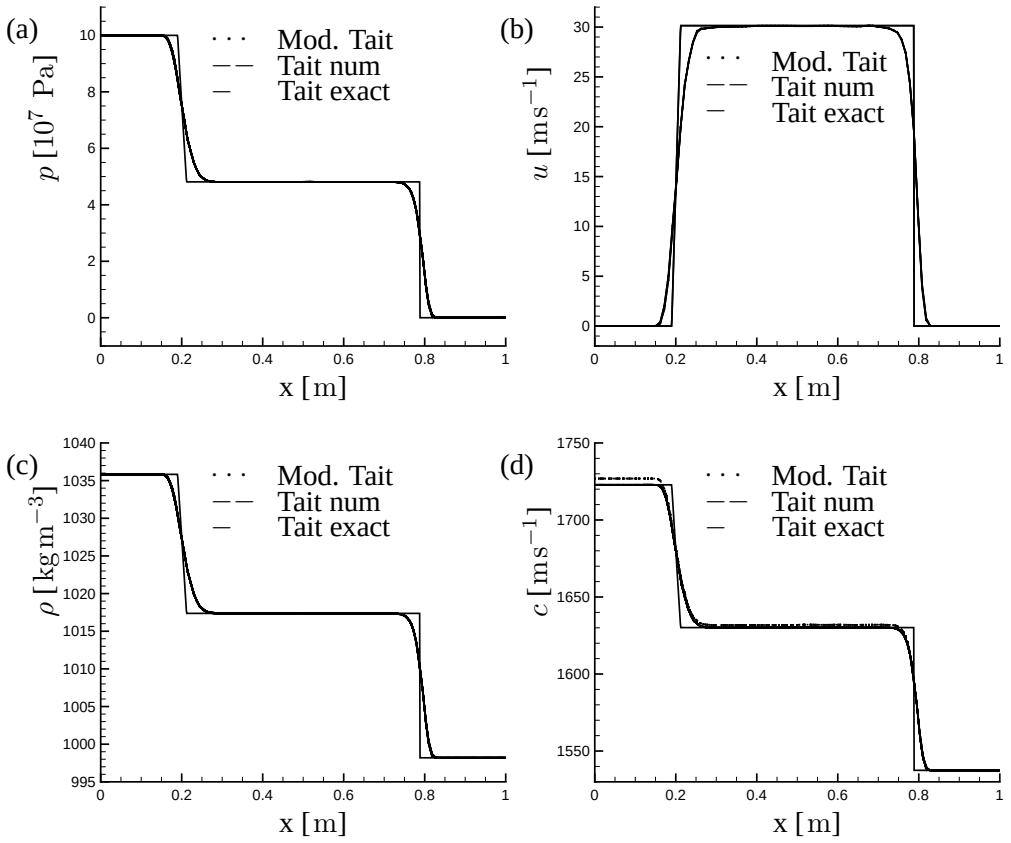

FIGURE 5.4: *Solution Riemann problem for liquid flow. a) pressure (b) velocity (c) density (d) speed of sound. Comparison of numerical solution for Tait equation of state (dashed) and modified Tait equation of state (dotted) with exact solution for Tait equation of state (solid) at* $t_2 = 1.8\times10^{-4}$ s. *Results are obtained with second-order hybrid HLLC/AUSM+up scheme on a triangular grid with 100 points in* x*-direction.* $Cfl = 0.8$, $p_{0L}=10^8$ Pa, $p_{0R}=10^4$ Pa, $u_{0L}=0$, $u_{0R}=0$, $T_{0L}=T_{0R}=293$ K.

5.3.2 Grid convergence

To assess the convergence of the numerical method for compressible liquid flow five triangular grids consisting of 50, 100, 200, 400 and 800 points in x-direction and 2, 4, 8, 16 and 32 points in y-direction are constructed. The numerical solutions at time-instant $t_2 = 1.8\times10^{-4}$ s are calculated with a CFL number equal to 0.8, resulting in the numerical time steps Δt_{cfl} for the five grids as presented in table 5.4.

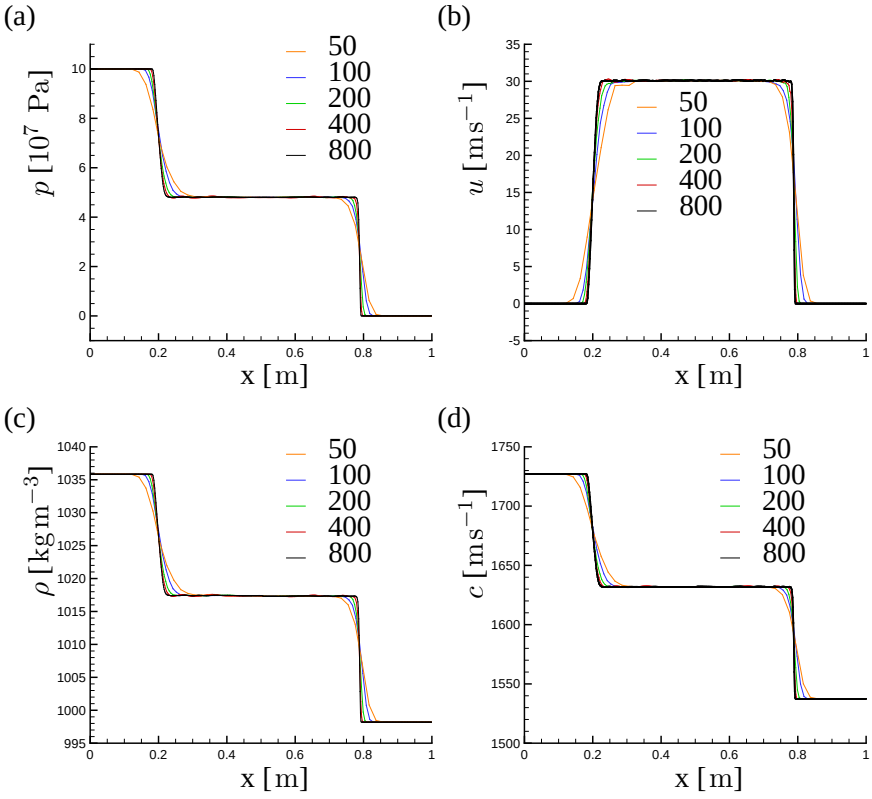

FIGURE 5.5: *Solution Riemann problem for liquid flow solution at* $t_2 = 1.8\times10^{-4}$ s. *(a) pressure (b) velocity (c) density (d) speed of sound. Results are obtained with second-order hybrid HLLC/AUSM+up scheme on triangular grids with 50, 100, 200, 400, 800 points in* x*-direction, respectively* $Cfl = 0.8$, $p_{0L}=10^8$ Pa, $p_{0R}=10^4$ Pa, $u_{0L}=0$, $u_{0R}=0$, $T_{0L}=T_{0R}=293$ K.

The numerical solutions for the pressure, velocity, density and speed of sound are presented in figure 5.5. It is shown that the discontinuities in the solution, i.e. the shock wave and the expansion wave, become steeper when the mesh is refined. Furthermore, the solution around the shock wave and the expansion wave center nicely

mesh	Δt_{cfl} [10^{-6} s]
50	1.671
100	1.170
200	0.523
400	0.290
800	0.127

TABLE 5.4: *Liquid Riemann problem. Numerical time steps Δt_{cfl} for five grids.*

around on the same positions for all five grids. We remark that the solution on the mesh with 400 points in x-direction experiences small oscillations in the center region. The origin of these oscillations is not clear. From these solutions we conclude that the numerical method converges towards the correct solution when the grid and the time-step are refined.

5.4 Water flow over a 2D cylinder

To assess the performance of the numerical method for low-Mach number liquid flow, the inviscid flow around a 2D cylinder is considered.

5.4.1 Geometry and computational domain

The circle cylinder has radius $R = 1$ m. An O-type mesh of quadrilaterals is used to construct the vertex-centered control volumes. The mesh consists of 128 nodes on the surface of the cylinder and 32 nodes in radial direction. The first 16 nodes away from the cylinder are located such that the grid is completely circular up to a radius of 4 cylinder radii. From the radius $r = 4R$ to the outer boundaries of the computational domain the grid is stretched, such that each quadrilateral is approximately 1.2 times longer than the previous quadrilateral.

The outer boundary at the x-axis is located at 40 times the radius of the cylinder. At the y-axis the outer boundaries are positioned at 65 times the radius of the cylinder. This results in a lens-shaped computational domain to ensure that the inflow and outflow boundary remain clearly distinct from each other and that during a simulation the normal component of the flow at the in- or outflow boundary always has the same sign, see for more details the thesis of Kelleners [109]. The computational mesh and a close-up around the cylinder are presented in figure 5.6.

5.4.2 Numerical method

The numerical simulation is started from an initial uniform flow with free stream Mach number $M_\infty = 6.5 \times 10^{-3}$, corresponding with a free-stream velocity of $U_\infty = 10$ ms^{-1}, at pressure $p_\infty = 1.0 \times 10^5$ Pa and temperature $T_\infty = 293$ K. For

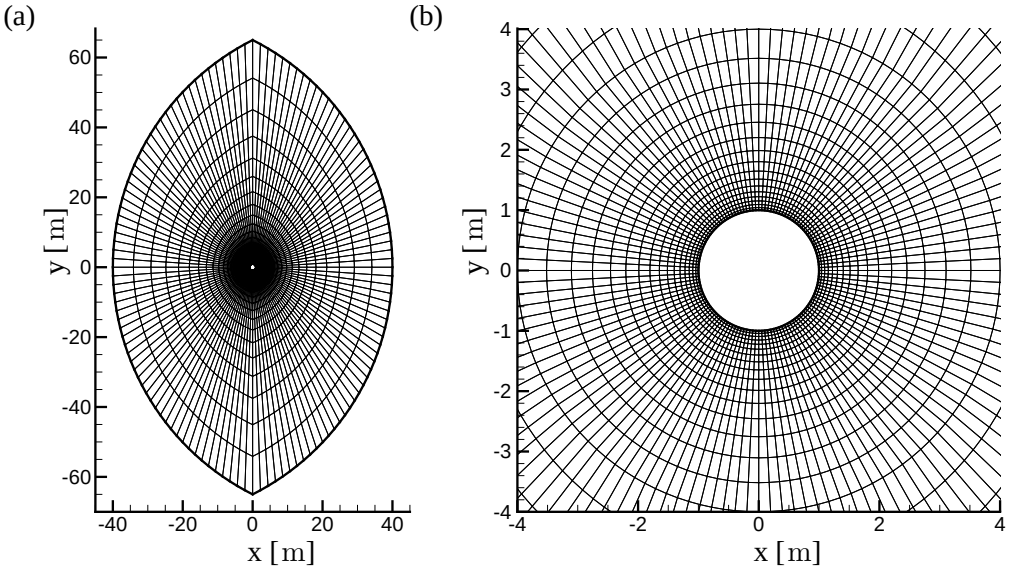

FIGURE 5.6: *(a) Computational domain,* 128×32 *nodes (b) Close-up of the mesh around the cylinder. Flow is from left to right.*

the cylinder surface the curvature-corrected solid wall boundary conditions of section 4.8.2 are chosen. For the in- and outflow boundary the non-reflective boundary conditions of section 4.8.1 are applied. The results in figures 5.7 and 5.8 are obtained with the second-order hybrid HLLC/AUSM flux scheme of Schmidt *et al.* [169] as described in section 4.7.2 with the limiter of Venkatakrishnan.

5.4.3 Results hybrid HLLC/AUSM flux scheme

The numerical solution for the Mach number M is presented in figure 5.7. The Mach number distribution is nearly perfect symmetrical with respect to the x- and y-axis. This indicates that the numerical solution is an accurate representation of this inviscid flow solution. The maximum Mach number is reached at the top and bottom of the cylinder and is equal to 0.013, which corresponds to a velocity of $2U_\infty$.

In figure 5.8 the numerical solution (squares) for the $-C_p$ coefficient and the tangential velocity $|\vec{\mathbf{u}}_{tan}|/U_\infty$ on the surface of the cylinder are compared with the analytical, incompressible flow solution (lines) given by, see e.g. Anderson [12]:

$$C_{p_{exact}} = 1 - 4\left(1 - \left(\frac{x}{R}\right)^2\right), \tag{5.5}$$

$$\frac{|\vec{\mathbf{u}}_{tan_{exact}}|}{U_\infty} = 2\sqrt{1 - \left(\frac{x}{R}\right)^2}. \tag{5.6}$$

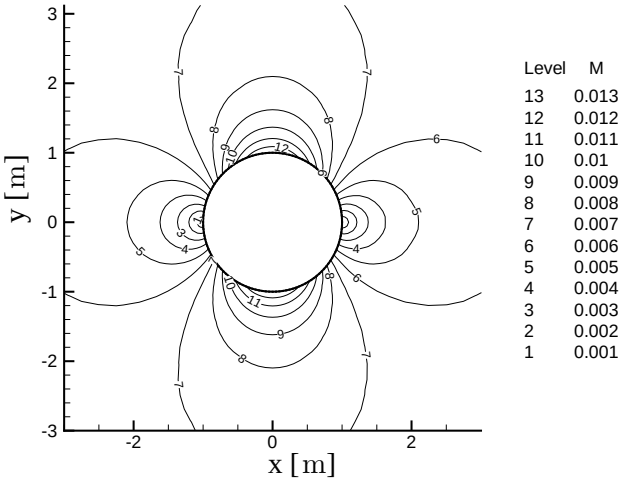

FIGURE 5.7: *Numerical solution for the Mach number for water flow around 2D cylinder,* $U_\infty = 10\ \mathrm{ms}^{-1}$, M_∞ = 6.5×10^{-3}, $p_\infty = 10^5\,\mathrm{Pa}$, $T_\infty = 293$ K. *Solution obtained with second-order hybrid HLLC/AUSM scheme. Non-reflective in- and outflow boundary conditions and Curvature Corrected Symmetry Technique for cylinder wall.* $CFL = 0.8$.

The numerical solution shows excellent agreement with the reference solution for this low Mach number. On the surface of the cylinder no oscillations in the pressure or velocity are present and the pressure is accurately obtained even in the downstream stagnation point.

The largest deviation for the $-C_p$ coefficient occurs at the top and bottom of the cylinder and is approximately equal to 1.8%. The numerically obtained lift and drag coefficient c_l and c_d are equal to 6.3×10^{-4} and 5.0×10^{-3}, resprectively. For inviscid low-Mach number flow these values should be equal to zero and thus these values are a measure for the global error of the solution on the surface of the cylinder. The L_2-norm defined in equation (5.2) for the pressure coefficient and tangential velocity with respect to the analytical solution are equal to $\mathcal{L}_2(C_p) = 1.2 \times 10^{-2}$ and $\mathcal{L}_2(\mathbf{u}_{tan}) = 9.7 \times 10^{-2}$, respectively. These values are compared in section 5.4.4 with the values obtained using other flux schemes and in section 5.4.5 with the results employing the classical symmetry technique for the solid wall boundary conditions.

5.4.4 Comparison with other flux schemes

In figure 5.9 the second-order solutions for the Mach number obtained with four other schemes of section 4.5 are presented, i.e. HLLC, JST, AUSM and AUSM+up for all

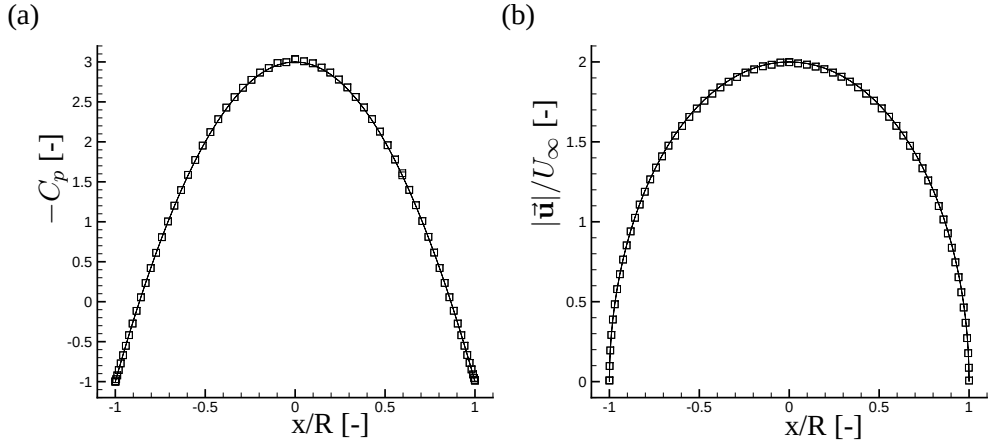

FIGURE 5.8: *Numerical solution (squares) and analytical solution (lines) for water flow around 2D cylinder for* $U_\infty = 10\ \mathrm{ms}^{-1}$ *corresponding to* $M_\infty = 6.5\times10^{-3}$ *at* $p_\infty = 10^5\,\mathrm{Pa}$ *and* $T_\infty = 293$ K. *Second-order hybrid HLLC/AUSM scheme. Non-reflective in- and outflow boundary conditions and Curvature Corrected Symmetry Technique for cylinder wall.* $CFL = 0.8$. *(a)* $-C_p$ *coefficient (b) relative tangential velocity* $|\vec{\mathbf{u}}|/U_\infty$ *on the surface of the cylinder.*

speeds. Note the differences with the results obtained with the hybrid HLLC/AUSM scheme presented in figure 5.7.

The Mach number distribution obtained with the HLLC scheme, see figure 5.9(a) indicates that this method is much too dissipative for this low-Mach number flow. The solution is symmetrical with respect to the x-axis, but there is clearly no symmetry with respect to the y-axis. The maximum Mach number on the surface of the cylinder is equal to 9.6×10^{-3}, but it is not obtained at the top and bottom ($x = 0$) of the cylinder, but at $x = -0.38\mathrm{m}$.

The Mach number distribution obtained with the AUSM scheme, figure 5.9(b), is inaccurate. At these low-Mach numbers the coupling between the pressure and velocity is lost resulting in the presented non-smooth solution. The Mach number distribution obtained with the JST scheme shown in figure 5.9(c) appears to be of better quality, but close to the surface of the cylinder a layer of high pressure appears, resulting in a completely inaccurate solution on the surface of the cylinder. The results in figure 5.9(d) obtained with the AUSM+-up for all speeds scheme are much better than for the other three schemes. However, the solution is not completely symmetrical with respect to the y-axis, as is the case for the result obtained with the hybrid HLLC/AUSM scheme presented in figure 5.7.

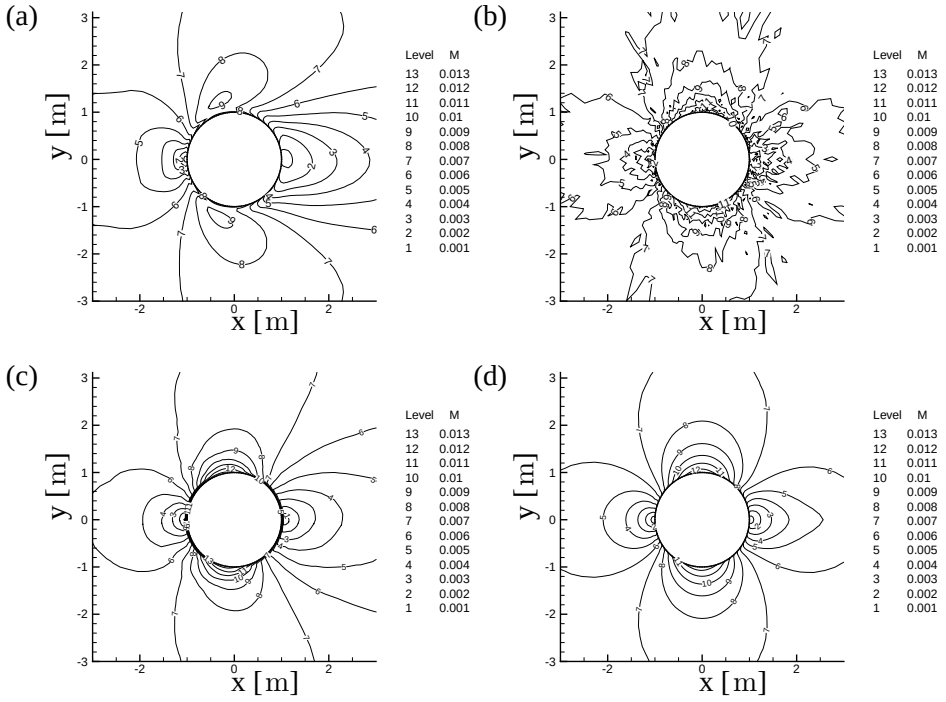

FIGURE 5.9: *Comparison of second-order results obtained with different flux schemes. Numerical solution for Mach number for water flow around 2D cylinder,* $U_\infty = 10\ \mathrm{ms}^{-1}$, $M_\infty = 6.5 \times 10^{-3}$, $p_\infty = 10^5\,\mathrm{Pa}$ *and* $T_\infty = 293\ \mathrm{K}$. $CFL = 0.8$. *Non-reflective in- and outflow boundary conditions and Curvature Corrected Symmetry Technique for cylinder wall. Solution obtained with (a) HLLC (b) AUSM (c) JST (d) AUSM+-up for all speeds.*

The lift and drag coefficients c_l and c_d as well as the L_2-norm for the pressure coefficient C_p and the tangential velocity $\mathbf{u}_{tan}$ as defined in equation (5.2) are presented in table 5.5 for the hybrid HLLC/AUSM flux scheme and the four "classical" flux schemes.

From the comparison of the solutions presented in figure 5.7 and 5.9 and from the numerically obtained lift and drag coefficients as well as the L_2-norm for C_p and u_{tan} presented in table 5.5 it can be concluded that the adaptation of the classical HLLC and AUSM schemes to the hybrid scheme as proposed by Schmidt *et al*. [169], results in a much improved solution for low-Mach number liquid flow.

flux scheme	c_l [-]	c_d [-]	$\mathcal{L}_2(C_p)$	$\mathcal{L}_2(\mathbf{u}_{tan})$	fig
hyb. HLLC/AUSM	6.3×10^{-4}	5.0×10^{-3}	1.2×10^{-2}	9.7×10^{-2}	5.7
HLLC	2.7×10^{-3}	0.28	0.87	4.68	5.9(a)
AUSM	6.47	-0.28	30..25	1.25	5.9(b)
JST	2.47	1.13×10^{3}	5.2×10^{2}	6.59	5.9(c)
AUSM+up fas	-1.1×10^{-4}	4.2×10^{-2}	8.3×10^{-2}	0.47	5.9(d)

TABLE 5.5: *Low-Mach number flow about 2D cylinder. Comparison of lift and drag coefficients as well as L_2-norm for C_p and the tangential velocity on the surface u_{tan}.*

5.4.5 Results for different solid wall boundary conditions

The results obtained with the Curvature-Corrected Symmetry Technique (CCST) and the classical Symmetry Technique (ST) presented in section 4.8.2 for the solid wall boundary conditions at the surface of the cylinder are compared applying the second-order hybrid HLLC/AUSM scheme. In figure 5.10 the results for the Mach number distribution are presented for the CCST and ST boundary conditions, respectively.

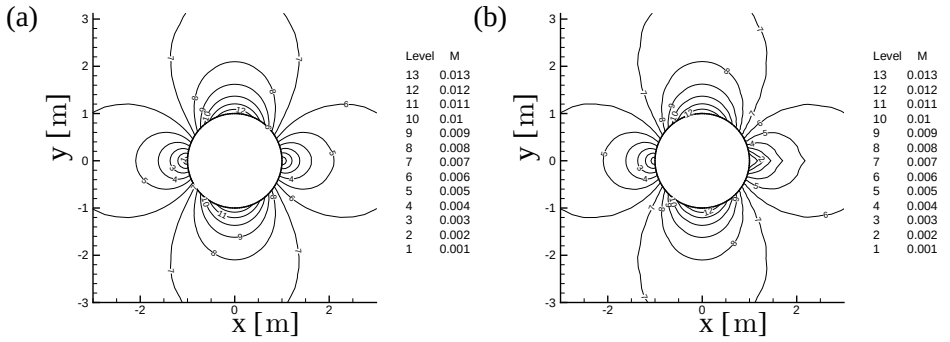

FIGURE 5.10: *Comparison of results for different solid wall boundary conditions. Mach number distribution for water flow around 2D cylinder, $U_\infty = 10\ \mathrm{ms}^{-1}$, $M_\infty = 6.5\times10^{-3}$, $p_\infty = 10^5\,\mathrm{Pa}$, $T_\infty = 293$ K. $CFL = 0.8$. Second-order hybrid HLLC/AUSM scheme with (a) Curvature-Corrected Symmetry Technique (b) Symmetry Technique.*

The solution for the Symmetry Technique presented in figure 5.10(b) shows a deviation from the symmetric solution compared with the solution obtained with the CCST technique presented in figure 5.10(a). For the ST technique a (numerics-induced) wake-like structure is formed behind the cylinder.

The lift and drag coefficients as well as the L_2-norm for C_p and $\mathbf{u}_{tan}$ are presented in

table 5.6. The wake-like structure for the ST technique is represented by the higher value for the drag coefficient c_d compared with the value found for the CCST technique.

Furthermore, the L_2-norm found for the pressure and velocity on the surface of the cylinder are found to be almost an order higher than for the CCST technique. From figure 5.10 and table 5.6 it is concluded that the CCST technique improves the accuracy of the solution for this cylinder test case.

bound. cond.	c_l [-]	c_d [-]	$\mathcal{L}_2(C_p)$	$\mathcal{L}_2(\mathbf{u}_{tan})$	fig
CCST	6.3×10^{-4}	5.0×10^{-3}	1.2×10^{-2}	9.7×10^{-2}	5.10(a)
ST	-3.5×10^{-4}	7.5×10^{-3}	8.5×10^{-2}	0.46	5.10(b)

TABLE 5.6: *Low-Mach number flow about 2D cylinder. Results with second-order hybrid HLLC/AUSM flux scheme. Comparison of lift and drag coefficients as well as L_2-norm for C_p and the tangential velocity on the surface $\mathbf{u}_{tan}$ for Curvature-Corrected Symmetry Technique (CCST) and Symmetry Technique (ST).*

5.4.6 Conclusions

In this section the low-Mach number single-phase water flow about a two-dimensional cylinder is calculated. The numerical solutions are compared with the analytical potential flow solution.

It is shown that the adaptation of the classical HLLC and AUSM scheme to the hybrid HLLC/AUSM scheme as originally proposed by Schmidt *et al*. [169], results in a much improved solution for low-Mach-number inviscid liquid flow about a two-dimensional cylinder.

Furthermore, it is shown that the Curvature-Corrected Symmetry Technique (CCST) for solid wall boundary conditions improves the accuracy of the solution compared with the classical Symmetry Technique (ST).

We have reduced the free-stream velocity U_∞ even further for the hybrid flux scheme. However, for $U_\infty \leq 1.0\ \mathrm{ms}^{-1}$, which corresponds to a Mach number $M = 6.5\times10^{-4}$, the solution starts to develop irregularities in the pressure and velocity on the surface of the cylinder. Schmidt *et al*. [170] succeeded in obtaining a solution for Mach numbers as low as $M = 10^{-4}$.

5.5 Water flow about a 2D NACA0012 foil

To assess the order of convergence of the numerical method the single-phase water flow about a two-dimensional NACA0012 hydrofoil at 4° angle of attack with chord length c equal to $c = 0.15\mathrm{m}$ is considered as computed on three hybrid meshes with different grid density. The inflow velocity is chosen equal to $U_\infty = 50\ \mathrm{ms}^{-1}$ corresponding with a free stream Mach number of $M_\infty = 0.0325$ at a free-stream pressure $p_\infty = 10^5\,\mathrm{Pa}$ and free-stream temperature $T_\infty = 293\mathrm{K}$, yielding a free stream density $\rho_\infty = 998.2\ \mathrm{kgm}^{-3}$.

5.5.1 Geometry of NACA foil

The section of the hydrofoil is presented in figure 5.11. The dimensionless half-thickness distribution $\bar{y}(\bar{x})$ is given by [4]:

$$\bar{y} = \frac{t}{0.20}\left(a_0\sqrt{\bar{x}} + a_1\bar{x} + a_2\bar{x}^2 + a_3\bar{x}^3 + a_4\bar{x}^4\right), \tag{5.7}$$

with $a_0 = 0.2969$, $a_1 = -0.126$, $a_2 = -0.3516$, $a_3 = 0.2843$, $a_4 = -0.1015$. t is the thickness parameter, here $t = 0.12$ and $\bar{x} = x/c$ is the dimensionless coordinate along the chord line ranging from 0 at the leading edge to 1 at the trailing edge. Note that with the definition in equation (5.7) the trailing edge has a finite thickness. Therefore, the trailing edge is extended using the profile definition of equation (5.7) until zero thickness at $\bar{x} = 1.0089304$.

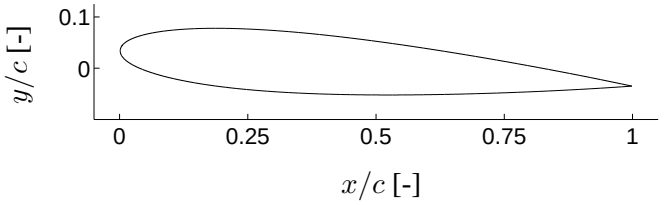

FIGURE 5.11: *Section of NACA0012 hydrofoil at 4° angle of attack.*

5.5.2 Computational domain and hybrid mesh

The computational domain is sketched in figure 5.12. The hydrofoil is located in a channel with height $2c$ and a length of $2c$ upstream of the hydrofoil and $3c$ downstream of the hydrofoil. The flow is from left to right.

The median dual mesh is constructed from a hybrid mesh consisting of a layer of quadrilateral elements around the foil and in part of the wake. The regions with the quadrilaterals are indicated with the circled numbers in figure 5.12. The region in the wake with quadrilaterals extends one chord length after the hydrofoil. The rest

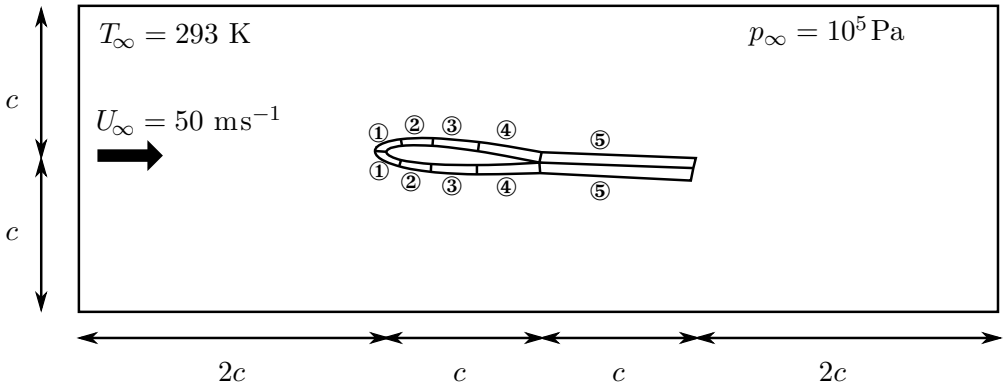

FIGURE 5.12: *Computational domain for 2D NACA0012 hydrofoil at* 4° *angle of attack in a channel.*

of the computational domain is filled with triangles to fit the mesh easily within the channel. Note that the hybrid mesh approach offers great flexibility in constructing the mesh for this computational domain.

Three different mesh densities are chosen in the regions around the hydrofoil indicated by the circled numbers in figure 5.12. The number of quadrilateral elements in the different regions are chosen such that the number of quadrilaterals along the foil is equal to 100, 200, and 400, respectively. The exact number of quadrilaterals in the different regions is listed in table 5.7. The variable n denotes the number of quadrilaterals in the direction perpendicular to the surface of the hydrofoil, i.e. the "thickness" of the quadrilateral layer.

number of points on foil	n	①	②	③	④	⑤	# quad's	# control volumes
100	10	15	10	10	15	26	1,520	4,041
200	20	30	20	20	30	52	6,080	10,419
400	40	60	40	40	60	104	24,320	31,976

TABLE 5.7: *Number of quadrilaterals per segment of the computational domain presented in figure 5.12 and total number of control volumes for each mesh.*

The triangular mesh around the quadrilateral layer is chosen such that the transition from the quadrilaterals to the triangles is relatively smooth. Furthermore, for the meshes of different density close to the foil, the triangles further away in the computational domain are approximately equal in size. The resulting meshes around the hydrofoil are presented in figure 5.13.

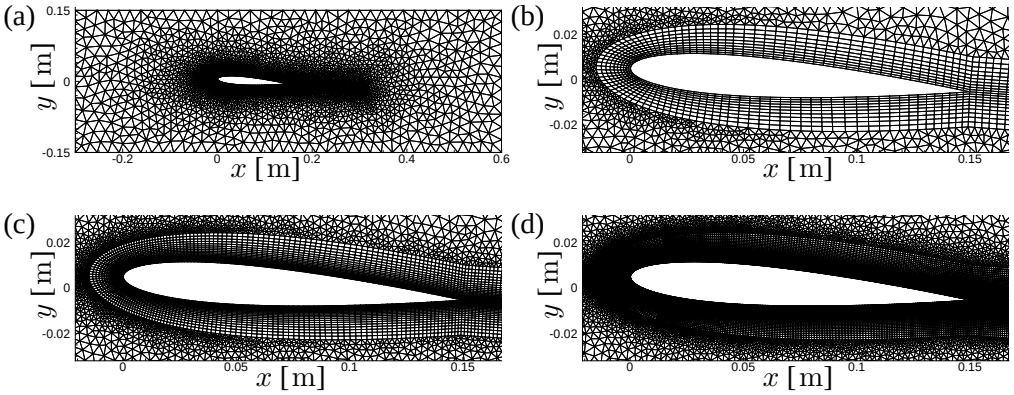

FIGURE 5.13: *(a) Computational mesh for water flow around 2D NACA0012 hydrofoil at 4° angle of attack in channel. (b)–(d) Close up of mesh around hydrofoil. Points on foil: (b) 100 (c) 200 (d) 400.*

5.5.3 Numerical method

The results are obtained with the hybrid HLLC/AUSM flux scheme as presented in section 4.7.2. In the following the first and second-order results are presented. The second-order results are obtained with the limiter method of Venkatakrishnan employing the primitive variables $[\rho, u, v, w, e]^T$. For the inflow the non-reflective boundary conditions are applied. For the outflow the asymptotic constant pressure boundary condition with p_∞ is used. The top and bottom of the channel as well as the surface of the hydrofoil are slip solid walls. For the surface of the hydrofoil the Curvature Corrected Symmetry Technique is applied. To accelerate the calculation towards the steady-state solution local time-stepping is applied.

5.5.4 Results for lift and drag forces

The lift and drag coefficients c_l and c_d for the three meshes are presented in table 5.8 and figure 5.14 for first- and second-order reconstruction, respectively.

number of points	first-order		second-order	
on foil	c_d [-]	c_l[-]	c_d[-]	c_l[-]
100	0.02517	0.4901	0.00687	0.5299
200	0.01425	0.5075	0.00236	0.5389
400	0.00991	0.5157	0.00110	0.5424

TABLE 5.8: *Lift and drag coefficients c_l, c_d for meshes of increasing grid density on surface of 2D NACA0012 foil at 4° angle of attack. First- and second-order results with hybrid HLLC/AUSM scheme.* $p_\infty = 10^5\,\mathrm{Pa}$, $U_\infty = 50\ \mathrm{ms}^{-1}$, $\rho_\infty = 998.2\ \mathrm{kgm}^{-3}$, $T_\infty = 293\ \mathrm{K}$.

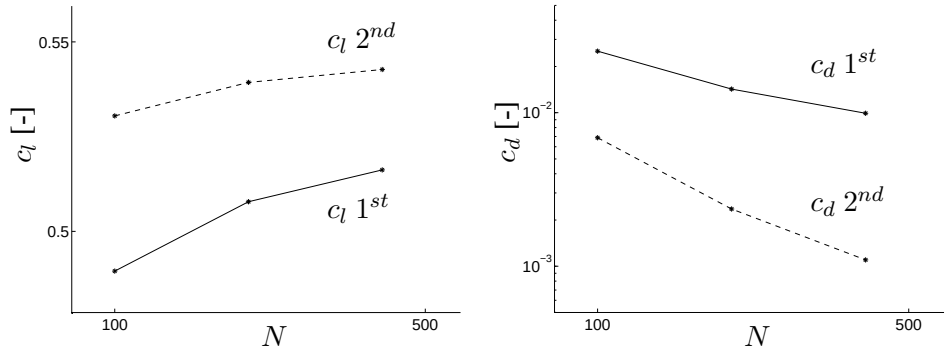

FIGURE 5.14: *Lift coefficient c_l (left) and drag coefficients c_d (right) for 2D NACA0012 foil at 4° angle of attack as a function of the number of points N on the surface of the foil. Presented are results obtained with first- and second-order reconstruction with hybrid HLLC/AUSM flux scheme.* $p_\infty = 10^5\,\mathrm{Pa}$, $U_\infty = 50\ \mathrm{ms}^{-1}$, $\rho_\infty = 998.2\ \mathrm{kgm}^{-3}$, $T_\infty = 293\ \mathrm{K}$.

The absence of viscous forces implies that the resultant drag force or drag coefficient exerted by the flow on the hydrofoil must be equal to zero. As illustrated in table 5.8 and figure 5.14 the calculated drag coefficient is not equal to zero, which is due to the action of numerical dissipation in the numerical method. The value of the drag coefficient c_d thus gives a measure for the global error. For increasing grid density or with second-order spatial reconstruction, this value must decrease. From the rate of decrease with increasing number of grid points on the foil the order of the numerical method can be obtained.

For increasing mesh density the lift and drag coefficients should converge to the grid-independent value. Richardson's extrapolation is employed to obtain the grid-independent value $c(0)$:

$$c(h) = c(0) + Ch^p \tag{5.8}$$

where $h = 1/N$ is a measure for the mesh density, $c(h)$ is the value of the coefficient at the grid with mesh density h, and C and p are constants, which are determined using the first- and second-order results for the lift and drag coefficients for the three meshes. In table 5.9 the values for $c(0)$, C and p are presented for the lift and drag coefficients for the first- and second-order spatial reconstruction.

From tables 5.8 and 5.9 we conclude that the first-order reconstruction method indeed gives results that are close to first-order. Also, we conclude that the second-order reconstruction method produces results that are close to second-order for single-phase water flow, when the drag coefficient is considered.

number of points on foil	first-order		second-order	
	c_d [-]	c_l[-]	c_d[-]	c_l[-]
c(0)	0.0070	0.5230	0.00061	0.5446
C	8.33	-4.88	29.91	-7.82
p	1.33	1.09	1.84	1.36

TABLE 5.9: *Richardson's extrapolation, values for $c_d(0)$,C,$c_l(0)$ and p for first- and second-order results for 2D NACA0012 foil at 4° angle of attack. Results obtained with hybrid HLLC/AUSM scheme. $p_\infty = 10^5\,\mathrm{Pa}$, $U_\infty = 50\ \mathrm{ms}^{-1}$, $\rho_\infty = 998.2\ \mathrm{kgm}^{-3}$, $T_\infty = 293\ \mathrm{K}$.*

Furthermore, we find that the second-order reconstruction method results in a smaller value for the drag coefficient for all meshes compared with the first-order reconstruction scheme. Stated more strongly, we find that the drag coefficient obtained with the second-order reconstruction method on the coarsest mesh is smaller than the drag coefficient obtained with the first-order reconstruction method on the finest mesh. In addition the lift coefficient obtained with the second-order method on the coarsest mesh is higher than the lift coefficient obtained with the first-order method on the finest mesh.

5.5.5 Numerical solutions

In figures 5.15(a) and (b) the first-order solution for the surface distribution of the $-C_p$ coefficient and the Mach number M are presented for the three meshes. The solution for the mesh with 400 points on the surface of the hydrofoil shows a lower value of $-C_p$ at the trailing edge than for the other meshes meaning that the stagnation point at the trailing edge is resolved better. Additionally, the maximum of $-C_p$ on the top surface of the foil is equal to 1.47 and is higher than for the 100 and 200 mesh, which have a maximum value of 1.27 and 1.40, respectively. The solution for the Mach number shows more difference between the solutions on the different meshes. The Mach number in the stagnation point at the trailing edge of the foil for the mesh with 400 points is equal to 0.0165.

In figures 5.15(c) and (d) the solutions using the second-order reconstruction method for the distribution of the $-C_p$ coefficient and the Mach number on the surface of the hydrofoil are presented for the three meshes. The trend of the solutions is comparable to the first-order solution. However, the maximum and minimum values of the solutions are much higher and lower, respectively, than for the first-order solutions. The maximum value of $-C_p$ for the 400 points mesh is now equal to 1.68 compared with 1.66 and 1.62 for the 200 and 100 mesh, respectively. The minimum value of the Mach number in the stagnation point at the trailing edge is equal to 0.0147 for the mesh with 400 points. Note that, the value becomes much lower for a finer mesh.

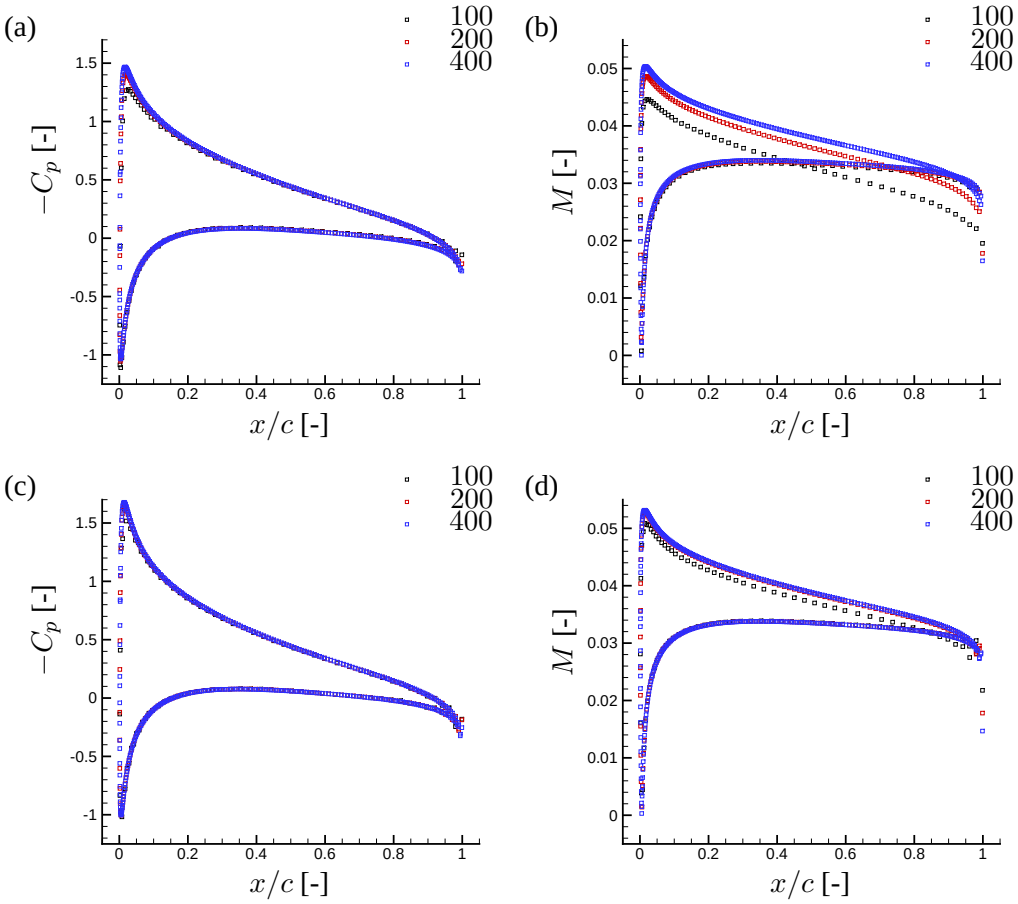

FIGURE 5.15: *Solutions for $-C_p$ coefficient (left) and Mach number M (right) on surface of the 2D NACA0012 foil at 4° angle of attack for meshes with increasing grid-density on the surface of the foil. Results obtained with first- (top) and second-order (bottom) reconstruction with hybrid HLLC/AUSM flux scheme. $p_\infty = 10^5\,\mathrm{Pa}$, $U_\infty = 50\ \mathrm{ms}^{-1}$, $T_\infty = 293$ K. (a) $-C_p$ coefficient first-order (b) Mach number M first-order (c) $-C_p$ coefficient second-order (d) Mach number M second-order.*

Also, note that the value of $-C_p$ at the stagnation point at the nose of the foil becomes much closer to -1 for all three meshes compared with the first-order solutions.

From tables 5.8 and figure 5.15 we conclude that the second-order solution obtained on the mesh with 100 points is of better quality than the first-order solution obtained on the mesh with 400 points. Furthermore, we conclude that the mesh with 200 points in combination with the second-order spatial reconstruction method leads to an already accurate solution on the surface of the hydrofoil. The difference between

the second-order solutions for the pressure coefficient $-C_p$ and the Mach number M obtained on the meshes with 200 and 400 points is relatively small.

In figure 5.16 the second-order solutions for pressure coefficient $-C_p$ and Mach number M are presented for the mesh with 200 points on the surface of the hydrofoil. The maximum value of $-C_p$ is equal to 1.65 and is obtained on the top surface of the foil close to the leading edge. The $-C_p$ values in the stagnation points on the nose and at the trailing edge of the foil are equal to -1.0024 and -0.278, respectively. The maximum value for the Mach number is equal to 0.053 on the top surface of the foil. The Mach number in the stagnation points are equal to 1.4×10^{-3} at the nose and 0.0178 at the trailing edge, respectively.

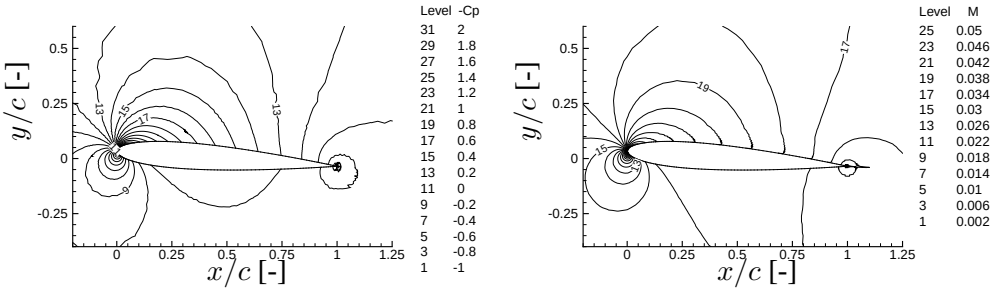

FIGURE 5.16: *Second-order solutions for 2D NACA0012 foil at* $4°$ *angle of attack obtained with hybrid HLLC/AUSM scheme on mesh with 200 points on the surface of the foil.* $p_\infty = 10^5\,\mathrm{Pa}$, $U_\infty = 50\ \mathrm{ms}^{-1}$, $T_\infty = 293$ K. *(left)* $-C_p$ *coefficient (right) Mach number* M.

5.6 Water flow about 2D NACA0015 at $6°$ for $U_\infty = 12\ \mathrm{ms}^{-1}$

In this section the single-phase water flow about a two-dimensional NACA0015 hydrofoil at $6°$ angle of attack is considered for a free-stream velocity $U_\infty = 12\ \mathrm{ms}^{-1}$. Wrobel [221] calculated the inviscid, incompressible flow for this foil applying a central discretization scheme with artificial dissipation. His second-order solution is used as a reference for the solution obtained with the present numerical method.

The chord length of the foil is $c = 0.13\mathrm{m}$. The half-thickness distribution of the foil is given by equation (5.7) where $t = 0.15$. The hydrofoil is located in a channel with height $2c$ and a length of $2c$ upstream of the hydrofoil and $3c$ downstream of the foil. The computational domain is presented in figure 5.17. The flow is from left to right.

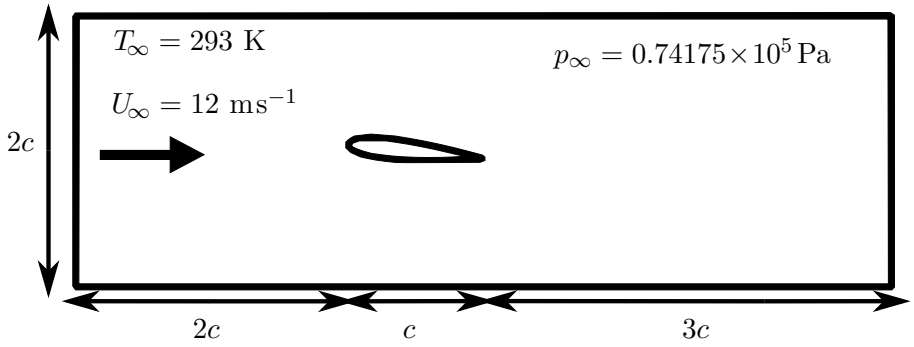

FIGURE 5.17: *Computational domain for 2D NACA0015 hydrofoil at* 6° *angle of attack in a channel.*

The computational domain is divided into triangular and quadrilateral elements as illustrated in figure 5.18, which shows a close-up around the hydrofoil. On the surface of the foil 200 quadrilaterals are positioned as explained in table 5.7. The total number of control volumes is equal to 10k, the number of triangles is equal to 8k and the number of quadrilaterals is equal to 6.5k.

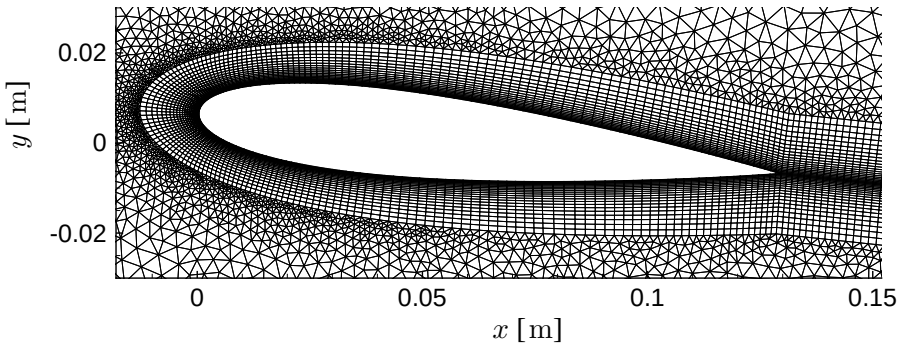

FIGURE 5.18: *Close-up of hybrid quadrilateral/triangular mesh for the 2D NACA0015 hydrofoil at* 6° *angle of attack in a channel. 200 quadrilaterals on the surface of the hydrofoil. Total: 10,419 control volumes, 7,939 triangles, 6,480 quadrilaterals.*

The free-stream velocity is set to $U_\infty = 12$ ms^{-1}, which results in a Mach number equal to $M_\infty = 7.8 \times 10^{-3}$ at a free-stream pressure $p_\infty = 0.74175 \times 10^5$ Pa and free-stream temperature $T_\infty = 293$ K, which yields a free stream density of $\rho_\infty = 998.2$ kgm^{-3}.

The results are obtained with the hybrid HLLC/AUSM flux scheme as presented in section 4.7.2. The first 50k time steps are calculated with the first-order spatial reconstruction method. Then, the calculation is continued with the MUSCL-type second-order reconstruction method applying the limiter of Venkatakrishnan employing the primitive variables $[\rho, u, v, w, e]^T$. For the inflow the non-reflective boundary conditions are applied. For the outflow the asymptotic constant pressure boundary condition with p_∞ is used. The top and bottom of the channel as well as the surface of the hydrofoil are no-slip solid walls. For the surface of the hydrofoil the Curvature-Corrected Symmetry Technique is employed. To accelerate the calculation towards the steady-state solution local time-stepping is employed.

The residuals for ρ and ρu are presented in figure 5.19. During the first 50k iterations, when the first-order reconstruction is employed, the residuals decrease rapidly. When the second-order reconstruction is switched on, the residuals stall at a level of $\mathcal{O}(10^{-4})$ for the density and of order $\mathcal{O}(10^{-3})$ for ρu. It is known that the limiter of Venkatakrishnan stalls the convergence to the steady-state solution. In the present calculation the limiter function switches on and off in the control volume around the trailing edge. To solve this stall in convergence Bramkamp [28] discusses a number of limiters for unstructured grids besides the limiter of Venkatakrishnan. More research is necessary to solve this problem in the future.

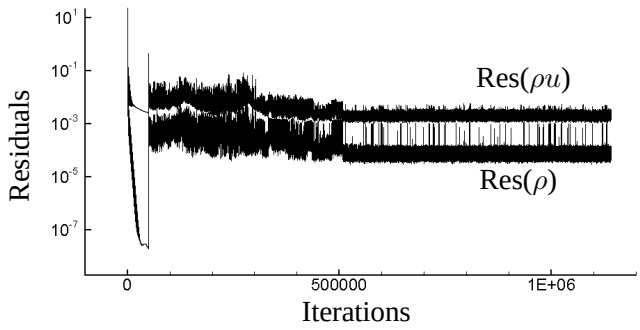

FIGURE 5.19: *Residuals for ρ and ρu as a function of iteration step on 2D NACA0015 hydrofoil at 6° angle of attack.* $p_\infty = 0.74175 \times 10^5\ \mathrm{Pa}$, $U_\infty = 12\ \mathrm{ms}^{-1}$, $\rho_\infty = 998.2\ \mathrm{kgm}^{-3}$, $T_\infty = 293\ \mathrm{K}$.

The lift and drag force are equal to $f_y = 7746\ \mathrm{Nm}^{-1}$ and $f_x = 33\ \mathrm{Nm}^{-1}$, respectively, which is equivalent to $c_l = 0.829$ and $c_d = 0.0035$, respectively. It must be noted that during the calculation the values for the lift and drag force vary up to 1.6% for the lift force and up to 28% for the drag force. This variation is caused due to

the problems with convergence to steady-state described above. The values for the lift and drag force presented above are the average values over the last 600k iterations.

The distribution of the $-C_p$ coefficient and the Mach number M on the surface of the foil are presented in figure 5.20. Note that the maximum values for $-C_p$ on the top surface of the hydrofoil is equal to 2.46 and in the stagnation point at the trailing edge $-C_p = -0.35$. The values for $-C_p$ and M in the point closest to the stagnation point on the nose of the foil are equal to -1.0057 and 1.5×10^{-4}, respectively.

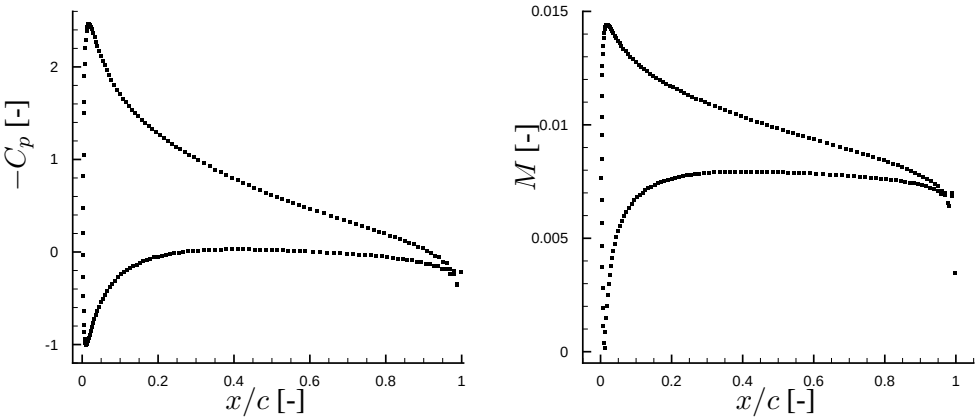

FIGURE 5.20: *Solution on surface of NACA0015 hydrofoil at* 6° *angle of attack in a channel.* $p_\infty = 0.74175 \times 10^5\,\mathrm{Pa}$, $U_\infty = 12\ \mathrm{ms}^{-1}$, $M_\infty = 7.8 \times 10^{-3}$, $\rho_\infty = 998.2\ \mathrm{kgm}^{-3}$, $T_\infty = 293\ \mathrm{K}$,. *Solutions obtained with second-order hybrid HLLC/AUSM flux scheme for* $-C_p$ *coefficient (left) and Mach number* M *(right) for hybrid mesh with 200 points on surface of hydrofoil.*

The small overshoots around the trailing edge of the hydrofoil are due to the treatment of the trailing edge in constructing the median dual mesh by the program Favomesh. The overshoots in the solution for the pressure coefficient C_p and Mach number M become smaller for finer (hybrid) meshes.

The control volume around the trailing edge is badly shaped. A solution to this problem is to split the control volume in an upper and lower control volume on the surface of the hydrofoil. This has been investigated in our group by Hospers [98], who showed that by splitting the control volume around the trailing edge the solution is then allowed to be discontinuous at the trailing edge. Currently, the program Favomesh has been adapted by H. de Vries to automate the splitting of the control volume around the trailing edge.

Compared with the results for the 2D NACA0012 at 4° angle of attack obtained in section 5.5 the overshoot is larger, because the 2D NACA0015 hydrofoil is placed at an higher angle of attack. Furthermore, the free-stream velocity in this section is equal to $U_\infty = 12\ \mathrm{ms}^{-1}$, whereas a free-stream velocity of $U_\infty = 50\ \mathrm{ms}^{-1}$ was chosen in the previous section. At lower free-stream velocities the numerical flux schemes are more sensitive to irregularities in the grid due to the low numerical dissipation.

Wrobel [221] reports lift and drag forces equal to $f_y = 7602\ \mathrm{Nm}^{-1}$ and $f_x = 30.7\ \mathrm{Nm}^{-1}$, respectively, which amount to $c_l = 0.813$ and $c_d = 0.0032$ in his calculation. His maximum $-C_p$ value on the top surface of the foil and in the stagnation point at the trailing edge are approximately equal to 2.5 and -0.25, respectively. Comparing the results of the present numerical method with the results of Wrobel, we conclude that the solution on the foil is accurately solved for with the present density-based numerical method on a hybrid quadrilateral/triangular mesh.

5.7 Single-phase water flow over 3D Twist11 hydrofoil

Foeth [67] has carried out experiments on a three-dimensional wall-to-wall twisted hydrofoil placed in a cavitation tunnel. The main objective of this section is to validate the numerical method utilizing the experimental data for single-phase water flow. Here, the interest is in the steady-state solution for uniform inflow conditions. The cavitating flow about the 3D Twist11 hydrofoil will be considered in section 6.4.

5.7.1 Geometry of 3D Twist11 hydrofoil

The hydrofoil is denoted by TwistXX hydrofoil, because of its varying geometric angle of attack from 0° at the tunnel walls to XX$^\circ$ angle of attack at mid-section, see Dang [51], Koop *et al*. [113] and Foeth [67]. The chord length of the foil is equal to $c = 0.15\mathrm{m}$. The foil spans the cavitation tunnel from wall to wall and it is symmetric with respect to its mid-span plane.

The hydrofoil has a spanwise varying distribution of the local geometric angle of attack $\alpha(\bar{y})$ to avoid interaction of the cavitation sheet with the tunnel wall. The local angle of attack $\alpha(\bar{y})$ is defined by a cubic polynomial, such that it is α_{wall} degrees at the tunnel wall, α_{max} degrees at mid-span and that its derivative in spanwise direction is zero at the wall as well as at mid-span:

$$\alpha(\bar{y}) = \alpha_{max}\left(2|\bar{y}|^3 - 3\bar{y}^2 + 1\right) + \alpha_{wall}, \tag{5.9}$$

where $\bar{y} = y/c$ is the dimensionless coordinate in span-wise direction $\bar{y} = [-1, 1]$, with $\bar{y} = 0$ is defined to be at the mid-plane of the span and $\bar{y} = 1$ at the tunnel wall at the starboard side. Note that α_{wall} is the rotation angle of the entire hydrofoil and is always equal to the local angle of attack at the tunnel wall.

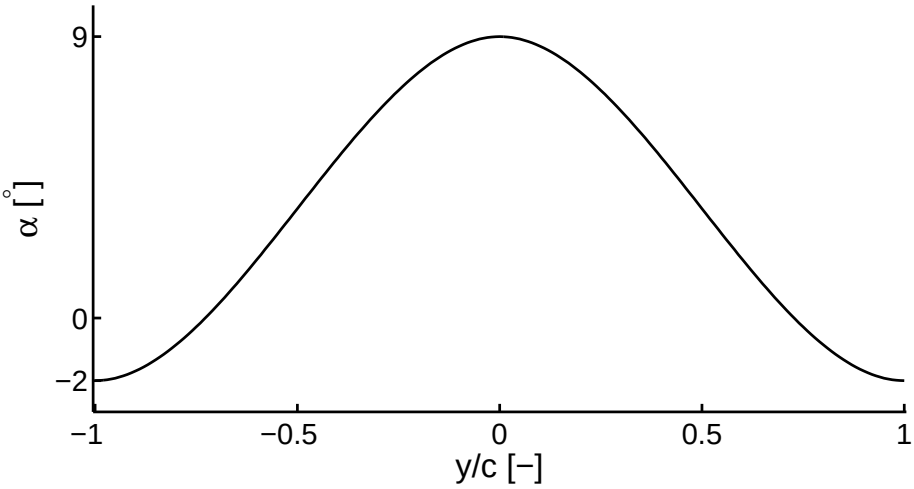

FIGURE 5.21: *Span-wise distribution of geometric angle of attack of Twist11 hydrofoil at* -2° *angle of attack.*

The sections of the hydrofoil rotate around $\bar{x} = x/c = 0.75$ to reduce the optical blocking of the mid-section plane by the hydrofoil when viewing from the sides of the foil, which is illustrated in figure 5.22(c), where the side view of the foil is presented.

The foil under consideration is the Twist11 at -2° angle of attack, yielding $\alpha_{max} = 11^\circ$ and $\alpha_{wall} = -2^\circ$ in equation (5.9). The size of the foil is $0.15\mathrm{m}$ in chord wise and $0.3\mathrm{m}$ in span-wise direction. The hydrofoil has a NACA0009 section with its half-thickness distribution given by equation (5.7) with $t = 0.09$. The hydrofoil is presented in figure 5.22, where a 3D view, top view, side view and front view are shown.

5.7.2 Experimental data

Foeth [66] measured the forces and moments exerted by the flow on the foil as well as local pressures on the surface of the hydrofoil. For the local pressure measurements 20 transducers were fitted in the foil at locations as presented in figure 5.23 and table 5.10, see for more details the thesis of Foeth [67].

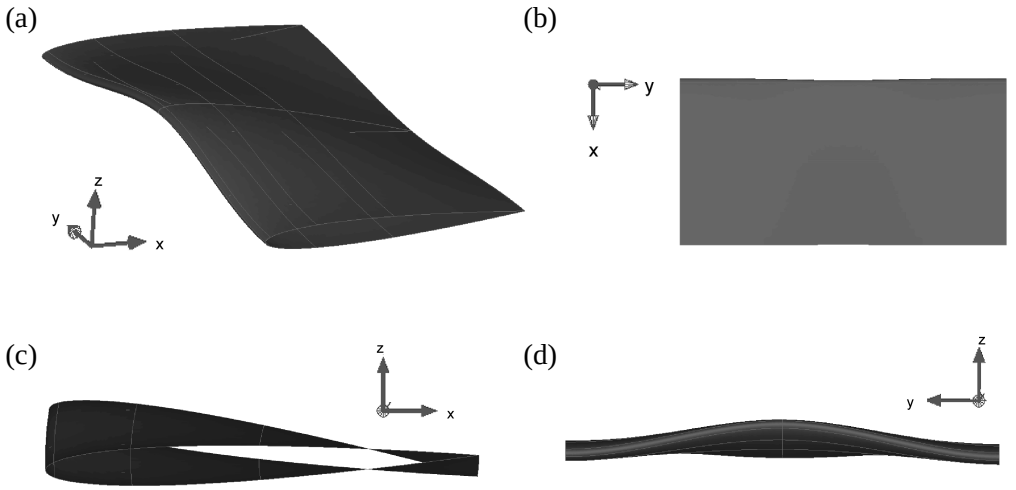

FIGURE 5.22: *3D Twist11 hydrofoil at -2° angle of attack, flow is in x-direction. (a) 3D view (b) top view (c) side view (d) front view.*

sensor	x/c	y/s	sensor	x/c	y/s	sensor	x/c	y/s
1	0.40	0.40	8	0.05	0.50	15	0.50	0.40
2	0.75	0.50	9	0.025	0.50	16	0.05	0.30
3	0.50	0.50	10	0.05	0.40	17	0.10	0.30
4	0.40	0.50	11	0.10	0.40	18	0.20	0.30
5	0.30	0.50	12	0.20	0.40	19	0.05	0.20
6	0.20	0.50	13	0.30	0.40	20	0.05	0.10
7	0.10	0.50	14	0.40	0.40			

TABLE 5.10: *Locations of the pressure transducers on the Twist11 hydrofoil in percent of chord and (full-)span position. All sensors are placed on the suction side, except sensor 1, which is placed on the pressure side.*

Foeth carried out single-phase flow experiments for three angles of attack, i.e. -1°, -2° and -3°. Here, the angle of attack of -2° is considered, because for this incidence cavitating flow experiments were conducted as well [66, 67]. Furthermore, for each angle of attack the pressures and forces were measured at various flow velocities. Here, the results for $U_\infty = 6.75\ \mathrm{ms}^{-1}$, $T_\infty = 297\ \mathrm{K}$ and $p_\infty = 0.97\times10^5\,\mathrm{Pa}$ are considered. For these flow conditions Foeth [66] reports a lift force of $455\mathrm{N}$, which amounts to a lift coefficient $C_L = 0.46$. There are no experimental results available for the drag force. The measurements for the local $-C_p$ values on the surface of the foil are presented in figure 5.27 together with the numerical results.

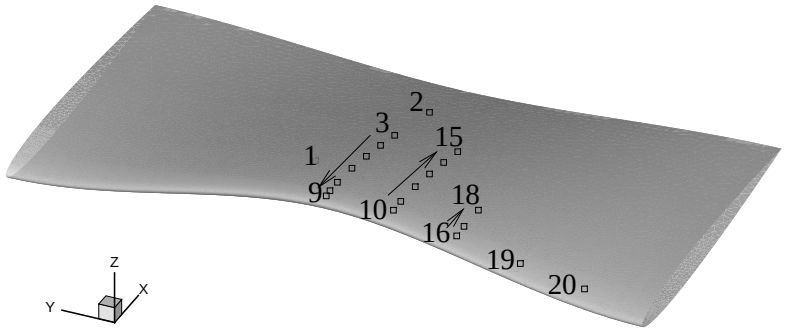

FIGURE 5.23: *Locations of the pressure sensors on 3D Twist11 hydrofoil at -2° angle of attack, flow is in x-direction. All sensors are placed on the suction side, except sensor 1, which is placed on the pressure side.*

5.7.3 Computational domain and mesh

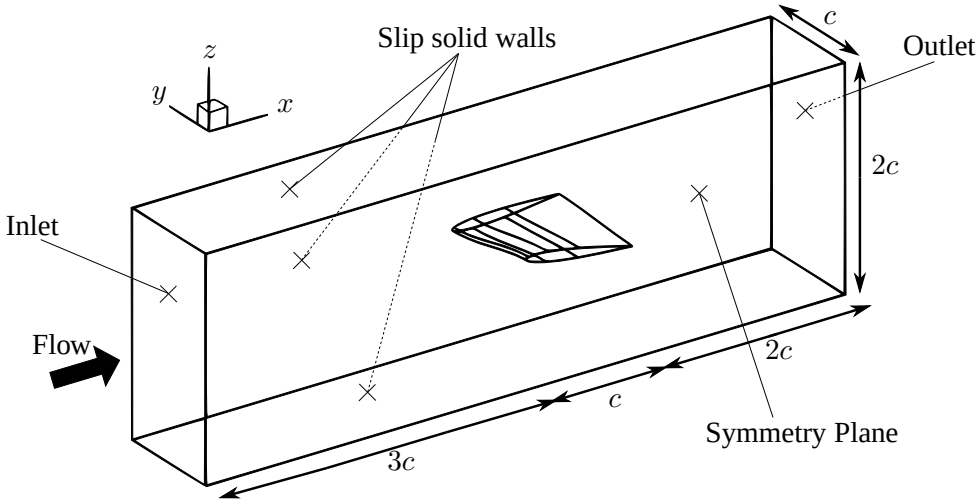

FIGURE 5.24: *Computational domain for 3D Twist11 hydrofoil at -2° angle of attack. The back side, top and bottom of the channel are slip solid walls, the front side is a symmetry plane, the left and right side are the in- and outflow. The surfaces of the foil are solid slip walls. Note that the flow is from left to right.*

For numerical purposes the length of the test section is increased to minimize the effects of the implementation of the inlet and outlet boundary conditions. The hydrofoil is located in a channel with height $2c$, a length of $3c$ upstream of the leading

edge, a length of $2c$ downstream of the trailing edge and a width of $s = c$. Note that for the numerical flow simulation only the starboard half of the test section and the foil is considered, because of its geometric symmetry and the assumed hydrodynamic symmetry.

The computational domain is divided into tetrahedral elements utilizing the software package ICEM-CFD. The surface of the foil is divided in 7 sub-surfaces, i.e. one surface wrapping around the leading edge and three surfaces on either side of the foil. Each surface has its own size of surface elements (ratio 1:4:6:8) to ensure a fine mesh around the nose of the foil and a somewhat coarser mesh on the surfaces closer to the trailing edge. Note that the tetrahedrons close to the foil are much smaller than the tetrahedrons further away in the flow field. The elements on the trailing edge are refined to reduce the effects of the badly-shaped control volumes around the trailing edge as explained in section 5.6.

Following a limited grid sensitivity study [113] it was concluded that for single-phase water flow a total number of around 350k tetrahedrons is adequate for a sufficiently accurate solution on the surface of the foil, which results in approximately 70k control volumes in the complete computational domain. This mesh is presented in figure 5.25. For cavitating flow a tetrahedral grid with a refinement along the suction side of the hydrofoil is considered. In this section that grid is referred to as the fine grid.

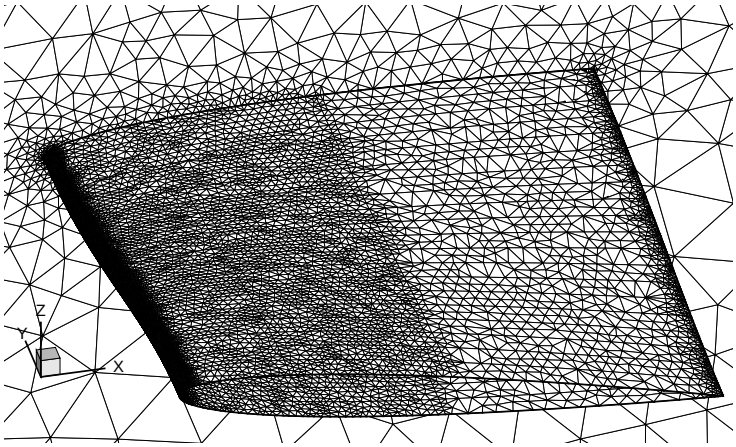

FIGURE 5.25: *Tetrahedral mesh for 3D Twist11 hydrofoil at -2° angle of attack. Presented are the surface meshes on the hydrofoil and tunnel side wall. Total: 356,638 tetrahedrons, 69,365 control volumes. Flow is from left to right.*

5.7.4 Numerical method and flow conditions

The numerical results are obtained with the hybrid HLLC/AUSM flux scheme as presented in section 4.7.2. The first 50k iteration steps are calculated with the first-order spatial reconstruction method. Then, the calculation is continued with the MUSCL-type second-order reconstruction method applying the limiter method of Venkatakrishnan employing the primitive variables $[\rho, u, v, w, e]^T$. For the inflow the non-reflective boundary conditions are applied. For the outflow the asymptotic constant pressure p_∞ boundary condition is used. The top and bottom of the channel are slip solid walls as well as the surface of the hydrofoil. The solid wall boundary conditions for the hydrofoil are calculated with the Curvature-Corrected Symmetry technique. To accelerate the calculation towards the steady-state solution local time-stepping is applied.

For single-phase flow the temperature is chosen equal to $T_\infty = 297$ K and the asymptotic outlet pressure is set to $p_\infty = 0.97 \times 10^5$ Pa, which yields a free stream density $\rho_\infty = 998.3\ \mathrm{kgm}^{-3}$. Corresponding to the experimental setup described in section 5.7.2 a free stream velocity $U_\infty = 6.75\ \mathrm{ms}^{-1}$ is chosen yielding a free stream Mach number $M_\infty = 0.0044$. These results are compared with results of a calculation at free stream velocity $U_\infty = 50\ \mathrm{ms}^{-1}$, $M_\infty = 0.0325$ with the same free-stream pressure p_∞ and temperature T_∞.

5.7.5 Convergence

The residuals for ρ and ρu are presented in figure 5.26 for $U_\infty = 6.75\ \mathrm{ms}^{-1}$ and $U_\infty = 50\ \mathrm{ms}^{-1}$, respectively. During the first 50k iterations, when the first-order reconstruction is employed, the residuals decrease rapidly. When the second-order reconstruction is switched on the residuals stall at a level of $\mathcal{O}(10^{-3})$ for the density and of order $\mathcal{O}(10^{-2})$ for ρu for $U_\infty = 50\ \mathrm{ms}^{-1}$. As mentioned in section 5.6 for the 2D calculation, it is known that the limiter of Venkatakrishnan stalls the convergence to the steady-state solution.

5.7.6 Numerical results for lift and drag forces

In table 5.11 the values of the lift and drag coefficients are presented for the free-stream velocity $U_\infty = 6.75\ \mathrm{ms}^{-1}$ on both grids and for $U_\infty = 50\ \mathrm{ms}^{-1}$ on the coarse grid. Note that only the star-board half of the hydrofoil has been calculated, so the calculated forces are multiplied by two to compare with the experimentally obtained forces. The reference surface S in equation (2.10) of the hydrofoil is equal to $2c^2$. Due to the problems with convergence the lift and drag force vary for $U_\infty = 6.75\ \mathrm{ms}^{-1}$ up to 1.9% and 20.4% for the lift and drag force, respectively. For $U_\infty = 50\ \mathrm{ms}^{-1}$ they vary up to 0.4% and 2.8%, respectively. The presented values for the lift and drag coefficients are the average values over the last 50k iterations.

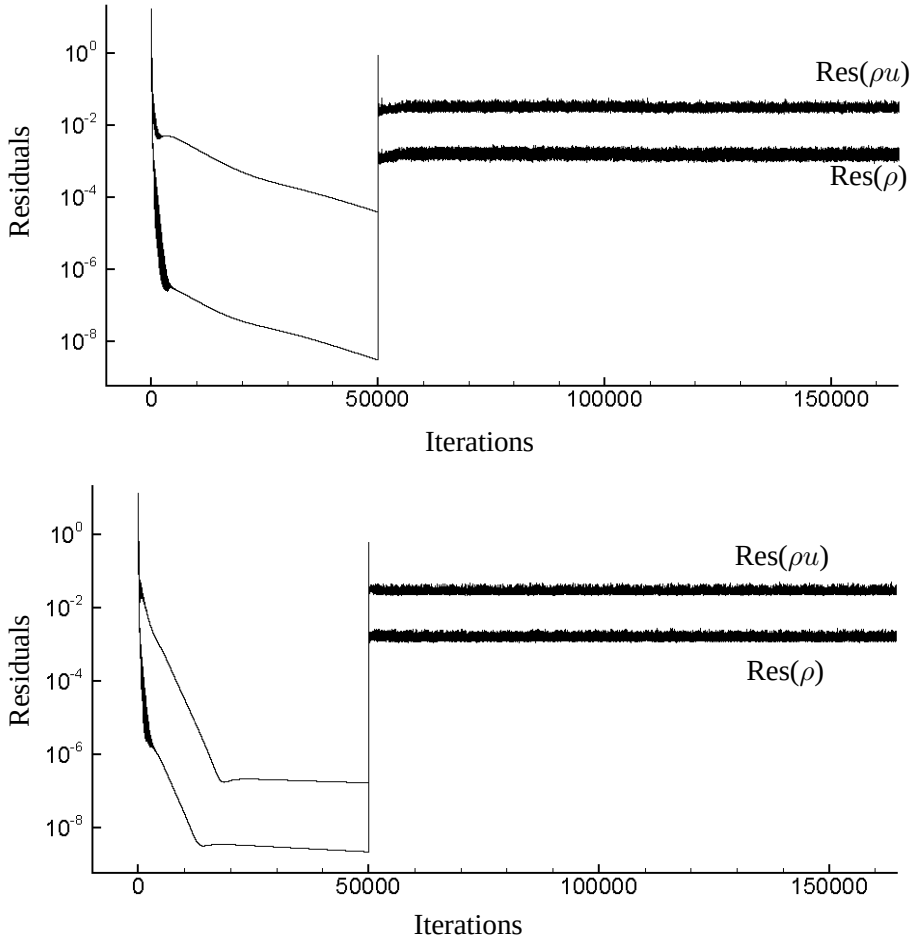

FIGURE 5.26: *Residuals for ρ and ρu as a function of iteration step on 3D Twist11 hydrofoil at $-2°$ angle of attack.* $p_\infty = 0.97\times10^5\,\mathrm{Pa}$, $\rho_\infty = 998.2\ \mathrm{kgm}^{-3}$, $T_\infty = 297$ K. *Top:* $U_\infty = 6.75\ \mathrm{ms}^{-1}$ *Bottom:* $U_\infty = 50\ \mathrm{ms}^{-1}$.

U_∞ $[\mathrm{ms}^{-1}]$	mesh	numerical C_D [-]	numerical C_L [-]	experimental C_L [-]
6.75	coarse	0.010	0.442	0.46
6.75	fine	0.0083	0.445	0.46
50	coarse	0.0098	0.454	-

TABLE 5.11: *3D Twist11 hydrofoil at $-2°$ angle of attack. Lift and drag coefficients C_L, C_D for velocities $U_\infty = 6.75\ \mathrm{ms}^{-1}$ on coarse and fine grid and $U_\infty = 50\ \mathrm{ms}^{-1}$ on coarse grid. Added are the experimentally obtained values for the lift coefficient.* $p_\infty = 0.97\times10^5\,\mathrm{Pa}$, $\rho_\infty = 998.3\ \mathrm{kgm}^{-3}$, $T_\infty = 297$ K.

The lift force for $U_\infty = 6.75\ \mathrm{ms}^{-1}$ is calculated to be equal to $451.8\mathrm{N}$. Note that this value correspond to within 1% with the measured value $455\mathrm{N}$ for $U_\infty = 6.75\ \mathrm{ms}^{-1}$. Furthermore, the experimentally obtained lift coefficient $C_L = 0.46$ is sufficient† accurately predicted by the present numerical method. From this we conclude that the calculated lift force corresponds satisfactory with the measured value for single-phase water flow at this low Mach number and angle of attack for which flow separation does not occur.

The calculated lift coefficient on the coarse and fine mesh are approximately equal to each other, which verifies that the coarse grid is adequate for a sufficiently accurate solution on the surface of the hydrofoil for single phase flow.

For inviscid flow at low Mach number the lift coefficient C_L for the velocities $U_\infty = 6.75\ \mathrm{ms}^{-1}$ and $U_\infty = 50\ \mathrm{ms}^{-1}$ should be about equal to each other. In table 5.11 is presented that the lift coefficient slightly differs for both free-stream velocities. The value for $U_\infty = 50\ \mathrm{ms}^{-1}$ is closer to the experimental value than for $U_\infty = 6.75\ \mathrm{ms}^{-1}$.

For this three-dimensional inviscid flow case the drag force will not be zero. The wake downstream of the trailing edge contains vorticity stemming from the difference in direction of the velocity over the suction side and the flow over the pressure side. At the trailing edge these two flows meet and generate a trailing vortex sheet. This trailing vorticity induces an upwash/downwash distribution at the foil which increases/reduces the local angle of attack experienced by the foil. This results in the so-called induced drag. In [113] we have investigated the up- and downwash on the foil by employing Prandtl's lifting-line theory, which is included in appendix D. In section 5.7.8 a visualization of the trailing vorticity is presented.

From the good agreement between the experimentally obtained lift force and the calculated value and the agreement between the calculated lift coefficients for both velocities, we conclude that the present numerical method is capable of accurately predicting the lift force on the foil for low speed 3D single-phase water flow.

5.7.7 Comparison with experimental pressure data

Foeth's experimentally obtained $-C_p$ values at the surface of the hydrofoil at the locations indicated in figure 5.23 are compared with the numerical results. The experimental values are grouped together for the same span positions, i.e. 50%, 40%,

†Foeth [66] mentions that his calibration was verified for each angle of attack by placing weights on the hydrofoil in an empty cavitation tunnel. A deviation of 3% from the calibrated value was found and Foeth applied a correction for this discrepancy.

30%, and 20% of the span. These values are denoted by the open squares in figure 5.27. At the same span positions slices are made through the numerical solution at the surface of the hydrofoil. These are presented with the closed circles in figure 5.27.

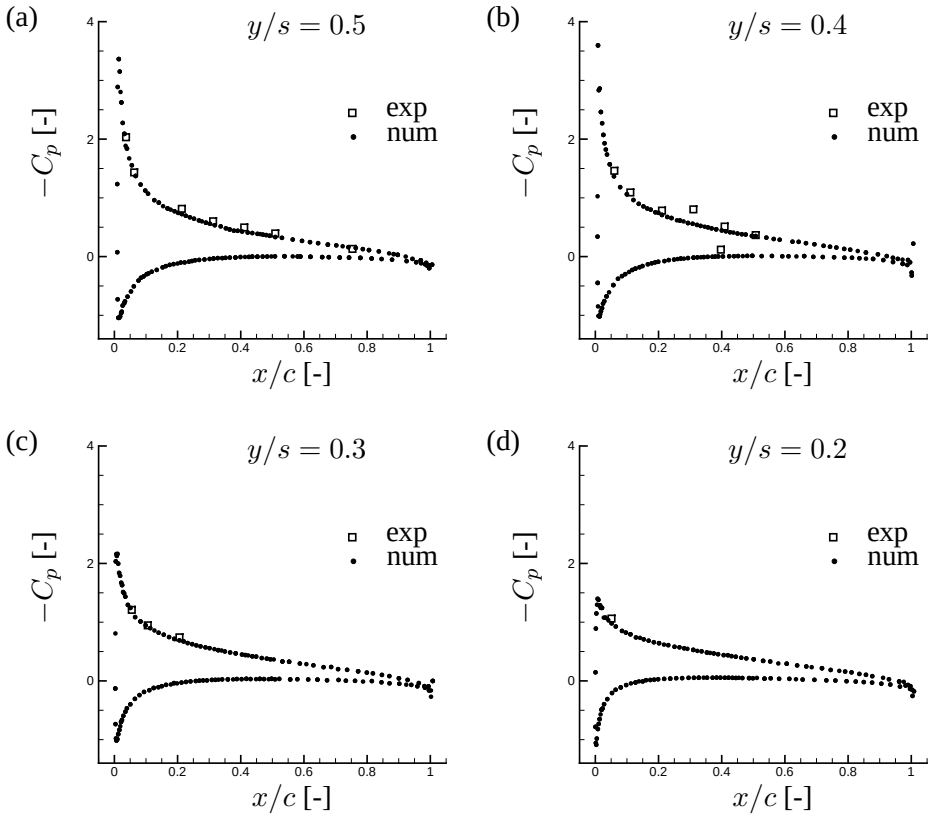

FIGURE 5.27: *3D Twist11 hydrofoil at -2° angle of attack. Experimental (open squares) and numerical (solid circles) distribution of the $-C_p$ coefficient for $U_\infty = 50\ \mathrm{ms}^{-1}$, $T_\infty = 297\ \mathrm{K}$, $p_\infty = 0.97\times10^5\,\mathrm{Pa}$, $\rho_\infty = 998.2\ \mathrm{kgm}^{-3}$. (a) $y/s = 0.5$, (b) $y/s = 0.4$, (c) $y/s = 0.3$, (d) $y/s = 0.2$.*

As can be seen in figure 5.27 the numerical results correspond reasonably well with the experimental data. However, the experimental value at $x/c = 0.3$ at 40% span appears to deviate from the numerical results. Foeth [66] mentions that the value from this pressure sensor is not trustworthy.

Furthermore, as can be seen in figure 5.27, an overshoot in $-C_p$ value at the trailing

edge is observed in the numerical results. This is caused by the relatively bad-shaped control volume around the trailing edge for a node-centered dual mesh. As explained in section 5.6 a possible solution is to split the control volumes around the trailing edge into an upper and lower control volume allowing a discontinuous solution at the trailing edge. Currently, within our group H. de Vries has adapted the program Favomesh to automate the splitting of the control volumes around the trailing edge. When the mesh is refined around the trailing edge, this overshoot reduces.

From figure 5.27 we conclude that the solution for the pressure on the surface of the 3D Twist11 hydrofoil at -2° angle of attack can be calculated accurately for single-phase water flow at low-Mach number.

5.7.8 Numerical results for flow solution

In figure 5.28 the distribution of $-C_p$ coefficient on the surface of the hydrofoil is presented for fully wetted water flow with $U_\infty = 50\ \mathrm{ms}^{-1}$. In the center on the suction side of the hydrofoil a clear low pressure region is visible. The design of the foil has been such that cavitation occurs in the center of the foil and that cavitation is avoided near the tunnel walls. Due to the span-wise varying angle of attack the pressure near the tunnel walls of the cavitation tunnel is much higher resulting in a lower $-C_p$ value.

To illustrate the generated vorticity in the wake of the hydrofoil an iso-contour of the x-component of the vorticity, i.e. $|\omega_x| / (U_\infty/c) = 0.4$, is presented in figure 5.29. The vortical wake of the hydrofoil is generated due to the difference in the direction of the velocity over the suction side and pressure side of the hydrofoil. At the trailing edge these two flows meet and generate a trailing vortex sheet. The vortex sheet rolls up further downstream in the domain into two regions of vorticity with their centers located at $\bar{y} = y/c = -0.5$ and $\bar{y} = y/c = 0.5$, respectively. Unfortunately, the mesh is too coarse further away from the hydrofoil to be able to resolve the roll-up of the vortex sheet more accurately.

This trailing vorticity induces an upwash/downwash at the foil, which increases/reduces the local angle of attack experienced by the foil. In the center of the foil a downwash is experienced by the foil, which reduces the occurrence of cavitation due to the lower effective angle of attack. At the tunnel walls the hydrofoil experiences an upwash, causing a higher effective angle of attack which induces an earlier onset of cavitation than expected by considering the negative local angle of attack at the tunnel walls.

In [113] we investigated the up- and downwash on the Twist08, Twist11 and Twist14 hydrofoils due to the vortical wake by means of Prandtl's classical lifting line theory.

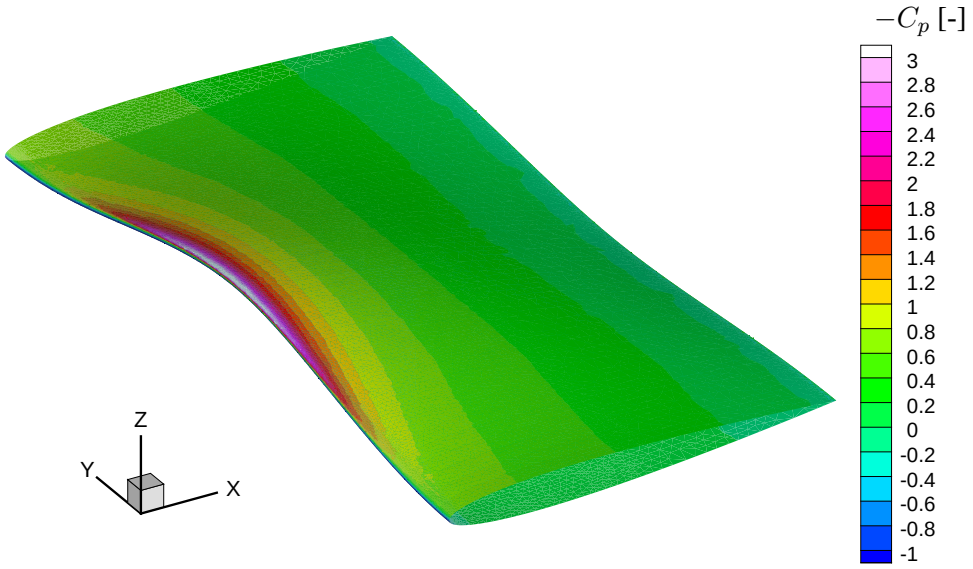

FIGURE 5.28: *3D Twist11 hydrofoil at -2° angle of attack. Distribution of $-C_p$ coefficient on surface of hydrofoil. Second-order hybrid HLLC/AUSM flux scheme on tetrahedral mesh.* $U_\infty = 50\ \mathrm{ms}^{-1}$, $T_\infty = 297\ \mathrm{K}$, $p_\infty = 0.97 \times 10^5\,\mathrm{Pa}$, $\rho_\infty = 998.2\ \mathrm{kgm}^{-3}$.

The lifting line theory for the Twist hydrofoil is included in appendix D. From this theory an estimate for the effective angle of attack of the 3D Twist11 hydrofoil is obtained. From the numerical results presented in figure 5.28 the calculated effective angle of attack at various locations y_0 along the span of the foil is obtained through

$$\alpha_{eff}(y_0) = \frac{c_l(y_0)}{2\pi}, \tag{5.10}$$

where $c_l(y_0)$ follows from

$$c_l(y_0) = -\int_0^1 \left\{ C_p^U\left(\frac{x}{c(y_0)}, y_0\right) - C_p^L\left(\frac{x}{c(y_0)}, y_0\right)\right\} \mathrm{d}\left(\frac{x}{c(y_0)}\right), \tag{5.11}$$

with $C_p^{U,L}$ the C_p distribution along the upper and lower side of the section located at spanwise locations y_0.

In figure 5.30 the estimated effective angle of attack $\alpha_{eff,PLL}$ obtained from Prandtl's lifting line theory, the calculated effective angle of attack $\alpha_{eff,num}$ obtained from the Euler calculations presented in figure 5.28 and the local geometric angle of attack α_{geom} are presented for the 3D Twist11 hydrofoil at -2° angle of attack. As illustrated in figure 5.30 both the estimated and calculated effective angle of attack are

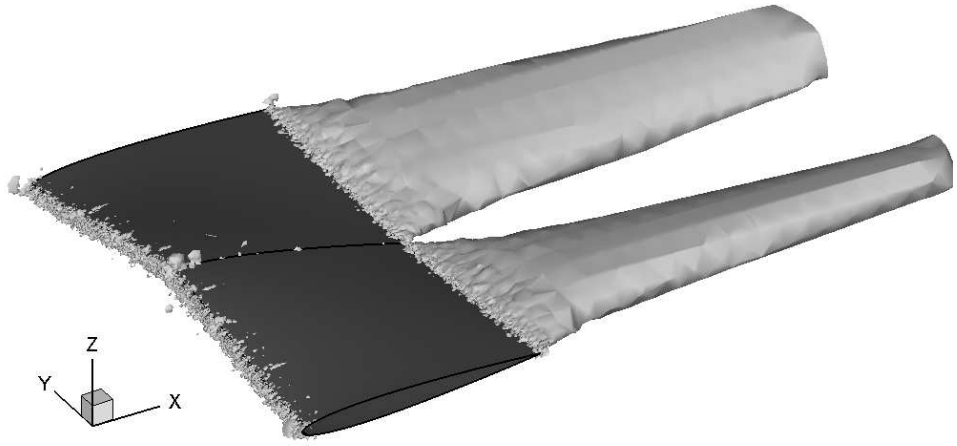

FIGURE 5.29: *3D Twist11 hydrofoil at $-2°$ angle of attack. Iso-contour of the x-component of vorticity $|\omega_x|/(U_\infty/c) = 0.4$. Second-order hybrid HLLC/AUSM flux scheme on tetrahedral mesh. $U_\infty = 50\ \mathrm{ms}^{-1}$, $T_\infty = 297$ K, $p_\infty = 0.97\times10^5\,\mathrm{Pa}$, $\rho_\infty = 998.2\ \mathrm{kgm}^{-3}$.*

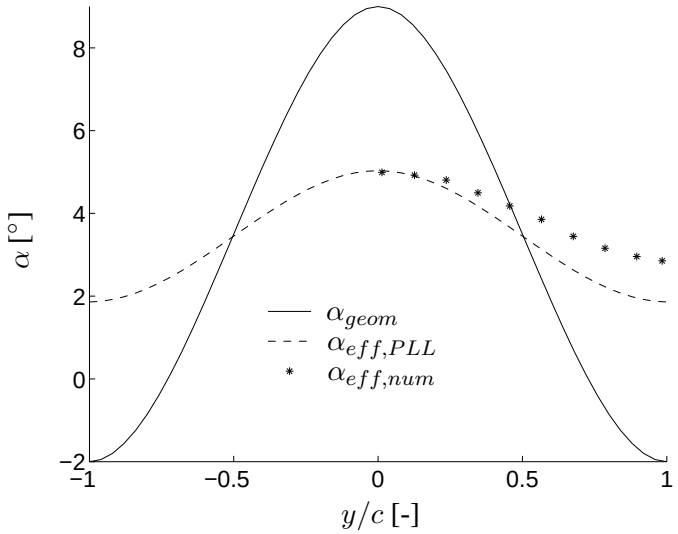

FIGURE 5.30: *Twist11 hydrofoil at $-2°$ angle of attack. Geometric angle of attack α_{geom} (solid line), the effective angle of attack as predicted from Prandtl's lifting line theory $\alpha_{eff,PLL}$ (dashed line) and the effective angle of attack as predicted from the Euler calculations $\alpha_{eff,num}$ (stars).*

higher than the local geometric angle of attack at the tunnel walls and lower at the mid-span plane. Thus, the vortical wake of the hydrofoil generates upwash at the tunnel walls and downwash at mid-section of the foil.

The downwash at mid-span derived from the Euler equations agrees quite well with the values found from Prandtl‘s lifting line theory. The upwash, which occurs near the tunnel walls, is higher in the Euler results compared to the result from lifting line theory. This might be due to the neglect in Prandtl's lifting line theory of the roll-up of the vortical wake, which is present in the solution obtained from the Euler equations. The center of vorticity will remain the same, see Hoeijmakers [94]. The roll-up effects the upwash apparently more near the wall than the downwash near the center of the foil. This needs to be explored further. Furthermore, we conclude that for fully wetted flow Prandtl's lifting line theory can be used in deriving a potentially interesting Twist distribution that subsequently can be explored further using the Euler method, see Koop *et al*. [113] and appendix D.

5.8 Conclusions on single-phase flow calculations

In this chapter the single-phase flow of water has been considered for 1D, 2D and 3D flow problems. It is judged essential to accurately calculate single phase water flow to be able to calculate cavitating flow correctly. In this chapter we have shown that the present numerical method is able to:

- accurately predict time-accurate wave and shock dynamics in liquid flow problems such as the "Water Hammer" problem and the Riemann problem for liquid flow;
- accurately calculate steady-state low-Mach number liquid flow, without the use of preconditioning methods, by employing a hybrid HLLC/AUSM flux scheme such as developed by Schmidt *et al*. [169, 170, 172];
- accurately calculate the steady-state water flow about two-dimensional hydrofoils;
- accurately predict the lift coefficient for the 3D Twist11 hydrofoil at -2° angle of attack for single-phase liquid flow under uniform inflow conditions;
- accurately predict the pressure coefficient C_p on the surface of the 3D Twist hydrofoil at -2° angle of attack compared to experimentally obtained local pressure data.

Furthermore, we conclude that the numerical method employing the MUSCL-type reconstruction method and the limiter of Venkatakrishnan is close to second-order

accuracy for the single phase water flow about two-dimensional hydrofoils.

The development and implementation of non-reflective boundary conditions for compressible water flow allow shock and expansion waves to leave the computational domain without reflection back into the domain. This is important for unsteady flow calculations. Furthermore, although not shown in detail in this chapter, the non-reflective boundary conditions improve the convergence to the steady-state solution because traveling shock and expansion waves are allowed to leave the computational domain without reflections.

The development and implementation of the Curvature-Corrected Symmetry Technique for the slip solid walls of the object in the flow improves the numerical solution near the surfaces of objects in the flow.

The results for steady-state low-Mach number flow have been improved by the hybrid HLLC/AUSM flux scheme as developed by Schmidt *et al*. [169]. Following discussions with Schmidt and Prof. Schnerr of the TU Munich we have implemented their formulation into the present edge-based numerical method for unstructured grids. For the hybrid flux scheme we have reduced the Mach number even further than presented. However, for $U_\infty \leq 1.0 \ \mathrm{ms}^{-1}$, which corresponds to a Mach number $M = 6.5 \times 10^{-4}$ the solution starts to develop irregularities in the pressure and velocity on the surface of the cylinder. Schmidt *et al*. [170] succeeded in obtaining a solution for Mach numbers as low as 10^{-4}.

Furthermore, we conclude that the badly-shaped control volumes around the trailing edge have a negative effect on the numerical solutions about hydrofoils. The pressure near the trailing edge of the hydrofoil experiences small under- and overshoots. Refining the grids near the trailing edge improves the numerical results. At present, within our group H. de Vries has adapted the pre-processing mesh program Favomesh to automate the splitting of the control volumes at the trailing edge into an upper and lower control volume on the surface of the hydrofoil.

Lastly, we have found that the limiter method of Venkatakrishnan sometimes stalls the convergence to the steady-state solution. A possible solution might be to implement one of the limiting methods described in the thesis of Bramkamp [28]. For unsteady flow calculations the limiter of Venkatakrishnan works satisfactory, under- and overshoots are not observed at sharp gradients or discontinuities in the flow.

NUMERICAL RESULTS CAVITATING FLOW

CHAPTER 6

In this chapter results of numerical simulations for cavitating flows are presented. The equilibrium cavitation model as presented in section 3.4 is applied to simulate the occurrence of cavitation. The two-phase flow regime is described as a homogeneous mixture in which the vapor and liquid components of the two-phase mixture remain in thermodynamic and mechanical equilibrium.

In section 6.2 one-dimensional test cases are considered to assess the convergence and stability of the numerical method for cavitating flow. First, the so-called "Closing Valve problem" of Berg *et al*. [22] is discussed. Then, the 1D test case of Saurel *et al*. [166] is presented, which illustrates the occurrence of cavitation by enforcing a left- and right-running expansion wave.

In section 6.3 the test case of Sauer [162] is presented, i.e. the cavitating flow about a 2D NACA 0015 section at 6° angle of attack at free stream velocity of $U_\infty = 12$ ms^{-1} and cavitation number $\sigma = 1.0$. Also, the cavitating flow at a different free-stream velocity of $U_\infty = 50$ ms^{-1}, but identical cavitation number $\sigma = 1.0$, is considered to investigate that flows with the same cavitation number result in the same cavitating flow characteristics.

In section 6.4 the cavitating flow about the 3D Twist11 hydrofoil at -2° angle of attack is simulated at the same cavitation number $\sigma = 1.1$ as in the experiments of Foeth [67]. The development of the re-entrant flow is presented and the formation of a cavitating horse-shoe vortex is investigated.

Lastly, in section 6.5 the steady-state cavitating flow about the 3D Elliptic 11 Rake hydrofoil is calculated, at the same cavitation number $\sigma = 0.68$ as in the experiments of Van der Hout [204], to show that the present edge-based numerical method is capable of predicting the cavitation pattern occurring in the flow about a complex geometry.

In table 6.1 the test cases for the two-dimensional and three-dimensional cavitating flow are summarized.

Foil	α [°]	U_∞ [ms^{-1}]	σ [-]	mesh
2D NACA0015	6.0	12, 50	1.0	hybrid quadrilateral/triangular
3D Twist11	-2.0	50	1.1	tetrahedral
3D Elliptic 11 Rake	3	50	0.68	tetrahedral

TABLE 6.1: *Test cases for 2D and 3D cavitating flow.*

6.1 Dimensionless total vapor volume

The dimensionless total vapor volume is calculated differently for the 1D, 2D and 3D test cases. For 1D flow the dimensionless total vapor volume $V_{vap,1D}$ is the total vapor volume divided by the volume of the computational domain V_{CD}:

$$V_{vap,1D} = \frac{1}{V_{CD}} \sum_{i=1}^{N} \alpha_i V_i, \tag{6.1}$$

where N is the total number of control volumes and where the void fraction α follows from equation (2.2) with the volume V of the fluid taken equal to the volume V_{cv} of the control volume. For flows about 2D hydrofoils the dimensionless total vapor volume $V_{vap,2D}$ is defined as

$$V_{vap,2D} = \frac{1}{c^2} \sum_{i=1}^{N} \alpha_i V_i, \tag{6.2}$$

where c is the chord length of the hydrofoil. For flows about 3D hydrofoils the dimensionless total vapor volume $V_{vap,3D}$ is defined as

$$V_{vap,3D} = \frac{1}{c^3} \sum_{i=1}^{N} \alpha_i V_i. \tag{6.3}$$

From now on the total vapor volumes $V_{vap,1D}$, $V_{vap,2D}$ and $V_{vap,3D}$ are denoted by V_{vap}. The test case considered defines which equation for V_{vap} is considered, i.e. equation (6.1), (6.2) or (6.3) for 1D, 2D or 3D flow test cases, respectively.

6.2 1D cavitating flow problems

6.2.1 "Closing Valve" problem

Berg *et al.* [22] investigated the cavitating flow in hydraulic pipelines. Here, their "Closing Valve" problem is calculated. Consider a uniform flow of water through a pipe of length $L = 0.1$ m. The initial velocity u_0 and the initial pressure p_0 are set to $u_0 = 1.0$ ms^{-1} and $p_0 = 10^5$ Pa, respectively. The initial temperature is denoted by T_0, which is equal to $T_0 = 293$ K. For these initial conditions the speed of sound equals $c_0 = 1537.7$ ms^{-1}.

At an arbitrary time, say $t = 0$ the entire inflow boundary is closed infinitely fast. Due to the inertia of the water an expansion wave starts traveling through the pipe. Consequently, the pressure at the inlet boundary may drop to the saturation pressure $p_{sat}(T_0)$ and the fluid starts to cavitate. All results are evaluated at the end-time $t = 5.0 \times 10^{-5}$ s, which is just before the expansion wave reaches the outflow boundary. The grid is constructed from quadrilaterals and in this section the influence of the grid size is investigated.

The results are obtained with the HLLC flux scheme as presented in section 4.5.2. In the following first and second-order results are presented. The second-order results are obtained with the limiter method of Venkatakrishnan employing the primitive variables $[\rho, u, v, w, e]^T$. For the outflow the non-reflective boundary conditions are applied. The inflow and side walls of the pipe are slip solid walls.

To assess the order of the convergence of the numerical method, the solution is calculated on five different grids, i.e. consisting of 50, 100, 200, 400, and 800 points in x-direction and 2, 4, 8, 16 and 32 points in y-direction, respectively. From now on the grids will be referred to by the number of grid points in x-direction. The total vapor volume V_{vap} defined in equation (6.1) is calculated at time $t = 5.0 \times 10^{-5}$ s. In table 6.2 the calculated total vapor volume is presented for the five different grids for first- and second-order spatial reconstruction. The table shows that the vapor volume remains small and appears to converge for increasing mesh density.

Richardson's extrapolation is applied to estimate the total vapor volume $V_{vap}(0)$ by

$$V_{vap}(h) = V_{vap}(0) + Ch^p, \tag{6.4}$$

for three grids with increasing mesh density. The values for $V_{vap}(0)$, C, and p are presented in table 6.3. Note that $V_{vap}(0)$ is equal to $4.6819 \times 10^{-4}\%$ and $p \approx 1$ for both the first- and second-order results. Thus, it is found that both the first-order method and the second-order method converge linearly only.

N	1^{st}-order V_{vap} $[10^{-4}\%]$	2^{nd}-order V_{vap} $[10^{-4}\%]$
50	4.67183	4.69074
100	4.67685	4.68631
200	4.67937	4.68410
400	4.68062	4.68299
800	4.68125	4.68243

TABLE 6.2: *Closing Valve problem. Total vapor volume at $t = 5.0\times10^{-5}$s, first- and second-order results for meshes with 50, 100, 200, 400 and 800 points in x-direction.*

N	1^{st}-order			2^{nd}-order		
	$V_{vap}(0)$ $[10^{-4}\%]$	C $[10^{-5}]$	p	$V_{vap}(0)$ $[10^{-4}\%]$	C $[10^{-5}]$	p
50/100/200	4.68191	-4.93	0.994	4.68190	4.48	1.003
100/200/400	4.68185	-5.27	1.011	4.68187	4.31	0.993
200/400/800	4.68189	-4.74	0.989	4.68186	4.18	0.987

TABLE 6.3: *Closing Valve problem. Grid convergence of total vapor volume. Constants obtained with Richardson's extrapolation.*

In figure 6.1 first and second-order solutions for the pressure p, the velocity u and the speed of sound c are presented for the five different meshes. The numerical time steps Δt_{cfl} are equal to the numerical time steps presented in table 5.4. In figure 6.2 the solution for the void fraction α and the Mach number M are presented. Note that for the results in figure 6.2 the scale of the x-axis is different in order to illustrate the region of interest, namely the region close to the closed inlet.

At $t = 5.0\times10^{-5}$s the right-running expansion wave, that appears as soon as the inlet closes, has almost reached the outflow boundary. However, the pressure in the tube cannot decrease below saturation pressure without forcing the liquid to cavitate. Thus, the pressure drops to saturation pressure and then remains constant. The vapor fraction α is equal to zero after the expansion wave has passed. The velocity then also remains constant. The decrease in velocity depends on the decrease in pressure. In the linearized case, see section 5.2, the difference in velocity is derived to be equal to $\Delta u = \Delta p/\rho_0 c_0 = 0.064\ \mathrm{ms}^{-1}$, which is confirmed in figure 6.1(d).

However, at the left boundary the velocity has to become equal to zero. Consequently, the fluid is forced to cavitate, i.e. the void fraction α increases to 1. This results in the formation of a liquid-vapor contact surface, followed by an expansion wave in the vapor, where the velocity decreases to zero. The speed at which the contact surface

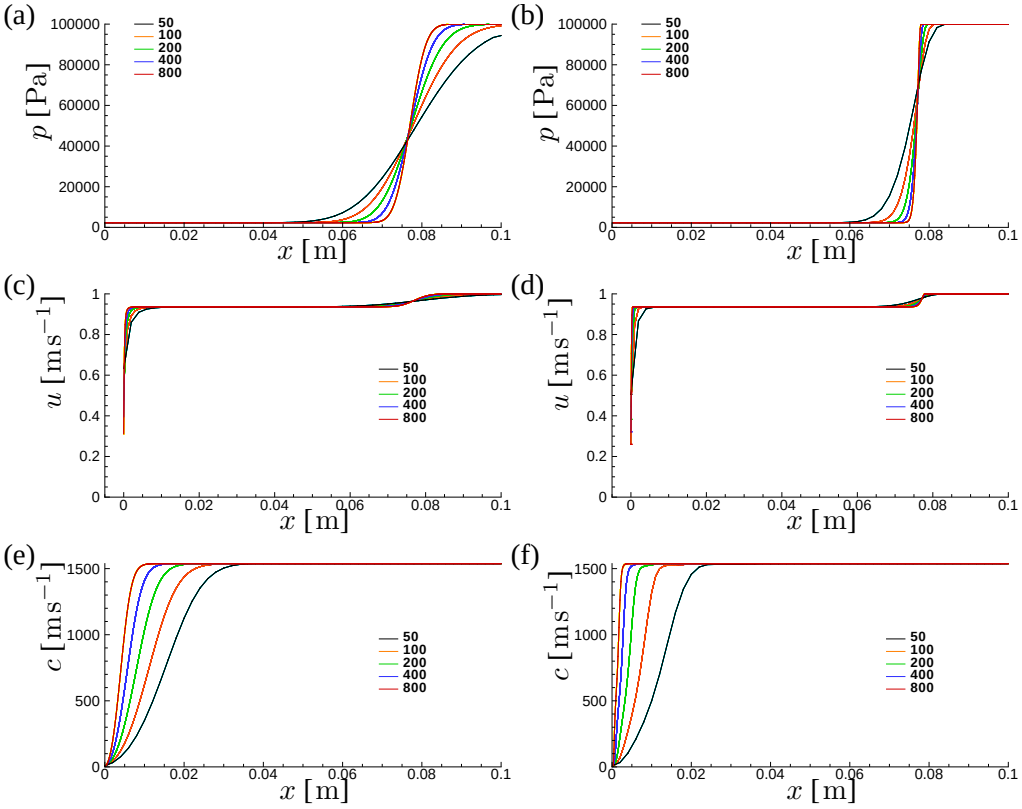

FIGURE 6.1: *Closing Valve problem. Flow is from left to right.* $t = 5.0 \times 10^{-5}$ s. *Results obtained with HLLC scheme: first-order spatial reconstruction (left) and second-order reconstruction (right).* $u_0 = 1.0$ ms^{-1}, $p_0 = 10^5$ Pa, $T_0 = 293$ K. *(a)–(b) pressure* p *(c)–(d) velocity* u *(e)–(f) speed of sound* c*. See figure 6.2 for the void fraction* α *and Mach number* M.

moves is much smaller than the velocity of the expansion wave in the liquid and thus, in the time considered, the contact surface is located close to the closed valve. The second expansion wave in the vapor is therefore not resolved resulting in a singular point at the left boundary. This also explains the value of $p \approx 1.0$ in table 6.3 for the second-order spatial reconstruction.

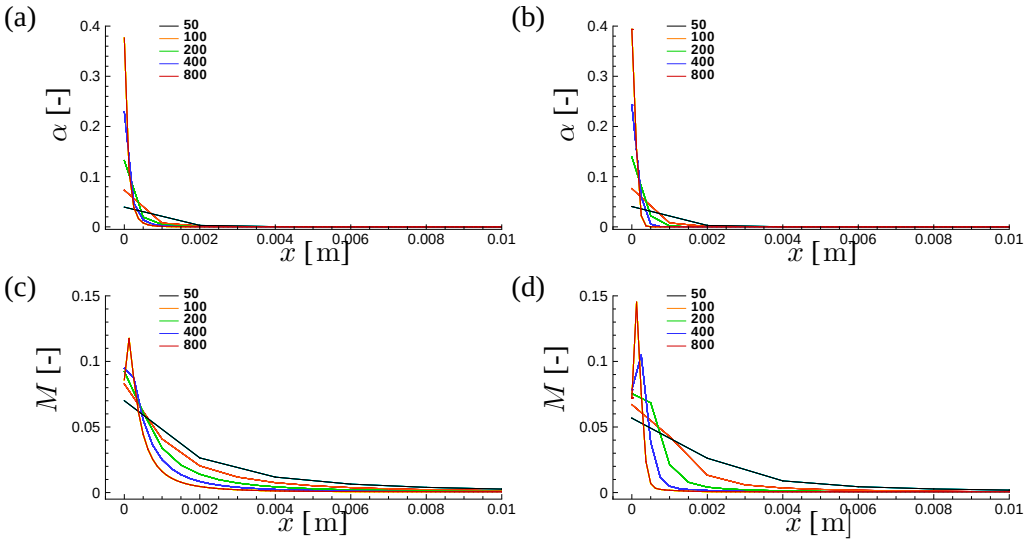

FIGURE 6.2: *Closing Valve problem. Flow is from left to right.* $t = 5.0 \times 10^{-5}$ s. *Results obtained with HLLC scheme: first-order spatial reconstruction (left) and second-order reconstruction (right).* $u_0 = 1.0$ ms^{-1}, $p_0 = 10^5$ Pa, $T_0 = 293$ K. *(a)–(b) void fraction* α *(c)–(d) Mach number* M. *Note the difference in scale of the* x*-axis compared with figure 6.1.*

6.2.2 Two symmetric expansion waves

Saurel *et al*. [166] presented an one-dimensional test case for cavitating flows for which evaporation in the fluid is forced by a left- and right-running expansion wave. Saurel *et al*. considered hypervelocity ($u = 3000$ ms^{-1}) underwater projectiles which is outside the scope of the present research. Thus, in this section the conditions defined by Schmidt *et al*. [169] are considered. The results are obtained with the second-order hybrid HLLC/AUSM+up flux scheme on a quadrilateral mesh consisting of 100 points in x-direction.

Initially, a tube with a length of 1m is completely filled with water at a temperature of $T_0 = 303.15$ K with $p_{sat}(T_0) = 4,254$Pa and $c_0 = 1539.6$ ms^{-1}. In the center of the tube, at $x = 0.5$ m, a diaphragm is placed separating two reservoirs of fluid. The water to the left of the membrane has an initial velocity of $u_{0L} = -10.0$ ms^{-1}, whereas the fluid to the right of the membrane has an initial velocity equal to $u_{0R} = 10.0$ ms^{-1}. The pressure on both sides of the membrane is set to $p_{0L} = p_{0R} = 0.9 \times 10^5$ Pa. At $t = 0$ the membrane is removed. The left and right ends of the tube are non-reflective outflow boundaries.

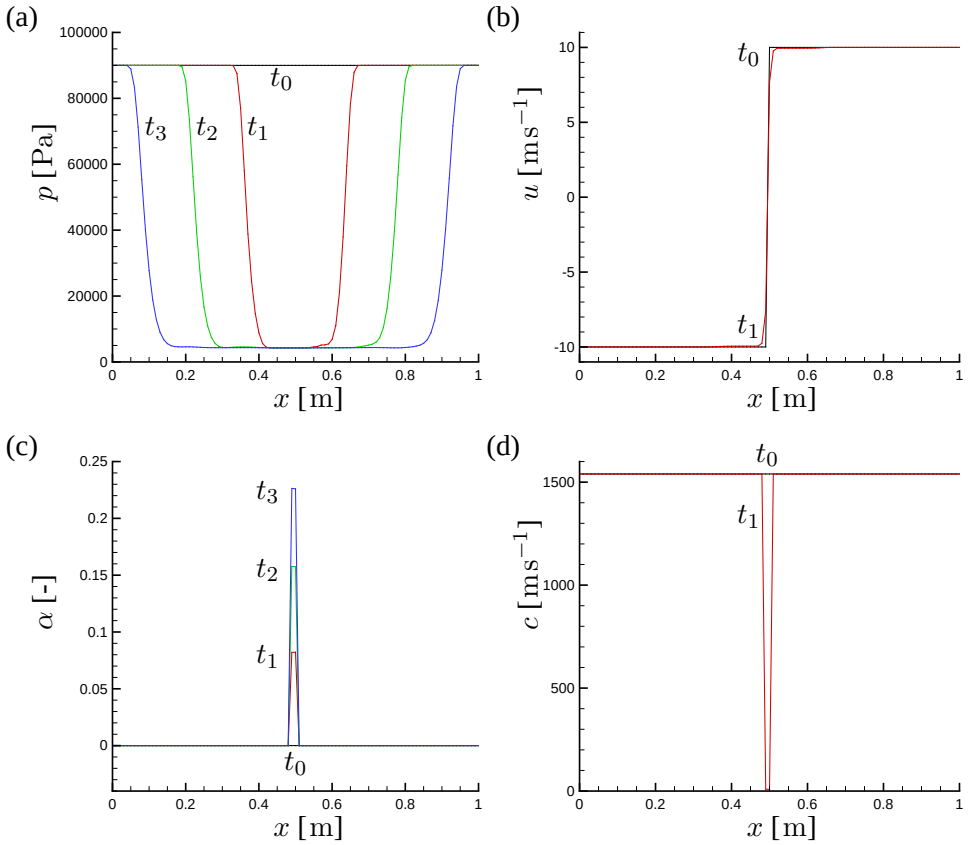

FIGURE 6.3: *Two symmetric expansion waves. Solution at time-instants t_0–t_3 with $t_N = 0 + N\Delta t$, where $\Delta t = 0.9\times10^{-4}$s. Results are obtained with second-order hybrid HLLC/AUSM+up scheme on a quadrilateral mesh with 100 points in x-direction. $\Delta t_{cfl} = 1.17\times10^{-6}$s, $u_{0L} = -10$ ms^{-1}, $u_{0R} = 10$ ms^{-1}, $p_{0L} = p_{0R} = 0.9\times10^5$ Pa, $T_{0L} = T_{0R} = 303.15$ K. (a) pressure p (b) velocity u (c) void fraction α (d) speed of sound c. Note that the solution for the velocity and speed of sound at time-instants t_2 and t_3 are to plotting accuracy equal to the solution at t_1.*

The solution to this test case corresponds to two rarefaction waves, one running to the left and the other running in opposite direction. In the rarefaction wave the pressure decreases rapidly to the saturation pressure, but the vapor fraction α remains equal to zero. Evaporation of the liquid takes place over the contact surface near the center of the domain. In the center region vapor is produced at constant temperature because of the assumption of local equilibrium during phase change and thus the pressure re-

mains constant at the saturation pressure $p_{sat}(T_0)$.

Results for the pressure p, velocity u, void fraction α and speed of sound c are presented in figure 6.3 for times $t_N = 0+N\Delta t$ with $\Delta t = 0.9\times10^{-4}s$ and $N = 0,\ldots,3$. All solutions are free of oscillations. At this early time the contact surfaces on either side of the center are positioned in a very small region around the centerline. Note the sharp transition in velocity from $u = -10\ \mathrm{ms}^{-1}$ to $u = 10\ \mathrm{ms}^{-1}$ at $x = 0.5\mathrm{m}$ and the dramatic decrease in speed of sound from $c \approx 1540\ \mathrm{ms}^{-1}$ to $c \approx 6\ \mathrm{ms}^{-1}$ at $x = 0.5\mathrm{m}$.

For the same initial conditions, the exact solution for single phase water flow without cavitation employing the Tait equation of state can be calculated. For single phase water flow, the pressure in the center of the domain reaches almost $-150\ \mathrm{bar}$ and the velocity becomes equal to zero over a relatively large part of the domain.

6.3 Unsteady cavitating flow about 2D NACA0015 at 6°

To verify the present density-based numerical method a standard two-dimensional test case of an unsteady cavitating flow is considered, see Sauer [162], Sauer & Schnerr [163] and Schnerr *et al.* [171]. At the presented conditions this test case shows to good approximation a 2D periodic unsteady cavitating flow with characteristic behavior such as the cyclic formation of a cavitation sheet, the formation of the re-entrant jet and the shedding of a vapor cloud. In this section the results obtained with the present numerical method are compared with the results of Schnerr *et al.* [171].

The two-dimensional test case is very well suited for numerical verification. Unfortunately, validation with experiments is not possible, because of the lack of data for the case of purely two-dimensional flow. As explained in section 2.3 the shedding on a two-dimensional hydrofoil will never be completely two-dimensional. In his thesis Sauer [162] refers to experiments for a two-dimensional hydrofoil of Keller & Arndt for the same flow conditions. As is clear from experiments on two-dimensional hydrofoils, the sheet cavity is always influenced by alternating side-wall effects as well as by the three-dimensional spherical propagation of shock waves. The local collapse along the closure line of the sheet cavity induces local side-flow resulting in random collapse and shedding of vapor along the span-wise closure line of the cavity sheet.

The hydrofoil considered is a 2D NACA0015 hydrofoil at 6° angle of attack with chord length $c = 0.13\mathrm{m}$. The solution for fully-wetted, i.e. single-phase water flow, was presented in section 5.6. The computational domain is presented in figure 5.17.

The inflow velocity U_∞ is set to $12\ \mathrm{ms}^{-1}$. For cavitating flow the free-stream pressure p_∞ is chosen such that the cavitation number, defined in equation (2.1), is equal to $\sigma = 1.0$ at $T_\infty = 293$ K with $p_{sat}(T_\infty) = 2,321\,\mathrm{Pa}$, yielding for the initial pressure $p_\infty = 0.742 \times 10^5\,\mathrm{Pa}$.

U_∞ $[\mathrm{ms}^{-1}]$	p_∞ $[10^5\,\mathrm{Pa}]$	T_∞ [K]	ρ_∞ $[\mathrm{kgm}^{-3}]$	c_∞ $[\mathrm{ms}^{-1}]$	σ [-]
12	0.742	293	998.2	1537.6	1.0

TABLE 6.4: *Conditions for cavitating flow about 2D NACA0015 hydrofoil at* $6°$ *angle of attack with chord length* $c = 0.13\mathrm{m}$.

For the inflow the non-reflective boundary condition is employed. For the outflow the asymptotic non-reflective pressure boundary condition is applied with free-stream pressure p_∞. The top and bottom of the channel are slip solid walls and for the slip solid wall of the hydrofoil the curvature-corrected symmetry technique is used. The results are obtained with the hybrid HLLC/AUSM flux scheme of section 4.7.2. A CFL number of 0.8 is employed for all simulations.

In the following first- and second-order results are compared, with the second-order results calculated with the limiter method of Venkatakrishnan employing the primitive variables $[\rho, u, v, w, e]^T$. When calculating the second-order results the first 50k time-steps are performed applying the first-order reconstruction.

Furthermore, two hybrid quadrilateral/triangular grids are considered, a coarse and a finer grid with 100 and 200 points on the surface of the hydrofoil, respectively. A close-up of the hybrid meshes around the hydrofoil is presented in figure 6.4. For both grids the total number of elements and total number of control volumes are presented in table 6.5. For more details on the construction of the hybrid mesh see section 5.5.2. For the chosen CFL number the corresponding numerical time step Δt_{cfl} is approximately equal to $\Delta t_{cfl} \approx 1.4 \times 10^{-7} s$ for the coarse mesh and $\Delta t_{cfl} \approx 3.9 \times 10^{-8} s$ for the fine mesh.

mesh	# points foil surface	# quad's	# triangles	# control volumes	Δt_{cfl} $[10^{-7}\mathrm{s}]$
coarse	100	1,520	4,747	3,995	1.4
fine	200	6,080	8,339	10,401	0.39
extrafine	400	24,320	14,873	31,998	0.11

TABLE 6.5: *Computational meshes for cavitating flow about 2D NACA0015 at* $6°$ *angle of attack.*

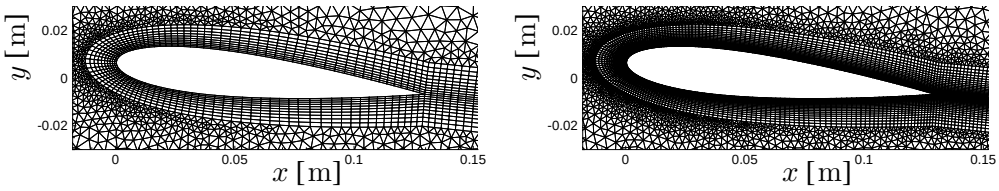

FIGURE 6.4: *Close-up of foil with hybrid quadrilateral/triangular mesh for 2D NACA0015 hydrofoil at* 6° *angle of attack. (left) coarse mesh: 100 points on surface of hydrofoil, 3,995 control volumes, 1,520 quadrilaterals, 4,747 triangles (right) fine mesh: 200 points on surface of hydrofoil, 10,401 control volumes, 6,080 quadrilaterals, 8,339 triangles.*

6.3.1 Results for total vapor volume

The total vapor volume V_{vap}, defined in equation (6.2), is a convenient parameter for understanding the transient evolution of the cavitating flow. The total vapor volume is calculated at each time step. After the start-up phase the growth and shedding of the vapor sheet and the collapse of the shed vapor cloud induce a self-oscillatory behavior, which is approximately periodic in time. It takes approximately $0.2\,\mathrm{s}$ in simulated time until a repeatable pattern in the variation of total vapor volume with time is observed. The time-histories of the total vapor volume V_{vap} during 4 cycles, sometime after the start-up phase, are presented in figure 6.5. The results are obtained applying the first- and second-order reconstruction on the coarse and fine mesh, respectively.

Applying the Fast Fourier Transform (FFT) on the time-history of the total vapor volume, the main frequency of the repeated pattern in the total vapor volume is found. The frequencies for the first- and second-order results on the coarse and fine grid are presented in table 6.6 together with the Strouhal number based on the chord length. Also presented are the average of the total vapor volume $\bar{V}_{vap}$ and the extremum values in total vapor volume.

From figure 6.5 and table 6.6 it becomes clear that for first-order reconstruction the mesh has a large influence on the frequency of the oscillation in the total vapor volume and thus on the calculated Strouhal number. The frequencies obtained for both meshes using the second-order reconstruction method agree reasonably well with each other.

The order of reconstruction and the mesh density have a large influence on the time-averaged value of the total vapor volume. When a higher order reconstruction or a finer mesh is employed, then the amount of vapor present above the hydrofoil in-

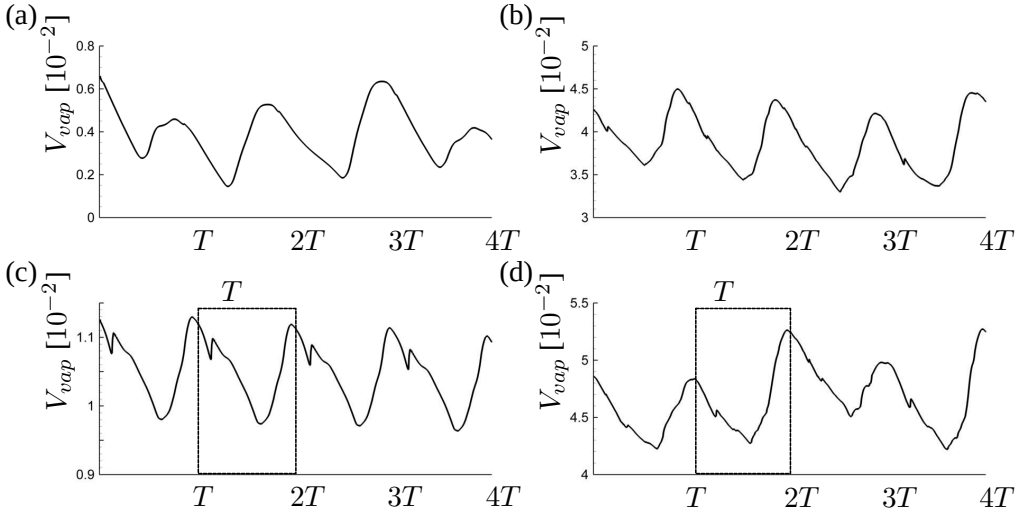

FIGURE 6.5: *Time-history of total vapor volume V_{vap} for unsteady cavitating flow about 2D NACA0015 hydrofoil at 6° angle of attack, $\sigma = 1.0$ with $U_\infty = 12\ \mathrm{ms}^{-1}$. Four shedding cycles after start-up phase. Note the difference in scale of the vertical axis. (a) first-order, coarse grid: $T = 5.03\times10^{-2}\,\mathrm{s}$ (b) second-order, coarse grid: $T = 4.23\times10^{-2}\,\mathrm{s}$ (c) first-order, fine grid: $T = 2.43\times10^{-2}\,\mathrm{s}$ (d) second-order, fine grid: $T = 4.13\times10^{-2}\,\mathrm{s}$.*

mesh	order	f [Hz]	St_c [-]	$\bar{V}_{vap}$ $[10^{-2}]$	$max\ V_{vap}$ [%]	$min\ V_{vap}$ [%]
100	1	19.9	0.216	0.39	170	37
200	1	41.1	0.445	1.05	108	92
400	1	40.9	0.443	1.82	120	75
100	2	23.6	0.256	3.87	116	85
200	2	24.2	0.262	4.65	113	91

TABLE 6.6: *Frequency, Strouhal number St_c, time-averaged total vapor volume $\bar{V}_{vap}$ and extreme values in total vapor volume for time-dependent total vapor volume for unsteady cavitating flow about 2D NACA0015 hydrofoil at 6° angle of attack. $c = 0.13\mathrm{m}$, $\sigma = 1.0$ with $U_\infty = 12\ \mathrm{ms}^{-1}$.*

creases up to a factor of 4. This finding is illustrated more clearly in section 6.3.3 where the solution for the void fraction for the first- and second order reconstruction on the fine mesh during the cycles shown in figure 6.5 is presented.

Furthermore, from table 6.6 it is clear that employing the first-order reconstruction method a different shedding frequency is found compared with the result of the second-order reconstruction method. The reason for this is not clear. A possibility

might be that due to the nonlinearity of the equations more solutions are possible. To study this further the first-order solution is continued with the second-order reconstruction and the second-order solution is continued with the first-order reconstruction. However, these additional calculations have not progressed far enough to draw conclusions.

In his thesis Sauer [162] reports a numerically obtained frequency of $f \approx 11$ Hz. Sauer used the pressure-based method CAVKA, which is first-order in space and time for cavitating flow. Employing their compressible density-based method CATUM Schnerr *et al*. [171] calculated a frequency of $f \approx 9$ Hz both for a first-order method on a coarse grid as well as for a second-order method on a fine grid. We remark that our coarse grid is coarser than their coarse grid and that our fine grid is finer than their fine grid. Schnerr *et al*. [171] refer to experiments of Keller & Arndt who found an experimentally observed frequency of $f \approx 16$Hz. Based on table 6.6 we have found a main frequency of $f \approx 24$Hz obtained with the second-order reconstruction method. We do not know the reason for the difference in main frequency compared to the one found by Schnerr *et al*. [171].

Based on the findings in table 6.6 we conclude that the first-order results on the fine mesh differ significantly from the one on the coarse mesh. To be able to obtain grid-converged first-order solutions the grid needs to be refined further. A first-order solution on a hybrid mesh with 400 points on the surface of the hydrofoil has been calculated to verify the results of the first-order solution on the fine mesh of table 6.6. For this 400-mesh the frequency is found to be equal to 40.9 Hz, which is close to the value found with the first-order scheme on the 200-mesh.

We conclude that the second-order results on the fine mesh correspond much better with the second-order results on the coarse mesh, than for the first-order results. Thus, applying the second-order reconstruction, the solution appears to depend more consistently on the mesh density. However, when using a finer mesh a better resolution in the shed vapor cloud and the sheet cavity is obtained and thus more local events are resolved.

6.3.2 Results for lift and drag coefficients

The time-history of the lift and drag coefficients during 4 cycles sometime after the start-up phase for the first- and second-order discretization on the coarse and fine grid are presented in figures 6.6 and 6.7. In table 6.7 the time-averaged lift and drag coefficients as well as the extremum values are presented. As a reference the second-order results on the fine mesh for single phase water flow are added. Due to cavitation a decrease by a factor of 1.5–1.7 in lift coefficient as well as a substantial drag is found. These values correspond with the values found by Sauer [163], who mentions that

this is in agreement with the experiments of Keller & Arndt. For the 400-mesh we find the value of $\bar{c}_d = 0.075$ for the time-averaged drag coefficient, which is equal to the value found by Sauer [163]. Applying the Fast Fourier Transform on the signal of the lift and drag coefficient the same main frequencies are found as in the time-history of the total vapor volume.

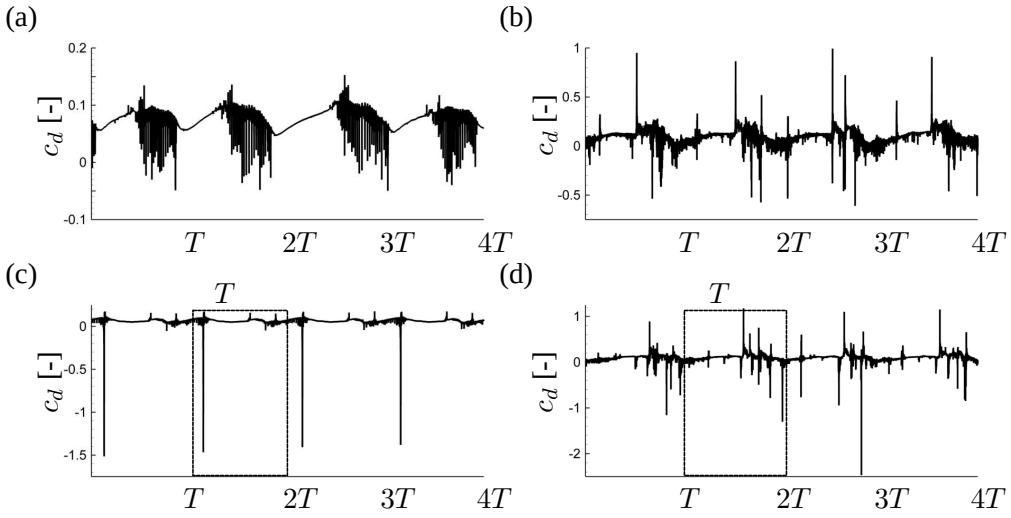

FIGURE 6.6: *Time-dependent drag coefficient c_d for unsteady cavitating flow about 2D NACA0015 hydrofoil at 6° angle of attack, $\sigma = 1.0$ with $U_\infty = 12\ \mathrm{ms}^{-1}$. Presented are four shedding cycles after start-up phase. Note the difference in scale of the vertical axis. (a) first-order, coarse grid: $T = 5.03\times10^{-2}\,\mathrm{s}$ (b) second-order, coarse grid: $T = 4.23\times10^{-2}\,\mathrm{s}$ (c) first-order, fine grid: $T = 2.43\times10^{-2}\,\mathrm{s}$ (d) second-order, fine grid: $T = 4.13\times10^{-2}\,\mathrm{s}$.*

During the time that the flow is periodic in terms of the total vapor volume, the lift and drag coefficients show high frequency pulses, which result from resolved physical (pressure) waves, which are generated by the collapse of shed vapor structures. Note that even for the first-order results obtained on the coarse mesh the lift coefficient becomes negative with values as low as $-0.5\bar{c}_l$. Schnerr *et al*. [171] explain that these negative lift pulses can be formed by either the formation of expansion waves as reflections of shocks at phase boundaries with constant pressure or by the pressure rise due to shocks impacting on the suction side of the foil. Both processes have been found in the present numerical simulations discussed in section 6.3.6 and we support the findings of Schnerr *et al*. [171].

From table 6.7 it is clear that when the second-order reconstruction is employed,

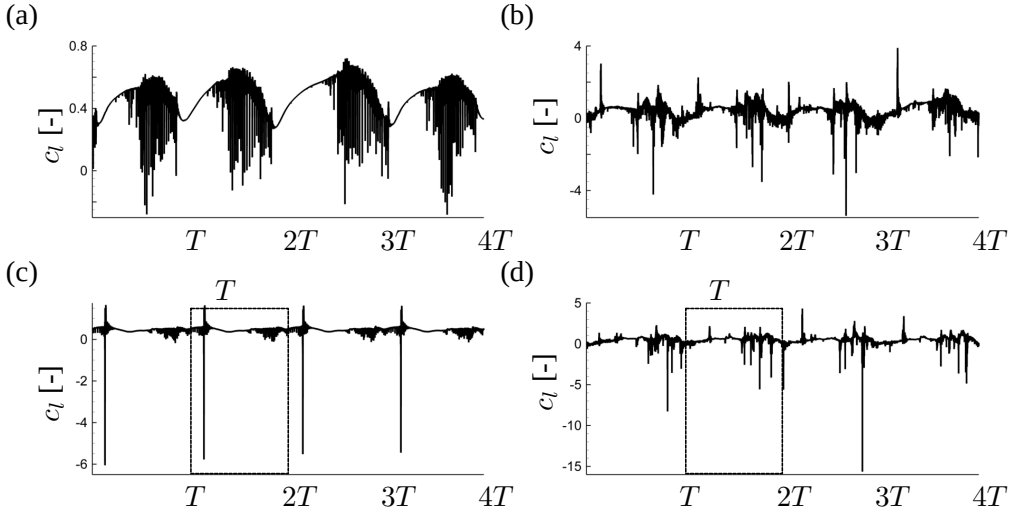

FIGURE 6.7: *Time-dependent lift coefficient c_l for unsteady cavitating flow about 2D NACA0015 hydrofoil at 6° angle of attack, $\sigma = 1.0$ with $U_\infty = 12\ \mathrm{ms}^{-1}$. Presented are four shedding cycles after start-up phase. Note the difference in scale of the y-axis. (a) first-order, coarse grid: $T = 5.03\times10^{-2}\,\mathrm{s}$ (b) second-order, coarse grid: $T = 4.23\times10^{-2}\,\mathrm{s}$ (c) first-order, fine grid: $T = 2.43\times10^{-2}\,\mathrm{s}$ (d) second-order, fine grid: $T = 4.13\times10^{-2}\,\mathrm{s}$.*

flow	mesh	order	$\bar{c}_l$ [-]	$min/max\ c_l$ [%]	$\bar{c}_d$ [-]	$min/max\ c_d$ [%]
cav	100	1	0.489	-58/ 148	0.080	-62/192
cav	200	1	0.484	-1250/ 341	0.066	-2302/267
cav	400	1	0.559	-1280/461	0.075	-2535/716
cav	100	2	0.515	-1051/757	0.108	-567/925
cav	200	2	0.546	-2864/ 791	0.109	-2270/1081
water	200	2	0.829	-	0.0035	-

TABLE 6.7: *Averaged and extremum values for lift and drag coefficients for unsteady cavitating flow about 2DNACA0015 hydrofoil at 6° angle of attack. $c = 0.13\mathrm{m}$, $\sigma = 1.0$ with $U_\infty = 12\ \mathrm{ms}^{-1}$. The last line in the table is the numerical result for single-phase water flow.*

the time-averaged values increase slightly compared to the first-order results. Also, a large increase in extremum values is observed. Schnerr *et al*. [171] observed the same large increase. It is clear that the loading of the hydrofoil changes dramatically during a shedding cycle. Furthermore, comparing the coarse grid results with those obtained on the fine grid we observe that the time-averaged values do not change

much. In contrast the extremum values again increase substantially, due to the collapse of the small-scale vapor structures. In the limit of an infinitesimally small mesh size, these vapor structures become very small vapor bubbles. However, currently it is impossible to combine the mesh resolution required to resolve these small-sized bubbles with the scale of the hydrofoil. A good validation test case for small-scale collapse might be the collapse of a single vapor bubble. However, at present the difficulty to resolve this testcase lies in the very large mesh density required to resolve the final stages of the collapsing bubble and in the application of the non-reflective boundary conditions to model far-field conditions.

6.3.3 Results during a cycle

In this section the cycles illustrated in figure 6.5–6.7 are considered. The solution for the void fraction α above the hydrofoil is presented for a number of equidistant time-intervals during the cycle. Furthermore, the time-history of the lift and drag coefficients are compared to those of the total vapor volume to correlate the occurring flow phenomena. To illustrate the dependence on the order of reconstruction both the first-order and second-order results for the 200-grid are discussed.

First order results on 200-grid

In figure 6.8 the solution for the void fraction α at 10 equidistant time-instants are presented, which illustrates the cyclic behavior of the vapor sheet and its shedding. Time-instant ⑩ is marked as the end or start of the shedding cycle. The period T of the cycle is $T = 0.0243s$ and $f_{cycle} = 41.1\ Hz$ with $St_c = 0.445$.

① The sheet cavity starts to grow at the leading edge of the hydrofoil. The shed vapor region that has convected about half a chord length from the previous shedding cycle is visible above the hydrofoil. ② The sheet cavity continues to grow. The shed vapor region is convected with the flow and starts to collapse. ③ The sheet cavity has reached its maximum length. The shed vapor region has collapsed. The process of the collapse of the vapor cloud is discussed in more detail in section 6.3.4. For the first-order results, at the instant of the collapse of the shed vapor region, the sheet cavity stops growing. It is an open question whether or not the sheet cavity stops growing due to the collapse of the shed vapor region. ④ A re-entrant flow develops at the closure region of the cavity sheet. Note the small vortical flow region at the end of the sheet. ⑤ The re-entrant jet containing liquid water travels upstream along the surface of the hydrofoil. ⑥ The re-entrant jet hits the liquid-vapor interface, disturbing the sheet cavity. The sheet is split into two regions, i.e. a large vapor structure around which a circulatory flow pattern is generated and the remaining part of the vapor sheet on the leading edge of the hydrofoil. ⑦ A re-entrant jet develops at the closure region of the remaining part of the vapor sheet causing this small sheet to collapse.

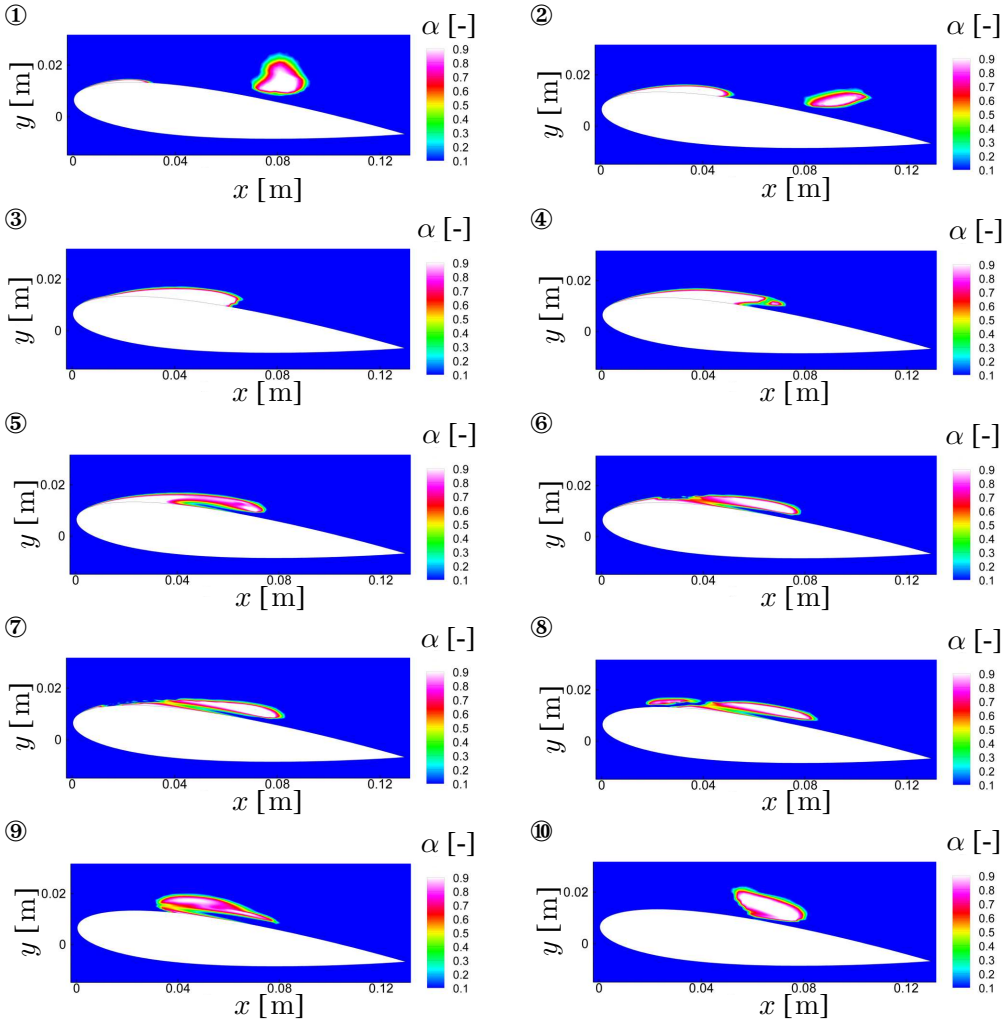

FIGURE 6.8: *Unsteady cavitating flow about 2D NACA0015 at 6° angle of attack. First order solution on 200-mesh for void fraction* α. $\sigma = 1.0$, $U_\infty = 12$ ms^{-1}, $T = 0.0243s$, $f_{cyc} = 41.1Hz$ ① $t = 1T/10$ ② $t = 2T/10$ ③ $t = 3T/10$ ④ $t = 4T/10$ ⑤ $t = 5T/10$ ⑥ $t = 6T/10$ ⑦ $t = 7T/10$ ⑧ $t = 8T/10$ ⑨ $t = 9T/10$ ⑩ $t = T$.

The large vapor structure slowly moves with the main flow. ⑧ The remaining part of the vapor sheet has collapsed resulting in a high pressure pulse on the leading edge of the hydrofoil sometime between picture ⑦ and ⑧, which is illustrated in figure 6.9. The maximum pressure just after the collapse at the leading edge is found to be equal to 19.5 bar occurring at the surface of the hydrofoil. This illustrates the high local pressure pulses on the foil due to the shedding of the sheet cavity. The disappearance of the first part of the sheet cavity at the leading edge combined with the shock wave

generates a second, small rotating vapor region as visible in picture ⑧ of figure 6.8. ⑨. The second small vortical flow region catches up with the large vapor structure shed earlier and the two regions merge. ⑩ The large shed vapor region rotates and is convected with the flow. Note the vertical extent of the vapor structure in pictures ⑩ and ①. The nose of the hydrofoil is now free of vapor and a new vapor sheet starts to grow. This process is repeated continuously.

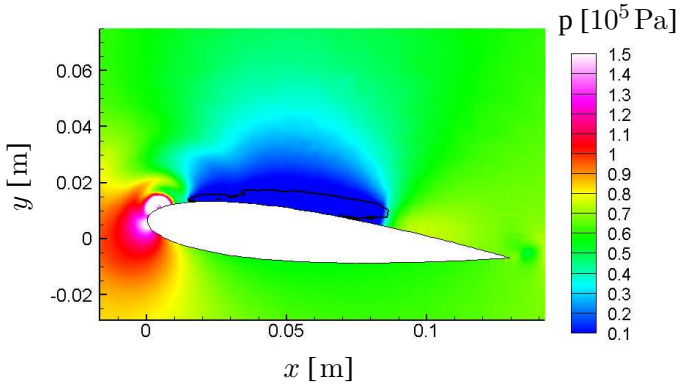

FIGURE 6.9: *Pressure distribution just after the collapse of the shed cavity at the leading edge between pictures ⑦ and ⑧. The black line denotes the void fraction equal to* $\alpha = 0.001$.

In figure 6.10 the first-order result for the total vapor volume V_{vap} during the cycle on the 200-mesh is presented. Also the lift and drag coefficients are plotted. The total vapor volume decreases between instants ① and ⑧ and increases between ⑧ and ①. The increase is caused by the growth and rapid merging of the shed vapor regions. The decrease starts with the collapse of the shed vapor region. The sharp increase between instants ② and ③ is caused by the reaction of the sheet cavity to the pressure pulse generated by the collapse of the shed vapor region as explained in more detail in section 6.3.4.

The lift and drag coefficients show large fluctuations from instant ⑦, corresponding with the collapse of the small sheet cavity on the leading edge of the hydrofoil, to instant ④ which corresponds with the formation of the re-entrant jet at the closure region of the large sheet cavity. From the disappearance of the sheet cavity at the leading edge and the subsequent shedding between time-instants ⑦ and ⑩ result in the disappearance and collapse of small vapor structures on the front part of the hydrofoil sending high frequency pressure waves through the domain. From instant ①, corresponding with the start of the growth of the vapor sheet, to just before instant ③ the pressure pulses change in behavior. Instead of the random pulses during ⑦–⑩

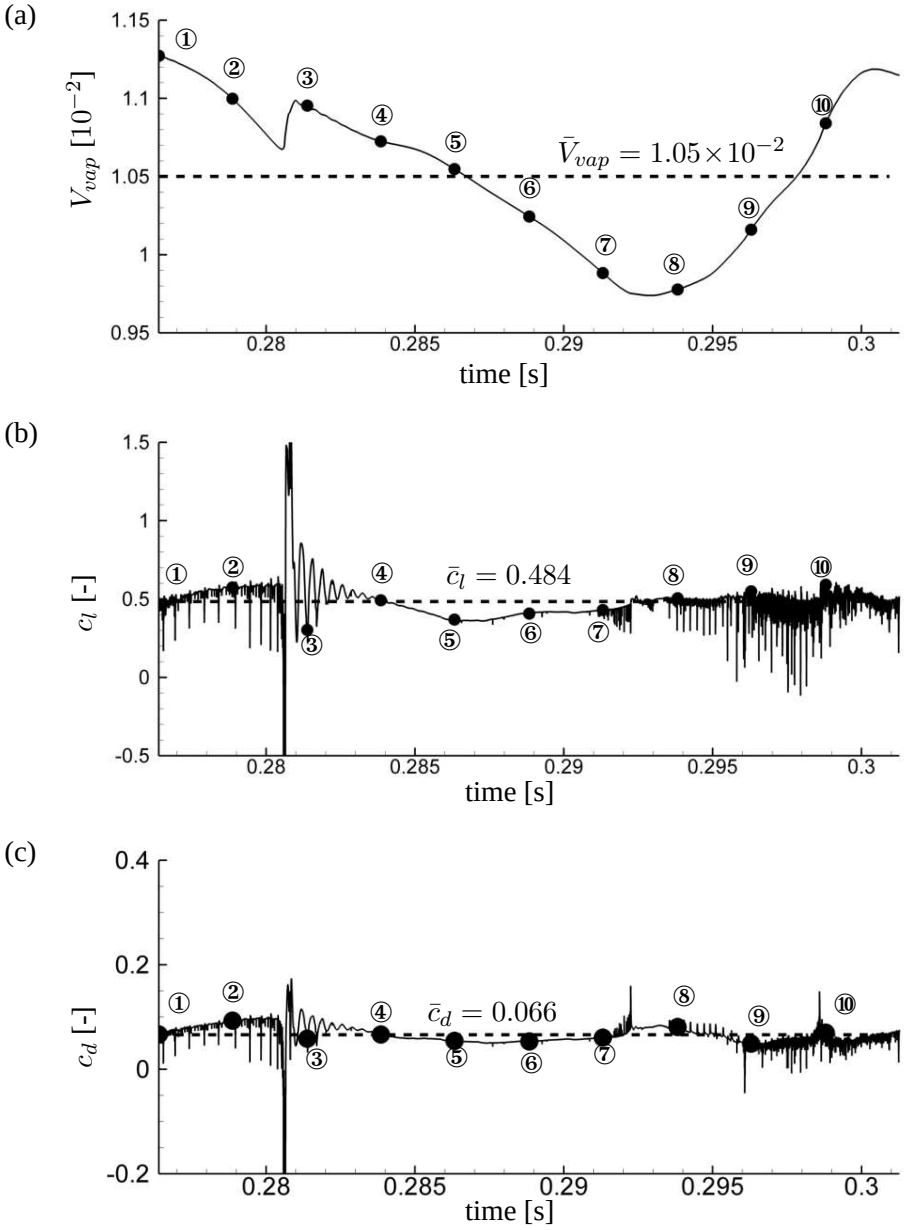

FIGURE 6.10: *Unsteady cavitating flow about 2D NACA0015 hydrofoil at* 6° *angle of attack.* $\sigma = 1.0$, $U_\infty = 12\ \mathrm{ms}^{-1}$ *. Solution for cycle indicated in figure 6.5 for first-order reconstruction on fine grid.* $T = 0.0243s$, $f = 41.1Hz$. $\Delta t_{cfl} = 1.4 \times 10^{-7}$ s. *(a) Total vapor volume (b) Lift coefficient* c_l *(c) Drag coefficient* c_d.

now the pressure pulses appear to be more structured in time. During the interval from ⑩ to ② only parts of the large shed vapor cloud disappear. Between instants ② and ③ the large shed vapor cloud collapses resulting in a high negative peak in the lift and drag coefficient followed by a high positive peak. The minimum lift and drag coefficient are equal to $c_l = -6.05$ and $c_d = -1.52$, respectively. Note that the scale of the vertical axis in figure 6.10 does not cover the complete range. These peaks are due to the collapse of the shed vapor cloud and its rebound, which is explained in more detail in section 6.3.4. During the time-interval between instants ④ and ⑦ the vapor volume decreases as well as the lift and drag coefficient. Also, the lift and drag coefficient do not show many oscillations. During this time-interval the cavity sheet has stopped growing in size and a re-entrant jet is moving upstream underneath the vapor sheet.

Comparing figure 6.8 and figure 6.10 we observe that when the cavity sheet is being shed and the shed vapor region is convected with the flow, see pictures ⑦-②, high-frequency pulses are observed. Between pictures ② and ③ the shed vapor region collapses causing large peaks in the lift and drag coefficient. In the time that the re-entrant jet is moving upstream underneath the sheet cavity and in the absence of a shed vapor region, see pictures ④-⑦, the lift and drag coefficient remain fairly constant and they do not show high-frequency pulses. Furthermore, it is found that the pressure on the foil at the location of the re-entrant jet, as visible in picture ⑤ and ⑥, is equal to the saturation pressure. Therefore, we conclude that the re-entrant jet is a flow of liquid at a pressure equal to the saturation pressure of $2.3 \times 10^3\,\mathrm{Pa}$. Between time-instants ⑦ and ⑧ the vapor sheet near the leading edge of the hydrofoil disappears, which is visible as the high peak in the drag coefficient, caused by the high pressure acting on the forward facing part of the hydrofoil.

Second order results on fine grid

In figure 6.11 the void fraction α at 10 equidistant time-instants are presented for the solution employing the second-order reconstruction on the 200-mesh. Compared to the first-order results much more vapor is produced and more complex vapor structures are observed. However, the main pattern of the shedding remains the same. Time-instant ⑩ is marked as the end or start of the shedding cycle. The period T of the cycle is $T = 0.0413s$ and $f_{cycle} = 24.2$ Hz.

① The sheet cavity starts to grow at the leading edge of the hydrofoil. The shed vapor regions from the previous shedding cycle are visible above the hydrofoil at about 80% chord-length. The last vapor region visible is produced due to flow around the trailing edge. ② The sheet cavity continues to grow. The shed vapor regions merge and are convected with the flow. Behind the hydrofoil the vapor region starts to col-

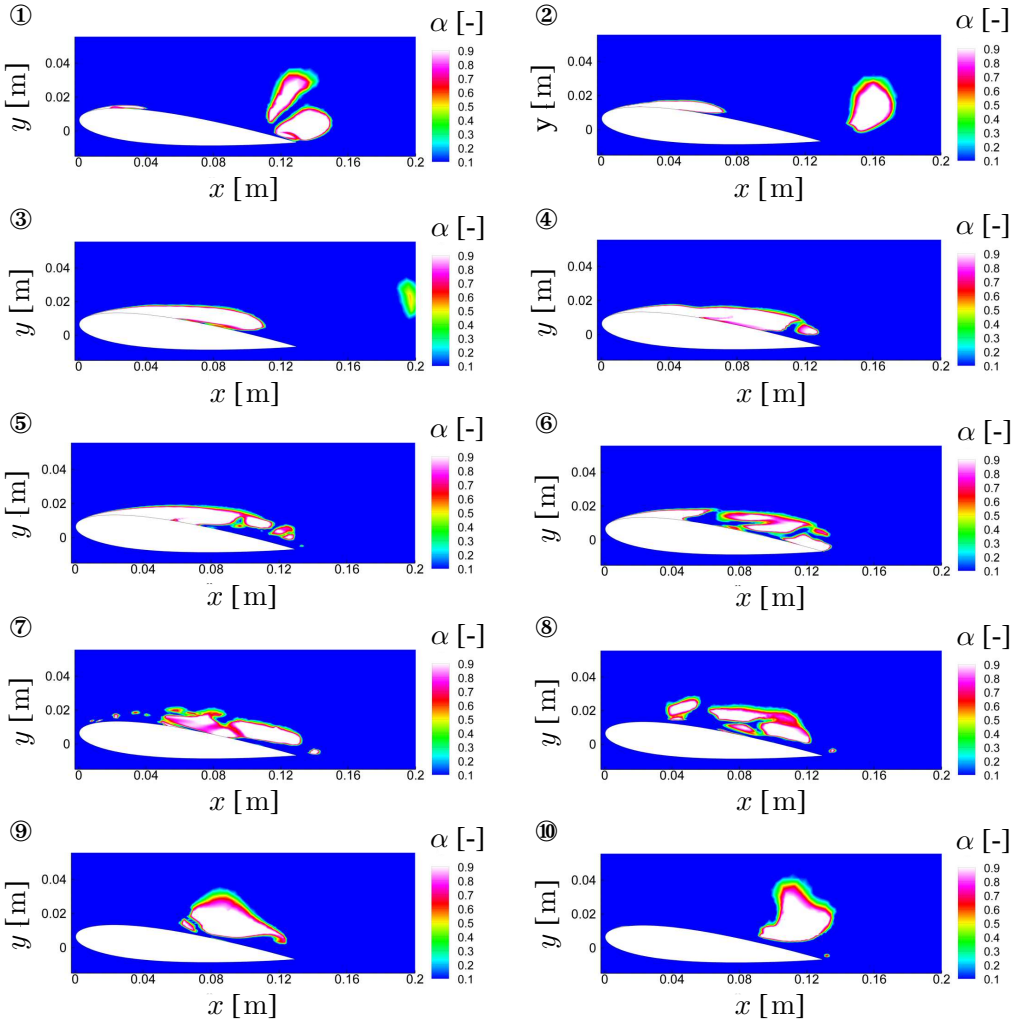

FIGURE 6.11: *Unsteady cavitating flow about 2D NACA0015 at 6° angle of attack. Second-order solution on 200-mesh for void fraction* α. $\sigma = 1.0$, $U_\infty = 12$ ms^{-1}, $T = 0.0413s$, $f_{cyc} = 24.2\mathrm{Hz}$ ① $t = 1T/10$ ② $t = 2T/10$ ③ $t = 3T/10$ ④ $t = 4T/10$ ⑤ $t = 5T/10$ ⑥ $t = 6T/10$ ⑦ $t = 7T/10$ ⑧ $t = 8T/10$ ⑨ $t = 9T/10$ ⑩ $t = T$.

lapse. ③ The sheet cavity has reached its maximum length, which is longer than in the result from the first-order reconstruction. The shed vapor region has almost completely collapsed. For the second-order results, at the instant of the collapse of the shed vapor region, the sheet cavity stops growing, just like as seen in the first-order solution. ④ A re-entrant flow develops at the closure region of the cavity sheet. Note the small vortical flow region at the end of the sheet. Also, the vapor-liquid interface oscillates due to the sudden stop of the growth of the sheet. ⑤ The re-entrant

jet travels upstream along the surface of the hydrofoil. Small vapor structures are shed from the main sheet cavity, which appears to break up in separate vapor regions. ⑥ The re-entrant jet hits the liquid-vapor interface, disturbing the sheet cavity. The sheet is split into two main regions, i.e. large shed vapor structures around which a circulatory flow is generated and the remaining part of the vapor sheet on the nose of the hydrofoil. ⑦ A re-entrant jet has developed at the closure region of the remaining part of the vapor sheet causing this small sheet to collapse. The collapse causes small vortical regions filled with vapor to emerge from the leading edge. The large shed vapor structures slowly move with the main flow. They rotate and merge into larger vapor regions. ⑧ The remaining part of the vapor sheet has completely collapsed resulting in high pressure pulses on the nose of the hydrofoil between picture ⑦ and ⑧. The disappearing of the first part of the sheet cavity at the leading edge combined with the shock wave generates small rotating vapor regions, which catch up with the larger shed vapor structures. ⑨ The small vortical regions have merged with the large shed vapor structures and they all merge into one larger, rotating vapor structure. ⑩ The large shed vapor region rotates and is convected with the flow. Note the height of the vapor structure in picture ⑩. The nose of the hydrofoil is now free of vapor and a new vapor sheet starts to grow. This process is repeated continuously.

In figure 6.12 the second-order results for the fine grid for the total vapor volume V_{vap} during the cycle is presented as well as the lift and drag coefficients. The total vapor volume decreases between instants ① and ⑦ and increases between ⑦ and ①. The increase is caused by the growth and rapid merging of the shed vapor regions. The decrease starts with the collapse of the shed vapor region. The sharp increase just after instant ③ is caused by the reaction of the sheet cavity to the pressure pulses generated by the collapse of the shed vapor region.

The lift and drag coefficients show large fluctuations from instant ⑦, corresponding with the collapse of the small sheet cavity on the leading edge of the hydrofoil, to instant ② which corresponds with the formation of the re-entrant jet at the closure region of the sheet cavity. The disappearing of the sheet cavity at the leading edge and its subsequent shedding between time-instants ⑦ and ⑩ result in the disappearing and collapse of many smaller-scale vapor structures sending high frequency pressure waves through the domain. Compared to the first-order results, the pressure pulses are much higher in amplitude and they occur more randomly. The maximum and minimum lift coefficient are now equal to $c_l = 2.1$ and $c_l = -5.6$, respectively. From instant ⑩, corresponding with the start of the growth of the vapor sheet, to just after instant ③ the pressure pulses change in behavior. Instead of the large random pulses during ⑦–⑩ now the pressure pulses appear to be more structured in time. During the interval from ⑩ to ② only parts of the large shed vapor cloud disappear.

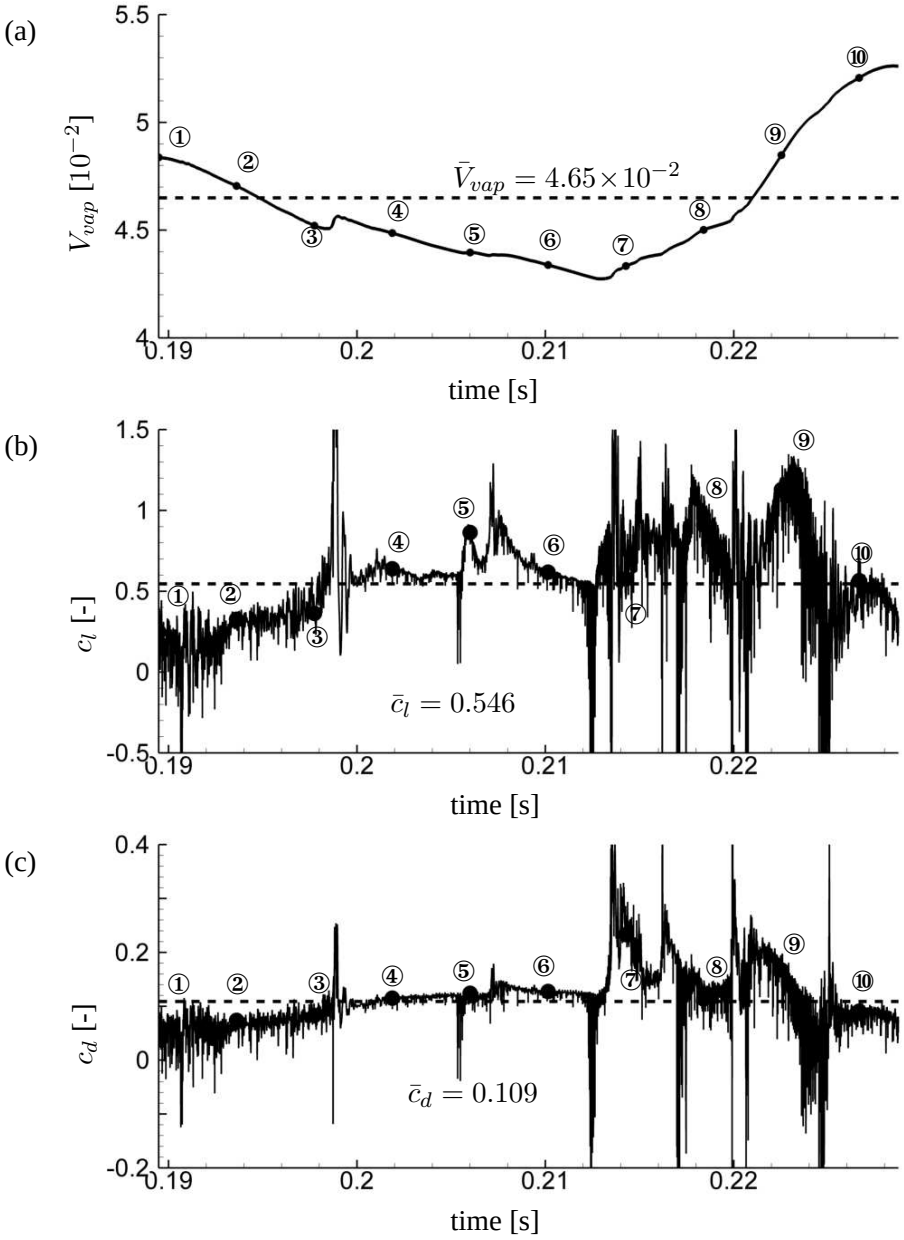

FIGURE 6.12: *Unsteady cavitating flow about 2D NACA0015 hydrofoil at* 6° *angle of attack.* $\sigma = 1.0$, $U_\infty = 12\ \mathrm{ms}^{-1}$. *Solution for cycle indicated in figure 6.5 for second-order reconstruction on fine grid.* $T = 0.0413\mathrm{s}$, $f = 24.2\mathrm{Hz}$. *(a) Total vapor volume (b) Lift coefficient* c_l *(c) Drag coefficient* c_d.

Just after instant ③ the large shed vapor cloud collapses resulting in a high negative peak in lift and drag coefficient followed by a high positive peak. Compared to the first-order results the maximum and minimum pressure pulse for the second-order results are much less, because the collapsing vapor region is located far behind the hydrofoil. During the time-interval between instants ③ and ⑥ the lift and drag coefficient do not show as many oscillations. During this time-interval the sheet cavity has stopped growing in size and a re-entrant jet is moving upstream underneath the vapor sheet.

Comparing figure 6.11 and figure 6.12 we observe that when the cavity sheet is being shed and the shed vapor region is convected with the flow, see pictures ⑦-③, high frequency pulses are observed. Just after picture ③ the shed vapor region collapses causing large peaks in the lift and drag coefficient. In the time that the re-entrant jet is moving upstream underneath the sheet cavity and in the absence of a shed vapor region, see pictures ④-⑥, the lift and drag coefficient remain fairly constant, although they do show some pressure pulses. Between time-instants ⑥ and ⑧ the vapor sheet near the leading edge of the hydrofoil disappears, which is visible as the high peaks in the lift and drag coefficients.

6.3.4 Collapse of convected vapor cloud

Between pictures ② and ③ of figure 6.8 the convected vapor region collapses near the trailing edge of the foil. In this section the process of the collapse and the rebound of the vapor region is discussed in more detail, see figure 6.13. The black line denotes a void fraction equal to $\alpha = 0.001$. Note that the scale of the pressure stops at 1.5 bar to better illustrate the occurring flow phenomena.

In figure 6.13(a) the convected vapor region reaches a region with higher pressure. Inside the vapor region the pressure is equal to the saturation pressure. This pressure difference induces a local flow field directed towards the center of the vapor region and causes the vapor region to collapse. The inwards moving liquid impacts at the center of the former vapor region and initiates an outward propagating circular shock as presented in figure 6.13(b). The maximum pressure in figure 6.13(b) is equal to 68.2 bar.

The shock wave hits the vapor sheet to the left on the suction side of the foil. Due to lower acoustic impedance ρc of the two-phase flow region compared to that of the liquid*, the shock wave is reflected as an expansion wave from the interface of

*The acoustic impedance Z is defined as: $Z = \rho c$. The reflection coefficient R from an interface is defined as

$$R = \frac{Z_2 - Z_1}{Z_2 + Z_1}, \tag{6.5}$$

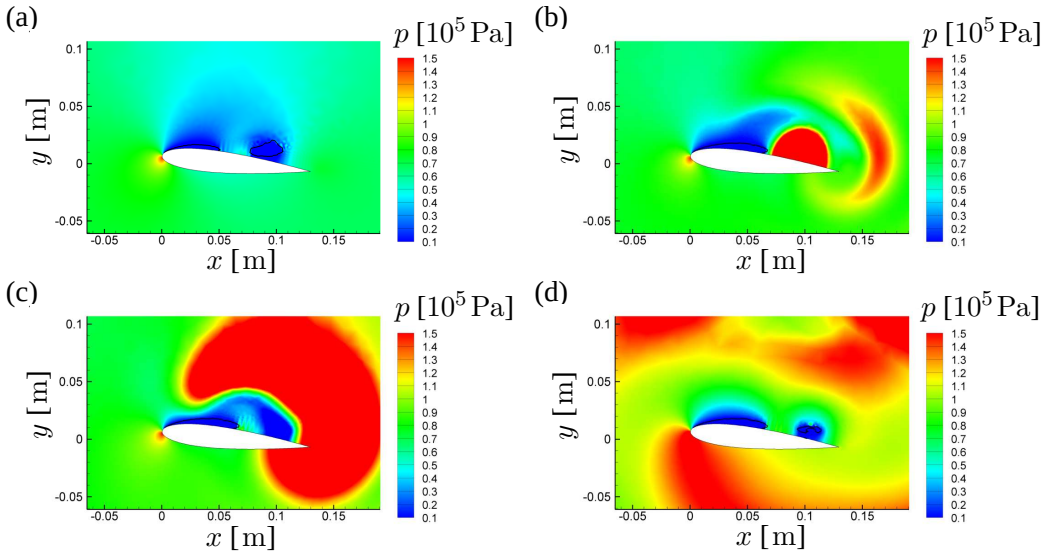

FIGURE 6.13: *Collapse of shed vapor region. Unsteady cavitating flow about 2D NACA0015 at 6° angle of attack. First-order solution on 200-mesh for pressure. The black line denotes* $\alpha = 0.001$. *(a)* $t = t_1$*: before collapse of vapor region (b)* $t_2 = t_1 + 2.22\times10^{-3}\,\mathrm{s}$*: collapse of vapor region (c)* $t_3 = t_2 + 46\times10^{-6}\,\mathrm{s}$*: reflection of shock wave from interface of sheet cavity (d)* $t_4 = t_3 + 74\times10^{-6}\,\mathrm{s}$*: rebound of vapor region.*

the sheet at which the pressure is constant. This process is illustrated figure 6.13(c), where the shock and expansion wave are running radially outward from the vapor sheet. The shock wave is visible as the circular region of high pressure. Above the sheet the shock wave has not reflected from the vapor sheet, while in the center the expansion wave is visible as the low pressure region. The shock wave is reflected from the tunnel top wall as visible in figure 6.13(d), which explains the oscillatory behavior observed in lift and drag coefficients in figure 6.10(b) and (c) between instants ③ and ④.

At the location of the former vapor region the pressure again returns to saturation pressure causing the liquid to cavitate again as shown in figure 6.13(d). The black line denotes a void fraction $\alpha = 0.001$. This new vapor region also collapses resulting in a second outward moving shock wave. The outward moving shocks interfere with the remaining vapor sheet on the suction side of the foil and the sheet's re-entrant jet. During the collapse of the vapor cloud the vapor sheet stops growing and a re-entrant jet is formed.

with $Z_1 = (\rho c)_{liquid} \approx \mathcal{O}(10^6)$ *and* $Z_2 = (\rho c)_{two-phase} \approx \mathcal{O}(10^2)$-$\mathcal{O}(10^3)$. *Note that when* $Z_2 << Z_1$ *then* $R \rightarrow -1$. *Thus, most of the acoustic energy is reflected with a* 180° *phase change.*

The maximum pressure in each control volume is calculated during the time-interval between figure 6.13(a) and the time-instant just after the second collapse of the vapor cloud. As presented in figure 6.14 the maximum pressure during this time-interval is found to be equal to 81.2 bar, which is the pressure peak at the time-instant of the collapse of the vapor cloud. Note the relatively high pressures occurring near the liquid-vapor interface of the sheet cavity, which indicates local collapse of vapor from the cavity sheet. The maximum pressure on the surface of the hydrofoil is found to be equal to 39.7 bar illustrating the high local pressure peaks on the foil during the collapse of the shed vapor cloud.

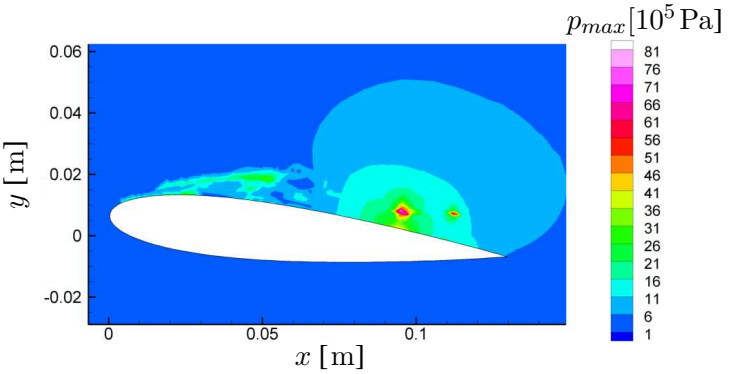

FIGURE 6.14: *Maximum pressure during the collapse and rebound of shed vapor region between pictures ② and ③ of figure 6.8. The maximum pressure is found to be equal to 81.2* bar. *Maximum pressure on surface of the foil is found to be equal to 39.8* bar.

6.3.5 Influence of free-stream velocity U_∞ at constant σ

To investigate the influence of the free-stream velocity U_∞ on the characteristics of the cavitating flow, a free-stream velocity of $U_\infty = 50\ \mathrm{ms}^{-1}$ is chosen, but fixing the value for the cavitation number, i.e. $\sigma = 1.0$ by increasing the reference pressure p_∞. The results are obtained on the 200-mesh presented in figure 6.4 employing the first- and second-order reconstruction method. The numerical time step Δ_{cfl} is equal to $\Delta_{cfl} \approx 3.77 \times 10^{-8} s$. The initial conditions are presented in table 6.8.

The behavior of the cavitation during the shedding cycle appears to be similar compared to the results for $U_\infty = 12\ \mathrm{ms}^{-1}$ at the same value of σ. In figures 6.15 and 6.16 the total vapor volume V_{vap}, the lift and drag coefficients c_l and c_d are presented for four periods in the periodic shedding phase. Applying a Fast Fourier Transform (FFT) on the "signal" of the total vapor volume, the frequency and corresponding

U_∞ $[\mathrm{ms}^{-1}]$	p_∞ $[10^5\,\mathrm{Pa}]$	T_∞ [K]	ρ_∞ $[\mathrm{kgm}^{-3}]$	c_∞ $[\mathrm{ms}^{-1}]$	σ [-]
50	12.5	293	998.7	1540.0	1.0

TABLE 6.8: *Conditions for cavitating flow about 2D NACA0015 hydrofoil at* 6° *angle of attack with chord length* $c = 0.13m$ *with* $U_\infty = 50\ \mathrm{ms}^{-1}$ *and* $\sigma = 1.0$.

Strouhal number based on the chord length are calculated. These are presented in table 6.9 together with the time-averaged and the extremum values.

order	f [Hz]	St_c [-]	$\bar{V}_{vap}$ $[10^{-2}]$	min/max V_{vap} [%]	$\bar{c}_l$ [-]	min/max c_l [%]	$\bar{c}_d$ [-]	min/max c_d [%]
1	186	0.48	1.02	84/118	0.49	-217/175	0.063	-489/173
2	106	0.28	5.06	67/139	0.64	-412/307	0.119	-526/434

TABLE 6.9: *Cavitating flow about 2D NACA0015 at* 6° *angle of attack with* $U_\infty = 50\ \mathrm{ms}^{-1}$, $\sigma = 1.0$. *Fine mesh with 200 nodes on hydrofoil controur. Frequency* f, *Strouhal number* St_c, *time-averaged total vapor volume* $\bar{V}_{vap}$, *extreme values in total vapor volume, time-averaged lift and drag coefficients* $\bar{c}_l$ *and* $\bar{c}_d$ *and extreme values in lift and drag coefficients.*

From table 6.9 we conclude that the Strouhal number St_c based on the chord length found for a free-stream velocity $U_\infty = 50\ \mathrm{ms}^{-1}$ for first- and second-order reconstruction on the 200-mesh are approximately equal to the values found for $U_\infty = 12\ \mathrm{ms}^{-1}$ presented in table 6.6. Thus, keeping the same value for σ results in the same characteristics of the shedding of the cavity sheet. However, for $U_\infty = 50\ \mathrm{ms}^{-1}$ the formation and shedding of vapor is much faster in time than for $U_\infty = 12\ \mathrm{ms}^{-1}$, which is illustrated by the higher value for the frequency. Furthermore, the time-averaged total vapor volume $\bar{V}_{vap}$ is approximately equal for $U_\infty = 50\ \mathrm{ms}^{-1}$ and $U_\infty = 12\ \mathrm{ms}^{-1}$. The maximum and minimum total vapor volume for $U_\infty = 50\ \mathrm{ms}^{-1}$ are slightly higher and lower, respectively, than for $U_\infty = 12\ \mathrm{ms}^{-1}$. Thus, to obtain the same shedding behavior, calculation time can be saved by taking a higher value for the free-stream velocity keeping the cavitation number σ the same. Furthermore, the periodic behavior is reached earlier in time resulting in a shorter start-up phase of the simulation.

Compared to the results for $U_\infty = 12\ \mathrm{ms}^{-1}$ the values for the time-averaged drag coefficient appears to be similar. However, the time-averaged lift coefficient for the second-order results is much higher for $U_\infty = 50\ \mathrm{ms}^{-1}$ compared to the one for $U_\infty = 12\ \mathrm{ms}^{-1}$. The extremum values of the lift and drag coefficients appear to be less than for $U_\infty = 12\ \mathrm{ms}^{-1}$.

As is illustrated in figures 6.15 and 6.16 the patterns of the total vapor volume, the lift and drag coefficient are found to follow the same global behavior as for $U_\infty = 12$ ms^{-1} as presented in figures 6.10 and 6.12. We have compared the results for the void fraction for $U_\infty = 50$ ms^{-1} with the results for the void fraction with $U_\infty = 12$ ms^{-1} illustrated in figures 6.8 and 6.11. Globally, the solutions for the void fraction appear to be similar, therefore, the solution for the void fraction for $U_\infty = 50$ ms^{-1} is omitted in this section.

6.3.6 Remark on development of cavitating flow after start-up

In this section the simulation of cavitating flow has been started from uniform water flow. A large number of time-steps need to be taken before the shedding of the sheet becomes periodic. Basically, at start-up of the simulation the uniform water flow hits the hydrofoil followed by a shock wave running from the leading edge of the foil in upstream direction until it leaves the domain through the inlet boundary. At the suction side of the foil and around the trailing edge an expansion wave is generated causing immediate evaporation of the water resulting in a vapor pocket. The left running shock wave and right running expansion wave are reflected back and forth from the top and bottom walls of the channel and from the hydrofoil before they disappear through the non-reflective in- and outlet.

Due to the ambient higher pressure the vapor pocket on the back of the hydrofoil disappears causing pressure waves to run through the domain. The pressure on the suction side of the foil becomes equal to the saturation pressure and a vapor sheet develops. This sheet grows in time until a re-entrant jet is formed causing the shedding of the vapor sheet. In the start-up phase of the calculation the transient pressure waves influence the speed and movement of the re-entrant jet and of the cavity sheet.

The processes described above are repeated continuously. After a certain time the initial pressure waves resulting from the start-up from uniform flow conditions have disappeared and the cavitating flow on the hydrofoil is allowed to grow and shed freely. On the fine grid presented in figure 6.4 about 2.5 million time steps have to be taken before this repeatable behavior is reached and thus it becomes clear that unsteady cavitating flow problems must be calculated for a long time before the initial flow disturbances disappear.

It is also possible to start from a steady-flow solution for single-phase water flow at the same free-stream conditions. The start-up phase is then reduced but it still takes many time steps before the periodic shedding behavior is observed. Applying the same free-stream conditions the same periodic behavior is predicted when started

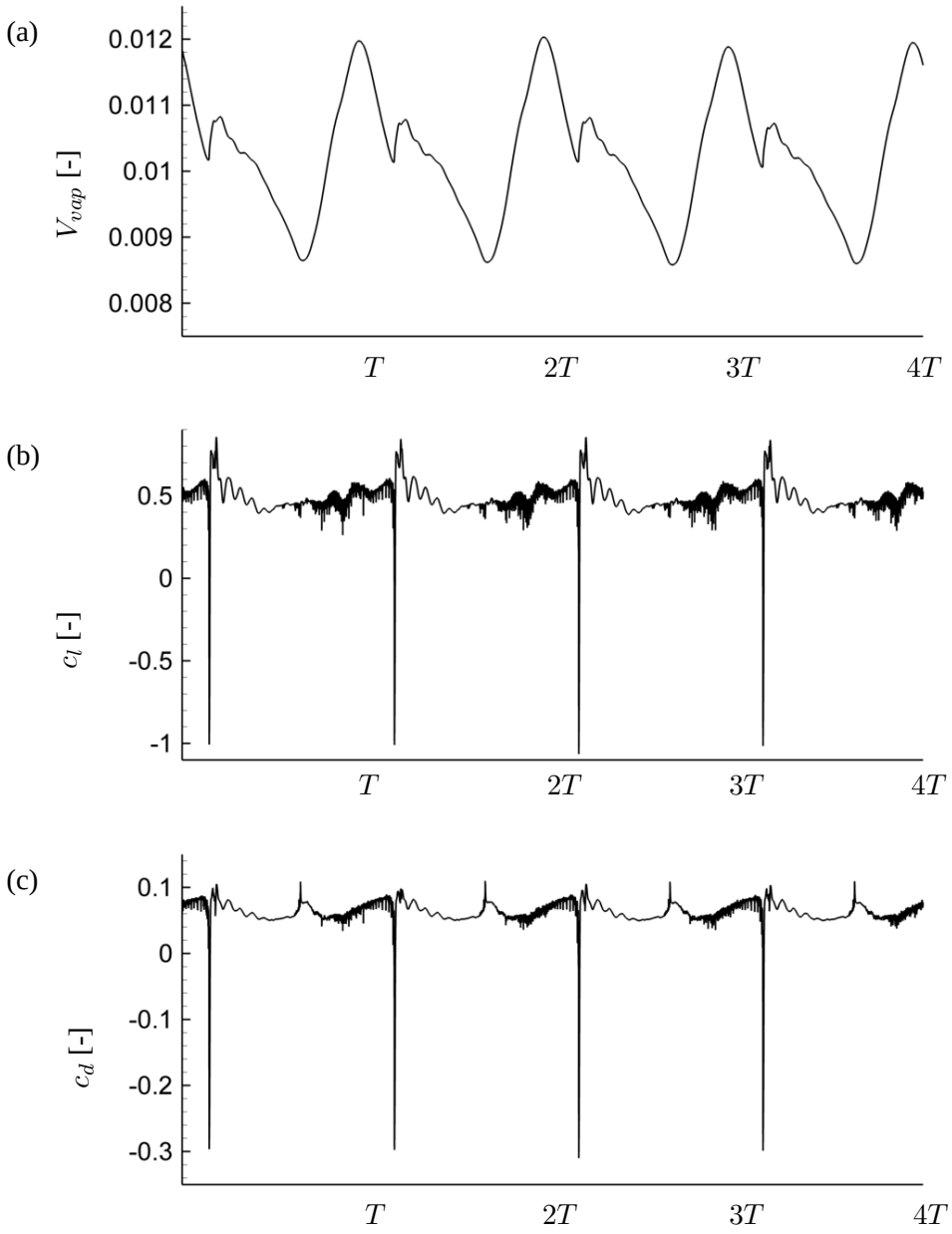

FIGURE 6.15: *Unsteady cavitating flow about 2D NACA0015 hydrofoil at* 6° *angle of attack.* $\sigma = 1.0$ $U_\infty = 50\ \mathrm{ms}^{-1}$. *First-order reconstruction on fine grid.* $T = 5.38\times10^{-3}\mathrm{s}$, $f = 186\mathrm{Hz}$, $S_{t_c} = 0.48$. *(a) Time-dependent vapor volume (b) Lift coefficient* c_l *(c) Drag coefficient* c_d.

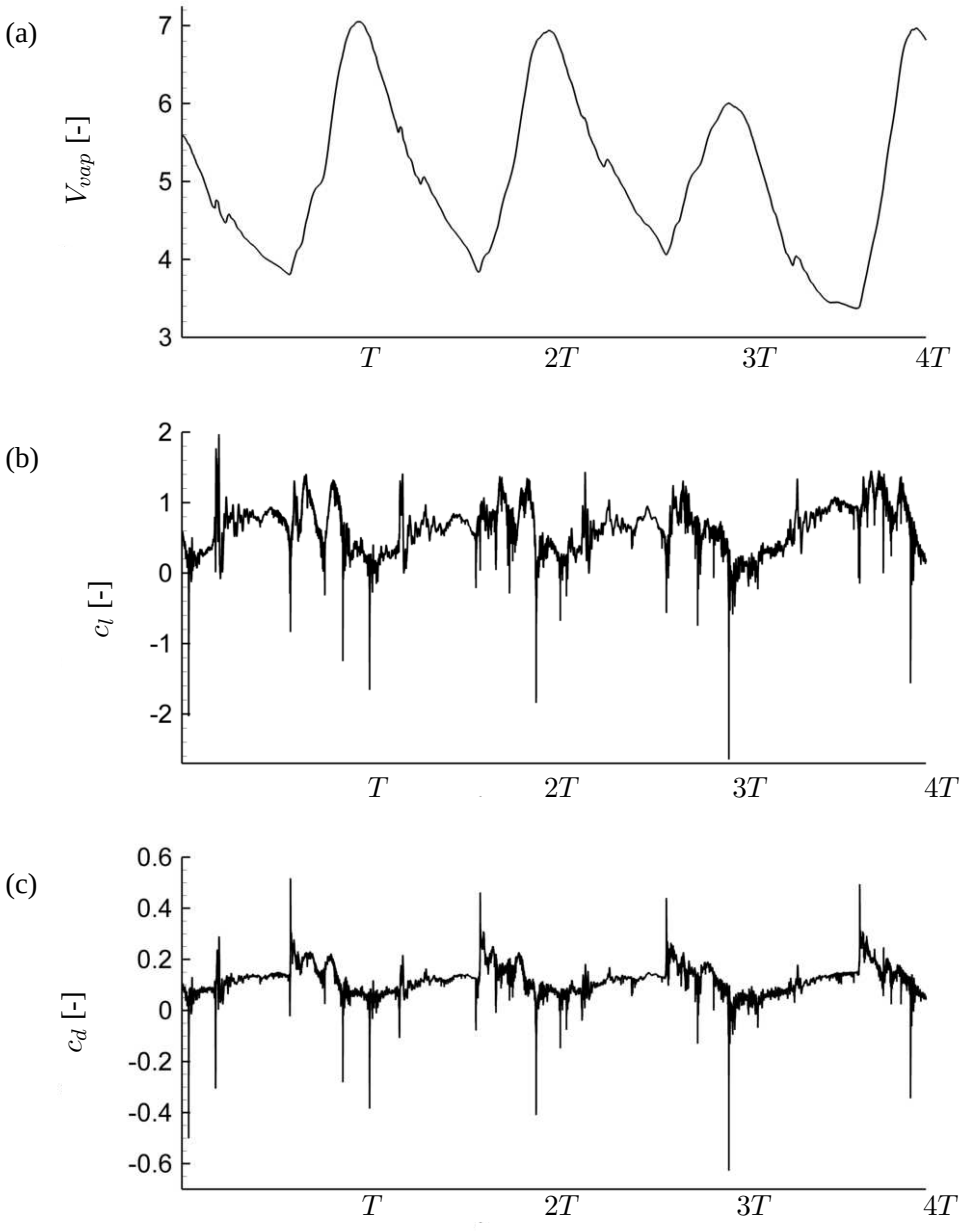

FIGURE 6.16: *Unsteady cavitating flow about 2D NACA0015 hydrofoil at* 6° *angle of attack.* $\sigma = 1.0$ $U_\infty = 50\ \mathrm{ms}^{-1}$. *Second-order reconstruction on fine grid.* $T = 9.43\times10^{-3}\mathrm{s}$, $f = 106\mathrm{Hz}$, $S_{t_c} = 0.28$. *(a) Time-dependent vapor volume (b) Lift coefficient* c_l *(c) Drag coefficient* c_d.

from an uniform flow solution or from a steady-flow solution for single-phase water flow.

To speed up the calculation towards the periodic cavitating flow, it might be worthwhile to investigate methods such as multi-grid, preconditioning and/or implicit time-integration, which allow larger numerical time steps to be taken. However, care should be taken that the larger numerical time steps still resolve the high-frequency pressure pulses, which we believe to have a major influence on the self-oscillatory behavior of the sheet cavity and its shedding.

6.4 Unsteady cavitating flow about 3D Twist11 hydrofoil

The unsteady cavitating flow about the 3D Twist11 hydrofoil at -2° angle of attack with chord length $c = 0.15\ \mathrm{m}$ is calculated, to compare the results obtained with the present edge-based numerical method with the experiments of Foeth [67]. Foeth carried out experiments for cavitating flow with steady and unsteady inflow. Here, only steady inflow is considered at the cavitation number $\sigma = 1.1$. An overview of the characteristics of the experiments has been provided in section 2.3. The focus in this section is on comparing the numerical results for the behavior and structure of the vapor sheet with the experiments of Foeth [67].

The geometry of the hydrofoil is presented in section 5.7.1 together with the computational domain as presented in figure 5.24. The geometry is symmetric with respect to the mid-span plane. It is assumed that the flow is also symmetric about this plane. Therefore, in order to save computational time only the starboard-half of the test section and the foil is considered. This assumption of the hydrodynamic symmetry is supported by the experimental findings, see Foeth [67], where it is shown that small scale structures are symmetric with respect to the mid-span plane. The solution for fully-wetted (single-phase) water flow has been presented in section 5.7.

To speed-up the formation and shedding of the cavity sheet in the numerical simulations, calculations are performed at a free-stream velocity of $U_\infty = 50\ \mathrm{ms}^{-1}$ at the same cavitation number $\sigma = 1.1$ as in the experiments of Foeth [67]. The free-stream conditions are presented in table 6.10.

U_∞ $[\mathrm{ms}^{-1}]$	p_∞ $[10^5\,\mathrm{Pa}]$	T_∞ [K]	σ [-]
50	13.75	297	1.1

TABLE 6.10: *Free-stream conditions for cavitating flow about 3D Twist11 hydrofoil at -2° angle of attack.*

For the inflow the non-reflective boundary condition is employed. For the outflow the asymptotic non-reflective pressure boundary condition is applied. The in- and outflow boundary conditions are an approximation of the flow conditions, since the cavitation tunnel does not have a prescribed flow at the in- and outlet. We have extended the computational domain compared with the cavitation tunnel to ensure that the in- and outflow are located away from regions with cavitation. The top and bottom of the channel are slip solid walls treated with the symmetry technique and for the slip solid wall of the hydrofoil the curvature-corrected symmetry technique is applied. The results are obtained with the second-order hybrid HLLC/AUSM flux

scheme of section 4.7.2 with the limiter method of Venkatakrishnan employing the primitive variables $[\rho, u, v, w, e]^T$.

Two grids are considered as presented in table 6.11: a coarse tetrahedral grid with 68k control volumes and a finer tetrahedral grid with 205k control volumes. The coarse tetrahedral mesh has been considered in section 5.7 for the single-phase water flow calculations. Employing the first-order reconstruction on the coarse mesh, the sheet cavity is found to become steady for this mesh. For the second-order reconstruction method on the coarse mesh we find that the resolution of the cavity sheet and its shedding is not adequate. The coarse mesh is too coarse to resolve the re-entrant jet and the shed vapor structures properly. The re-entrant flow is captured within one computational control volume and the sheet cavity occasionally sheds vortical vapor regions, which quickly dissipate.

To improve the resolution in the region with cavitation, the finer mesh is obtained by refining the region along the suction side of the hydrofoil to approximately 10% chord length in normal direction to ensure that the sheet cavity is located in this refined region. With the use of prismatic layers on top of the hydrofoil the resolution of the mesh near the surface of the hydrofoil can be improved even further in order to capture the re-entrant and side-entrant flows more accurately. However, for the global behavior of the shedding of the sheet cavity this is not found necessary. The first-order solution on the coarse grid has been used as the initial solution for the numerical solutions performed on the fine grid by employing the solution-interpolation method Grid2Grid, see Hospers [98].

A close-up of the fine mesh around the hydrofoil is presented in figure 6.17. The total number of elements and number of tetrahedrons for both meshes are presented in table 6.11 along with the corresponding numerical time step Δt_{cfl} for the chosen CFL number of 0.8.

mesh	# control volumes	# tetrahedrons	Δt_{cfl} $[10^{-8}\text{s}]$
coarse	69,365	356,638	2.65
fine	205,520	1,095,685	1.01

TABLE 6.11: *Number of control volumes, number of tetrahedrons and numerical time step Δt_{cfl} for cavitating flow simulations with $CFL = 0.8$.*

To accelerate the calculations the numerical method has been parallelized by decomposing the computational mesh in 8 equal-sized blocks. The results indicate that the obtained speed-up is almost linear with the number of processors. However, the par-

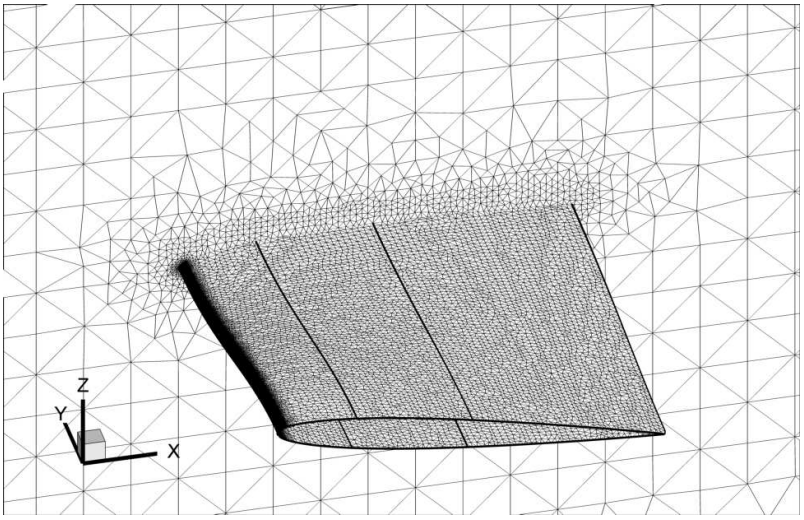

FIGURE 6.17: *Close-up of fine tetrahedral mesh for 3D Twist11 hydrofoil at -2° angle of attack. 205,520 control volumes, 1,095,685 tetrahedrons.*

allelization needs to be optimized further.

On a Quad-Core Xeon X5460 3.16GHz /2x6MB cache, 1333 FSB, 8GB memory computer and employing the parallelization for 8 processors it takes approximately 1h to calculate 500 time steps using the second-order reconstruction method on the fine mesh. This corresponds with $5 \times 10^{-6}\,\mathrm{s}$ in simulation time. In this case the small tetrahedral elements at the leading edge of the foil restrict the numerical time step. These small elements are necessary to resolve the high curvature of the nose of the NACA0009 hydrofoil. A thicker hydrofoil such as the NACA0015 as presented in section 6.3 would allow for larger elements to be used at the leading edge of the foil.

6.4.1 Total vapor volume

The transient evolution of the cavitating flow can be illustrated with the total vapor volume as defined in equation (6.3) as a function of time. In figure 6.18 the total vapor volume is presented for the present numerical simulation which progressed up to $10\,\mathrm{ms}$. From Foeth [67] it follows that the shedding cycle takes about $38\,\mathrm{ms}$ at a free stream velocity of $6.58\,\mathrm{ms}^{-1}$. For the present case of $50\,\mathrm{ms}^{-1}$ this would correspond with a shedding cycle of $5\,\mathrm{ms}$.

Figure 6.18 clearly indicates that the time period covered does not contain shedding cycles. The flow is not yet periodic in time and the calculation should be continued further. In this section the formation of re-entrant flow and the formation of a cavitating horse-shoe vortex is discussed. Both phenomena are quite similar to the ones observed in the experiments of Foeth [67].

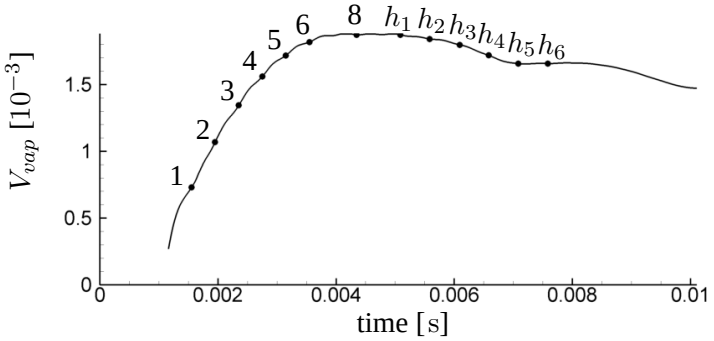

FIGURE 6.18: *Total vapor volume 3D Twist11 hydrofoil at -2° angle of attack, $\sigma = 1.1$. Fine grid, second-order hybrid HLLC/AUSM flux scheme. Points 1–6 correspond with figure 6.19(1)–(6) and with figure 6.20(1)–(6). Point 8 corresponds with figure 6.21. Points h_i correspond with the solutions of the cavitating horse-shoe vortex presented in figures 6.22(1)–(6) and point h_3 corresponds with figure 6.23.*

The black dots refer to the solutions presented in figures 6.19–6.23. The points 1–6 correspond with figure 6.19(1)–(6) and 6.20(1)–(6). Point 8 corresponds with figure 6.21. The points h_i correspond with figure 6.22(1)–(6) and point h_3 corresponds with figure 6.23.

6.4.2 Re-entrant flow

In this section the re-entrant flow on the surface of the hydrofoil and the onset of shedding of the sheet cavity is illustrated for the first shedding cycle. During the growth of the sheet, a re-entrant flow is already moving upstream underneath the vapor sheet, which is confirmed by the experimental results of Foeth [67].

As illustrated in figure 6.18 by the points 1–8 we select a number of time-instants t_N during the part of the cycle in which the sheet cavity grows to its longest extent. Here, $t_N = t_0 + N\Delta$, where t_0 approximately corresponds with the start of the growth of the sheet. Furthermore, $N = 1, 2, \ldots$ and $\Delta t = 4.0 \times 10^{-4}$s, which corresponds to 40k numerical time-steps.

In the left pictures of figure 6.19 two iso-contours of the void fraction, i.e. $\alpha = 0.05$ and $\alpha = 0.5$ are presented. In the right pictures of figure 6.19 the streamlines on the surface of the hydrofoil are shown colored by value of the void fraction α. The vectors indicate the direction of the flow. The time-interval between each picture (1)–(6) is $\Delta t = 4.0 \times 10^{-4}$ s. The total time presented in figure 6.19 is 2.4×10^{-3} s.

At the time-instants of figure 6.19, the left pictures of figure 6.20 gives the contours

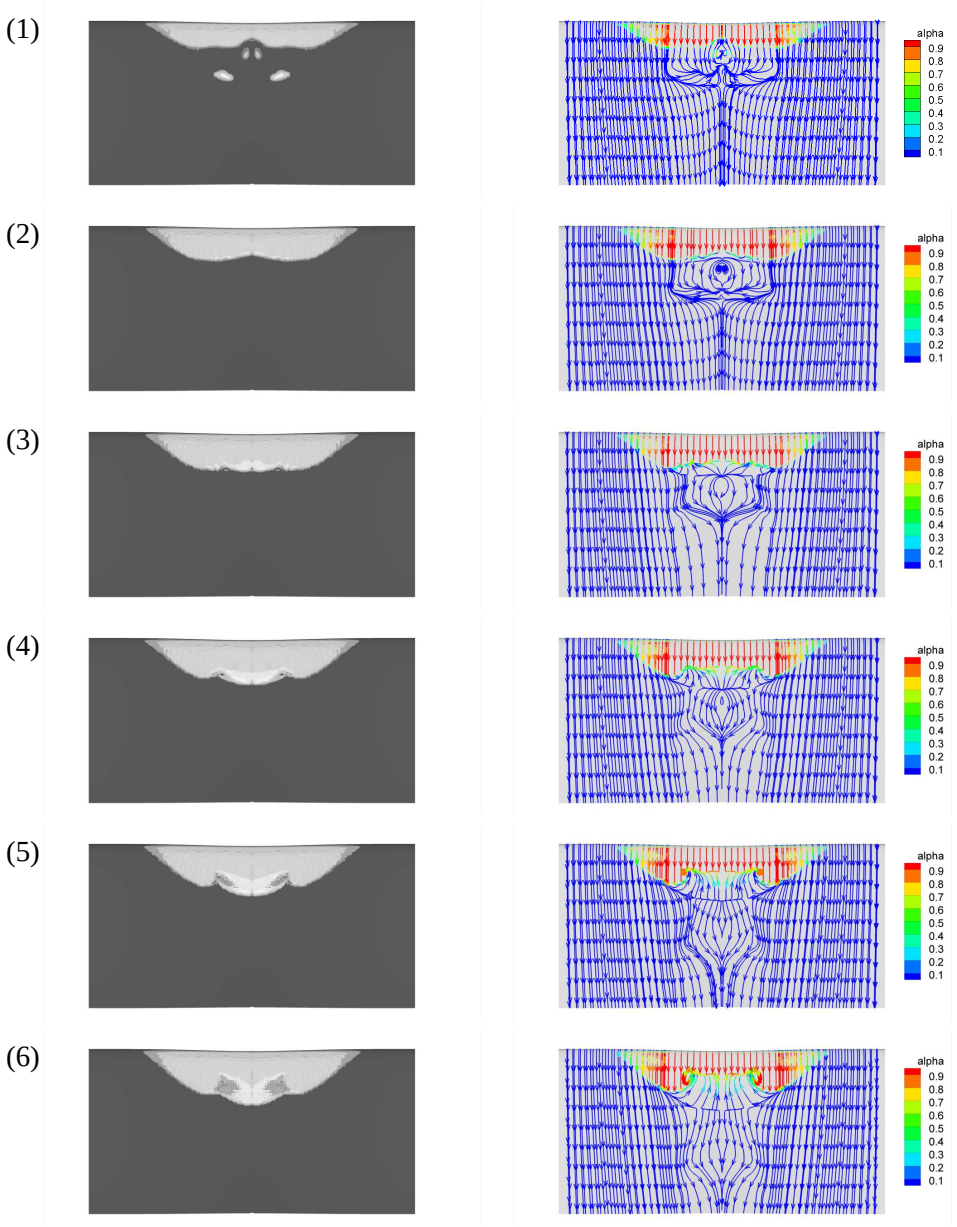

FIGURE 6.19: *Re-entrant flow for 3D Twist11 hydrofoil at* $-2°$ *angle of attack,* $\sigma = 1.1$. *Fine grid, second-order hybrid HLLC/AUSM flux scheme.* Δt *between rows:* $\Delta t = 4.0 \times 10^{-4}$ s. *Pictures (1)–(6) correspond with points 1–6 in figure 6.18. (left) iso-contours* $\alpha = 0.05$ *and* $\alpha = 0.5$. *(right) streamlines on surface of the hydrofoil colored by value of the void fraction.*

of the y-component of the vorticity $\omega_y/\left(U_\infty/c\right)$ at the plane of symmetry. The y-direction is pointing into the picture. Two contours of the void fraction, i.e. $\alpha = 0.05$ and $\alpha = 0.5$, are indicated with the thick black lines. The streamlines on the plane of symmetry are given by the thin black lines to visualize the flow pattern. In the right pictures of figure 6.20 the pressure on the surface of the hydrofoil and the plane of symmetry is presented together with two iso-surfaces $\alpha = 0.05$ and $\alpha = 0.5$ of the void fraction.

In figure 6.19(1) the vapor sheet is at the leading edge of the foil and growing. Shed vapor structures produced earlier are still visible. Around these vapor structures a circulatory flow is generated as illustrated in the right picture by the reversed flow region on the surface of the hydrofoil underneath the vapor regions. The circulatory flow region around the shed vapor structures is clearly visible in the left picture of figure 6.20(1). Furthermore, at the closure of the sheet cavity a region with high vorticity has developed, which will drive the re-entrant flow. As shown in the right picture of figure 6.20(1) the pressure underneath the vapor sheet is equal to the saturation pressure approximately equal to $p_{sat}(T) \approx 3,000\,\mathrm{Pa}$ at $T = 297\mathrm{K}$. Also, the low pressure around the shed vapor structures is visible.

In picture 6.19(2) the earlier shed vapor regions have disappeared and the region with circulatory flow is convected with the flow. At the same time a re-entrant flow is starting to develop at the closure line of the sheet cavity as illustrated in pictures 6.19(2) and 6.19(3) starting as a side-entrant jet. The pressure pulse due to the collapse of the vapor structures is not visible due to the large time-interval between pictures (2) and (3), i.e. $\Delta t = 4.0 \times 10^{-4}\,\mathrm{s}^\dagger$.

In pictures 6.19(4)–6.19(6) the re-entrant jet moves upstream underneath the sheet cavity. This flow is mainly a flow of liquid indicated by the blue color of the streamlines. The vortical flow regions are convected further downstream with the flow. In picture 6.19(3) the re-entrant flow appears to be directed outward from the plane of symmetry. In picture 6.19(4) a small side-entrant flow has developed at the outline of the sheet cavity. In picture 6.19(6) the re-entrant flow is fully developed and side-entrant flow is visible. The re-entrant flow presented in the left pictures of figures 6.19(4)–6.19(6) show very close agreement with figure 5.14 of the thesis of Foeth [67].

In the surface streamline pattern in the right pictures of figure 6.19 a region with retarded flow is seen. The location of this region on the surface corresponds with the

†*Note that during this time the pressure pulse has traveled approximately* $1540 \times 4.0 \cdot 10^{-4}\,\mathrm{m} = 0.616\,\mathrm{m}$. *The chord length of the foil is* $c = 0.15\,\mathrm{m}$.

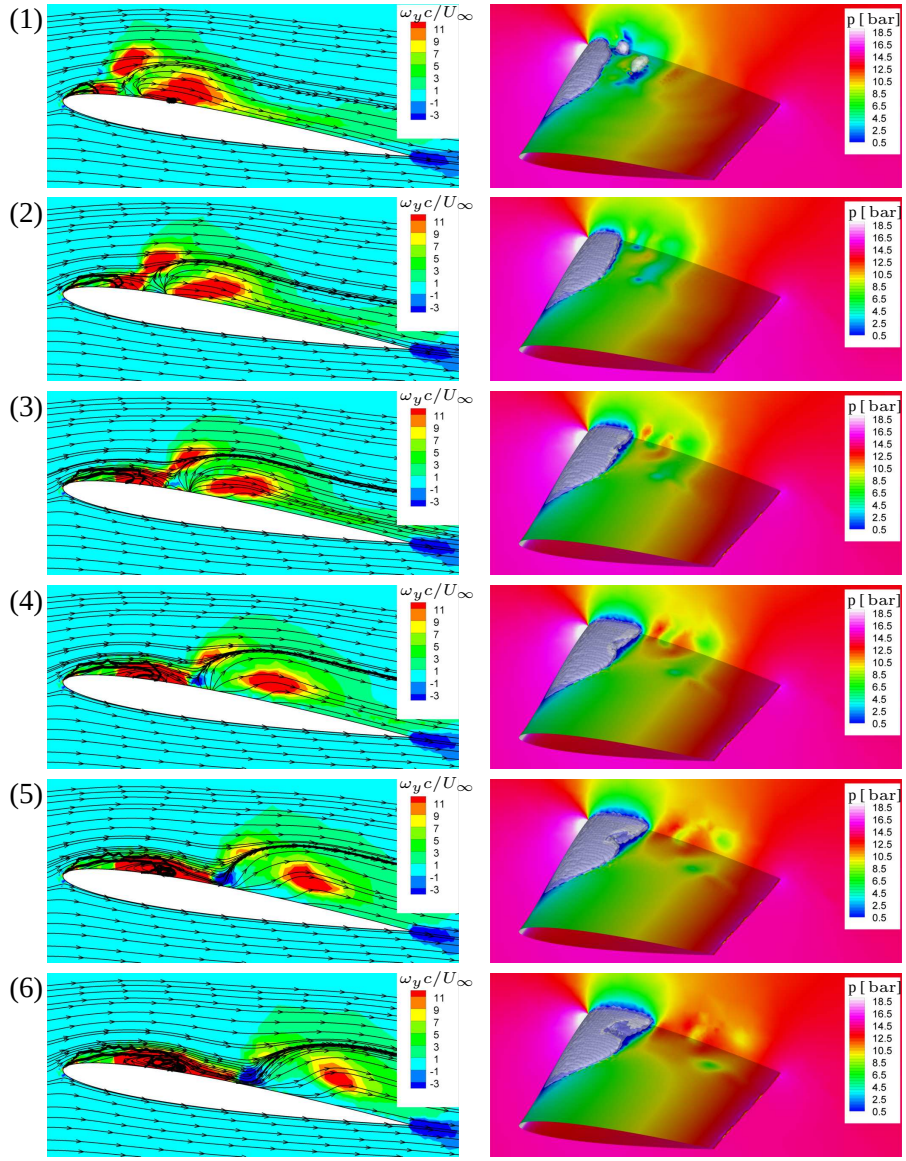

FIGURE 6.20: *3D Twist11 hydrofoil at* -2° *angle of attack,* $\sigma = 1.1$. *Fine grid, second-order hybrid HLLC/AUSM scheme.* Δt *between rows:* $\Delta t = 4.0 \times 10^{-4}$s. *Pictures (1)–(6) correspond with points 1–6 in figure 6.18. (left) streamlines on symmetry plane. Contours of* y*-component of vorticity* $\omega_y c/U_\infty$. y*-axis is pointing into the picture. Thick black lines denote contours* $\alpha = 0.05$ *and* $\alpha = 0.5$. *(right) pressure on surface of hydrofoil and on symmetry plane. Iso-contours* $\alpha = 0.05$ *and* $\alpha = 0.5$.

location of the large vortical structure in figure 6.20.

As visible in the left picture of figure 6.20(4) by the streamlines on the symmetry plane, a small vortical region is created at the closure region of the sheet cavity. This vortical region becomes stronger and larger as visible in the left pictures of figures 6.20(5) and (6). This results in the cut off of the first vapor structures, which is indicated by the separated region at the closure of the sheet cavity denoted by the thick black line representing a void fraction equal to $\alpha = 0.5$.

In figure 5.19 of the thesis of Foeth [67] the cut-off of the first vortical structure at the closure line of the sheet cavity is discussed in detail. The sketch from the results of the experiments corresponds fairly well with the left picture in figure 6.20(6). The re-entrant jets have met at mid-span. Then, they are reflected outward and are impinging through the sheet cavity above the re-entrant flow as sketched in figure 2.8(b) in chapter 2 of this thesis. The fluid impinging on the interface isolates a region of vapor as visible in the left picture of figure 6.19(6). Around this vapor region a circulatory flow pattern is observed as illustrated by the streamlines in the left picture of figure 6.20(6). This region with circulatory flow is detached from the sheet cavity and advected with the flow. Thus, the impingement and detachment of the vapor structure is captured in the present numerical simulations based on the Euler equations. This suggests that these phenomena appear to be inertial in nature.

Note that in figure 6.19(6) a sharp interface between the liquid in the re-entrant jet and the vapor in the cavity above the re-entrant flow does not appear to be present in the numerical simulation. The interface between the liquid and vapor is captured within 2–3 computational cells. Refining the grid close to the surface of the hydrofoil by employing prismatic layers will improve the accuracy of capturing the re-entrant flow.

Figure 6.21 presents the solution at time-instant t_8, which corresponds with point 8 in figure 6.18 and which is $2\Delta t$ later than the results shown in figures 6.19(6) and 6.20(6). Presented are the outline of the sheet cavity, the streamlines and the pressure on the surface of the hydrofoil. Compare figures 2.8(b)–(d) with figures 6.21(a)–(b). In figure 6.21(a) it is shown that the vapor in the center of the hydrofoil is now detached from the main sheet cavity. Also, two side-lobes of the sheet cavity have formed. In figure 6.21(b) the re-entrant flow is clearly moving towards the leading edge of the foil. Note the sharp transition from liquid to vapor at the mid-span of the hydrofoil.

In figure 6.21(c) the pressure on the surface of the hydrofoil together with the two iso-contours $\alpha = 0.05$ and $\alpha = 0.5$ are given. Note that at mid-span between the

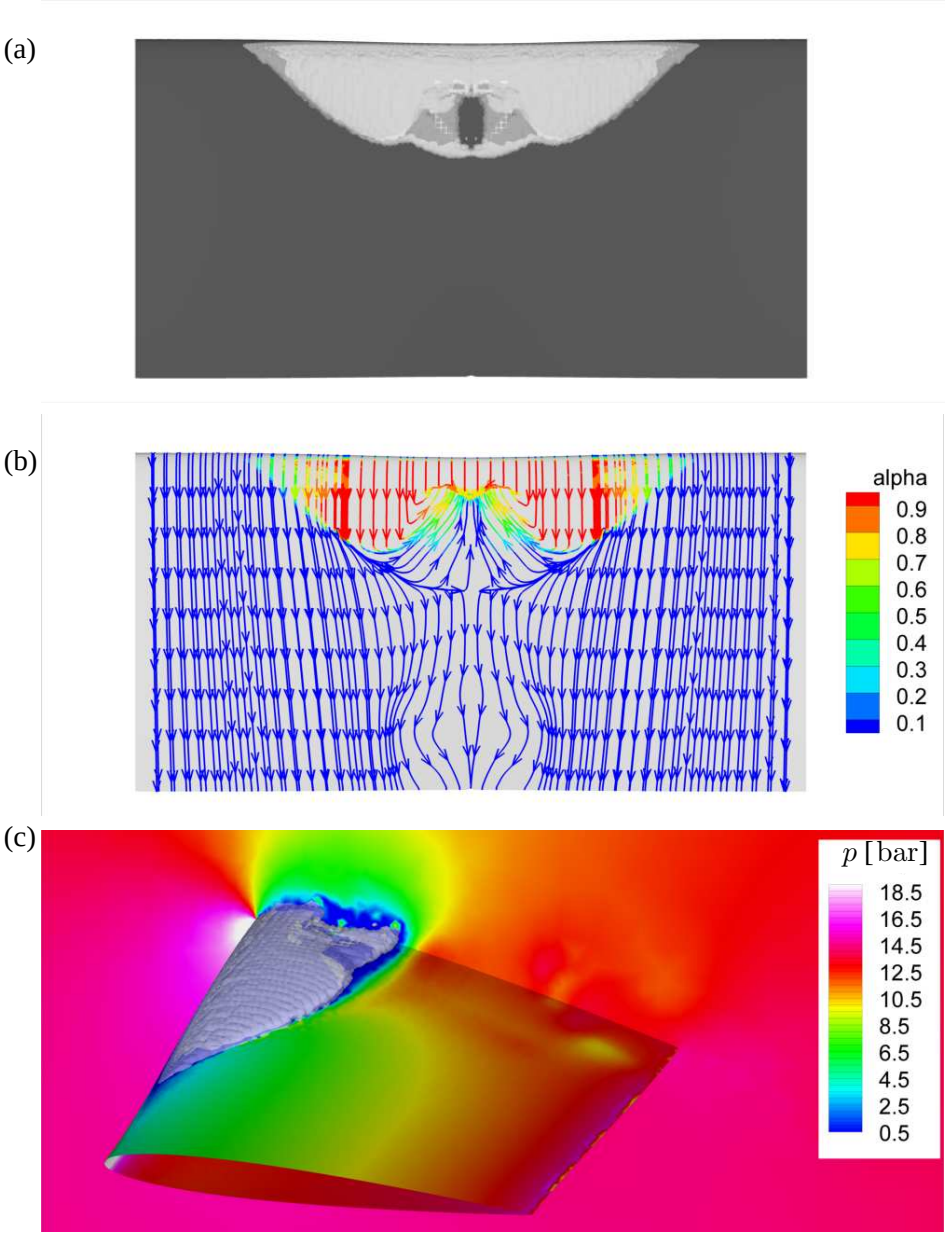

FIGURE 6.21: *3D Twist11 hydrofoil at* $-2°$ *angle of attack.* $\sigma = 1.1$, $T = 297\mathrm{K}$, $p_{sat}(T) = 0.03\mathrm{bar}$. *Fine grid, second-order hybrid HLLC/AUSM scheme. Time-instant* t_8*, which corresponds with point 8 in figure 6.18. (a) Iso-surfaces* $\alpha = 0.05$ *and* $\alpha = 0.5$ *(b) Streamlines on surface of hydrofoil colored by the value of the void fraction. (c) pressure on surface of hydrofoil and on symmetry plane. Iso-contours* $\alpha = 0.05$ *and* $\alpha = 0.5$.

detached vapor structure and the main sheet cavity a "hole" in the vapor appears. Here, at the edge of the sheet cavity and the edge of the shed vapor structure pressure pulses are observed due to the collapse of (small) vapor regions.

6.4.3 Formation of a cavitating horse-shoe vortex

A very distinct feature of the shedding of the sheet cavity on the 3D Twist11 hydrofoil is the formation of a cavitating horse-shoe vortex at the center of the hydrofoil. See for instance the experimental results of Foeth [67] reported in figures 2.7(c)–(k).

In figure 6.22(1)–(6) the formation and convection of such a cavitating horse-shoe vortex in the numerical simulation is illustrated. Presented are a top view and a side view of the hydrofoil, the sheet cavity and the horse-shoe vortex. The time-instants presented correspond with points h_1–h_6 in figure 6.18.

In figure 6.22(1) the shed vapor region in the center of the foil detaches from the sheet cavity and forms a horse-shoe vortex. The center of the vortex is convected upward, primarily by its self-induced velocity.

The horse-shoe vortex is convected with the flow and is about to collapse in figure 6.22(6). The height of the horse-shoe vortex is clearly visible in figure 6.22(3) and (4). It reaches up to 2–3 times the thickness of the sheet cavity. In the experiments of Foeth the height of the shed vapor cloud is found to be an important feature.

The sheet cavity at the center of the hydrofoil starts to grow again. The side-lobs of the sheet are clearly visible. The shape of the remaining of the sheet cavity correspond very well with the experimental results. Refer to the sketches of the sheet presented in figure 2.8(c) and (d).

As comparison a picture of the experimental results is presented in figure 6.23(b). Foeth [66] reports that the conditions for this picture were slightly different, i.e. $\alpha = -1^\circ$ and $\sigma = 1.13$. However, the effects of the slight increase in angle of attack are counteracted by the slight increase in cavitation number and thus, the two conditions are very similar. Foeth [66] mentions that the overall shedding of the sheet cavity did not change much compared to the conditions presented in this section, i.e. $\alpha = -2^\circ$ and $\sigma = 1.1$.

Figure 6.23 illustrates that the calculated shape of the sheet cavity and of the cavitating horse-shoe vortex are quite similar to the experimental observations.

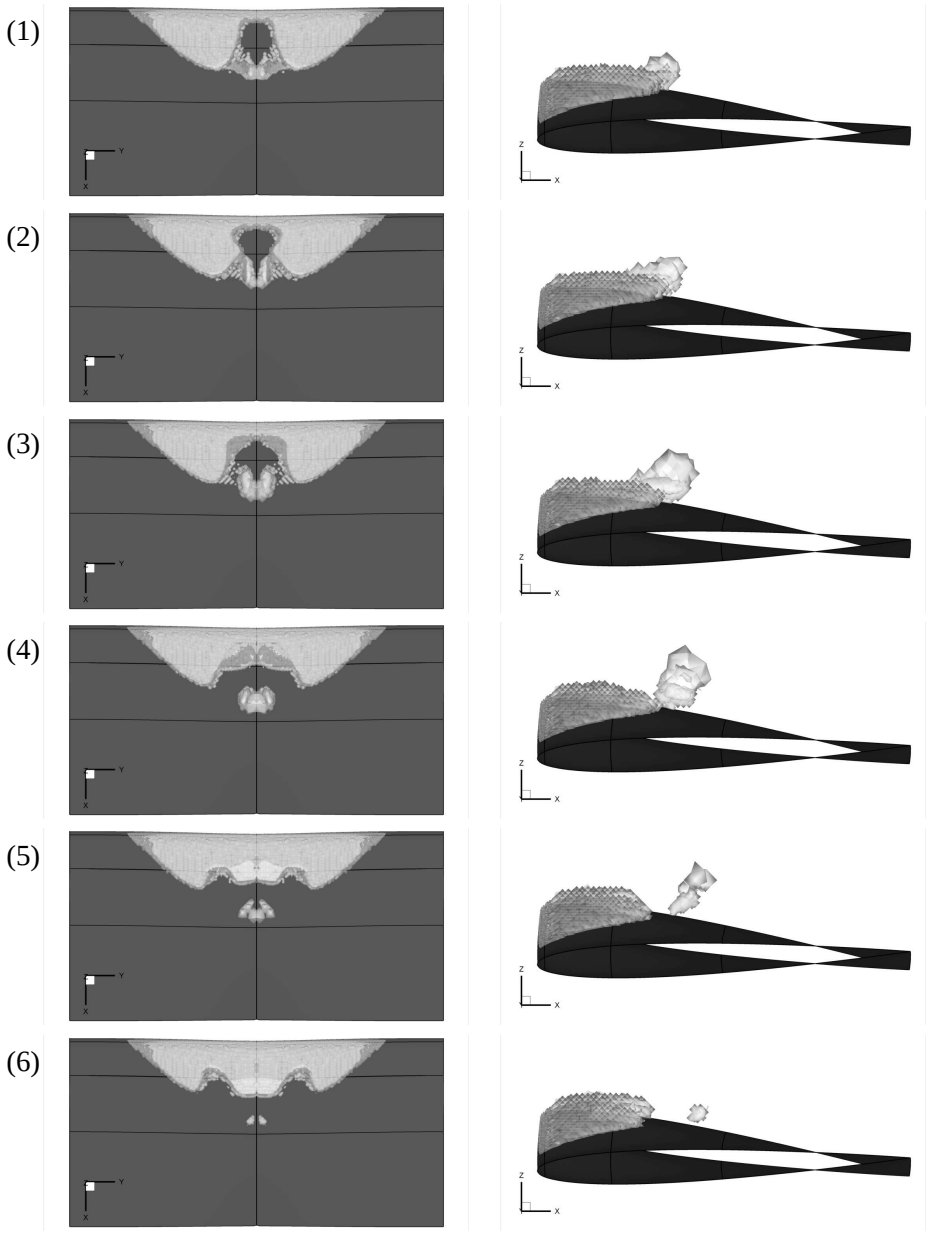

FIGURE 6.22: *Formation of a horse-shoe vortex on 3D Twist11 hydrofoil at* -2° *angle of attack,* $\sigma = 1.1$*. Fine grid, second-order hybrid HLLC/AUSM scheme. Time step between rows is equal to* $\Delta t = 5.0 \times 10^{-4}\mathrm{s}$*, which corresponds to 50k time steps. Figures (1)–(6) corresponds with points* h_1*–*h_6 *in figure 6.18. Iso-contours of void fraction equal to* $\alpha = 10^{-3}$ *and* $\alpha = 0.5$*. (left) Top view (right) side view.*

(a)

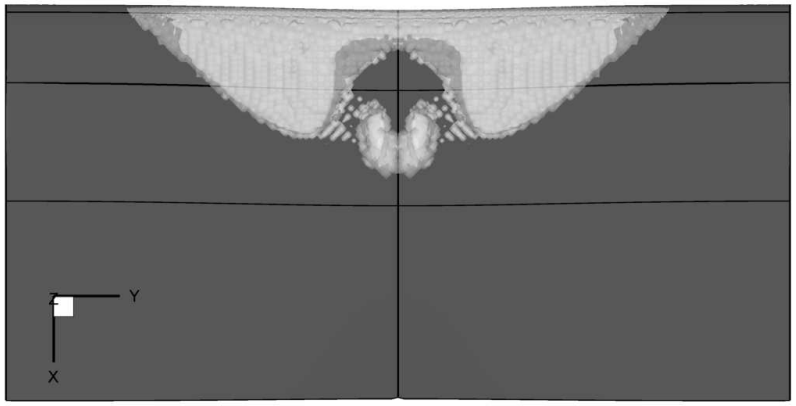

(b)

FIGURE 6.23: *Cavitating horse-shoe vortex on 3D Twist11 hydrofoil. (a) Numerical result at* -2° *angle of attack,* $\sigma = 1.1$*. Fine grid, second-order hybrid HLLC/AUSM scheme. Iso-surfaces* $\alpha = 10^{-3}$ *and* $\alpha = 0.5$ *(b) Experimental result obtained from Foeth [67], angle of attack* -1°*,* $\sigma = 1.13$*.*

6.4.4 Conclusions 3D Twist11 hydrofoil

In this section the numerical results for the cavitating flow about the 3D Twist11 hydrofoil at -2° angle of attack are presented. We have shown that the shape of the sheet cavity and the outline of the closure region as predicted by the results of the present numerical method compare quite well with the experimental results of Foeth [67].

The development of a re-entrant flow is predicted in close agreement with that seen in the experiments of Foeth. During the growth of the sheet, a re-entrant jet is already moving upstream underneath the vapor sheet, as is observed in the experiments. The predicted re-entrant flow is a flow of liquid.

The impingement of the re-entrant flow on the cavity interface and the detachment of the first vortical structure is captured in the present numerical simulations based on the Euler equations. This suggests that these phenomena appear to be inertial of nature.

The formation of a cavitating horse-shoe vortex and its advection with the flow is captured in the present numerical simulations. The numerical results agree quite well with the experimental observations.

At present the calculation times are too long to investigate the shedding of the sheet cavity on 3D configurations for long enough times. The total number of computational cells should be reduced drastically without losing the required grid resolution. Employing prismatic elements or hexahedral elements close to the surface of the hydrofoil might help since then larger aspect ratios for the computational cells can be chosen than for tetrahedral elements.

To speed up the calculation towards the periodic cavitating flow, it might be worthwhile to investigate methods such as multi-grid, preconditioning and/or implicit time-integration, which allow larger numerical time steps to be taken. However, the larger admissible numerical time steps should still resolve the high-frequency pressure pulses, which we believe to have a major influence on the self-oscillatory behavior of the sheet cavity and its shedding.

6.5 Cavitating flow about 3D Elliptic 11 Rake hydrofoil

In the cavitation tunnel at Delft University of Technology van der Hout [204] has carried out cavitating flow experiments on a three-dimensional finite-span skewed hydrofoil of elliptic planform. The purpose was to investigate the interaction between sheet and vortex cavitation for steady and unsteady inflow conditions. Here, the interest is in steady, cavitating flow solutions at uniform inflow conditions. The objective of this section is to show that the outline and shape of the sheet cavity on a complex three-dimensional geometry can be predicted with the present edge-based numerical method employing the equilibrium cavitation model. In our group this 3D elliptic hydrofoil has been studied by Ton [193] to investigate the numerical method of vorticity confinement in compressible flow of a perfect gas.[‡]

6.5.1 Geometry of 3D Elliptic 11 Rake hydrofoil

The hydrofoil considered is the so-called Elliptic 11 Rake hydrofoil. The section of the hydrofoil is a NACA0009 section defined in equation (5.7) with thickness $t = 0.09$. The chord length $c(\bar{y})$ is a function of the dimensionless span-wise coordinate $\bar{y}$ defined by the expression

$$c(\bar{y}) = \sqrt{C_R^2(1-\bar{y}^2) + \bar{y}^2 C_T^2}, \tag{6.6}$$

where $\bar{y} = y/s$ with s the semi-span of the hydrofoil, C_R is the chord-length of the root section of the hydrofoil, i.e. at $\bar{y} = 0$, and C_T is the chord length at the tip of the hydrofoil at $\bar{y} = 1$. The hydrofoil has a swept leading edge, i.e. a translation of the leading edge of the section in x-direction. The x-coordinate of the midpoint of the local section chord-line, denoted as x_0, is defined as

$$x_0(\bar{y}) = -c(\bar{y}) + C_R. \tag{6.7}$$

The hydrofoil is twisted by a rotation around the mid-chord-point $x = x_0(\bar{y})$ of the local section. The twist angle is defined as,

$$\alpha(\bar{y}) = \alpha_T \left(\frac{e^{\gamma_a \bar{y}} - 1}{e^{\gamma_a} - 1} \right) \bar{y} + \beta, \tag{6.8}$$

where β is the global rotation angle, equivalent to the angle of attack of the hydrofoil at its root section. In this section the foil has an angle of attack of $\beta = 3^\circ$. α_T is the local rotation angle at the tip and γ_a is a twist-distribution shape parameter. Finally,

[‡] *The computational meshes in this section have been provided by Ton, for which the author would like to express his gratitude.*

the foil is given rake, i.e. a translation along the z-axis, by defining the z-coordinate of the midpoint of the local chord-line, denoted as z_0, as

$$z_0(\bar{y}) = R_T \bar{y} \left(\frac{e^{\gamma_R \bar{y}} - 1}{e^{\gamma_R} - 1} \right), \tag{6.9}$$

where R_T is the rake at the tip and γ_R is a rake-distribution shape parameter. In table 6.12 the parameters used by Van der Hout for this foil are presented. In figure 6.24 a 3D view, a top view, a side view and a front view of the hydrofoil are presented.

parameter	value	parameter	value
s	0.2 m	R_T	0.02 m
C_R	0.15 m	γ_a	7.0
C_T	0.05 m	γ_R	1.0
α_T	11°		

TABLE 6.12: *Parameters for 3D Elliptic 11 Rake hydrofoil.*

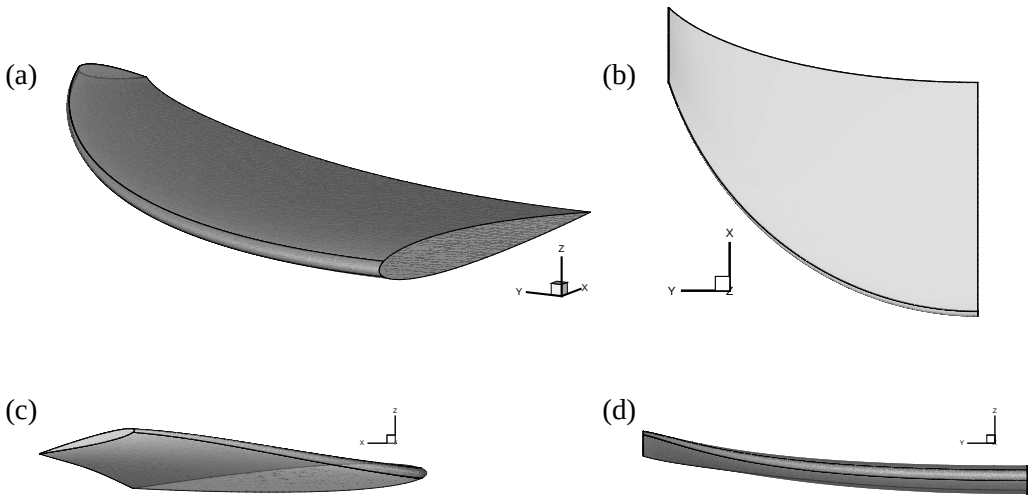

FIGURE 6.24: *3D Elliptic 11 Rake hydrofoil at $\beta = 3°$ angle of attack, flow is in x-direction. (a) 3D view (b) top view (c) side view (d) front view.*

6.5.2 Computational domain and mesh

The computational domain fits the test-section of the cavitation tunnel at Delft University of Technology. For numerical purposes the test-section has been extended

from a length of 0.6 m to a length of 0.9 m. Thus, the computational domain is a rectangular box with dimensions 0.9m×0.3m×0.3m, i.e. $6 \times 2 \times 2$ chord lengths C_R. The origin of the domain is taken as the midpoint of the chord-line of the hydrofoil at the root section of the foil. The foil is mounted to the tunnel wall and the tip of the foil is located at $2/3$ of the width of the tunnel. The computational domain is presented in figure 6.25.

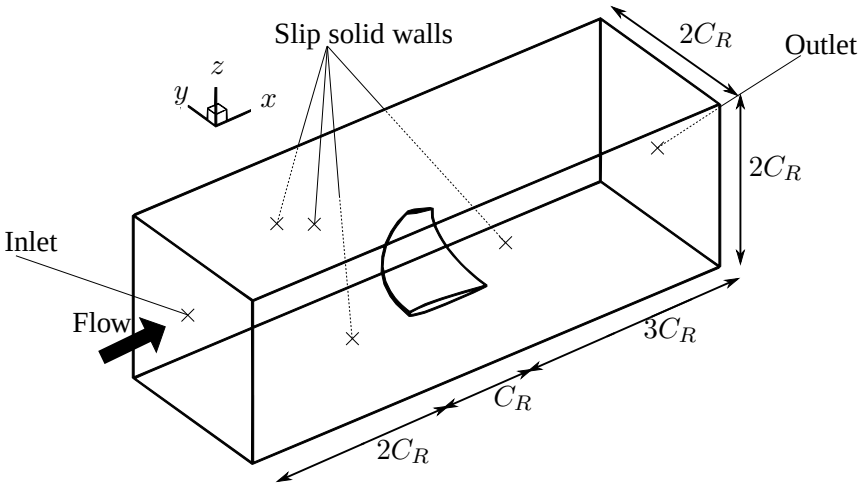

FIGURE 6.25: *Computational domain for 3D Elliptic 11 Rake Hydrofoil at* 3° *angle of attack. The flow is from left to right. The walls of the channel are slip solid walls, the left and right side are the in- and outflow, respectively. The surfaces of the foil are solid slip walls.*

Two computational meshes have been constructed utilizing the software package ICEM-CFD: a coarse grid containing 270k tetrahedral elements and a finer grid consisting of 567k tetrahedrons. The coarse grid is only used to obtain a suitable initial solution for the numerical simulations performed on the fine grid and is not discussed further.

In figure 6.26 the fine mesh for the complete domain is presented. Note that the computational domain is rotated compared with the view shown in figure 6.25. The fine grid features a cylindrically refined region with its axis located along the expected path of the tip vortex. This cylindrical region is visible in figure 6.26 at the outflow boundary. In figure 6.27 a close-up of the surface mesh in the tip region of the hydrofoil is shown. The grid is refined in the regions around the trailing edge, the wing tip and the leading edge.

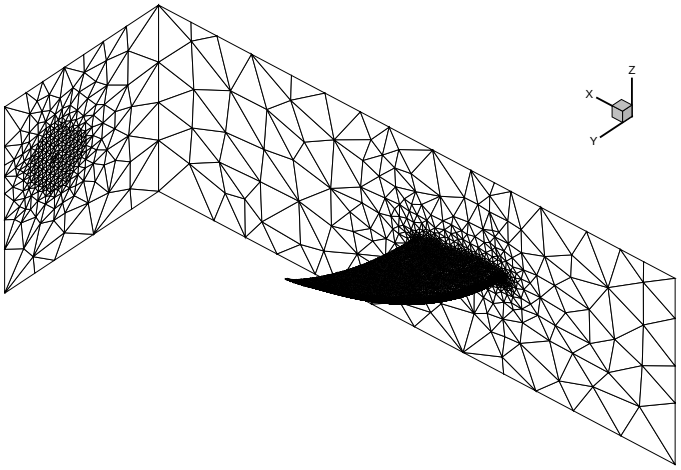

FIGURE 6.26: *Surface mesh of the fine grid for 3D Elliptic 11 Rake Hydrofoil at $\beta = 3^\circ$ angle of attack. Note the cylindrical refined region in the expected path of the vortex. This cylindrical regions starts at the tip of the foil.*

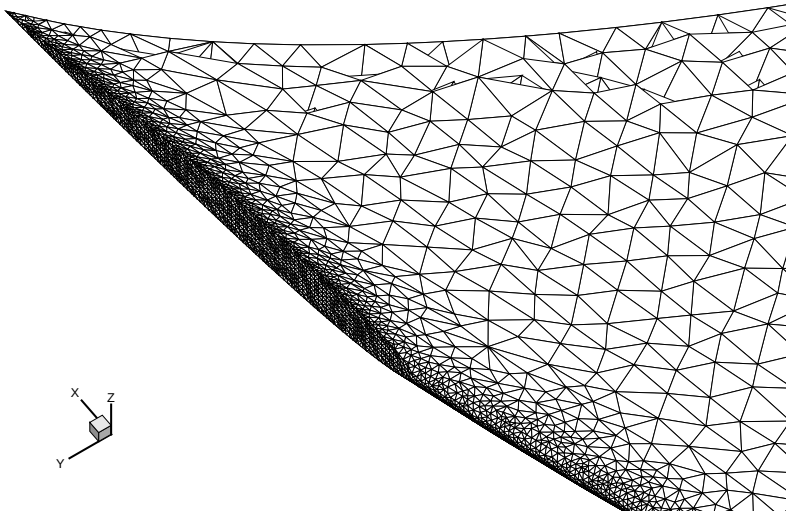

FIGURE 6.27: *Surface mesh of the fine grid in the region around the tip of the 3D Elliptic 11 Rake Hydrofoil at $\beta = 3^\circ$ angle of attack.*

6.5.3 Flow conditions and numerical set-up

To compare the numerical results with the results of the experiments of Van der Hout [204] the case chosen is for a cavitation number of $\sigma = 0.68$ and a free-stream temperature $T_\infty = 293\mathrm{K}$. To speed up the formation of the sheet cavity the free-stream velocity is set to $U_\infty = 50\ \mathrm{ms}^{-1}$ yielding a free-stream pressure equal to

$p_\infty = 8.51 \times 10^5$ Pa, a free-stream density of $\rho_\infty = 998.6\ \mathrm{kg\,m^{-3}}$ and a free-stream speed of sound equal to $c_\infty = 1539.2\ \mathrm{m\,s^{-1}}$.

For the inflow the non-reflective boundary condition is employed. For the outflow the asymptotic non-reflective pressure boundary condition for water flow is applied as in this simulation it is expected that the tip vortex will not cavitate when it reaches the outflow boundary. The conditions at the walls of the channel are slip solid walls treated by the solid wall symmetry technique. The conditions at the slip solid walls of the hydrofoil are treated by the curvature-corrected symmetry technique. The results are obtained with the hybrid HLLC/AUSM flux scheme of section 4.7.2.

Although a steady-flow solution is pursued, the results are obtained time-accurately. We have found that applying local time-stepping to this cavitating flow problem did not result in a converging solution. The differences in the time step taken for the different control volumes become too large due to the large difference in speed of sound for a control volume completely filled with water compared to that of a control volume containing some vapor, i.e. $c_{liq} \approx 1500\ \mathrm{m\,s^{-1}}$ and $c_{\alpha=0.5} \approx 5\ \mathrm{m\,s^{-1}}$.

The route towards the final solution is the following. The first-order solution on the coarse grid is calculated for 50k time steps and then continued with the second-order spatial reconstruction method with the limiter of Venkatakrishnan applied to the primitive variables $[\rho, u, v, w, e]^T$. When the flow solution has become reasonably steady, this solution is then interpolated to the finer grid using the solution interpolation program Grid2Grid, see Hospers [98]. This initialization route reduces the time necessary for the flow field to develop. The calculation is then continued on the fine grid by employing the second-order spatial reconstruction.

6.5.4 Forces and total vapor volume

In the experiments of Van der Hout [204] the cavitating flow for $\sigma = 0.68$ about the 3D Elliptic 11 Rake Foil was found to be fairly steady except for a slow oscillating motion of the cavitating trailing vortex. The mesh further away from the hydrofoil is still too coarse to resolve the cavitation in the trailing vortex accurately, so a steady-flow solution is obtained. The total vapor volume, as defined in equation (6.3) with c taken equal to C_R, reaches a constant value equal to $V_{vap} = 0.23$.

Figure 6.28 presents the force coefficients for the cavitating flow about the hydrofoil. The force coefficients are calculated with equations (2.10) and (2.11) with the

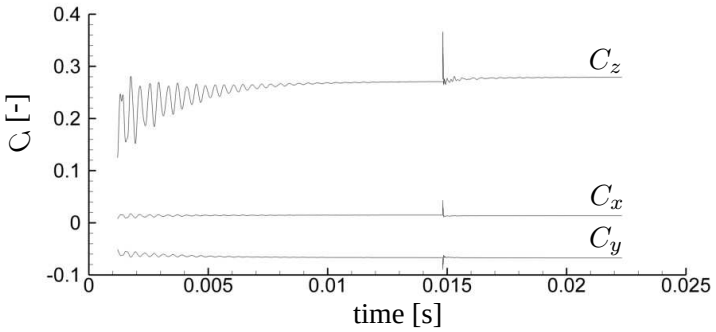

FIGURE 6.28: *Cavitating flow about 3D Elliptic 11 Rake Hydrofoil at* 3° *angle of attack. Fine mesh, 567k tetrhahedrons.* $\sigma = 0.68$*. Force coefficients* C_x*,* C_y *and* C_z *on the foil.*

projected surface area S equal to

$$S = s \int_0^1 c(\hat{y}) \mathrm{d}\hat{y}, \tag{6.10}$$

which evaluates to $S = 0.024584\ \mathrm{m}^2$. Due to computer problems with writing of the data files the information for the first 60k iterations or approximately $10^{-3}\mathrm{s}$ is lost. This did not influence the calculation. When the solution became steady at approximately $t \approx 0.015\mathrm{s}$, the second-order solution on the coarse grid has been interpolated to the fine grid, which is visible as the peaks in the plot of the force coefficients. Then the second-order calculation is continued on the fine grid and the values for the force coefficients become constant.

data	C_x [-]	C_y [-]	C_z [-]
Numerical result	0.0137	-0.067	0.277
Experiments Van der Hout [204]	0.0336	-0.0276	0.269

TABLE 6.13: *Force coefficients for 3D Elliptic 11 Rake hydrofoil at* 3° *angle of attack,* $\sigma = 0.68$*.*

The calculated force coefficients and the measured values of Van der Hout are presented in table 6.13. It is shown that the lift coefficient C_z is predicted to within 3% from the experimental result. The predicted drag coefficient C_x and the side force coefficient C_y show a deviation up to 250% compared with the experiments. The reason for these large differences is not known.

6.5.5 Flow solutions

Van der Hout [204] reported that the sheet cavity near the tip of the foil is approximately steady. Besides some small disturbances, the appearance of the cavity does not change much in time and the shedding of vapor clouds is absent. In figure 6.29 the iso-contour of the computed void fraction $\alpha = 0.01$ is presented together with an experimental result of van der Hout [204] for cavitating flow.

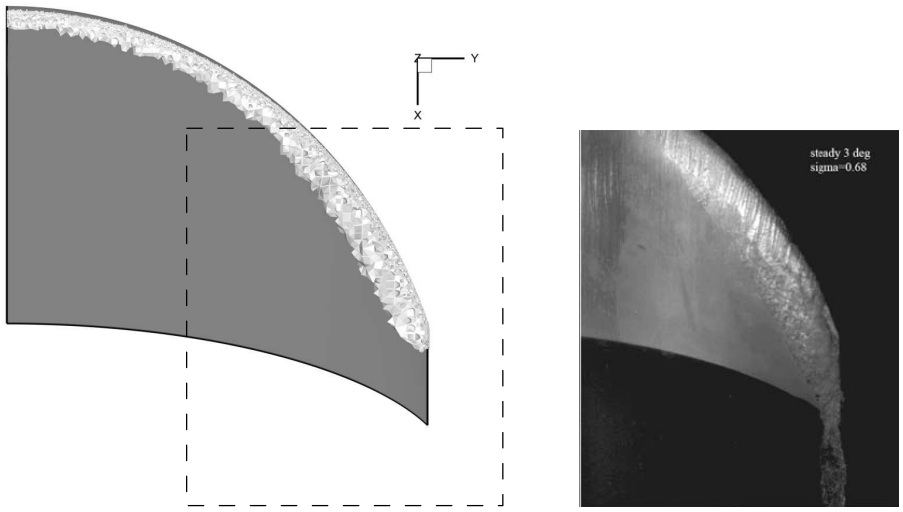

FIGURE 6.29: *3D Elliptic 11 Rake Hydrofoil at* 3° *angle of attack.* $\sigma = 0.68$, $T = 293\,\mathrm{K}$. *Left: Numerical solution. Iso-contour of* $\alpha = 0.01$. *Right: Experimental result Van der Hout [204], photograph taken from [204]. The dashed box denotes the outline of the picture on the right.*

The dashed box denotes the outline of the photograph of the experimental result. As can be seen in figure 6.29 the outline and shape of the sheet cavity are reasonably well predicted. Thus, this demonstrates that the present numerical method is capable of predicting the shape of a sheet cavity on a complex three-dimensional geometry.

However, in the numerical result the amount of vapor present in the tip vortex is not enough to obtain a value for the void fraction larger or equal to $\alpha = 0.01$. Therefore, in the region where the tip vortex is located, there is not an iso-surface $\alpha = 0.01$ of the void fraction visible. Due to numerical dissipation the vorticity distribution in the core of the vortex is not compact enough to generate a sufficiently high enough azimuthal velocity to result in a larger region with the pressure equal to the saturation pressure.

Within the scope of this research Ton [193] has investigated the so-called "Vorticity Confinement" method to improve the prediction of the vorticity distribution within the vortex core and to capture the vortex core over a much longer distance behind the foil. The confinement technique might be an alternative for local grid adaption. Ton showed that it is indeed possible to improve the numerical result for a given mesh. However, it was also concluded that the vorticity confinement method requires fine-tuning for every new case. It is therefore not robust nor user-friendly and this method needs further exploration.

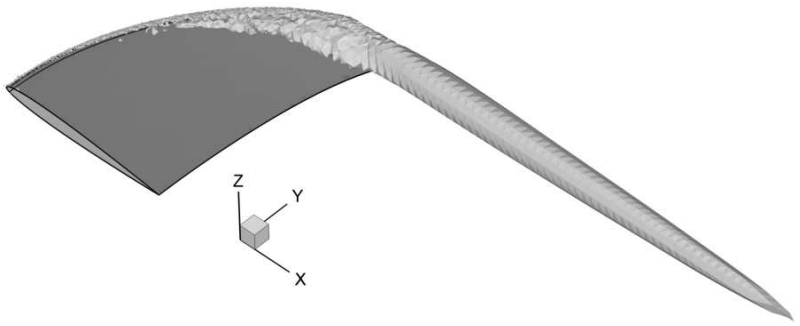

FIGURE 6.30: *3D Elliptic 11 Rake Hydrofoil at* 3° *angle of attack.* $\sigma = 0.68$, $T = 293\mathrm{K}$. *Numerical solution. Iso-contour* $\omega_x / (U_\infty / C_R) = 2$ *of the component in* x*-direction of the vorticity.*

In figure 6.30 the iso-contour $\omega_x / (U_\infty / C_R) = 2$ of the component in x-direction of the vorticity is presented, clearly indicating the region of the tip vortex. As can be seen in figure 6.30 the vortex core can be distinguished about three chord lengths C_R downstream of the trailing edge, so almost up to the outflow boundary. However, apparently the magnitude of the vorticity in the core is not high enough to reduce the pressure to the saturation pressure.

In this section numerical solutions for steady cavitating flow about the 3D Elliptic Rake hydrofoil have been presented. Van der Hout also conducted experiments for unsteady inflow conditions by placing two hydrofoils with oscillating trailing edge flaps upstream of the Rake hydrofoil. In the present study a numerical simulation of such an unsteady forcing case has not been pursued.

On ship propellers sheet cavitation and tip vortex cavitation occur simultaneously and interact with each other, while simultaneously subject to unsteady inflow. In the future research should be carried out both numerically as well as experimentally to

investigate the interaction between sheet cavitation and a (cavitating) tip vortex. In this section we have shown that the present numerical method is capable of accurately predicting the outline of the sheet cavity. Currently the main difficulty lies in predicting the cavitating trailing vortex.

6.6 Conclusions cavitating flow calculations

In this chapter numerical solutions for cavitating flow have been considered for 1D, 2D and 3D flow problems. We have shown that the present numerical method employing the equilibrium cavitation model is able to:

- predict the formation of cavitation in one-dimensional flow problems, such as the "Closing Valve problem" and the cavitating Riemann problem featuring two expansion waves;
- predict the periodic unsteady cavitating flow about a 2D NACA0015 at 6° angle of attack at a cavitation number $\sigma = 1.0$ with characteristic behavior such as the cyclic formation of a sheet cavity, the formation of the re-entrant jet and the shedding of a vapor cloud;
- predict the collapse of a vapor cloud and the subsequent high pressure pulses on the surface of the hydrofoil, which is important for the prediction of erosion and noise;
- predict the unsteady loading of the hydrofoil due to the dynamics of the cavitating flow about the hydrofoil and due to the collapse of shed vapor structures;
- predict the shape of the sheet cavity and the outline of the closure region on the 3D Twist11 hydrofoil at -2° angle of attack. This result correlates to the experiments of Foeth [67];
- predict the onset of shedding of the sheet cavity on the 3D Twist11 hydrofoil at -2° angle of attack, i.e. the development of a re-entrant jet and the subsequent shedding of a cavitating horse-shoe vortex. These predicted phenomena show close agreement with the experiments of Foeth [67];
- predict the shape of the sheet cavity on a complex 3D geometry, such as the 3D Elliptic Rake hydrofoil. This result compares favorably with the results of the experiments of Van der Hout [204];
- predict the lift coefficient C_z to within 3% compared to the experiments of Van der Hout [204] for the cavitating flow about the 3D Elliptic Rake Hydrofoil.

The calculation times required by the present numerical method for the shedding of a cavity sheet on a three-dimensional geometry such as the Twist hydrofoils are so demanding that parallelization of the numerical method is required to speed up the calculations. Preliminary results of a parallelization of the method indicate that an almost linear speed-up with the number of processors can be obtained. The parallelization of the numerical method needs to be optimized further.

We have presented the onset of the shedding of the sheet cavity on the 3D Twist hydrofoil. With the parallelization of the numerical method implemented, the calculations performed in this thesis for the 3D Twist hydrofoil need to be continued on a grid with a higher resolution near the surface of the hydrofoil in order to capture the formation and direction of the re-entrant jet more accurately. To save computational resources prismatic elements close to the surface of the hydrofoil or hexahedral elements can be employed. Furthermore, the numerical prediction of the dynamics of the shedding should be compared one-to-one with the experiments of Foeth [67] to further validate the numerical method.

For two-dimensional cavitating flow the strong pressure pulses generated due to the collapse of shed vapor structures are predicted with the numerical method. In section 6.3.3 we have illustrated that at the instant of the collapse of the shed vapor region, the sheet cavity stops growing. It is an open question if the sheet cavity stops growing due to the collapse of the shed vapor region. The influence of the pressure pulses on the shedding mechanism should be investigated both numerically as well as experimentally, especially the influence on the formation of the re-entrant jet.

The numerical method might be validated for the collapse of shed vapor structures and resulting pressure pulses by investigating the collapse of a single vapor bubble. Currently, the difficulty lies in the very fine grid resolution needed for the final stages of the collapse of the bubble and in the application of the non-reflective boundary conditions to model far-field conditions.

DISCUSSION AND RECOMMENDATIONS

CHAPTER 7

In this chapter the conclusions of the present research are formulated and recommendations are given for future work. The conclusions and recommendations are discussed chapter by chapter of this thesis.

7.1 Physical aspects of cavitation

This research has been conducted in close collaboration with the Department of Maritime Technology at Delft University of Technology. Within this collaboration a number of hydrofoil configurations have been designed employing numerical simulations and experiments. The 3D Twist11 hydrofoil has been designed to have a clear and controllable three-dimensional sheet cavity. It has been shown that the shape of the cavity and the closure line of the cavity determine the direction of the re-entrant flow and that the re-entrant flow from the sides dictates the behavior of the shedding cycle. Therefore, the shedding of a sheet cavity is governed by the direction and momentum of the re-entrant and side-entrant jets and their impingement on the cavity surface. These effects are inertia driven.

The dynamics of sheet cavitation generate strong pressure pulses due to the collapse of shed vapor structures. Within experiments it is a difficult task to capture and/or visualize these pressure pulses and the associated unsteady loading of the foils. In the present numerical results for cavitating flows these pressure pulses are predicted in detail. In order to further validate the numerical method it is important to gain more knowledge experimentally on the strength of the pulses in combination with unsteady sheet cavitation. Furthermore, the influence of the pressure pulses on the shedding mechanism should be investigated both numerically as experimentally, especially the influence on the formation of the re-entrant jet.

The present research focussed on sheet cavitation on a stationary hydrofoil located in uniform inflow conditions. Foeth *et al.* [67] conducted experiments on hydrofoils

placed behind two stacked hydrofoils with oscillating flaps generating an unsteady inflow. Currently research is conducted within our group to model these oscillating hydrofoils employing so-called "transpiration" boundary conditions. This research should be extended to numerically investigate the influence of unsteady inflow on the shedding of the cavitation sheet and compare the results to those of the experiments of Foeth. Besides the oscillating hydrofoils placed upstream of the cavitating hydrofoil, numerical investigations can be carried out for a cavitating hydrofoil oscillating in pitch and/or heave.

In section 6.5 steady-flow numerical solutions for cavitating flow about the 3D Elliptic Rake hydrofoil have been presented. Van der Hout [204] conducted experiments on the 3D Elliptic Rake hydrofoil for steady and unsteady inflow conditions. On ship propellers sheet cavitation and tip vortex cavitation occur simultaneously and interact with each other. Future work should be carried out both numerically as well as experimentally, to investigate the interaction between the sheet cavity and the (cavitating) vortex.

7.2 Mathematical models for cavitating flows

In chapter 3 the mathematical model is discussed for a compressible homogeneous water-vapor mixture at equilibrium saturation conditions. This model does not have any empirical free parameters for phase-transition and thus offers a general applicable model for cavitation. It is shown that with the employed equations of state for the three phases, the experimental data for the density, pressure and speed of sound are accurately represented.

Concerning the equation of state for compressible water it is shown that the modified Tait equation of state proposed by Saurel *et al*. [166] agrees accurately with experimental data. The stiffened gas equation of state for water has also been investigated. It is shown that close to saturation conditions the stiffened gas equation of state does not agree with experimental data.

We have also investigated a barotropic model for cavitation as well as non-equilibrium cavitation models employing a transport equation for the void fraction and source terms for phase transition, see appendices F and G. We recommend to investigate the possibility to include in the present numerical method an additional transport equation for the volume or mass fraction of vapor to be able to include non-equilibrium effects through source terms.

The non-equilibrium models offer more flexibility to describe phase transition in cav-

itation and to include thermodynamic effects. However, in the existing (incompressible-flow) models this flexibility comes at the prize of user-defined free parameters in particular in the source terms. These empirical parameters must be chosen very carefully. More research should be conducted to obtain the adequate values for these parameters in order to enable prediction of cavitation with smaller uncertainty. Source terms without empirical parameters such as proposed by Senocak & Shyy [173] or source terms based on thermodynamic considerations as proposed by Iben *et al*. [100] should be considered in order to remove the dependency on user-defined free parameters. Furthermore, in the present numerical method we experienced numerical instabilities when the density ratio ρ_l/ρ_v was increased to a value exceeding 100. One of the possibilities for these instabilities might be the JST flux scheme, which we have used in combination with the non-equilibrium models. Employing a different flux scheme such as the HLLC flux scheme as described in chapter 4 might reduce the numerical instabilities.

Besides the difficulty of accurately describing some type of finite-rate production and/or destruction source term, a major challenge lies in the fact that when a fully compressible water-vapor medium is considered, the hyperbolicity needs to be preserved. When both water and vapor are present in one computational control volume two different pressures need to be accounted for through appropriate equations of state. Furthermore, the pressure in the liquid phase will become "negative", i.e. a tensile stress. So when returning to a positive pressure in the vapor phase an inflection point is created in the p-v-diagram resulting in complex-valued eigenvalues.

Concerning the barotropic model for cavitation we conclude that this simple description reduces the computational effort. However, as discussed in section 3.1 the baroclinic production term in the vorticity transport equation (proportional to $\nabla\rho \times \nabla p$) is not present in this model since the gradient in pressure is parallel to the gradient in density. Furthermore, we have found that for steady-flow solutions too much cavitation is predicted due to the assumed smooth transition of the density of the fluid from the liquid density to the vapor density. Steepening the transition curve improves the results, but numerical instabilities occur when the transition is chosen too steep. At present it is expected that the instabilities are caused by the JST flux scheme, which has been employed for the barotropic method. Combining the barotropic model with a different flux scheme such as the HLLC flux scheme as presented in chapter 4 might reduce the numerical instabilities. Furthermore, we have employed the dual-time stepping technique to extend the barotropic cavitation model to unsteady flows. For design purposes this model can be developed further, since it gives a simple and reasonable first estimate of cavitating flows.

7.3 Numerical methods

In the present research an edge-based finite-volume method has been developed. Within the scope of this project we extended the in-house mesh-preprocessing program Favomesh, such that it can handle 2D and 3D grids consisting of any element type, i.e. quadrilaterals and/or triangles in 2D and hexahedrons, prisms, tetrahedrons and/or pyramids in 3D. This enabled the improvement of the grid-resolution close to hydrofoils where cavitation occurs, see the MSc. thesis of Hospers [98]. This offers great flexibility in constructing meshes of good quality with locally refined regions to be used to simulate cavitating flows about complex 3D geometries.

In the numerical steady-flow results small numerical oscillations in the solution are experienced at the trailing edge of the hydrofoils. These turned out to be due to the treatment of the trailing edge in constructing the median dual mesh by the mesh-prepocessing program Favomesh. The control volume around the trailing edge is not properly shaped. Refining the grid around the trailing edge does improve the numerical results somewhat. However, a solution to this problem is to split the control volume in an upper and lower control volume corresponding to the upper and lower side of the hydrofoil. This solution has been investigated in our group by Hospers [98]. At present the splitting of the control volume in Favomesh has been automated for general 3D meshes by H. de Vries. Another possibility might be to employ a cell-centered dual mesh, for which the control volumes for the numerical method are formed by the elements of the mesh.

It has been found that the JST flux scheme is not suited for simulating cavitating flows due to numerics-induced under- and overshoots at contact surfaces. These numerical oscillations result in a negative value of the density in case the density ratio ρ_l/ρ_v across the contact surface becomes too large.

The HLLC and the AUSM family of flux schemes have been investigated for cavitating flows. Following the research of Schmidt *et al.* [169] it was found that for steady low-Mach number liquid flows these flux schemes do not produce accurate results. Following Schmidt *et al.* a hybrid HLLC/AUSM flux scheme has been implemented, which improves the numerical results for flows at low Mach number. With the present implementation of the hybrid flux scheme on an unstructured mesh solutions at low-Mach numbers could be obtained. For structured meshes, however, Schmidt *et al.* [170] obtained excellent results at even lower Mach number.

Besides the adaptation of the flux scheme, preconditioning can be employed to simulate low-Mach number flows. We have developed a preconditioning method for cavitating flows based on the method of Weiss & Smith [218]. However, it was found that

for unsteady cavitating flows this method becomes inefficient due to the small physical time step that needs to be taken in order to capture the unsteady flow phenomena.

We investigated and implemented a MUSCL-type reconstruction method for unstructured grids. The limiter of Venkatakrishnan is employed for steady and unsteady flow simulations. It was found that this limiter stalls the convergence towards the steady-state flow solution. More research needs to be carried out to improve the convergence towards a steady-flow solution. A possible solution might be to implement one of the limiting methods described in the thesis of Bramkamp [28]. For unsteady flow calculations the limiter of Venkatakrishnan works satisfactorily, under- and overshoots are not observed at sharp gradients or discontinuities in the flow.

In section 4.8 non-reflective in- and outflow boundaries for arbitrary equations of state have been developed and implemented in the present numerical method. These boundary conditions allow waves in the flow solution to leave the computational domain without any reflection at the boundary of the computational domain. This is necessary to avoid that spurious reflected waves interfere with the time-dependent cavitating flow solution. Furthermore, the non-reflective boundary conditions improve the convergence to the steady-flow solution.

The development and implementation of the Curvature-Corrected Symmetry Technique for the solid walls with slip conditions improves the numerical solution of the flow near the surfaces.

7.4 Single-phase flow calculations

In chapter 5 the single-phase flow of water has been considered for 1D, 2D and 3D flow problems. It is was judged to be essential to show that the numerical method is able to accurately calculate single phase water flow before attempting to calculate cavitating flows. In chapter 5 it is shown that the present numerical method is able to:

- accurately predict time-accurate wave and shock dynamics in liquid flow problems such as the “Water Hammer” problem and the Riemann problem for liquid flow;
- accurately calculate steady-state low-Mach number liquid flow, without the use of preconditioning methods, by employing a hybrid HLLC/AUSM flux scheme such as developed by Schmidt *et al*. [169, 170];
- accurately calculate the steady-state water flow about two-dimensional hydrofoils;

- accurately predict the lift coefficient for steady-state water flow about the 3D Twist11 hydrofoil at -2° angle of attack;
- accurately predict the pressure coefficient C_p on the surface of the 3D Twist hydrofoil at -2° angle of attack in comparison to experimentally obtained surface pressure data.

Furthermore, we conclude that the numerical method employing the MUSCL-type reconstruction method and the limiter of Venkatakrishnan is close to second-order accuracy for the single phase water flow about two-dimensional hydrofoils.

7.5 Cavitating flow calculations

In chapter 6 numerical results for cavitating flows are presented for 1D, 2D and 3D flow problems. It is shown that the present numerical method employing the equilibrium cavitation model is capable to:

- accurately predict the formation of cavitation for one-dimensional flow such as the so-called "Closing Valve" problem in 1D and the cavitating Riemann problem of two outward running expansion waves;
- predict the periodic unsteady cavitating flow about a 2D NACA0015 at 6° angle of attack at cavitation number $\sigma = 1.0$ with characteristic behavior, such as the cyclic formation of a sheet cavity, the formation of the re-entrant jet and the shedding of a vapor cloud;
- predict the collapse of a shed vapor structure and capture the subsequent pressure wave dynamics in the liquid and on the surface of the hydrofoil, which is important for the prediction of erosion and noise;
- predict the unsteady loading of the hydrofoil due to the dynamics of the cavitating flow and due to the collapse of shed vapor structures;
- accurately predict the shape of a sheet cavity and the outline of the closure region on the 3D Twist11 hydrofoil at -2° angle of attack compared to the experiments of Foeth [67];
- predict the onset of shedding of a cavity sheet on the 3D Twist11 hydrofoil at -2° angle of attack, i.e. the development of a re-entrant jet and the subsequent shedding of a cavitating horse-shoe vortex. These predicted phenomena show close agreement with the experiments of Foeth [67];
- predict the shape of the sheet cavity on a complex 3D geometry, such as the 3D Elliptic Rake hydrofoil compared to the experiments of Van der Hout [204];

- predict the lift coefficient C_z to within 3% compared to the experiments of Van der Hout [204] for the cavitating flow about the 3D Elliptic Rake Hydrofoil.

Currently, the calculation of unsteady cavitating flows about 3D geometries requires too long calculation times. Work has been started to develop a parallelized version of the numerical method. Preliminary results indicate that the implementation in the parallelization results in a speed-up that is almost linear with the number of processors. This speed-up is necessary to validate the present numerical method with the experiments of Foeth. The parallelization of the numerical method needs to be optimized further. Other accelerating techniques such as multi-grid methods and implicit time-integration methods should be investigated.

We have presented the onset of the shedding of the sheet cavity on the 3D Twist hydrofoil. With the parallelization of the numerical method implemented, the calculations performed in this thesis for the 3D Twist hydrofoil need to be continued on a grid with a higher resolution near the surface of the hydrofoil in order to capture the formation and direction of the re-entrant jets more accurately. Furthermore, the numerical prediction of the dynamics of the shedding should be compared one-to-one with the experiments of Foeth to further validate the numerical method.

For two-dimensional cavitating flow the strong pressure pulses generated due to the collapse of shed vapor structures are predicted with the numerical method. In section 6.3.3 we have illustrated that at the instant of the collapse of the shed vapor region, the sheet cavity stops growing. It is an open question whether or not the sheet cavity stops growing due to the collapse of the shed vapor region. The influence of the pressure pulses on the shedding mechanism should be investigated both numerically as well as experimentally, especially the influence on the formation of the re-entrant jet.

The numerical method could be validated for the collapse of shed vapor structures and resulting pressure pulses by investigating the collapse of a single vapor bubble. Currently, the difficulty lies in the very fine grid resolution needed for the final stages of the collapse of the bubble and in the application of the non-reflective boundary conditions to model far-field conditions.

7.6 Future research

Besides the recommendations stated in the above sections the following subjects should be investigated further in order to increase the knowledge on cavitating flows, to improve the current mathematical model and numerical method and to extend the numerical method to other research fields:

- Investigate methods such as preconditioning and implicit time-integration for cavitating flows. Questions to be addressed are: can the start-up phase in numerical simulations of cavitating flows towards (semi)-periodic shedding be accelerated? Can unsteady flow phenomena in compressible liquids such as pressure wave-dynamics be captured efficiently? Can the quasi-periodic shedding cycles and the pressure wave-dynamics generated by collapsing vapor structures be simulated efficiently?

- Investigate the interaction between sheet cavitation and a (cavitating) tip vortex. One of the difficulties lies in accurately predicting the internal structure of the (cavitating) vortex. Within the scope of this research Ton [193] has investigated the so-called "Vorticity Confinement" method. It was shown that it is indeed possible to improve the numerical results for tip vortices. However, it was also concluded that the vorticity confinement method is not yet robust and needs to be explored further.

- Extend the numerical method to the flow in rotating fluid machinery. Many cavitating flows occur in rotating devices such as pumps and ship propellers and it is recommended to extend the present investigation to these interesting flow problems.

- Investigate the collapse of a single vapor bubble to validate the numerical method for the collapse of shed vapor structures and resulting pressure pulses. An interesting flow problem to be investigated is the collapse of a single or of multiple vapor bubbles close to a solid wall. This enables to predict the pressure pulses on the wall and to relate these pulses to susceptibility for erosion. Currently, the difficulty lies in the very fine grid resolution needed for the final stages of the collapse of the bubble and in the application of the non-reflective boundary conditions to account for far-field conditions.

- Investigate effects of viscosity. In the current numerical method the flow is assumed to be an inviscid flow. For the shedding of the sheet cavity viscosity does not play a role. However, effects of viscosity do play a role in flows close to solid walls. Therefore, effects due to viscosity can be included in the mathematical model. A possible difficulty lies in implementing an appropriate turbulence model for compressible two-phase flow.

REFERENCES

[1] The International Association for the Properties of Water and Steam; http://www.iapws.org/.

[2] NIST Chemistry Webbook; http://webbook.nist.gov/chemistry.

[3] ITTC 1999. Final report of the Specialist Committee on Computational Method for Propeller Cavitation. In *Proceedings of 22nd International Towing Tank Conference*, volume 3, 1999.

[4] I.H. Abbott and A.E. von Doenhoff. *Theory of Wing Sections*. Dover Publications, inc., 1959.

[5] R. Abgrall. How to Prevent Pressure Oscillations in Multicomponent Flow Calculations: A Quasi Conservative Approach. *Journal of Computational Physics*, 125:150–160, 1996.

[6] R. Abgrall and S. Karni. Computations of Compressible Multifluids. *Journal of Computational Physics*, 169:594–623, 2001.

[7] R. Abgrall and R. Saurel. Discrete Equations for Physical and Numerical Compressible Multiphase Mixtures. *Journal of Computational Physics*, 186:361–396, 2003.

[8] V. Ahuja and A. Hosangadi. A Numerical Study of Cavitation in Cryogenic Fluids Part 1: Mean Flow Parametric Studies. In *Sixth International Symposium on Cavitation*, 2006.

[9] V. Ahuja, A. Hosangadi, and S. Arunajatesan. Simulations of Cavitating Flows using Hybrid Unstructured Meshes. *Journal of Fluids Engineering*, 123:331–340, 2001.

[10] G.D. van Albada, B. van Leer, and W.W. Roberts. A Comparative Study of Computational Methods in Cosmic Gas Dynamics. *Astronomy and Astrophysics*, 108:76–84, 1982.

[11] G. Allaire, S. Clerc, and S. Kokh. A Five-Equation Model for the Simulation of Interfaces between Compressible Fluids. *Journal of Computational Physics*, 181:577–616, 2002.

[12] J.D. Anderson. *Fundamentals of Aerodynamics*. McGraw-Hill, inc., 3rd edition, 2001.

[13] N. Andrianov, R. Saurel, and G. Warnecke. A Simple Method for Compressible Multiphase Mixtures and Interfaces. *International Journal for Numerical Methods in Fluids*, 41:109–131, 2003.

[14] V.H. Arakeri. Viscous Effects on the Position of Cavitation Separating from Smooth Bodies. *Journal of Fluid Mechanics*, 68:779–799, 1975.

[15] R.E.A. Arndt. Cavitation in Vortical Flows. *Annual Review in Fluid Mechanics*, 34:143–175, 2002.

[16] R.E.A. Arndt, C.C.S. Song, M. Kjeldsen, J. He., and A. Keller. Instability of Partial Cavitation: A Numerical/Experimental Approach. In *Proceedings of 23rd Symposium on Naval Hydrodynamics*, 2000.

[17] J.A. Astolfi, J.B. Leroux, P. Dorange, J.Y. Billard, F. Deniset, and S. de La Fuente. An Experimental Investigation of Cavitation Inception and Development on a Two-Dimensional Hydrofoil. *Journal of Ship Research*, 44(4):259–269, 2000.

[18] M.R. Baer and J.W. Nunziato. A Two-Phase Mixture Theory for the Deflagration-to-Detonation Transition (DDT) in Reactive Granular Materials. *International journal of Multiphase flow*, 12:861–889, 1986.

[19] T. Barberon and P. Helluy. Finite Volume Simulation of Cavitating Flows. *Computer & Fluids*, 34:832–858, 2005.

[20] T.J. Barth and D.C. Jespersen. The Design and Application of Upwind Schemes on Unstructured Meshes. *AIAA paper*, 89-0366, 1989.

[21] P. Batten, N. Clarke, C. Lambert, and D.M. Causon. On the Choice of Wavespeeds for the HLLC Riemann Solver. *SIAM J. Sci. Comput.*, 18:1553–1570, 1997.

[22] A. Berg, U. Iben, A. Meister, and J. Schmidt. Modeling and Simulation of Cavitation in Hydraulic Pipelines based on the Thermodynamic and Caloric Properties of Liquid and Steam. *Shock Waves*, 14:111–121, 2005.

[23] S.J. Billet and E.F. Toro. Unsplit WAF-type Schemes for Three-Dimensional Hyperbolic Conservation Laws. In E.F. Toro and J.F. Clarke, editors, *Numerical Methods for Wave Propagation*, volume 47 of *Fluid Mechanics and its Applications*, pages 75–124. Kluwer Academic Publishers, 1998.

[24] G. Birkhoff and E.H. Zarantonello. *Jets, Wakes, and Cavities*. Academic Press Inc., 1957.

[25] J. Blazek. *Computational Fluid Dynamics: Principles and Applications*. Elsevier, 2 edition, 2005.

[26] Y.A. Bouziad, M. Farhat, F. Guennon, K. Miyagawa, J.L. Kueny, and F. Avellan. Physical Modeling and Simulation of Leading Edge Cavitation, Application to an Industrial Inducer. In *Fifth international Symposium on Cavitation*, 2003.

[27] Y.A. Bouziad, F. Guennoun, M. Farhat, and F. Avellan. Numerical Simulation of Leading Edge Cavitation. *Proceedings of ASME FEDSM 03*, FEDSM2003-45312, 2003.

[28] F.D. Bramkamp. *Unstructured h-Adaptive Finite-Volume Schemes for Compressible Viscous Fluid Flow*. PhD thesis, Aachen University of Technology, 2003.

[29] C.E. Brennen. *Cavitation and Bubble Dynamics*. Oxford University Press, 1995.

[30] C.E. Brennen. *Fundamentals of Multiphase Flows*. Cambridge Unversity Press, 2005.

[31] C.E. Brennen, T. Colonius, and F. Auria. Computing Shock Waves in Cloud Cavitation. In *Third International Symposium on Cavitation*, 1998.

[32] L.J. Briggs. Limiting Negative Pressure of Water. *Journal of Applied Physics*, 21:721–722, 1950.

[33] M. Callenaere, J.P. Franc, J.M. Michel, and M. Riondet. The Cavitation Instability induced by the Development of a Re-entrant Jet. *Journal of Fluid Mechanics*, 444:223–256, 2001.

[34] C.E. Castro and E.F. Toro. A Riemann Solver and Upwind Methods for a Two-phase Flow Model in Non-Conservative Form. *International Journal of Numerical Methods in Fluids*, 50:275–307, 2006.

[35] C.H. Chang and M.S. Liou. A Robust and Accurate Approach to Computing Compressible Multiphase Flow: Stratified Flow Model and AUSM+-up scheme. *Journal of Computational Physics*, 225:840–873, 2007.

[36] T.J. Chen and C.H. Cooke. A New Averaging Scheme for the Riemann Problem in Pure Water. *Mathl. Comput. Modelling*, 25:25–36, 1997.

[37] Y. Chen and D.D. Heister. A Numerical Treatment of Attached Cavitation. *Journal of Fluids Enigineering*, 116:613–618, 1994.

[38] Y. Chen and S.D. Heister. Modeling of Hydrodynamic Nonequilibrium in Cavitating Flows. *Jounral of Fluids Engineering*, 118:172–178, 1996.

[39] A.J. Chorin. A Numerical Method for Solving Incompressible Viscous Flow Problems. *Journal of Computational Physics*, 2(1):12–26, 1967.

[40] J.P. Cocchi, Saurel R., and J.C. Loraud. Treatment of Interface Problems with Godunov-type Schemes. *Shock Waves*, 5:347–357, 1996.

[41] J.P. Cocchi and R. Saurel. A Riemann Problem based Method for the Resolution of Compressible Multimaterial Flows. *Journal of Computational Physics*, 137:265–298, 1997.

[42] T. Colonius. Modeling Artificial Boundary Conditions for Compressible Flow. *Annu. Rev. Fluid Mech.*, 36:315–345, 2004.

[43] T. Colonius, F. d'Auria, and C.E. Brennen. Acoustic Saturation in Bubbly Cavitating Flow adjacent to an Oscillating Wall. *Physics of Fluids*, 12(11):2757–2761, 2000.

[44] O. Coutier-Delgosha, F. Deniset, J.A. Astolfi, and J.B. Leroux. Numerical Prediction of Cavitating Flow on a Two-Dimensional Symmetrical Hydrofoil and Comparison to Experiments. *Journal of Fluids Engineering*, 129:279–292, 2007.

[45] O. Coutier-Delgosha, R. Fortes-Patella, J.L. Reboud, N. Hakimi, and C. Hirsch. Numerical Simulation of Cavitating Flow in 2D and 3D Inducer Geometries. *International journal for Numerical Methods in Fluids*, 48:135–167, 2005.

[46] O. Coutier-Delgosha, R. Fortes-Patella, J.L. Reboud, N. Hakimi, and C. Hirsch. Stability of Preconditioned Navier-Stokes Equations associated with a Cavitation Method. *Computers & Fluids*, 34:319–349, 2005.

[47] O. Coutier-Delgosha, R. Fortes-Patella, J.L. Reboud, M. Hofmann, and B. Stoffel. Experimental and Numerical Studies in a Centrifugal Pump with Two-Dimensional curved Blades in Cavitating condition. *Journal of fluids engineering, Transactions of the ASME*, 125:970–978, 2003.

[48] O. Coutier-Delgosha, J.L. Reboud, and Y. Delannoy. Numerical Simulation of the Usteady Behavior of Cavitating Flows. *International Journal of Numerical Methods*, 42:527–548, 2003.

[49] A. Dadone. Symmetry Techniques for the Numerical Solution of the 2D Euler Equations at Impermeable Boundaries. *International Journal for Numerical methods in fluids*, 28:1093–1108, 1998.

[50] J. Dang. *Numerical Simulation of Unsteady Partial Cavity Flows*. PhD thesis, Delft University, 2001.

[51] J. Dang and G. Kuiper. Re-entrant Jet modeling of Partial Cavity Flow on Three-Dimensional Hydrofoils. *Trans. ASME: Journal of Fluids Engineering*, 121:781–787, 1999.

[52] D.L. Darmofal and P.J. Schmid. The Importance of Eigenvectors for Local Preconditioners of the Euler Equations. *Journal of Computational Physics*, 127:346–362, 1996.

[53] M.S. Darwish and F. Moukalled. TVD Schemes for Unstructured Grids. *International Journal of Heat and Mass Transfer*, 46:599–611, 2003.

[54] D. Dauby, A. Leroyer, and M. Visonneau. Computations of 2D Cavitating Flows and Tip Vortex Flows with an Unstructured RANSE Solver. *Sixth International Symposium on Cavitation*, 2006.

[55] D.F. de Lange. *Observation and Modeling of Cloud Formation behind a Sheet Cavity*. PhD thesis, University of Twente, 1996.

[56] D.F. de Lange and G.J. de Bruin. Sheet Cavitation and Cloud Cavitation, Re-entrant Jet and Three-Dimensionality. *Applied Scientific Research*, 58:91–114, 1998.

[57] C.F. Delale, G.H. Schnerr, and J. Sauer. Quasi-One-Dimensional Steady-State Cavitating Nozzle Flows. *Journal of Fluid Mechanics*, 427:167–204, 2001.

[58] Y. Delannoy and J.L. Kueny. Two-Phase Flow Approach in Unsteady Cavitation Modeling. *Cavitation and multiphase flow forum*, pages 153–158, 1990.

[59] M. Deshpande, J. Feng, and C. Merkle. Numerical Modeling of the Thermodynamic Effects of Cavitation. *Journal of Fluids Engineering*, 119:420–427, 1997.

[60] L. Dieval, M. Arnoud, and R. Marcer. Numerical Modeling of Unsteady Cavitating Flows by a VoF Method. In *Third International Symposium on Cavitation*, 1998.

[61] W. Dijkhuizen. *Derivation of Closures for Bubbly Flows using Direct Numerical Simulations*. PhD thesis, University of Twente, 2008.

[62] D.A. Drew. Mathematical Modeling of Two-Phase Flow. *Annual Review of Fluid Mechanics*, 15:261–291, 1983.

[63] J.R. Edwards and R.K. Franklin. Low-Diffusion Flux-Splitting Methods for Real Fluid Flows with Phase Transitions. *AIAA Journal*, 38:1624–1633, 2000.

[64] M. Feistauer, J. Felcman, and I. Straskraba. *Mathematical and Computational Methods for Compressible Flow*. Numerical Mathematics and Scientific Computation. Oxford Science Publications, 2003.

[65] J.C. Fisher. The Fracture of Liquids. *Journal of Applied Pysics*, 19:1062–1067, 1948.

[66] E.J. Foeth. Pressure and Lift Measurements on the Twist11 Hydrofoil. private communication.

[67] E.J. Foeth. *The Structure of Three-Dimensional Sheet Cavitation*. PhD thesis, Delft University of Technology, 2008.

[68] E.J. Foeth, C.W.H. van Doorne, T. van Terwisga, and B. Wieneke. Time resolved PIV and Flow Visualization of 3D Sheet Cavitation. *Experiments in Fluids*, 2006.

[69] E.J. Foeth and T. van Terwisga. The Structure of Unsteady Cavitation. Part 1: Observations of an Attached Cavity on a Three-Dimensional Hydrofoil. *CAV2006: Sixth International Symposium on Cavitation, Wageningen*, 2006.

[70] J.P. Franc. Partial Cavity Instabilities and Re-Entrant Jet. In *CAV2001: Fourth International Symposium on Cavitation*. California Institute of Technology, Pasadena, USA, 2001.

[71] J.P. Franc. Cavitation. In *Fluid Dynamics of Cavitation and Cavitating Turbopumps*. CISM, International Centre For Mechanical Sciences, 2005.

[72] J.P. Franc and J.M. Michel. Attached Cavitation and the Boundary Layer: Experimental Investigation and Numerical Treatment. *Journal of Fluid Mechanics*, 154:63–90, 1985.

[73] J.P. Franc and J.M. Michel. Unsteady Attached Cavitation on an Oscillating Hydrofoil. *Journal of Fluid Mechanics*, 193:171–189, 1988.

[74] J.P. Franc and J.M. Michel. *Fundamentals of Cavitation*. Kluwer Academic Publishers, 2004.

[75] S. Fujikawa and T. Akamatsu. Effects of the Non-Equilibrium Condensation of Vapour on the Pressure Wave produced by the Collapse of a Bubble in a Liquid. *Journal of Fluid Mechanics*, 97:481–512, 1980.

[76] R.A. Furness and S.P. Hutton. Experimental and Theoretical Studies of Two-Dimensional Fixed-type Cavities. *ASME Transactions Journal of Fluids Engineering*, 97:515–521, 1975.

[77] T. Gallouët, J.M. Hérard, and N. Seguin. Some recent Finite Volume Schemes to compute Euler Equations using Real Gas EOS. *International Journal for Numerical Methods in Fluids*, 39:1073–1138, 2002.

[78] J.R. Garcia-Cascales and H. Paillére. Application of AUSM Schemes to Multi-Dimensional Compressible Two-Phase Flow Problems. *Nuclear Engineering and Design*, 236:1225–1239, 2006.

[79] S.K. Godunov. A Difference Scheme for Numerical Computation Discontinuous Solution of Hydrodynamic Equations. *Math. Sbornik (in Russian)*, 47:271–306, 1959.

[80] S. Gopalan and J. Katz. Flow Structure and Modeling Issues in the Closure Region of Attached Cavitation. *Physics of Fluids*, 12:985–911, 2000.

[81] H. Guillard and A. Murrone. On the Behavior of Upwind Schemes in the Low Mach Number Limit: II. Godunov type schemes. *Computers & Fluids*, 33:655–675, 2004.

[82] H. Guillard and C. Viozat. On the Behaviour of Upwind Schemes in the Low Mach Number Limit. *Computers & Fluids*, 28:63–86, 1999.

[83] R.A. Habing. *Flow and Plate Motion in Compressor Valves*. PhD thesis, University of Twente, 2005.

[84] K.K. Haller, Y. Ventikos, and D. Poulikakos. Wave Structure in the Contact Line Region during High Speed Droplet Impact on a Surface: Solution of the

Riemann Problem for the Stiffened Gas Equation of State. *Journal of Applied Physics*, 93(5):3090–3097, March 2003.

[85] F.H. Harlow and A.A. Amsden. Fluid dynamics, Monograph LA-4700. Los Alamos National Laboratory, Los Alamos, NM, 1971.

[86] A. Harten. High Resolution Schemes for Hyperbolic Conservation Laws. *Journal of Computational Physics*, 49:357–393, 1983.

[87] A. Harten, P.D. Lax, and B. van Leer. On Upstream Differencing and Godunov-type Schemes for Hyperbolic Conservation Laws. *Siam Review*, 25:35–61, 1983.

[88] A.T.J. Hayward. Compressibility Equations for Liquids: a Comparative Study. *British Journal of Applied Physics*, 18:965–977, 1967.

[89] H. Helmholtz. On Discontinuous Movements of Fluids. *Philosophical Magazine*, 36:337–346, 1868.

[90] C. Hirsch. *Numerical Computation of Internal and External Flows. Volume 1: Fundamentals of Numerical Discretization*. Wiley, 1989.

[91] C. Hirsch. *Numerical Computation of Internal and External Flows. Volume 2: Computational Methods for Inviscid and Viscous Flows*. Wiley, 1990.

[92] R. Hirschi, Ph. Dupont, F. Avellan, J.N. Favre, J.F. Guelich, and E. Parkinson. Centrifugal Pump Performance Drop due to Leading Edge Cavitation: Numerical Predictions compared with Model Tests. *Journal of Fluids Engineering*, 120:705–711, 1998.

[93] C.W. Hirt and B.D. Nichols. Volume of Fluid (VoF) Method for the Dynamics of Free Boundaries. *Journal of computational physics*, 39:201–225, 1981.

[94] H.W.M. Hoeijmakers. *Computational Aerodynamics of Ordered Vortex Flows*. PhD thesis, Delft University of Technology, 1989.

[95] H.W.M. Hoeijmakers, M.E. Janssens, and W. Kwan. Numerical Simulation of Sheet Cavitation. In *Third International Symposium on Cavitation*, 1998.

[96] A. Hosangadi and V. Ahuja. Numerical Study of Cavitation in Cryogenic Fluids. *Journal of Fluids Engineering*, 127:267–281, 2005.

[97] A. Hosangadi and V. Ahuja. A Numerical Study of Cavitation in Cryogenic Fluids Part 2: New Unsteady Model for Dense Cloud Cavitation. *Sixth International Symposium on Cavitation*, 2006.

[98] J.M. Hospers. Development and Application of Hybrid Grids for Finite Volume Methods. Master's thesis, University of Twente, 2007.

[99] T. Huuva. *Large Eddy Simulation of Cavitating and Non-Cavitating Flow*. PhD thesis, Chalmers University of Technology, 2008.

[100] U. Iben, F. Wrona, C.D. Munz, and M. Beck. Cavitation in Hydraulic Tools based on Thermodynamic Properties of Liquid and Gas. *Journal of Fluids Engineering*, 124:1011–1017, 2002.

[101] Y. Iga, M. Nohmi, A. Goto, and T. Ikohagi. Numerical Analysis of Cavitation Instabilities Arising in the Three-Blade Cascade. *Journal of Fluids Engineering*, 126:419–429, 2004.

[102] Y. Iga, M. Nohmi, A. Goto, B.R. Shin, and T. Ikohagi. Numerical Study of Sheet Cavitation Breakoff Phenomenon on a Cascade Hydrofoil. *Journal of Fluids Engineering*, 125:643–651, 2003.

[103] T. Ikeda, S. Yoshizawa, M. Tosaki, S. Allen, J.S. Takagi, N. Ohta, T. Kitamura, and Y. Matsumoto. Cloud Cavitation Control for Lithotripsy using High-Intensity Focused Ultrasound. *Ultrasound in Medicine and Biology*, 32:1383–1397, 2006.

[104] M.J. Ivings, D.M. Causon, and E.F. Toro. On Riemann Solvers for Compressible Liquids. *International Journal for Numerical Methods in Fluids*, 28:395–418, 1998.

[105] A. Jameson, T.J. Baker, and N.P. Weatherill. Calculation of Inviscid Transonic Flow over a Complete Aircraft. *AIAA journal*, 86:86–0103, 1986.

[106] A. Jameson, W. Schmidt, and E. Turkel. Numerical Solution of the Euler Equations by Finite Volume Methods Using Runge-Kutta Time-Stepping Schemes. *AIAA paper*, 91-1259, 1981.

[107] E. Johnsen and T. Colonius. Compressible Multi-Component Flow Calculations and Shock-Bubble Interaction. In *Sixth International Symposium on Cavitation, CAV2006, Wageningen, the Netherlands, 2006*. Marin, 2006.

[108] Y. Kawanami, H. Kato, H. Yamaguchi, M. Tanimura, and Y. Tagaya. Mechanism and Control of Cloud Cavitation. *Journal of Fluids Engineering, Transactions of the ASME*, 119:788–794, 1997.

[109] P.H. Kelleners. *An Edge-based Finite Volume Method for Inviscid Compressible Flow with Condensation*. PhD thesis, University of Twente, 2007.

[110] S.A. Kinnas and N.E. Fine. A Numerical Nonlinear Analysis of the Flow around Two- and Three-Dimensional Partially Cavitating Hydrofoils. *Journal of Fluid Mechanics*, 254:151–181, 1993.

[111] G. Kirchhoff. Zur Theorie freier Flüssigkeitsstrahlen. *J. reine angew. Math.*, 70:289–298, 1869.

[112] R.T. Knapp, J.W. Daily, and F.G. Hammitt. *Cavitation*. McGraw-Hill Book Company, 1970.

[113] A.H. Koop, H.W.M. Hoeijmakers, G.H. Schnerr, and E.J. Foeth. Design of Twisted Cavitating Hydrofoil using a Barotropic Flow Method. *Sixth International Symposium on Cavitation, CAV2006*, 2006.

[114] B. Koren. Improving Euler Computations atllow-Mach numbers. *International Journal of Computational Fluid Dynamics*, 6:51–70, 1996.

[115] B. Koren and B. van Leer. Analysis of Preconditioning and Multigrid for Euler Flows with Low-Subsonic Regions. *Advances in Computational Mathematics*, 4:127–144, 1995.

[116] A. Kubota, H. Kato, and H. Yamaguchi. A New Modelling of Cavitating Flows; A Numerical Study of Unsteady Cavitation on a Hydrofoil Section. *Journal of Fluid Mechanics*, 240:59–96, 1992.

[117] R.F. Kunz, D.A. Boger, T.S. Chyczewski, D.R. Stinebring, H.J. Gibeling, and T.R Govindan. Multi-Phase CFD Analysis of Natural and Ventilated Cavitation about Submerged Bodies. In *Proceedings of 3rd ASME/JSME Joint Fluids Engineering Conference*, pages ASME Paper FEDSM99–7364, 1999.

[118] R.F. Kunz, D.A. Boger, D.R Stinebring, S. Chyczewski, J.W. Lindau, H.J. Gibeling, S. Venkateswaran, and T.R. Govindan. A Preconditioned Navier-Stokes Method for Two-Phase Flows with Application to Cavitation Prediction. *Computers and Fluids*, 29:849–875, 2000.

[119] R.F. Kunz, W.K. Cope, and S. Venkateswaran. Development of an Implicit Method for Multi-Fluid Flow Simulations. *Journal of Computational Physics*, 152:78–101, 1999.

[120] R.F. Kunz, T.A. Kaday, J.W. Lindau, and L.J. Peltier. Unsteady RANS and Detached Eddy Simulations of Cavitating Flow over a Hydrofoil. *Fifth International Symposium on Cavitation, CAV2003*, Cav03-OS:1–12, 2003.

[121] K.R. Labertaux and S.L. Ceccio. Partial Cavity Flows. Part 1. Cavities forming on Models without Spanwise Variation. *Journal of Fluid Mechanics*, 431:1–41, 2001.

[122] C.B. Laney. *Computational Gasdynamics*. Cambridge University Press, 1st edition, 1998. ISBN 0 521 57069 7.

[123] Q. Le, J.P. Franc, and J.M. Michel. Partial Cavities: Global Behavior and Mean Pressure Distribution. *Journal of Fluids Engineering*, 115:243–248, 1993.

[124] O. Le Métayer, J. Massoni, and R. Saurel. Élaboration de lois d'état d'un liquide et de sa vapeur pour les modèles d'écoulements diphasiques; Elaborating Equations of State of a Liquid and its Vapor for Two-Phase Flow Models. *International Journal of Thermal Sciences*, 43:265–276, 2004. in french.

[125] O. Le Métayer, J. Massoni, and R. Saurel. Modelling Evaporation Fronts with Reactive Riemann Solvers. *Journal of Computational Physics*, 205:567–610, 2005.

[126] B. van Leer. Towards the Ultimate Conservative Difference Scheme III. Upstream-Centered Finite-Difference Schemes for Ideal Compressible Flow. *Journal of Computational Physics*, 23:263–275, 1977.

[127] van B. Leer. Towards the Ultimate Conservative Difference Scheme V. A Second-order Sequel to Godunov's Method. *Journal of Computational Physics*, 32:101–136, 1979.

[128] R.J. Leveque. *Finite Volume Methods for Hyperbolic Problems*. Cambridge University Press, 2002.

[129] J.W. Lindau, R.F. Kunz, D.A. Boger, D.R. Stinebring, and H.J. Gibeling. High Reynolds Number, Unsteady, Multiphase CFD Modeling of Cavitating Flows. *Journal of Fluids Engineering*, 124:607–616, September 2002.

[130] M.S. Liou. A Sequel to AUSM: AUSM+. *Journal of Computational Physics*, 129:364–382, 1996.

[131] M.S. Liou. Ten Years in the Making - AUSM-family. *AIAA Paper 2001-2521*, 2001.

[132] M.S. Liou. A sequel to AUSM, Part II: AUSM+-up for all speeds. *Journal of Computational Physics*, 214:137–170, 2006.

[133] M.S. Liou and J. Steffen. A New Flux Splitting Scheme. *Journal of Computational Physics*, 107:23–39, 1993.

[134] Rayleigh (Lord). The Pressure Developed in a Liquid during the Collapse of a Sperical Cavity. *Philosophical Magazine*, 34:94, 1917.

[135] H. Luo, J.D. Baum, and R. Löhner. On the Computation of Multi-Material Flows using ALE Formulation. *Journal of Computational Phsyics*, 194:303–328, 2004.

[136] S.P. Marsh. *LASL Shock Hugoniot Data*. University of California Press, 1980.

[137] R.B Medvitz, R.F. Kunz, D.A. Boger, A.M. Lindau, J.W. Yocum, and L.L. Pauley. Performance Analysis of Cavitating Flow in Centrifugal Pumps using Multiphase CFD. *Journal of Fluids Engineering*, 124:377–383, June 2002.

[138] R. Menikoff and B.J. Plohr. The Riemann Problem for Fluid Flow of Real Materials. *Reviews of Modern Physics*, 61:75–129, 1989.

[139] C.L. Merkle, J.Z. Feng, and P.E.O. Buelow. Computational Modeling of the Dynamics of Sheet Cavitation. In *Proceedings of 3rd International Symposium on Cavitation, Grenoble*, volume 2, pages 307–311, 1998.

[140] B Molin, L. Dieval, R. Marcer, and M. Arnaud. Non-Stationary Model for Cavitating Sheet by the Use of a Potential Method and a VoF Method. *6th Journées des l'Hydromenamique*, pages 31–44, 1997.

[141] K.A. Mørch. Reflections on Cavitation Nuclei in Water. *Physics of Fluids*, 19:072104, 2007.

[142] M. Mulas, S. Chibbaro, G. Delussu, I. Di Piazza, and M. Talice. Efficient Parallel Computations of Flows of Arbitrary Fluids for all Regimes of Reynolds, Mach and Grashof numbers. *International Journal of Numerical Methods for heat and Fluid Flow*, 12:637–657, 2002.

[143] A. Murrone and H. Guillard. A Five-Equation Reduced Model for Compressible Two-Phase Flow Problems. *Journal of Computational Physics*, 202:664–698, 2005.

[144] M.D. Neaves and J.R. Edwards. All-Speed Time-Accurate Underwater Projectile Calculations using a Preconditioning Algorithm. *Journal of Fluids Engineering*, 128:284–296, 2006.

[145] H. Paillère, C. Corre, and J.R. Garcia Cascales. On the Extension of the AUSM+ scheme to Compressible Two-Fluid Models. *Computer & Fluids*, 32:891–916, 2003.

[146] T. Persson, G. Bark, R. Bensow, N. Berchiche, and C. Fureby. Large Eddy Simulation of the Cavitating Flow around a Wing Section. In *Sixth International Symposium on Cavitation*, 2006.

[147] M.S. Plesset. The Dynamics of Cavitation Bubbles. *Journal of Applied Mechanics*, 16:277, 1949.

[148] M.S. Plesset and A. Prosperetti. Bubble Dynamics and Cavitation. *Annual Review of Fluid Mechanics*, 9:145–185, 1977.

[149] T.J. Poinsot and S.K. Lele. Boundary Conditions for Direct Simulations of Compressible Viscous Flows. *Journal of Computational Physics*, 101:104–129, 1992.

[150] L. Prandtl. Tragflügeltheory. II C. *Göttingen Nachrichten*, 1919.

[151] A.T. Preston, T. Colonius, and C.E. Brennen. A Numerical Investigation of Unsteady Bubbly Cavitating Nozzle Flows. *Physics of Fluids*, 14:300–311, 2002.

[152] A.T. Preston, T. Colonius, and C.E. Brennen. A Reduced-Order Model of Diffusive Effects on the Dynamics of Bubbles. *Physics of Fluids*, 19:123302, 2007.

[153] F. Put. *Numerical Simulation of Condensation in Transonic Flows*. PhD thesis, University of Twente, 2003.

[154] Q. Qin. *Numerical Modeling of Natural and Ventilated Cavitating Flows*. PhD thesis, University of Minnesota, 2004.

[155] J.J. Quirk and S. Karni. On the Dynamics of a Shock-Bubble Interaction. *Journal of Fluid Mechanics*, 318:129–163, 1996.

[156] J.L. Reboud, O. Coutier-Delgosha, B. Pouffary, and R. Fortes-Patella. Numerical Simulation of Unsteady Cavitating Flows: some Applications and Open Problems. In *Fifth International Symposium on Cavitation*, 2003.

[157] J.L. Reboud and Y. Delannoy. Two-Phase Flow Modeling of Unsteady Cavitation. In *Second International Symposium on Cavitation, Tokyo*, 1994.

[158] G.E. Reisman, Y.C. Wang, and C.E. Brennen. Observations of Shock Waves in Cloud Cavitation. *Journal of Fluid Mechanics*, 355:255–283, 1998.

[159] A. Rizzi. Numerical Implementation of Solid-Body Boundary Conditions for the Euler Equations. *Zeitschrift angewandter Mathematik und Mechanik*, 58:301–304, 1978.

[160] D.H. Rudy and J.C. Strikwerda. A Non-Rreflecting Outflow Boundary Condition for Subsonic Navier-Stokes Calculations. *Journal of Computational Physics*, 36:55–70, 1980.

[161] Y. Saito, R. Takami, and I. Nakamori. Numerical Analysis of Unsteady Behavior of Cloud Cavitation around a NACA0015 Foil. *Comuter Mechanics*, 40:85–96, 2007.

[162] J. Sauer. *Instationär kavitierende Strömungen - Ein neues Modell, basierend auf Front Capturing (VoF) und Blasendynamik*. PhD thesis, Karlsruhe University, 2000.

[163] J. Sauer and G.H. Schnerr. Unsteady Cavitating Flow - A New Cavitation Model Based on a Modified Front Capturing Method and Bubble Dynamics. In *Fluids Engineering Summer Conference, Proceedings of FEDSM'00*, 2000.

[164] R. Saurel and R. Abgrall. A Multi-Phase Godunov Method for Compressible Multi-Fluid and Multi-Phase Flows. *Journal of Computational Physics*, 150:425–467, 1999.

[165] R. Saurel and R. Abgrall. A Simple Method for Compressible Multi-Fluid Flows. *SIAM J. SCI. Comput.*, 21(3):1115–1145, 1999.

[166] R. Saurel, J.P. Cocchi, and P.B. Butler. A Numerical Study of Cavitation in the Wake of a Hypervelocity Underwater Profile. *Journal of Propulsion and power*, 15(4):513–522, 1999.

[167] R. Saurel and O. Lemetayer. A Multi-Phase Model for Compressible Flows with Interfaces, Shocks, Detonation Waves and Cavitation. *Journal of Fluid Mechanics*, 431:239–271, 2001.

[168] E. Schmidt. *Properties of Water and Steam in SI-Units; 0-800 °C, 0-1000 bar*. Springer-Verlag, R. Oldenbourg, 4th, enlarged printing edition, 1989.

[169] S.J. Schmidt, I.H. Sezal, and G.H. Schnerr. Compressible Simulation of High-Speed Hydrodynamics with Phase Change. *ECCOMAS CFD*, 2006.

[170] S.J. Schmidt, I.H. Sezal, G.H. Schnerr, and M. Talhamer. Riemann Techniques for the Simulation of Compressible Liquid Flows with Phase-Transition at all Mach numbers - Shock and Wave Dynamics in Cavitating 3D Micro and Macro Systems. In *46th AIAA Aerospace Sciences Meeting and Exhibit*, number AIAA 2008-1238, 2008.

[171] G.H. Schnerr, S.J. Schmidt, I.H. Sezal, and M. Thalhamer. Schock and Wave Dynamics of Compressible Liquid Flows with Special Emphasis on Unsteady Load on Hydrofoils and on Cavitation in Injection Nozzles. In *Proceedings CAV2006*, Sixth International Symposium on Cavitation, Wageningen, The Netherlands, 2006. CD-ROM publication.

[172] G.H. Schnerr, I.H. Sezal, and S.J. Schmidt. Numerical Investigation of Three-Dimensional Cloud Cavitation with Special Emphasis on Collapse Induced Shock Dynamics. *Physics of Fluids*, 20:040703, 2008.

[173] I. Senocak and W. Shyy. Evaluation of Cavitation Models for Navier-Stokes Computations. *Proceedings of ASME FEDSM 02*, FEDSM2002-31011, 2002.

[174] I. Senocak and W. Shyy. Interfacial Dynamics-Based Modeling of Turbulent Cavitating Flows. Part 1: Model Development and Steady-State Computations. *International journal for numerical methods in fluids*, 44:975–995, 2004.

[175] I. Senocak and W. Shyy. Interfacial Dynamics-Based Modeling of Turbulent Cavitating Flows. Part 2: Time-Dependent Computations. *International journal for numerical methods in fluids*, 44:997–1016, 2004.

[176] E.J. Shaughnessy, I.M. Katz, and J.P. Schaffer. *Introduction to Fluid Mechanics*. Oxford University Press, 2005.

[177] B.R. Shin, S. Yamamoto, and X. Yuan. Application of Preconditioning Method to Gas-Liquid Two-Phase Flow Computations. *Journal of Fluids Engineering*, 126:605–612, 2004.

[178] K.M. Shyue. An Efficient Shock-Capturing Algorithm for Compressible Multi-Component Problems. *Journal of Computational Physics*, 142:208–242, 1998.

[179] K.M. Shyue. A Fluid-Mixture Type Algorithm for Compressible Multi-Component Flow with Van der Waals Equation of State. *Journal of Computational Physics*, 156:43–88, 1999.

[180] K.M. Shyue. A Wave-Propagation based Volume Tracking Method for Compressible Multi-Component Flow in Two Space Dimensions. *Journal of Computational Physics*, 215:219–244, 2006.

[181] O. Simin. Water Hammer. *Proc. 24th Annual Convention of the American Water Works Association*, pages 341–424, 1904.

[182] A.K. Singhal, M.M. Athavale, H. Li, and Y. Jiang. Mathematical Basis and Validation of the Full Cavitation Model. *Journal of Fluids Engineering*, 124:617–624, 2002.

[183] E. Sinibaldi, F. Beux, and M.V. Salvetti. A Nmerical Method for 3D Barotropic Flows in Turbomachinery. *Flow Turbulence Combust*, 76:371–381, 2006.

[184] R.E. Sonntag, C. Borgnakke, and G.J. van Wylen. *Fundamentals of Thermodynamics*. John Wiley & Sons, Inc., sixth edition edition, 2003.

[185] A. Suresh. Positivity-Preserving Schemes in Multi-Dimensions. *SIAM J. Sci. Comput.*, 22(4):1184–1198, 2000.

[186] R. Susan-Resiga, S. Muntean, I. Anton, and S. Bernad. Numerical Investigation of 3D Cavitating Flow in Francis Turbines. *Conference on Modeling Fluid Flow (CMFF03)*, 2003.

[187] M. Sussman, K.M. Smith, M.Y. Hussaini, M. Ohta, and R. Zhi-Wei. A Sharp Interface Method for Incompressible Two-Phase Flows. *Journal of Computational Physics*, 221:469–505, 2007.

[188] R.K. Sweby. High-Resolution Schemes using Flux Limiters for Hyperbolic Conservation Laws. *SIAM Journal on Numerical Analysis*, 21(5):995–1011, 1984.

[189] K.W. Thompson. Time Dependent Boundary Conditions for Hyperbolic Systems. *Journal of Computational Physics*, 68:1–24, 1987.

[190] K.W. Thompson. Time Dependent Boundary Conditions for Hyperbolic Systems, II. *Journal of Computational Physics*, 89:439–461, 1990.

[191] J. (Sir) Thornycroft and S.W. Barnaby. Torpedo Boat Destroyers. *Minutes of Proceedings of the Institution of Civil Engineers*, 122:51–103, 1895.

[192] A.S. Tijsseling and A. Anderson. Johannes von Kries and the History of Water Hammer. *Journal of Hydraulic Engineering*, 1:1–8, 2007.

[193] T.A. Ton. Vorticity Confinement in Compressible Flow, Implementation and Validation. Master's thesis, University of Twente, 2008.

[194] E.F. Toro. *Riemann Solvers and Numerical Methods for Fluid Dynamics; A Practical Introduction*. Springer, 2nd edition, 1998.

[195] E.F. Toro, M. Spruce, and W. Speares. Restoration of the Contact Surface in the HLL-Riemann Solver. *Shock Waves*, 4:25–34, 1994.

[196] D.H. Trevena. *Cavitation and Tension in Liquids*. Adam Hilger, 1987.

[197] M.P. Tulin. Steady Two-Dimensional Cavity Flows about Slender Bodies. *David Taylor Model Basin Report 834*, 1953.

[198] E. Turkel. Preconditioned Methods for Solving the Incompressible and Low-Speed Compressible Equations. *Journal of Computational Physics*, 72:277–298, 1987.

[199] E. Turkel. Review of Preconditioning Methods for Fluid Dynamics. *Applied Numerical Mathematics*, 12:257–284, 1993.

[200] E. Turkel, R. Radespiel, and N. Kroll. Assessment of Preconditioning Methods for Multi-Dimensional Aerodynamics. *Computers & Fluids*, 26:613–634, 1997.

[201] O. Ubbink. *Numerical Prediction of Two-Fluid Systems with Sharp Interfaces*. PhD thesis, Imperial College, London, 1997.

[202] O. Ubbink and R.I. Issa. A Method for Capturing Sharp Fluid Interfaces on Arbitrary Meshes. *Journal of Computational Physics*, 153:26–50, 1999.

[203] J.S. Uhlman. The Surface Singularity Method Applied to Partially Cavitating Hydrofoils. *Journal of Ship Research*, 31(2):107–124, June 1987.

[204] A.J. Van der Hout. The Interaction of Sheet and Vortex Cavitation. Master's thesis, Delft University of Techology, 2007.

[205] S.P. van der Pijl. *Computation of Bubbly Flows with a Mass-Conserving Level-Set Method*. PhD thesis, Delft University of Technology, 2005.

[206] G.N.V.B. Vaz. *Modeling of Sheet Cavitation on Hydrofoils and Marine Propellers using Boundary Element Methods*. PhD thesis, Universidade Técnica de Lisboa, 2005.

[207] C. Veldhuis. Simulation of Cavitating Flows by solving the Three-Dimensional Preconditioned Euler Equations. Master's thesis, University of Twente, 2002.

[208] V. Venkatakrishnan. Convergence to Steady-State Solutions of the Euler Equations on Unstructured Grids with Limiters. *Journal of Computational Physics*, 118:120–130, 1995.

[209] S. Venkateswaran, J.W. Lindau, R.F. Kunz, and C.L. Merkle. Preconditioning Algorithms for the Computation of Multi-Phase Mixture Flows. *AIAA Journal*, pages 2001–0279, 2001.

[210] S. Venkateswaran, J.W. Lindau, R.F. Kunz, and L. Merkle. Computation of Multi-Phase Mixture Flows with Compressibility Effects. *Journal of Computational Physics*, 180:54–77, 2002.

[211] Y. Ventikos and G. Tzabiras. A Numerical Method for the Simulation of Steady and Unsteady Cavitating Flows. *Computers & Fluids*, 29:63–88, 2000.

[212] A.J.J. Verhoeff. *Aerodynamics of Wind Turbine Rotors*. PhD thesis, University of Twente, 2005.

[213] W. Wagner, J.R. Cooper, A. Dittman, J. Kijima, H.J. Kretzchmar, A. Kruse, R. Mareš, K. Oguchi, H. Sato, I. Stöcker, O. Šifner, Y. Takaishi, I. Tanishita, J. Trübenbach, and Th. Willkommen. The IAPWS Industrial Formulation 1997 for the Thermodynamic Properties of Water and Steam. *Journal of Engineering for Gas Turbines and Power*, 122:150–182, 2000.

[214] G.B. Wallis. *One-Dimensional Two-phase Flow*. McGraw-Hill Book Company, 1969.

[215] Y.C. Wang and C.E. Brennen. One-Dimensional Bubbly Cavitating Flows Through a Converging-Diverging Nozzle. *Journal of fluids engineering*, 120:166–170, 1998.

[216] Y.C. Wang and C.E. Brennen. Numerical Computation of Shock Waves in a Spherical Cloud of Cavitation Bubbles. *Journal of Fluids Engineering*, 121:872–880, 1999.

[217] Z.J. Wang and Y. Sun. Curvature-Based Wall Boundary Condition for the Euler Equations on Unstructured Grids. *AIAA Journal*, 41:27–33, 2003.

[218] J.M. Weiss and W.A. Smith. Preconditioning Applied to Variable and Constant Density Flows. *AIAA Journal*, 33(11):2050–2057, november 1995.

[219] P. Wesseling. *Principles of Computational Fluid Dynamics*, volume 29 of *Springer series in Computational Mathematics*. Springer, 2001.

[220] N. Wikström, G. Bark, and C. Fureby. Large Eddy Simulation of Cavitating Submerged Objects. *the Eigth International Conference on Numerical Ship Hydrodynamics*, 2003.

[221] K.M. Wrobel. *Modelling and Numerical Simulation of Flows with Evaporation and Condensation*. PhD thesis, University of Twente, 2006.

[222] T.Y-T. Wu. Cavity and Wake Flows. *Annual Reviews of Fluid Mechanics*, 4:243–284, 1972.

[223] W. Yuan, J. Sauer, and G.H. Schnerr. Modeling and Computation of Unsteady Cavitation Flows in Injection Nozzles. *Mec. Ind.*, 2:383–394, 2001.

[224] W. Yuan and G.H. Schnerr. Numerical Smulation of Two-Phase Flow in Injection Nozzles: Interaction of Cavitation and External Jet Formation. *Journal of Fluids Engineering*, 125:963–969, november 2003.

[225] L. Zhou and Z. Wang. Numerical Simulation of Cavitation Around a Hydrofoil and Evaluation of a RNG κ-ϵ Model. *Journal of Fluids Engineering*, 130:011302, 2008.

[226] P.J. Zwart. Numerical Modelling of Free Surface Flows and Cavitating Flows. *VKI lecture series: Industial Two-Phase flow CFD*, 2005.

[227] P.J. Zwart, A.G. Gerber, and T. Belamri. A Two-Phase Flow Model for Predicting Cavitation Dynamics. *ICMF 2004 International Conference on Multiphase Flow*, 2004.

TIME-DEPENDENT BOUNDARY CONDITIONS

In this appendix the time-dependent boundary conditions for the 3D unsteady Euler equations are derived. The method of Thompson [189, 190] for time-dependent non-reflecting boundary conditions is generalized for arbitrary equations of state and for arbitrary orientation of the boundary.

Consider the three-dimensional Euler equations in partial differential conservation form

$$\frac{\partial \mathbf{U}}{\partial t} + \frac{\partial \mathbf{F}_x(\mathbf{U})}{\partial x} + \frac{\partial \mathbf{F}_y(\mathbf{U})}{\partial y} + \frac{\partial \mathbf{F}_z(\mathbf{U})}{\partial z} = \mathbf{0}, \tag{A.1}$$

where $\mathbf{U} = [\rho, \rho u, \rho v, \rho w, \rho E]^T$ is the vector of conserved variables, with ρ the density, $\vec{\mathbf{u}} = [u, v, w]^T$ the velocity vector, $E = e + \frac{1}{2}\vec{\mathbf{u}}\cdot\vec{\mathbf{u}}$ the specific total energy, e the specific internal energy, and where $\mathbf{F}_x(\mathbf{U})$, $\mathbf{F}_y(\mathbf{U})$ and $\mathbf{F}_z(\mathbf{U})$ form the components of the vector of fluxes in the x-, y- and z-direction, respectively, defined by

$$\mathbf{F}_x(\mathbf{U}) = \begin{bmatrix} \rho u \\ \rho u^2 + p \\ \rho uv \\ \rho uw \\ \rho uH \end{bmatrix}, \quad \mathbf{F}_y(\mathbf{U}) = \begin{bmatrix} \rho v \\ \rho vu \\ \rho v^2 + p \\ \rho vw \\ \rho vH \end{bmatrix}, \quad \mathbf{F}_z(\mathbf{U}) = \begin{bmatrix} \rho w \\ \rho wu \\ \rho wv \\ \rho w^2 + p \\ \rho wH \end{bmatrix},$$

where $H = E + p/\rho = h + \frac{1}{2}\vec{\mathbf{u}}\cdot\vec{\mathbf{u}}$ is the specific total enthalpy. Equations of state are required to close the system, e.g. $p = p(\rho, T)$ and $e = e(\rho, T)$. Here we choose as equations of state $\rho = \rho(p, T)$ and $h = h(p, T)$ [142].

The conservation laws can be converted to an equivalent set of wave equations, which represent nonlinear waves propagating at characteristic speeds. These speeds are functions of the local solution and may vary in space and time. Unfortunately, in multi-dimensional problems no unique direction of propagation exists, because the coefficient matrices involved are not simultaneously diagonalizable [91]. Fortunately, the boundary condition analysis only requires that any one coordinate direction be diagonizable at a time, i.e. the coordinate directed along the outward unit normal vector

$\vec{\mathbf{n}}$ on the boundary considered.

First, adopt a local coordinate system $(\hat{x}, \hat{y}, \hat{z})$ with $\hat{x}$ the coordinate directed along the outward unit normal vector $\vec{\mathbf{n}}$ and where $\hat{y}$, $\hat{z}$ are coordinates in mutually orthogonal tangential directions along the boundary. Equation (A.1) can be rewritten in terms of the rotated conserved variables $\hat{\mathbf{U}} = [\rho, \rho\hat{u}, \rho\hat{v}, \rho\hat{w}, \rho E]^T$ by multiplying with the rotation matrix $\mathbf{T}$ as defined in equation (4.21) yielding

$$\frac{\partial \hat{\mathbf{U}}}{\partial t} + \frac{\partial \hat{\mathbf{F}}_{\hat{x}}(\hat{\mathbf{U}})}{\partial \hat{x}} + \frac{\partial \hat{\mathbf{F}}_{\hat{y}}(\hat{\mathbf{U}})}{\partial \hat{y}} + \frac{\partial \hat{\mathbf{F}}_{\hat{z}}(\hat{\mathbf{U}})}{\partial \hat{z}} = \mathbf{0}. \tag{A.2}$$

In the present study the wave-speed analysis is carried out using the primitive variables $\hat{\mathbf{Q}} = [p, \hat{u}, \hat{v}, \hat{w}, T]^T$ rather than the conserved variables. Then we may write

$$\frac{\partial \hat{\mathbf{U}}}{\partial t} = \mathbf{P}\frac{\partial \hat{\mathbf{Q}}}{\partial t}, \tag{A.3}$$

with $\mathbf{P}$ the matrix with elements $P_{ij} = \frac{\partial \hat{U}_i}{\partial \hat{Q}_j}$. The matrix $\mathbf{P}$ is given by

$$\mathbf{P} = \begin{bmatrix} \rho_p & 0 & 0 & 0 & \rho_T \\ \hat{u}\rho_p & \rho & 0 & 0 & \hat{u}\rho_T \\ \hat{v}\rho_p & 0 & \rho & 0 & \hat{v}\rho_T \\ \hat{w}\rho_p & 0 & 0 & \rho & \hat{w}\rho_T \\ H\rho_p - 1 + \rho h_p & \rho\hat{u} & \rho\hat{v} & \rho\hat{w} & \rho_T H + \rho h_T \end{bmatrix}, \tag{A.4}$$

where we used that $\rho E = \rho(h + \frac{1}{2}\vec{\mathbf{u}} \cdot \vec{\mathbf{u}}) - p$ and where $\rho_p = \left(\frac{\partial \rho}{\partial p}\right)_T$, $\rho_T = \left(\frac{\partial \rho}{\partial T}\right)_p$, $h_p = \left(\frac{\partial h}{\partial p}\right)_T$ and $h_T = \left(\frac{\partial h}{\partial T}\right)_p$.

The inverse of matrix $\mathbf{P}$ is denoted by $\mathbf{P}^{-1}$ and is given by

$$\mathbf{P}^{-1} = \begin{bmatrix} \dfrac{\rho h_T + \rho_T(H - \vec{\hat{\mathbf{u}}}\cdot\vec{\hat{\mathbf{u}}})}{\phi} & \hat{u}\dfrac{\rho_T}{\phi} & \hat{v}\dfrac{\rho_T}{\phi} & \hat{w}\dfrac{\rho_T}{\phi} & -\dfrac{\rho_T}{\phi} \\ -\dfrac{\hat{u}}{\rho} & \dfrac{1}{\rho} & 0 & 0 & 0 \\ -\dfrac{\hat{v}}{\rho} & 0 & \dfrac{1}{\rho} & 0 & 0 \\ -\dfrac{\hat{w}}{\rho} & 0 & 0 & \dfrac{1}{\rho} & 0 \\ \dfrac{-\rho_p(H - \vec{\hat{\mathbf{u}}}\cdot\vec{\hat{\mathbf{u}}}) + 1 - \rho h_p}{\phi} & -\hat{u}\dfrac{\rho_p}{\phi} & -\hat{v}\dfrac{\rho_p}{\phi} & -\hat{w}\dfrac{\rho_p}{\phi} & \dfrac{\rho_p}{\phi} \end{bmatrix},$$

where ϕ is defined by

$$\phi = \rho\rho_p h_T + \rho_T(1 - \rho h_p). \tag{A.5}$$

Note that, $\vec{\hat{\mathbf{u}}}\cdot\vec{\hat{\mathbf{u}}} = \vec{\mathbf{u}}\cdot\vec{\mathbf{u}}$. Similarly to equation (A.3), we may write

$$\frac{\partial \hat{\mathbf{F}}_{\hat{x}}}{\partial \hat{x}} = \tilde{\mathbf{A}}_1 \frac{\partial \hat{\mathbf{Q}}}{\partial \hat{x}}, \tag{A.6}$$

$$\frac{\partial \hat{\mathbf{F}}_{\hat{y}}}{\partial \hat{y}} = \tilde{\mathbf{A}}_2 \frac{\partial \hat{\mathbf{Q}}}{\partial \hat{y}}, \tag{A.7}$$

$$\frac{\partial \hat{\mathbf{F}}_{\hat{z}}}{\partial \hat{z}} = \tilde{\mathbf{A}}_3 \frac{\partial \hat{\mathbf{Q}}}{\partial \hat{z}}, \tag{A.8}$$

where the Jacobian matrices $\tilde{\mathbf{A}}$ with elements $\tilde{A}_{ij} = \frac{\partial \hat{F}_i}{\partial \hat{Q}_j}$ are given by

$$\tilde{\mathbf{A}}_1 = \begin{bmatrix} \hat{u}\rho_p & \rho & 0 & 0 & \hat{u}\rho_T \\ \hat{u}^2\rho_p + 1 & 2\rho\hat{u} & 0 & 0 & \hat{u}^2\rho_T \\ \hat{u}\hat{v}\rho_p & \rho\hat{v} & \rho\hat{u} & 0 & \hat{u}\hat{v}\rho_T \\ \hat{u}\hat{w}\rho_p & \rho\hat{w} & 0 & \rho\hat{u} & \hat{u}\hat{w}\rho_T \\ \hat{u}H\rho_p + \rho\hat{u}h_p & \rho H + \rho\hat{u}^2 & \rho\hat{u}\hat{v} & \rho\hat{u}\hat{w} & \rho_T\hat{u}H + \rho\hat{u}h_T \end{bmatrix}, \tag{A.9}$$

$$\tilde{\mathbf{A}}_2 = \begin{bmatrix} \hat{v}\rho_p & 0 & \rho & 0 & \hat{v}\rho_T \\ \hat{u}\hat{v}\rho_p & \rho\hat{v} & \rho\hat{u} & 0 & \hat{u}\hat{v}\rho_T \\ \hat{v}^2\rho_p + 1 & 0 & 2\rho\hat{v} & 0 & \hat{v}^2\rho_T \\ \hat{v}\hat{w}\rho_p & 0 & \rho\hat{w} & \rho\hat{v} & \hat{v}\hat{w}\rho_T \\ \hat{v}H\rho_p + \rho\hat{v}h_p & \rho\hat{u}\hat{v} & \rho H + \rho\hat{v}^2 & \rho\hat{v}\hat{w} & \rho_T\hat{v}H + \rho\hat{v}h_T \end{bmatrix}, \tag{A.10}$$

$$\tilde{\mathbf{A}}_3 = \begin{bmatrix} \hat{w}\rho_p & 0 & 0 & \rho & \hat{w}\rho_T \\ \hat{u}\hat{w}\rho_p & \rho\hat{w} & 0 & \rho\hat{u} & \hat{u}\hat{w}\rho_T \\ \hat{v}\hat{w}\rho_p & 0 & \rho\hat{w} & \rho\hat{v} & \hat{v}\hat{w}\rho_T \\ \hat{w}^2\rho_p + 1 & 0 & 0 & 2\rho\hat{w} & \hat{w}^2\rho_T \\ \hat{w}H\rho_p + \rho\hat{w}h_p & \rho\hat{u}\hat{w} & \rho\hat{v}\hat{w} & \rho H + \rho\hat{w}^2 & \rho_T\hat{w}H + \rho\hat{w}h_T \end{bmatrix}. \quad \text{(A.11)}$$

Transforming the conservation form (A.2) into primitive form and multiplying by $\mathbf{P}^{-1}$ gives:

$$\frac{\partial\hat{\mathbf{Q}}}{\partial t} + \mathbf{A}_1\frac{\partial\hat{\mathbf{Q}}}{\partial\hat{x}} + \mathbf{A}_2\frac{\partial\hat{\mathbf{Q}}}{\partial\hat{y}} + \mathbf{A}_3\frac{\partial\hat{\mathbf{Q}}}{\partial\hat{z}} = \mathbf{0}, \quad \text{(A.12)}$$

with $\mathbf{A}_k = \mathbf{P}^{-1}\tilde{\mathbf{A}}_k$ equal to

$$\mathbf{A}_1 = \begin{bmatrix} \hat{u} & \frac{\rho^2 h_T}{\phi} & 0 & 0 & 0 \\ \frac{1}{\rho} & \hat{u} & 0 & 0 & 0 \\ 0 & 0 & \hat{u} & 0 & 0 \\ 0 & 0 & 0 & \hat{u} & 0 \\ 0 & \frac{\rho(1-\rho h_p)}{\phi} & 0 & 0 & \hat{u} \end{bmatrix}, \quad \mathbf{A}_2 = \begin{bmatrix} \hat{v} & 0 & \frac{\rho^2 h_T}{\phi} & 0 & 0 \\ 0 & \hat{v} & 0 & 0 & 0 \\ \frac{1}{\rho} & 0 & \hat{v} & 0 & 0 \\ 0 & 0 & 0 & \hat{v} & 0 \\ 0 & 0 & \frac{\rho(1-\rho h_p)}{\phi} & 0 & \hat{v} \end{bmatrix},$$

$$\mathbf{A}_3 = \begin{bmatrix} \hat{w} & 0 & 0 & \frac{\rho^2 h_T}{\phi} & 0 \\ 0 & \hat{w} & 0 & 0 & 0 \\ 0 & 0 & \hat{w} & 0 & 0 \\ \frac{1}{\rho} & 0 & 0 & \hat{w} & 0 \\ 0 & 0 & 0 & \frac{\rho(1-\rho h_p)}{\phi} & \hat{w} \end{bmatrix}.$$

Now consider the wave speeds associated with the Jacobi matrix of the flux in normal direction $\hat{x}$. Therefore, rewrite equation (A.12) as

$$\frac{\partial\hat{\mathbf{Q}}}{\partial t} + \mathbf{A}_1\frac{\partial\hat{\mathbf{Q}}}{\partial\hat{x}} + \mathbf{C} = \mathbf{0}, \quad \text{(A.13)}$$

with

$$\mathbf{C} = \mathbf{A}_2 \frac{\partial \hat{\mathbf{Q}}}{\partial \hat{y}} + \mathbf{A}_3 \frac{\partial \hat{\mathbf{Q}}}{\partial \hat{z}}. \tag{A.14}$$

The 5 left and right eigenvectors $\mathbf{L}_i$ and $\mathbf{R}_i$ of matrix $\mathbf{A}_1$ satisfy

$$\mathbf{L}_i^T \mathbf{A}_1 = \lambda_i \mathbf{L}_i^T \quad \text{and} \quad \mathbf{A}_1 \mathbf{R}_i = \lambda_i \mathbf{R}_i, \tag{A.15}$$

respectively, where the eigenvalues λ_i are derived from

$$|\mathbf{A}_1 - \lambda \mathbf{I}| = 0. \tag{A.16}$$

The characteristic polynomial is found to be:

$$(\hat{u} - \lambda)^3 \left[(\hat{u} - \lambda)^2 - \frac{\rho h_T}{\phi} \right] = 0. \tag{A.17}$$

The eigenvalues are real, ordered $\lambda_1 < \lambda_2 = \lambda_3 = \lambda_4 < \lambda_5$ and read

$$\lambda_1 = \hat{u} - c, \quad \lambda_2 = \hat{u}, \quad \lambda_3 = \hat{u}, \quad \lambda_4 = \hat{u}, \quad \lambda_5 = \hat{u} + c, \tag{A.18}$$

where the speed of sound c is given by

$$c^2 = \frac{\rho h_T}{\phi} = \frac{\rho h_T}{\rho \rho_p h_T + \rho_T (1 - \rho h_p)}. \tag{A.19}$$

Defining

$$\psi = \frac{1 - \rho h_p}{h_T}, \tag{A.20}$$

and using equation (A.19) the matrices $\mathbf{A}_k$ become

$$\mathbf{A}_1 = \begin{bmatrix} \hat{u} & \rho c^2 & 0 & 0 & 0 \\ \frac{1}{\rho} & \hat{u} & 0 & 0 & 0 \\ 0 & 0 & \hat{u} & 0 & 0 \\ 0 & 0 & 0 & \hat{u} & 0 \\ 0 & \psi c^2 & 0 & 0 & \hat{u} \end{bmatrix}, \mathbf{A}_2 = \begin{bmatrix} \hat{v} & 0 & \rho c^2 & 0 & 0 \\ 0 & \hat{v} & 0 & 0 & 0 \\ \frac{1}{\rho} & 0 & \hat{v} & 0 & 0 \\ 0 & 0 & 0 & \hat{v} & 0 \\ 0 & 0 & \psi c^2 & 0 & \hat{v} \end{bmatrix},$$

$$\mathbf{A}_3 = \begin{bmatrix} \hat{w} & 0 & 0 & \rho c^2 & 0 \\ 0 & \hat{w} & 0 & 0 & 0 \\ 0 & 0 & \hat{w} & 0 & 0 \\ \frac{1}{\rho} & 0 & 0 & \hat{w} & 0 \\ 0 & 0 & 0 & \psi c^2 & \hat{w} \end{bmatrix}.$$

The left and right eigenvectors of matrix $\mathbf{A}_1$ follow from equation (A.15) with some specific choices for the degrees of freedom including the one due to the multiplicity of the eigenvalue $\lambda = \hat{u}$:

$$\mathbf{L}_1 = \begin{bmatrix} 1 \\ -\rho c \\ 0 \\ 0 \\ 0 \end{bmatrix}, \ \mathbf{L}_2 = \begin{bmatrix} -\frac{\psi}{\rho} \\ 0 \\ 0 \\ 0 \\ 1 \end{bmatrix}, \ \mathbf{L}_3 = \begin{bmatrix} 0 \\ 0 \\ 1 \\ 0 \\ 0 \end{bmatrix}, \ \mathbf{L}_4 = \begin{bmatrix} 0 \\ 0 \\ 0 \\ 1 \\ 0 \end{bmatrix}, \ \mathbf{L}_5 = \begin{bmatrix} 1 \\ \rho c \\ 0 \\ 0 \\ 0 \end{bmatrix},$$

$$\mathbf{R}_1 = \begin{bmatrix} \frac{1}{2} \\ -\frac{1}{2\rho c} \\ 0 \\ 0 \\ \frac{\psi}{2\rho} \end{bmatrix}, \ \mathbf{R}_2 = \begin{bmatrix} 0 \\ 0 \\ 0 \\ 0 \\ 1 \end{bmatrix}, \ \mathbf{R}_3 = \begin{bmatrix} 0 \\ 0 \\ 1 \\ 0 \\ 0 \end{bmatrix}, \ \mathbf{R}_4 = \begin{bmatrix} 0 \\ 0 \\ 0 \\ 1 \\ 0 \end{bmatrix}, \ \mathbf{R}_5 = \begin{bmatrix} \frac{1}{2} \\ \frac{1}{2\rho c} \\ 0 \\ 0 \\ \frac{\psi}{2\rho} \end{bmatrix}.$$

Note that with the choices made, the left and right eigenvectors are bi-orthonormal, i.e.

$$\mathbf{L}_i^T \mathbf{R}_j = 0 \qquad \text{for} \quad i \neq j \tag{A.21}$$

$$\mathbf{L}_i^T \mathbf{R}_j = 1 \qquad \text{for} \quad i = j. \tag{A.22}$$

A diagonalizing similarity transformation may be generated for $\mathbf{A}_1$ by forming the matrix $\mathbf{S}$ such that its columns are the right eigenvectors and its inverse $\mathbf{S}^{-1}$ whose rows are the left eigenvectors. The matrix $\mathbf{S}$ and its inverse are therefore given by

$$\mathbf{S} = \begin{bmatrix} \frac{1}{2} & 0 & 0 & 0 & \frac{1}{2} \\ -\frac{1}{2\rho c} & 0 & 0 & 0 & \frac{1}{2\rho c} \\ 0 & 0 & 1 & 0 & 0 \\ 0 & 0 & 0 & 1 & 0 \\ \frac{\psi}{2\rho} & 1 & 0 & 0 & \frac{\psi}{2\rho} \end{bmatrix}, \quad \mathbf{S}^{-1} = \begin{bmatrix} 1 & -\rho c & 0 & 0 & 0 \\ -\frac{\psi}{\rho} & 0 & 0 & 0 & 1 \\ 0 & 0 & 1 & 0 & 0 \\ 0 & 0 & 0 & 1 & 0 \\ 1 & \rho c & 0 & 0 & 0 \end{bmatrix}. \tag{A.23}$$

The similarity transformation is then

$$\mathbf{S}^{-1} \mathbf{A}_1 \mathbf{S} = \mathbf{\Lambda}, \tag{A.24}$$

where $\mathbf{\Lambda}$ is the diagonal matrix of the eigenvalues. Applying this transformation to equation (A.13) gives

$$\mathbf{S}^{-1} \frac{\partial \hat{\mathbf{Q}}}{\partial t} + \mathbf{\Lambda} \mathbf{S}^{-1} \frac{\partial \hat{\mathbf{Q}}}{\partial \hat{x}} + \mathbf{S}^{-1} \mathbf{C} = \mathbf{0}. \tag{A.25}$$

Alternatively, the component form is obtained by multiplying equation (A.13) with $\mathbf{L}_i^T$:

$$\mathbf{L}_i^T \frac{\partial \hat{\mathbf{Q}}}{\partial t} + \lambda_i \mathbf{L}_i^T \frac{\partial \hat{\mathbf{Q}}}{\partial \hat{x}} + \mathbf{L}_i^T \mathbf{C} = 0, \quad \text{for } i = 1, .., 5 \tag{A.26}$$

Defining the column vector $\mathfrak{L}$ with components $\mathfrak{L}_i$ as

$$\mathfrak{L}_i = \lambda_i \mathbf{L}_i^T \frac{\partial \hat{\mathbf{Q}}}{\partial \hat{x}}, \tag{A.27}$$

gives

$$\begin{aligned}
\mathfrak{L}_1 &= \lambda_1 \left(\frac{\partial p}{\partial \hat{x}} - \rho c \frac{\partial \hat{u}}{\partial \hat{x}} \right) && \text{(A.28)} \\
\mathfrak{L}_2 &= \lambda_2 \left(-\frac{\psi}{\rho} \frac{\partial p}{\partial \hat{x}} + \frac{\partial T}{\partial \hat{x}} \right) && \text{(A.29)} \\
\mathfrak{L}_3 &= \lambda_3 \frac{\partial \hat{v}}{\partial \hat{x}} && \text{(A.30)} \\
\mathfrak{L}_4 &= \lambda_4 \frac{\partial \hat{w}}{\partial \hat{x}} && \text{(A.31)} \\
\mathfrak{L}_5 &= \lambda_5 \left(\frac{\partial p}{\partial \hat{x}} + \rho c \frac{\partial \hat{u}}{\partial \hat{x}} \right), && \text{(A.32)}
\end{aligned}$$

or writing in terms of $\frac{\partial \hat{\mathbf{Q}}}{\partial \hat{x}}$

$$\begin{aligned}
\frac{\partial p}{\partial \hat{x}} &= \frac{1}{2} \left(\frac{\mathfrak{L}_5}{\lambda_5} + \frac{\mathfrak{L}_1}{\lambda_1} \right) && \text{(A.33)} \\
\frac{\partial \hat{u}}{\partial \hat{x}} &= \frac{1}{2\rho c} \left(\frac{\mathfrak{L}_5}{\lambda_5} - \frac{\mathfrak{L}_1}{\lambda_1} \right) && \text{(A.34)} \\
\frac{\partial \hat{v}}{\partial \hat{x}} &= \frac{\mathfrak{L}_3}{\lambda_3} && \text{(A.35)} \\
\frac{\partial \hat{w}}{\partial \hat{x}} &= \frac{\mathfrak{L}_4}{\lambda_4} && \text{(A.36)} \\
\frac{\partial T}{\partial \hat{x}} &= \frac{\mathfrak{L}_2}{\lambda_2} + \frac{\psi}{2\rho} \left(\frac{\mathfrak{L}_5}{\lambda_5} + \frac{\mathfrak{L}_1}{\lambda_1} \right). && \text{(A.37)}
\end{aligned}$$

Equation (A.26) can now be written as

$$\mathbf{L}_i^T \frac{\partial \hat{\mathbf{Q}}}{\partial t} + \mathfrak{L}_i + \mathbf{L}_i^T \mathbf{C} = 0. \tag{A.38}$$

The problem of implementing boundary conditions is now reduced to the problem of computing the appropriate values for the $\mathfrak{L}_i$ terms. Given the values for $\mathfrak{L}_i$ equation (A.25) can be solved for $\frac{\partial \hat{\mathbf{Q}}}{\partial t}$ by multiplying by $\mathbf{S}$ giving:

$$\frac{\partial \hat{\mathbf{Q}}}{\partial t} + \mathbf{S}\mathfrak{L} + \mathbf{C} = 0, \tag{A.39}$$

where

$$\mathbf{S}\mathfrak{L} = \begin{bmatrix} \frac{1}{2}\left(\mathfrak{L}_1 + \mathfrak{L}_5\right) \\ \frac{1}{2\rho c}\left(-\mathfrak{L}_1 + \mathfrak{L}_5\right) \\ \mathfrak{L}_3 \\ \mathfrak{L}_4 \\ \frac{\psi}{2\rho}\left(\mathfrak{L}_1 + \mathfrak{L}_5\right) + \mathfrak{L}_2 \end{bmatrix} = \begin{bmatrix} d_1 \\ d_2 \\ d_3 \\ d_4 \\ d_5 \end{bmatrix}. \tag{A.40}$$

Written in full the primitive form (A.39) becomes

$$\frac{\partial p}{\partial t} + d_1 + \hat{v}\frac{\partial p}{\partial \hat{y}} + \hat{w}\frac{\partial p}{\partial \hat{z}} + \rho c^2\left(\frac{\partial \hat{v}}{\partial \hat{y}} + \frac{\partial \hat{w}}{\partial \hat{z}}\right) = 0 \tag{A.41}$$

$$\frac{\partial \hat{u}}{\partial t} + d_2 + \hat{v}\frac{\partial \hat{u}}{\partial \hat{y}} + \hat{w}\frac{\partial \hat{u}}{\partial \hat{z}} = 0 \tag{A.42}$$

$$\frac{\partial \hat{v}}{\partial t} + d_3 + \hat{v}\frac{\partial \hat{v}}{\partial \hat{y}} + \hat{w}\frac{\partial \hat{v}}{\partial \hat{z}} + \frac{1}{\rho}\frac{\partial p}{\partial \hat{y}} = 0 \tag{A.43}$$

$$\frac{\partial \hat{w}}{\partial t} + d_4 + \hat{v}\frac{\partial \hat{w}}{\partial \hat{y}} + \hat{w}\frac{\partial \hat{w}}{\partial \hat{z}} + \frac{1}{\rho}\frac{\partial p}{\partial \hat{z}} = 0 \tag{A.44}$$

$$\frac{\partial T}{\partial t} + d_5 + \hat{v}\frac{\partial T}{\partial \hat{y}} + \hat{w}\frac{\partial T}{\partial \hat{z}} + \psi c^2\left(\frac{\partial \hat{v}}{\partial \hat{y}} + \frac{\partial \hat{w}}{\partial \hat{z}}\right) = 0, \tag{A.45}$$

where the d_i's are defined in equation (A.40). The spatial derivatives in normal direction in the definitions of $\mathfrak{L}_i$ in equations (A.28)-(A.32) are calculated by employing a first order forward discretizaton

$$\frac{\partial \phi}{\partial \hat{x}} = \frac{\phi_g - \phi_i}{\Delta \hat{x}}, \tag{A.46}$$

where ϕ_g denotes the value of variable ϕ in the ghost cell at the previous time-level and $\Delta\hat{x}$ is the distance between the ghost cell and the center of gravity of the control volume, which is equal to the characteristic length ℓ of the control volume defined as the diameter of the smallest inscribed sphere of the control volume. The time derivatives in equations (A.41)–(A.45) are calculated with the time integration method described in section 4.4 to obtain the new rotated primitive variables $\hat{\mathbf{Q}}_g^+$ in the ghost cells yielding:

$$\hat{\mathbf{Q}}_g^+ = \hat{\mathbf{Q}}_g - \Delta t\left(\mathbf{d} + \mathbf{C}\right), \tag{A.47}$$

with $\mathbf{d}$ and $\mathbf{C}$ defined in equations (A.40) and (A.14), respectively. The new rotated primitive variables $\hat{\mathbf{Q}}_g^+$ are then rotated back to (x, y, z) coordinates by multiplying with the inverse $\mathbf{T}^{-1}$ of the rotation matrix defined in equation (4.21). The new conserved variables $\mathbf{U}_g^+$ in the ghost points can then be obtained through the appropriate equations of state $\rho_g^+ = \rho(p_g^+, T_g^+)$ and $h_g^+ = h(p_g^+, T_g^+)$.

The dependance of the characteristics on an arbitrary equation of state turned out to be reduced to the formulation of the two variables c, the speed of sound defined in equation (A.19), and ψ defined in equation (A.20).

ROTATIONAL INVARIANCE OF 3D EULER EQUATIONS

APPENDIX B

The rotational invariance property of the Euler equations is a well known property and is formulated as:

$$\vec{\mathbf{F}}(\mathbf{U}) \cdot \vec{\mathbf{n}} = \mathbf{T}^{-1}\mathbf{F}_x(\mathbf{TU}), \tag{B.1}$$

with $\vec{\mathbf{F}}(\mathbf{U})$ and $\mathbf{F}_x(\mathbf{U})$ defined in equation (4.2), $\mathbf{T}$ the rotation matrix and $\mathbf{T}^{-1}$ its inverse to be defined later on and $\vec{\mathbf{n}}$ the unit normal vector. Toro [194] presented the proof for the rotational invariance property for the Euler equations for two-dimensional flow. Billet & Toro [23] stated this property for three-dimensional flow in terms of the unit normal vector $\vec{\mathbf{n}} = [\cos\alpha\cos\beta, \sin\alpha\cos\beta, \sin\beta]^T$ as well as the hyperbolicity property of the Euler equations employing the perfect gas equation of state. In this appendix the proof of the rotational invariance of the Euler equations for three-dimensional flow is presented in terms of the unit vector $\vec{\mathbf{n}} = [n_x, n_y, n_z]^T$ without making a specific choice for the tangential unit vectors. This approach is very practical for implementation in the numerical method and provides a general description for the rotational invariance property.

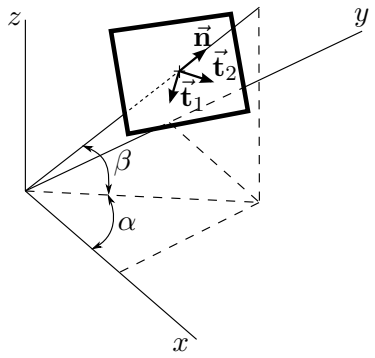

FIGURE B.1: *General unit normal vector $\vec{\mathbf{n}} = [n_x, n_y, n_z]^T$ in three-dimensional domain in (x, y, z)-space with tangential vectors $\vec{\mathbf{t}}_1$ and $\vec{\mathbf{t}}_2$. The angles α and β rotate the original coordinates (x, y, z) about the z-axis and y-axis, respectively.*

B.1 Proof of the rotational invariance property

The Euler equations for three-dimensional flow satisfy the rotational invariance property:

$$\mathbf{F}_x(\mathbf{U})n_x + \mathbf{F}_y(\mathbf{U})n_y + \mathbf{F}_z(\mathbf{U})n_z = \mathbf{T}^{-1}\mathbf{F}_x(\mathbf{TU}), \tag{B.2}$$

for all unit vectors $\mathbf{n} = [n_x, n_y, n_z]^T$ *and vectors* $\mathbf{U}$ *with* $\mathbf{F}_x$*,* $\mathbf{F}_y$ *and* $\mathbf{F}_z$ *the three components of the flux vector defined in equation (4.2) and with* $\mathbf{T}$ *the rotation matrix and* $\mathbf{T}^{-1}$ *its inverse, namely*

$$\mathbf{T} = \begin{bmatrix} 1 & 0 & 0 & 0 & 0 \\ 0 & n_x & n_y & n_z & 0 \\ 0 & t_{1,x} & t_{1,y} & t_{1,z} & 0 \\ 0 & t_{2,x} & t_{2,y} & t_{2,z} & 0 \\ 0 & 0 & 0 & 0 & 1 \end{bmatrix}, \quad \mathbf{T}^{-1} = \begin{bmatrix} 1 & 0 & 0 & 0 & 0 \\ 0 & n_x & t_{1,x} & t_{2,x} & 0 \\ 0 & n_y & t_{1,y} & t_{2,y} & 0 \\ 0 & n_z & t_{1,z} & t_{2,z} & 0 \\ 0 & 0 & 0 & 0 & 1 \end{bmatrix}, \tag{B.3}$$

where the unit vectors $\vec{\mathbf{n}}$*,* $\vec{\mathbf{t}}_1$ *and* $\vec{\mathbf{t}}_2$ *form a orthogonal system, i.e.* $\vec{\mathbf{n}}\cdot\vec{\mathbf{t}}_1 = 0$*,* $\vec{\mathbf{n}}\cdot\vec{\mathbf{t}}_2 = 0$ *and* $\vec{\mathbf{t}}_1\cdot\vec{\mathbf{t}}_2 = 0$*. Note that* $\vec{\mathbf{n}} = \vec{\mathbf{t}}_1 \times \vec{\mathbf{t}}_2$*.*

Proof. First we calculate $\hat{\mathbf{U}} = \mathbf{TU}$:

$$\mathbf{TU} = [\rho, \rho\hat{u}, \rho\hat{v}, \rho\hat{w}, \rho E]^T, \tag{B.4}$$

with $\hat{u} = \vec{\mathbf{u}} \cdot \vec{\mathbf{n}} = un_x + vn_y + wn_z$, $\hat{v} = \vec{\mathbf{u}} \cdot \vec{\mathbf{t}}_1$, and $\hat{w} = \vec{\mathbf{u}} \cdot \vec{\mathbf{t}}_2$. Note that $\mathbf{u} = (\vec{\mathbf{u}}\cdot\vec{\mathbf{n}})\,\vec{\mathbf{n}} + \left(\vec{\mathbf{u}}\cdot\vec{\mathbf{t}}_1\right)\vec{\mathbf{t}}_1 + \left(\vec{\mathbf{u}}\cdot\vec{\mathbf{t}}_2\right)\vec{\mathbf{t}}_2 = \hat{u}\vec{\mathbf{n}} + \hat{v}\vec{\mathbf{t}}_1 + \hat{w}\vec{\mathbf{t}}_2$. The vector $\mathbf{F}_x(\mathbf{TU})$ now reads

$$\mathbf{F}_x(\mathbf{TU}) = \begin{bmatrix} \rho\hat{u} \\ \rho\hat{u}^2 + p \\ \rho\hat{u}\hat{v} \\ \rho\hat{u}\hat{w} \\ \hat{u}(\rho E + p) \end{bmatrix}. \tag{B.5}$$

Rotating the vector $\mathbf{F}_x(\mathbf{TU})$ back to (x, y, z) coordinates yields:

$$\mathbf{T}^{-1}\mathbf{F}_x(\mathbf{TU}) = \begin{bmatrix} \rho\hat{u} \\ \rho\hat{u}(\hat{u}n_x + \hat{v}t_{1,x} + \hat{w}t_{2,x}) + pn_x \\ \rho\hat{u}(\hat{u}n_y + \hat{v}t_{1,y} + \hat{w}t_{2,y}) + pn_y \\ \rho\hat{u}(\hat{u}n_z + \hat{v}t_{1,z} + \hat{w}t_{2,z}) + pn_z \\ \hat{u}(\rho E + p) \end{bmatrix}. \tag{B.6}$$

Substituting $\hat{u}$, $\hat{v}$ and $\hat{w}$ and collecting the terms in u^2, uv, uw, v^2, vw, w^2 yields

$$\mathbf{T}^{-1}\mathbf{F}_x(\mathbf{TU}) = \mathbf{F}_x(\mathbf{U})n_x + \mathbf{F}_y(\mathbf{U})n_y + \mathbf{F}_z(\mathbf{U})n_z. \tag{B.7}$$

LINEAR ACOUSTICS FOR WATER HAMMER PROBLEM

APPENDIX C

In section 5.2 the Joukowsky equation, an approximation of the solution for the "Water Hammer" problem is presented. The Joukowsky equation is derived using linearized acoustic theory [181]. As presented in section 5.2 the pressure change Δp across the shock wave in water is of the order of 15 bar. This would suggest that it is inappropriate to apply linearized acoustics to this problem. In this appendix the validity of the linearization is verified.

The Euler equations for one-dimensional isentropic flow read:

$$\frac{\partial \rho}{\partial t} + \rho \frac{\partial u}{\partial x} + u \frac{\partial \rho}{\partial x} = 0, \tag{C.1}$$

$$\rho \frac{\partial u}{\partial t} + \rho u \frac{\partial u}{\partial x} + \frac{\partial p}{\partial x} = 0, \tag{C.2}$$

$$p = f(\rho). \tag{C.3}$$

Consider the situation that the acoustic wave propagates through an uniform flow field with density ρ_0, velocity u_0 and pressure p_0. Assume that the solution for the density ρ, velocity u and pressure p of the Euler equations can be written as a perturbation to the uniform flow solution:

$$\rho(x,t) = \rho_0 + \rho_0 \rho', \tag{C.4}$$

$$u(x,t) = u_0 + c_0 u', \tag{C.5}$$

$$p(x,t) = p_0 + \Delta p, \tag{C.6}$$

where the primed variables denote the dimensionless perturbations to the initial states. Substitution in the Euler equations (C.1) and (C.2) yields

$$\rho_0 \left(\frac{\partial \rho'}{\partial t} + c_0 \frac{\partial u'}{\partial x} + u_0 \frac{\partial \rho'}{\partial x} + c_0 \rho' \frac{\partial u'}{\partial x} + c_0 u' \frac{\partial \rho'}{\partial x} \right) = 0,$$

$$\rho_0 c_0 \left(\frac{\partial u'}{\partial t} + u_0 \frac{\partial u'}{\partial x} + \rho' \frac{\partial u'}{\partial t} + \frac{\partial u'}{\partial x} \left(u_0 \rho' + u' + \rho' u' \right) \right) + \frac{\partial (\Delta p)}{\partial x} = 0.$$

Assuming that $\rho' = \mathcal{O}(\epsilon)$ and $u' = \mathcal{O}(\epsilon)$ and linearizing yields

$$\frac{\partial \rho'}{\partial t} + c_0 \frac{\partial u'}{\partial x} + u_0 \frac{\partial \rho'}{\partial x} = 0, \tag{C.7}$$

$$\frac{\partial u'}{\partial t} + u_0 \frac{\partial u'}{\partial x} + \frac{1}{\rho_0 c_0} \frac{\partial (\Delta p)}{\partial x} = 0. \tag{C.8}$$

To write the pressure perturbation in terms of the density perturbation we can start from equation (C.3):

$$p_0 + \Delta p = f(\rho_0 + \rho_0 \rho') = f(\rho_0) + \rho_0 f'(\rho_0)\rho' + ... \tag{C.9}$$

Since $p_0 = f(\rho_0)$ and $f'(\rho_0) = c_0^2$ we find

$$\frac{\Delta p}{p_0} = \frac{\rho_0 c_0^2}{p_0} \rho'. \tag{C.10}$$

we recognize that small perturbations in the density result in perturbations in the pressure that have an amplification factor of $\rho_0 c_0^2 / p_0$. For the flow of a perfect gas this amplification factor is equal to γ, which for air is equal to $\gamma = 1.4$. For the flow of water the amplification factor is of the order of 2.25×10^4, illustrating the large pressure pulses possible in water flow even for small perturbations in density and velocity.

Eliminating Δp in equations (C.7) and (C.8) with equation (C.10) yields

$$\frac{\partial}{\partial t} \begin{bmatrix} \rho' \\ u' \end{bmatrix} + \begin{bmatrix} u_0 & c_0 \\ c_0 & u_0 \end{bmatrix} \frac{\partial}{\partial x} \begin{bmatrix} \rho' \\ u' \end{bmatrix} = 0. \tag{C.11}$$

The eigenvalues are:

$$\lambda_1 = u_0 + c_0, \quad \lambda_2 = u_0 - c_0, \tag{C.12}$$

and the corresponding left eigenvectors satisfy:

$$\mathbf{L}_1 = \begin{bmatrix} 1 \\ 1 \end{bmatrix}, \quad \mathbf{L}_2 = \begin{bmatrix} -1 \\ 1 \end{bmatrix}. \tag{C.13}$$

The compatibility relations are obtained from

$$\mathbf{L}_i^T \frac{d}{ds_i} \begin{bmatrix} \rho' \\ u' \end{bmatrix} = 0 \quad \text{along} \quad \frac{dx}{dt} = \lambda_i, \tag{C.14}$$

which yields in terms of Δp

$$\frac{1}{\rho_0 c_0^2} \Delta p + u' = \text{constant}, \qquad \text{along} \quad \frac{dx}{dt} = u_0 + c_0, \tag{C.15}$$

$$-\frac{1}{\rho_0 c_0^2} \Delta p + u' = \text{constant}, \qquad \text{along} \quad \frac{dx}{dt} = u_0 - c_0, \tag{C.16}$$

Equation (C.16) is written in dimensionless form. In dimensional form we recognize the Joukowksy equation (5.3) along the characteristic $\frac{dx}{dt} = u_0 - c_0$.

LIFTING LINE THEORY FOR 3D TWIST HYDROFOIL

APPENDIX D

For the fully wetted flow around the Twisted hydrofoil Prandtl‘s classical lifting-line theory is applied to estimate the spanwise distribution of the local effective angle of attack of the foil. This local effective angle of attack determines to a large extent the pressure distribution on the foil and thus the sheet cavitation on the foil. In the lifting line theory a finite wing is modeled by a single spanwise lifting line along which the circulation $\Gamma(y)$ varies as presented in figure D.1. A system of vortices with strengths $\gamma = d\Gamma/dy$ trails from the lifting line in downstream direction, representing the wake of the foil. This wake induces a down- or upwash at the lifting line, lowering or increasing the local effective angle of attack of the foil.

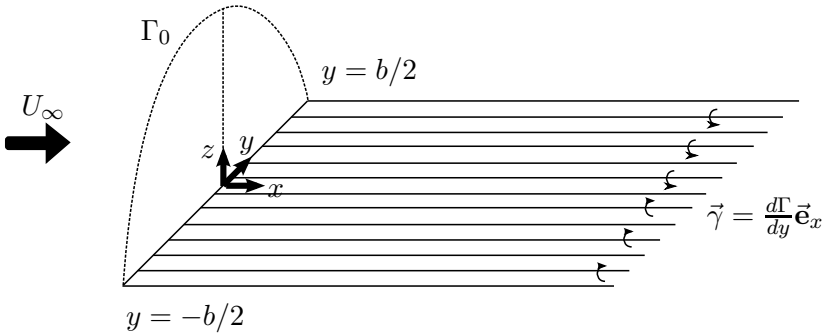

FIGURE D.1: *The lifting line model of a finite wing and its wake.*

The circulation distribution $\Gamma(y)$ is determined from Prandtl‘s lifting line theory [150], see e.g. Anderson [12]. The semi-infinite trailing vortex sheet induces a downwash w at a point y_0 located at the lifting line given by

$$w(y_0) = -\frac{1}{4\pi} \int_{-b/2}^{b/2} \frac{\frac{d\Gamma}{dy}(y)}{y_0 - y} \mathrm{d}y, \tag{D.1}$$

with b the span of the foil. For small angles of attack the induced angle of attack α_i is

$$\alpha_i \approx -\frac{w(y_0)}{U_\infty} = \frac{1}{4\pi U_\infty} \int_{-b/2}^{b/2} \frac{\frac{d\Gamma}{dy}(y)}{y_0 - y} \mathrm{d}y. \tag{D.2}$$

The lift $\ell(y_0)$ of a local section follows from the Kutta-Joukowski theorem as

$$\ell(y_0) = \rho_\infty U_\infty \Gamma(y_0), \tag{D.3}$$

which in Prandtl‘s lifting-line theory is expressed as

$$\ell(y_0) = \frac{1}{2}\rho_\infty U_\infty^2 c(y_0) c_l(y_0), \tag{D.4}$$

with $c(y_0)$ the chord of the section at y_0. The lift coefficient $c_l(y_0)$ is given by

$$c_l(y_0) = 2\pi \alpha_{eff}(y_0), \tag{D.5}$$

where the effective angle of attack α_{eff} is equal to

$$\alpha_{eff}(y_0) = \alpha(y_0) - \alpha_i(y_0) - \alpha_{\ell=0}(y_0), \tag{D.6}$$

with $\alpha(y_0)$ the geometric angle of attack and $\alpha_{\ell=0}(y_0)$ the zero-lift angle of the section. Equating equation (D.3) and (D.4) then results in Prandtl‘s fundamental integral equation of lifting line theory for the circulation distribution $\Gamma(y)$

$$\alpha(y_0) = \frac{\Gamma(y_0)}{\pi U_\infty c(y_0)} + \alpha_{\ell=0}(y_0) + \frac{1}{4\pi U_\infty} \int_{-b/2}^{b/2} \frac{\frac{d\Gamma}{dy}(y)}{y_0 - y} \mathrm{d}y. \tag{D.7}$$

This integral equation is solved iteratively for given $\alpha(y_0)$, $\alpha_{\ell=0}(y_0)$, $c(y_0)$, and U_∞. Once $\Gamma(y_0)$ is computed, $c_l(y_0)$ follows from equations (D.3) and (D.4) as

$$c_l(y_0) = \frac{2\Gamma(y_0)}{U_\infty c(y_0)}, \tag{D.8}$$

while from equations (D.5) and (D.6) we then find the induced angle of attack $\alpha_i(y_0)$ as

$$\alpha_i(y_0) = \alpha(y_0) - \alpha_{\ell=0}(y_0) - \frac{c_l(y_0)}{2\pi}. \tag{D.9}$$

The Twist hydrofoil is not a finite foil, but it extends to the channel walls, i.e. in effect it is an infinite-span foil with periodically varying twist. Furthermore, the foil is located in a hexahedron with a square cross-section. The influence of all tunnel walls on the flow around the hydrofoil can be accounted for by introducing a series

of images of the model of the lifting line. The influence experienced by the foil in the channel is the induced velocity from the vortex systems of these images. For a square tunnel of width b a doubly infinite series of images is required, situated at the points $(y = mb, z = nb)$, where m and n assume all positive and negative integers. The induced angle of attack in equation (D.2) can now be written as

$$\alpha_i(y_0) = \frac{1}{4\pi U_\infty} \sum_{m=-\infty}^{\infty} \sum_{n=-\infty}^{\infty} \int_{b/2-mb}^{b/2+mb} \frac{\frac{d\Gamma}{dy}(y_m)(y_0 - y_m)}{(y_0 - y_m)^2 + (z_0 - z_n)^2} \mathrm{d}y_m. \qquad \text{(D.10)}$$

The solution of equation (D.7) for $\Gamma(y_0)$ is obtained by discretizing the integral in equation (D.7) and solving the set of discretized equations iteratively as described in Anderson [12]. The resulting circulation distribution $\Gamma\left(\frac{y}{c}\right)$ for the Twist08 at 0° angle of attack and Twist11 hydrofoil at -3° angle of attack in the test section are presented in figure D.2.

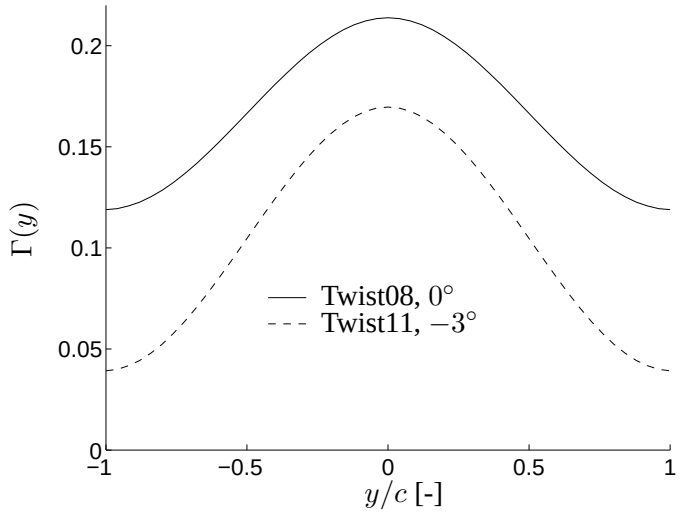

FIGURE D.2: *Circulation distribution $\Gamma(y)$ as a function of the spanwise coordinate $\frac{y}{c}$ for the Twist08 foil at 0° angle of attack (solid) and the Twist11 foil at -3° (dashed).*

The effect of the foil extending up to the channel walls is clearly seen in that $\Gamma(y)$ near the wall is no longer varying as the square root of the distance from the wall, while also at the wall the circulation is not zero. The wall boundary condition implies that $d\Gamma/dy = 0$ at the walls.

Note that for the Twist11 hydrofoil at -3° $\Gamma(y)$ has a lower value over the complete span than the Twist08 foil. So for the Twist11 foil also the local value of $c_l(y)$ will be lower along the whole span, especially near the wall. The latter is important, because we want to avoid cavitation. Also, note that compared to Twist08 $\Gamma(y)$ has a more 3D shape for the Twist11 hydrofoil at -3° angle of attack. The geometric angle of attack α_{geom} and the effective angle of attack α_{eff} for the Twist08 at 0° angle of attack and the Twist11 foil at -3° angle of attack are presented in figure D.3(a) and (b), respectively.

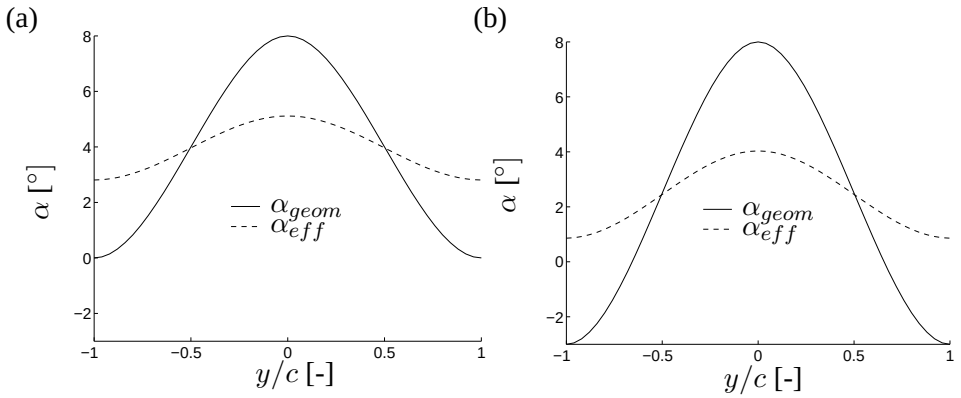

FIGURE D.3: *Geometric angle of attack α_{geom} (solid) and effective angle of attack α_{eff} (dashed) for (a) Twist08 at 0° angle of attack (b) Twist11 at -3° angle of attack.*

In Table 1 the effective angle of attack at the tunnel walls and at midspan are presented for five different configurations. Note that the effective angle of attack at the tunnel wall and at midspan is linearly dependent on the incidence of the foil as a whole.

Due to the spanwise varying lift distribution of the hydrofoil the associated vortical wake generates downwash in the central part of the hydrofoil and upwash near the tunnel walls. For the Twist08 hydrofoil at 0° angle of attack the effective angle of attack at the center is lowered from 8° to about 5°, while at the tunnel wall it is increased from 0° to almost 3°. So in order to prevent the cavity from reaching the tunnel wall, the geometric angle of attack of the hydrofoil has to be decreased in order to have a zero effective angle of attack near the tunnel wall. In the central part of the hydrofoil this then results in a much lower effective angle of attack than the geometric angle of attack and consequently in a cavity that is smaller than desired.

The Twist11 foil design results in a more three dimensional distribution of the effective angle of attack, which will produce a more triangular shaped cavitation sheet.

Foil	angle of attack [°]	α_{geom} wall [°]	α_{eff} wall [°]	α_{geom} mid-span [°]	α_{eff} mid-span [°]
Twist08	0	0	2.8	8.0	5.1
Twist08	-3	-3	-0.2	5.0	2.1
Twist11	0	0	3.9	11.0	7.0
Twist11	-2	-2	1.9	9.0	5.0
Twist11	-3	-3	0.9	8.0	4.0
Twist14	0	0	4.9	14.0	9.0
Twist14	-5	-5	-0.1	9.0	4.0

TABLE 4.1: *Effective angle of attack at tunnel walls and at midspan for the Twist08, Twist11, and Twist14 foils at various angle of attack.*

Furthermore with incidence $-3°$, the effective angle of attack at the tunnel wall will be small refraining the cavitation sheet of reaching the tunnel walls, while at midspan the effective angle of attack is still around $4°$, which is high enough for a substantial cavity sheet.

MAXWELL RELATIONS OF THERMODYNAMICS

The classical Maxwell relations of thermodynamics in terms of the independent variables specific volume $v = 1/\rho$ and temperature T read

$$\left(\frac{\partial e}{\partial T}\right)_v = c_v(T,v), \qquad \left(\frac{\partial e}{\partial v}\right)_T = -p + T\left(\frac{\partial p}{\partial T}\right)_v,$$

$$\left(\frac{\partial h}{\partial T}\right)_v = c_v(T,v) + v\left(\frac{\partial p}{\partial T}\right)_v, \qquad \left(\frac{\partial h}{\partial v}\right)_T = T\left(\frac{\partial p}{\partial T}\right)_v + v\left(\frac{\partial p}{\partial v}\right)_T,$$

$$\left(\frac{\partial S}{\partial T}\right)_v = \frac{1}{T}c_v(T,v), \qquad \left(\frac{\partial S}{\partial v}\right)_T = \left(\frac{\partial p}{\partial T}\right)_v,$$

where $e(v,T)$ is the specific internal energy, $p(T,v)$ the pressure $h(T,v)$ the specific enthalpy defined by $h = e + p/\rho$, $S(T,v)$ the entropy and $c_v(T,v)$ the specific heat constant at constant volume, assumed to be given. Taking and equating cross derivatives for $e(v,T)$ yields:

$$\left(\frac{\partial c_v(T,v)}{\partial v}\right)_T = T\left(\frac{\partial^2 p}{\partial T^2}\right)_v. \tag{E.1}$$

In terms of the independent variables p and T the Maxwell relations yield:

$$\left(\frac{\partial e}{\partial T}\right)_p = c_p(T,p) - p\left(\frac{\partial v}{\partial T}\right)_p, \qquad \left(\frac{\partial e}{\partial p}\right)_T = -T\left(\frac{\partial v}{\partial T}\right)_p - p\left(\frac{\partial v}{\partial p}\right)_T,$$

$$\left(\frac{\partial h}{\partial T}\right)_p = c_p(T,p), \qquad \left(\frac{\partial h}{\partial p}\right)_T = v(T,p) - T\left(\frac{\partial v}{\partial T}\right)_p,$$

$$\left(\frac{\partial S}{\partial T}\right)_p = \frac{1}{T}c_p(T,p), \qquad \left(\frac{\partial S}{\partial p}\right)_T = -\left(\frac{\partial v}{\partial T}\right)_p,$$

where $c_p(T,p)$ is the specific heat constant at constant pressure, assumed to be given. Taking and equating cross derivatives for $e(T,p)$ yields:

$$\left(\frac{\partial c_p(T,p)}{\partial p}\right)_T = -T\left(\frac{\partial^2 v}{\partial T^2}\right)_p. \tag{E.2}$$

From above expressions it can be derived that

$$c_p(T,p) - c_v(T,v) = T\left(\frac{\partial p}{\partial T}\right)_v \left(\frac{\partial v}{\partial T}\right)_p. \tag{E.3}$$

To derive the value of a quantity $f(x,y)$ of two variables x and y the partial derivatives can be integrated using either one of the following expressions with (x_{ref}, y_{ref}) some reference state

$$\begin{aligned} f(x,y) &= \int_{x_{ref}}^{x}\left(\frac{\partial f}{\partial x}\right)_y(\hat{x},y)\mathrm{d}\hat{x} + \int_{y_{ref}}^{y}\left(\frac{\partial f}{\partial y}\right)_x(x,\hat{y})\mathrm{d}\hat{y} \\ &\quad - \int_{x_{ref}}^{x}\int_{y_{ref}}^{y}\left(\frac{\partial^2 f}{\partial x \partial y}\right)(\hat{x},\hat{y})\mathrm{d}\hat{y}\mathrm{d}\hat{x} + f(x_{ref},y_{ref}), \end{aligned} \tag{E.4}$$

$$f(x,y) = \int_{x_{ref}}^{x}\left(\frac{\partial f}{\partial x}\right)_y(\hat{x},y_{ref})\mathrm{d}\hat{x} + \int_{y_{ref}}^{y}\left(\frac{\partial f}{\partial y}\right)_x(x,\hat{y})\mathrm{d}\hat{y} + f(x_{ref},y_{ref}),$$

$$f(x,y) = \int_{x_{ref}}^{x}\left(\frac{\partial f}{\partial x}\right)_y(\hat{x},y)\mathrm{d}\hat{x} + \int_{y_{ref}}^{y}\left(\frac{\partial f}{\partial y}\right)_x(x_{ref},\hat{y})\mathrm{d}\hat{y} + f(x_{ref},y_{ref}).$$

BAROTROPIC MODEL FOR CAVITATING FLOW

APPENDIX F

Delannoy & Kueny [58] were among the first to model cavitating flows by adopting a barotropic equation of state $\rho = \rho(p)$, directly coupling the pressure with the density. In this model it is further assumed that the vapor and the liquid share the same velocity and pressure. Furthermore, the effects of viscosity and heat conduction are neglected. Note that with the barotropic equation of state the equation for the total energy of the mixture is not needed anymore. Under these assumptions the two-phase flow is described by the following (Euler) equations for the mixture:

$$\frac{\partial \mathbf{U}}{\partial t} + \frac{\partial \mathbf{F}_x(\mathbf{U})}{\partial x} + \frac{\partial \mathbf{F}_y(\mathbf{U})}{\partial y} + \frac{\partial \mathbf{F}_z(\mathbf{U})}{\partial x} = 0, \tag{F.1}$$

where $\mathbf{U} = [\rho, \rho u, \rho v, \rho w]^T$ is the vector of conserved variables and $\mathbf{F}_x(\mathbf{U})$, $\mathbf{F}_y(\mathbf{U})$ and $\mathbf{F}_z(\mathbf{U})$ are the flux vectors given as

$$\mathbf{F} = \left[\begin{array}{ccc} \mathbf{F}_x(\mathbf{U}) & \mathbf{F}_y(\mathbf{U}) & \mathbf{F}_z(\mathbf{U}) \end{array} \right] = \left[\begin{array}{ccc} \rho u & \rho v & \rho w \\ \rho u^2 + p & \rho uv & \rho uw \\ \rho uv & \rho v^2 + p & \rho vw \\ \rho uw & \rho vw & \rho w^2 + p \end{array} \right], \tag{F.2}$$

respectively, where ρ is the density of the mixture, $\vec{\mathbf{u}} = [u, v, w]$ the velocity vector and p the pressure. The barotropic equation of state for cavitating flows is such that the mixture density equals the liquid density ρ_l when the pressure is above the saturation pressure p_{sat} and equals the vapor density ρ_v when the pressure is below the saturation pressure. Between these two states there is a smooth transition region. An appropriate equation of state is, see Koop *et al*. [113] and Veldhuis [207]:

$$\frac{\rho(p)}{\rho_l} = \frac{1}{2}\left[\Delta_+ + \Delta_- \tanh\left(\frac{C_p + \sigma}{\Delta_-}\frac{U_\infty^2}{a^2}\right)\right], \tag{F.3}$$

with Δ_+ and Δ_- given by

$$\Delta_+ = \frac{\rho_l + \rho_v}{\rho_l}, \quad \Delta_- = \frac{\rho_l - \rho_v}{\rho_l}, \tag{F.4}$$

and where U_∞^2 is a reference velocity and parameter a is directly related to the minimum speed of sound in the vapor/liquid mixture $(dp/d\rho)_{min} = a^2/\Delta_-$. The pressure coefficient C_p is given by

$$C_p = \frac{p - p_\infty}{\frac{1}{2}\rho_l U_\infty^2}, \tag{F.5}$$

and the cavitation number σ by

$$\sigma = \frac{p_\infty - p_{sat}}{\frac{1}{2}\rho_l U_\infty^2}, \tag{F.6}$$

with p_∞ a reference pressure and p_{sat} the saturation pressure at a reference temperature. A plot of the above equation of state is presented in figure F.1 using a reference temperature $T = 300$ K at which the densities for the vapor and liquid are equal to $\rho_l = 996.5\ \mathrm{kg m^{-3}}$ and $\rho_v = 0.0256\ \mathrm{kg m^{-3}}$, respectively and at which the saturation pressure is equal to $p_{sat} = 3,537$ Pa.

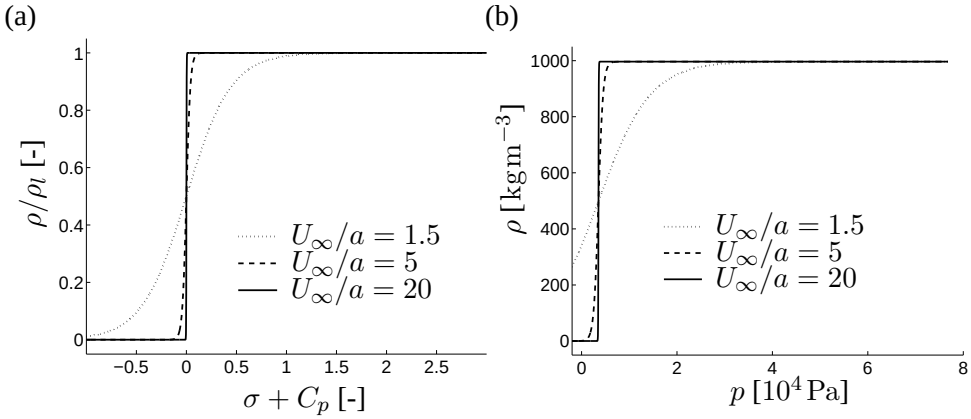

FIGURE F.1: *Barotropic equation of state for U_∞/a equal to 1.5 (dotted), 5 (dashed) and 20 (solid), respectively at $T = 300K$. The saturation liquid and vapor densities are equal to $\rho_l = 996.5\ \mathrm{kg m^{-3}}$ and $\rho_v = 0.0256\ \mathrm{kg m^{-3}}$, respectively and the saturation pressure is $p_{sat} = 3,537$ Pa. (a) Density ratio ρ/ρ_l as a function of $\sigma + C_p$. (b) Density ρ as a function of pressure p.*

NON-EQUILIBRIUM MODEL FOR CAVITATING FLOW

APPENDIX G

Within the scope of the present research we have investigated non-equilibrium models for cavitation. We followed conventional approaches by assuming that the liquid and vapor phase have a constant density. To solve the governing equations we have applied the JST flux scheme [106] and the pre-conditioner method of Weiss & Smith [218]. As discussed in section 3.5 we encountered some difficulties with the JST scheme and drawbacks of the conventional cavitation models. In this appendix we present the non-equilibrium models considered. Results are not presented, more research needs to be carried out to obtain satisfactory results.

To account for non-equilibrium effects an additional equation for either the vapor mass or liquid mass is to be introduced. Define the void fraction α as the fraction of vapor volume V_v and the volume V_{cv} of the control volume, i.e. $\alpha = \frac{V_v}{V_{cv}}$. Furthermore, define the vapor mass fraction μ as the fraction of vapor mass m_v within a computational control volume and the total mass m_{cv} within the control volume, i.e. $\mu = \frac{m_v}{m_{cv}}$. Then the continuity equation for the vapor mass can be written in one of the following equivalent forms:

$$\frac{\partial \alpha \rho_v}{\partial t} + \nabla \cdot (\alpha \rho_v \vec{\mathbf{u}}) = \mathcal{M}_v, \tag{G.1}$$

or

$$\frac{\partial \mu \rho}{\partial t} + \nabla \cdot (\mu \rho \vec{\mathbf{u}}) = \mathcal{M}_v. \tag{G.2}$$

Note that, $\alpha\rho_v = \mu\rho = m_v/V_{cv}$ and that $\rho = \alpha\rho_v + (1-\alpha)\rho_l$ where ρ_v and ρ_l denote the densities of pure liquid and pure vapor, respectively, which are assumed to be constant within the scope of this model. Assuming the temperature to remain constant, then the energy equation is decoupled from the other equations and we have the following set of equations:

$$\frac{\partial \mathbf{U}}{\partial t} + \frac{\partial \mathbf{F}_x(\mathbf{U})}{\partial x} + \frac{\partial \mathbf{F}_y(\mathbf{U})}{\partial y} + \frac{\partial \mathbf{F}_z(\mathbf{U})}{\partial z} = \mathbf{S}, \tag{G.3}$$

where $\mathbf{U} = [\rho, \rho u, \rho v, \rho w, \alpha\rho_v]^T$ is the vector of conserved variables, $\mathbf{F}_x(\mathbf{U})$, $\mathbf{F}_y(\mathbf{U})$ and $\mathbf{F}_z(\mathbf{U})$ are the flux vectors given by

$$\mathbf{F} = \left[\begin{array}{ccc} \mathbf{F}_x(\mathbf{U}) & \mathbf{F}_y(\mathbf{U}) & \mathbf{F}_z(\mathbf{U}) \end{array} \right] = \left[\begin{array}{ccc} \rho u & \rho v & \rho w \\ \rho u^2 + p & \rho uv & \rho uw \\ \rho uv & \rho v^2 + p & \rho vw \\ \rho uw & \rho vw & \rho w^2 + p \\ \alpha\rho_v u & \alpha\rho_v v & \alpha\rho_v w \end{array} \right], \quad \text{(G.4)}$$

and where $\mathbf{S}$ is the source term given by $\mathbf{S} = [0, 0, 0, 0, \mathcal{M}_v]^T$. The source term $\mathcal{M}_v$ describes the rate of change of the vapor mass due to vaporization and condensation. In this section we describe the model of Kunz *et al*. [117] based on mass transfer rates and the model of Sauer [162], Sauer & Schnerr [163] and Yuan & Schnerr [224] based on bubble dynamics.

G.1 Source term of Kunz *et al*. [117]

Kunz *et al*. [117] modeled the source term $\mathcal{M}_v$ based on the (empirical) mass transfer rates of Merkle *et al*. [139]. Many authors have adopted these mass transfer rates in various forms using different values for the empirical constants in the model. Here we follow the notation of Kunz *et al*. [117].

The source term $\mathcal{M}_v$ is written as

$$\mathcal{M}_v = \mathcal{M}_{lv} - \mathcal{M}_{vl}. \quad \text{(G.5)}$$

For transition of liquid to vapor $\mathcal{M}_{lv}$ is modeled as being proportional to the liquid volume fraction $1 - \alpha$ and the difference of the pressure with the saturation pressure

$$\mathcal{M}_{lv} = C_{prod} \frac{\rho_v(1-\alpha)}{\frac{1}{2}\rho_l U_\infty^2 t_\infty} \min(0, p - p_{sat}), \quad \text{(G.6)}$$

where C_{prod} is an empirical constant, U_∞ is the mean flow velocity and t_∞ is a mean flow time-scale taken equal to $t_\infty = 1.0\text{s}$ or $t_\infty = U_\infty/c$. Note that, both options are used in the literature. For the transfer from vapor to liquid a simplified form of the Ginzburg-Landau potential [117] is employed:

$$\mathcal{M}_{vl} = C_{dest} \frac{\rho_v(1-\alpha)^2\alpha}{t_\infty}. \quad \text{(G.7)}$$

Here also, C_{dest} is an empirical constant. Various authors have adopted these source terms for the production and destruction of vapor. As presented in table 7.1 these authors use different values for the empirical constants C_{prod} and C_{dest}. Wikström [220] mentions that C_{prod} and C_{dest} must be set as high as possible in order to simulate almost instant transition.

Article	C_{prod}	C_{dest}
Kunz *et al.* (1999) [117]	0.2	0.2
Kunz *et al.* (2000) [118]	100	100
Medvitz *et al.* (2002) [137]	100	1000
Wikström *et al.* (2003)	1000	1000
Lindau *et al.* (2002) [129]	100,000	200
Huuva (2008) [99]	1000	1000

TABLE 7.1: *Employed values for C_{prod} and C_{dest} found in the literature.*

G.2 Source term of Sauer [162]

Kubota *et al.* [116] were among the first to model the two-phase fluid as a dispersed mixture of an incompressible liquid and tiny vapor bubbles, which grow or collapse according to their surroundings, i.e. the local pressure and temperature. Sauer [162], Sauer & Schnerr [163] and Yuan & Schnerr [224] adopted this approach within a Volume of Fluid (VoF) framework. It is their model [162] for the source term $\mathcal{M}_v$ that is described in this section.

The fluid is considered as a dispersed two-phase flow with vapor bubbles which grow and collapse and thus change the void fraction in a computational control volume. The void fraction is defined as the fraction of the volume of vapor V_v within a control volume with volume $V_{cv} = V_v + V_l$ and it may be written in terms of the total volume of the bubbles within a control volume:

$$\alpha \equiv \frac{V_v}{V_v + V_l} = \frac{N_{bubbles}\frac{4}{3}\pi R^3}{N_{bubbles}\frac{4}{3}\pi R^3 + V_l} = \frac{n_0 V_l \cdot \frac{4}{3}\pi R^3}{n_0 V_l \cdot \frac{4}{3}\pi R^3 + V_l} = \frac{n_0 \cdot \frac{4}{3}\pi R^3}{n_0 \cdot \frac{4}{3}\pi R^3 + 1},$$

where V_v and V_l are the volumes occupied by the vapor and the liquid, respectively. All bubbles in the control volume are assumed to have the same radius R. $N_{bubbles}$ is the number of bubbles within the control volume and it is equal to the bubble concentration n_0 per unit volume of pure liquid times the volume V_l occupied by the liquid within the control volume. The rate of change $\mathcal{M}_v$ of the vapor mass due to phase transition does now depend on the number of bubbles per control volume times the volume change of a single bubble:

$$\mathcal{M}_v = \rho_v \frac{n_0}{1 + \frac{4}{3}\pi n_0 R^3} \frac{d}{dt}\left(\frac{4}{3}\pi R^3\right). \tag{G.8}$$

Under the assumption that effects of bubble-bubble interactions and bubble coalescence can be neglected and that the bubbles remain spherical, the Rayleigh-Plesset equation, see eg. Brennen [29], is adopted to describe the bubble growth and collapse:

$$R\frac{d^2R}{dt^2} + \frac{3}{2}\left(\frac{dR}{dt}\right)^2 = \frac{p - p_\infty}{\rho_l} - \frac{2\sigma}{\rho_l R} - \frac{4\mu}{\rho_l R}\frac{dR}{dt}, \tag{G.9}$$

where σ is the surface tension and μ is the viscosity of the liquid. Neglecting viscosity, the surface tension and second-order terms, the Rayleigh equation results, which may be considered for the so-called inertia-controlled bubble growth:

$$\frac{dR}{dt} = \sqrt{\frac{2}{3}\left(\frac{p - p_\infty}{\rho_l}\right)}, \tag{G.10}$$

where p is the pressure in the liquid at the bubble boundary and p_∞ is the pressure in the liquid at a large distance from the bubble. Within the scope of this model p is set equal to the saturation pressure p_{sat} and p_∞ to the pressure in the control volume. To account for the collapse of the bubble as well, the rate of change of the bubble radius can be written as:

$$\frac{dR}{dt} = sign(p_{sat} - p)\sqrt{\frac{2}{3}\frac{|p_{sat} - p|}{\rho_l}}. \tag{G.11}$$

Finally, the source term $\mathcal{M}_v$ reads

$$\mathcal{M}_v = sign(p_{sat} - p)\frac{\rho_v n_0 \cdot 4\pi R^2}{\left(1 + n_0 \cdot \frac{4}{3}\pi R^3\right)}\sqrt{\frac{2}{3}\frac{|p_{sat} - p|}{\rho_l}}. \tag{G.12}$$

G.3 Remark on extension to compressible flows

In the formulation above it is assumed that ρ_l and ρ_v remain constant and that the temperature remains constant. To obtain a fully compressible flow formulation these assumptions must be relaxed. In addition to the system of equations in equation (G.3), the equation for conservation of total energy and appropriate equations of state for water, two-phase mixture and vapor must be formulated. Assuming that the two-phase mixture is allowed to be in non-equilibrium, we must account for two pressures, i.e. a liquid pressure and a vapor pressure, within a computational control volume. As discussed in section 3.5 a major challenge lies in preserving the hyperbolicity of the system of equations. The pressure in the liquid phase will become "negative", i.e. a tensile stress. When returning to a positive pressure in the vapor phase from a negative pressure in the liquid phase an inflection point is created in the p-v-curve resulting in complex eigenvalues. The question is which equation of state can be used for this regime. The acoustic eigenvalues for the Sanchez-Lacombe equation of state, see Edwards & Liou [63], for densities between the spinodal values or the Van der Waals equation of state are complex-valued, implying that the system of Euler equations coupled with these equations of state is not hyperbolic. The equations of state discussed in section 3.3 need to be accompanied with an appropriate equation of state for the vapor phase.

ACKNOWLEDGMENT

During the course of the last years many people have contributed in various ways to the work presented in this thesis. In particular I would like to thank the following people.

First of all, I would like to thank Prof. Hoeijmakers for the supervision and guidance of this research. Harry, thanks for the many discussions on cavitation and numerical methods and for the pleasant (work) environment you have provided.

I would like to thank Prof. Schnerr for his critical view on my work and for sharing his extensive knowledge on the physical and numerical aspects of cavitating flows. Furthermore, I would like to thank the members of his group at TU Munich for the support during my PhD period. Especially, I would like to thank Steffen Schmidt for the time and effort he has spent in helping me.

This work has been conducted in close collaboration with the Department of Maritime Technology at Delft University of Technology. I would like to thank Evert-Jan Foeth, the experimental counterpart of this project, for his contribution during the informal project meetings at Marin. I enjoyed your presentations, during which you presented your work with great detail and relativating humor.

The basis for the numerical method for cavitating flow presented in this thesis has been the unstructured-grid finite-volume method EFD-FLOW for numerically simulating flows with condensation, as developed by Frits Put and Philip Kelleners, which is gratefully acknowledged. In particular I would like to thank Philip Kelleners for sharing his knowledge and for providing the numerical program Favomesh, the mesh-preprocessing program. Christian Veldhuis and Remco Habing I would like to thank for providing their versions of EFD-FLOW-Barotropic and the preconditioned version of EFD-FLOW, respectively.

I would like to thank MARIN for hosting the informal meetings, which were held every six weeks. Especially, I would like to thank Prof. van Terwisga of MARIN/Delft University of Technology, Prof. Kuiper and Do Ligtelijn of Wärtsilä Propulsion Netherlands for their contributions during the informal meetings.

During my PhD period I had the opportunity to stay in the group of Prof. Colonius at California Institute of Technology, Pasadena, USA, from September to December 2006. I would like thank Prof. Colonius for this opportunity to work in his group. Tim, you and your colleagues shared your knowledge on cavitating flows and on numerical methods without reservation and with great pleasure. Especially, I would like to thank Prof. Brennen and Eric Johnsen for their advice and help. Furthermore, I would like to thank Natalie Vriend and Mark Hesselink for their support and friendliness during non-working hours.

This project has been financed by the Netherlands Technology Foundation STW as project TSF.6170. I would like to thank STW for their contribution. Furthermore, I would like to thank all the members of the user committee (MARIN, Wärtsilä Propulsion Netherlands, Van Voorden Gieterij BV, IHC Holland NV, Koninklijke Marine, Holland Roer Propeller, Flowserve BV, MTI Holland BV, Shell BV, Twister BV) for their participation in this project. Also thanks to Leo Korstanje and Corine Meulemans of STW for their contribution to the formal meetings of the user committee and their genuine interest in the project.

I had the pleasure to co-supervise the MSc. students Tijmen Ton and Jacco Hospers. Tijmen worked on the challenging subject ”Vorticity Confinement in Compressible Flow; Implementation and Validation”. Jacco investigated the concept of hybrid meshes in his thesis “Development and Application of Hybrid Grids for Finite Volume Methods”. Jacco and Tijmen many thanks for your valuable research in relation with my PhD thesis.

Many thanks go to the people of the group Technische Stromingsleer of University of Twente; My (former) roommates Arie, Hein, Marco, Sander and Pieter I would like to thank for the help and discussions on many subjects. Further, thanks go to my colleague PhD and MSc. students, especially to Remko, Philip, Rutger, Ryan, Remco, Jurjen, Jacco and Tijmen for making these years a very pleasant time. I would like to thank Wouter den Breeijen for all the help with computer related matters and the secretary Anjenet Mettivier-Meijer for administrative issues.

I would like to express my gratitude to my friends and family for their support and friendship over the years. I would like to thank my parents Henk and Jeanie and my brother Olger for all their enduring support and love during my life. Finally, I would like to thank Emily for all her patience, laughter and love during the last years.

Arjen Koop, August 2008

ABOUT THE AUTHOR

June 1st, 1979	Born in Willemstad, Curaçao, Netherlands Antilles
1996	VWO, CSG Jan Arentsz, Alkmaar, the Netherlands
1997	Layton High School, Layton, USA
1997 - 2003	Study Applied Mathematics, University of Twente, the Netherlands Department of Applied Analysis and Mathematical Physics MSc. thesis: "*A mathematical model for the efficacy and toxicity of aminoglycosides*" Supervisors: prof. dr. E. van Groesen, dr. S. van Gils, dr. C. Neef
2002	Internship at Oxford Centre for Industrial and Applied Mathematics (OCIAM), Oxford University, UK and United Kingdom Atomic Energy Authority (UKAEA), Culham, UK Subject: "*Impact of Poloidal flows on Toroidal Tokamak Plasma MHD equilibrium*" Supervisors: prof. H. Ockendon and dr. C. Roach
2004 - 2008	PhD student, University of Twente, the Netherlands Department of Engineering Fluid Dynamics Thesis: "*Numerical Simulation of Unsteady, Three-Dimensional Sheet Cavitation*" Supervisors: prof. dr. ir. H. Hoeijmakers and prof. dr. -ing. habil. G. Schnerr
2006	Internship at California Institute of Technology, Pasadena, USA Group of prof. Colonius and prof. Brennen
2008 - present	Project Manager CFD Offshore, MARIN